AD-A116 818 CAIRO CENTER FOR COMBUSTION (EGYPT) F/G 21/5
SPRAY MODELLING FOR MULTIFUEL ENGINES.(U)
JUL 82 M M ELKOTB DA-ERO-79-G-0017
UNCLASSIFIED NL

1 OF 3
AD A
116 818

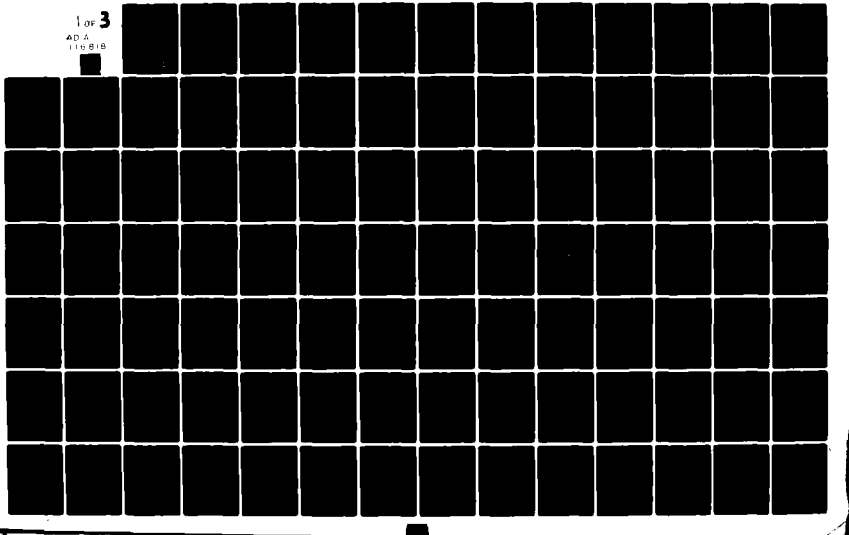

(2)

AD

SPRAY MODELLING FOR MULTIFUEL ENGINES

Second Annual Technical Report

by

ELKOTB, M.M.

Professor of Combustion
Cairo University

July 1982

EUROPEAN RESEARCH OFFICE
United States Army
London England
GRANT NUMBER DA-ERO-79-G-0017
CAIRO CENTER FOR COMBUSTION

UNCLASSIFIED

SECURITY CLASSIFICATION OF THIS PAGE *(When Data Entered)*

R&D 2690-AN

REPORT DOCUMENTATION PAGE	READ INSTRUCTIONS BEFORE COMPLETING FORM
1. REPORT NUMBER / 2. GOVT ACCESSION NO. AD-A116 846	3. RECIPIENT'S CATALOG NUMBER
4. TITLE *(and Subtitle)* Spray Modelling for Multifuel Engines	5. TYPE OF REPORT & PERIOD COVERED Second Annual Technical Rep. April 80 - April 81
	6. PERFORMING ORG. REPORT NUMBER
7. AUTHOR(s) M.M. Elkotb	8. CONTRACT OR GRANT NUMBER(s) DA-ERO-79-G-0017
9. PERFORMING ORGANIZATION NAME AND ADDRESS Cairo University Egypt	10. PROGRAM ELEMENT, PROJECT, TASK AREA & WORK UNIT NUMBERS 6.11.02A 1T161102BH57-06
11. CONTROLLING OFFICE NAME AND ADDRESS USARDSG-UK Box 65 FPO NY 09510	12. REPORT DATE July 1982
	13. NUMBER OF PAGES 202
14. MONITORING AGENCY NAME & ADDRESS *(if different from Controlling Office)*	15. SECURITY CLASS. *(of this report)* Unclassified
	15a. DECLASSIFICATION/DOWNGRADING SCHEDULE

16. DISTRIBUTION STATEMENT *(of this Report)*

Approved for Public Release Distribution Unlimited

17. DISTRIBUTION STATEMENT *(of the abstract entered in Block 20, if different from Report)*

18. SUPPLEMENTARY NOTES

19. KEY WORDS *(Continue on reverse side if necessary and identify by block number)*

20. ABSTRACT *(Continue on reverse side if necessary and identify by block number)*

The present project deals with the fuel spray modelling in multifuel engines using the droplet behaviour approach. The analysis given in the First Annual Report showed that the spray is affected by air flow field, heat transfer, fuel atomization, droplet behaviour, fuel evaporation and chemical kinetics. The present work deals with the flow field, spray modelling and fuel atomization inside multifuel engine swirl chambers.

DD FORM 1 JAN 73 1473 EDITION OF 1 NOV 65 IS OBSOLETE

UNCLASSIFIED

SECURITY CLASSIFICATION OF THIS PAGE *(When Data Entered)*

20. Contd.

Prediction of the flow field is based on the solution of the finite difference from the governing differential equations for the transport of mass, momentum and energy. The turbulence kinetic energy K and its dissipation rate ε model of turbulence has been used. A special technique has been used to satisfy compressibility, streamline curvature, non-isotropy resulting from the operating conditions and swirl chamber geometry, local continuity and reduction of the mass source at each grid node to zero.

Experiments are performed in a set up that allowed variation of swirl chamber geometry and operating conditions to measure the air velocity components and turbulence fluctuating velocities using a temperature compensated hot wire anemometer. A careful comparison of the air velocity and the predicted values over a wide range of conditions has been included to establish generalized equations for the coefficient of turbulence. Furthermore, results for the effect of engine speed and swirl chamber geometry on the flow velocity and turbulence intensity are obtained and discussed.

A new technique for the measurement of air flow velocity inside reciprocating engines based on the microphone condenser has been established. Experiments are performed on a calibrating set up to clarify the effect of medium density on the velocity measurements. Comparison with the results obtained by hot wire anemometer confirms the accuracy of the microphone condenser anemometer.

Prediction of the air flow field with the suggested model which includes the derived coefficient of turbulence shows a fairly good agreement with the measurements. Reasonable values of the turbulence mixing length at wide range of conditions have been obtained. The solution of the fuel trajectories, size and temperature histories is carried to evaluate the source terms in the gas-phase equation. Experiments have been planned to photograph the spray for various conditions to validate the model.

Analytical and experimental investigation of the atomization quality of multifuel intermittent sprays has been carried out. The effect of fuel properties and operating conditions on size distribution and mean diameter at any instant in the vicinity of the nozzle of a pintle type is studied using an automatic slide sampling technique which is built in a simulating model for multifuel engine combustion chamber. The physical properties of multifuel are firstly determined and expressions for viscosity, surface tension and density are developed.

Droplet size distribution in number fractions has been determined at various conditions. It is found that the distribution is affected by fuel pressure and properties and slightly affected by medium density. Unique comulative distribution curve is obtained. Dimensionless mathematical expressions based on seven of the known statistical distribution functions relating the droplet size distribution and mean droplet diameter with physical properties, nozzle geometry and working conditions are developed and compared. Relations are also determined for different types of mean droplet diameter as well as the maximum diameter.

AD

SPRAY MODELLING FOR MULTIFUEL ENGINES

Second Annual Technical Report

by

ELKOTB, M.M.

Professor of Combustion
Cairo University

July 1982

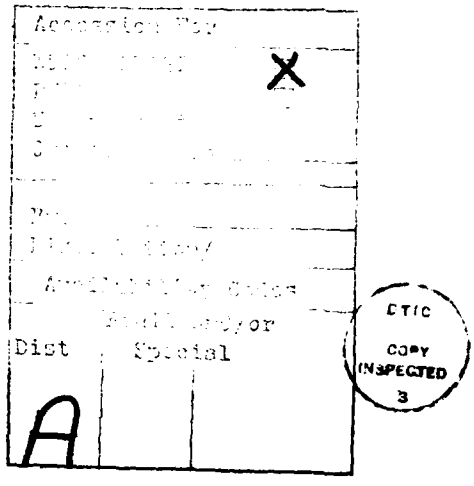

EUROPEAN RESEARCH OFFICE
United States Army
London England
GRANT NUMBER DA_ERO_79_G_0017
CAIRO CENTER FOR COMBUSTION

ACKNOWLEDGEMENT

The authors are appreciative of the financial support for this work which was provided by THE EUROPEAN RESEARCH OFFICE through Grant Number DA-ERO-79G-0017 .

CONTENTS

	Page
ACKNOWLEDGMENTS	2
SUMMARY	3
LIST OF FIGURES	5
CHAPTER 1 INTRODUCTION	17
CHAPTER 2 MATHEMATICAL MODELLING OF FLOW IN SWIRL CHAMBERS OF MULTIFUEL ENGINES	21
2.1 Introduction	21
2.2 Review of Previous Work	21
2.3 Plan of the Present Work	26
2.4 The Governing Conservation Equations	27
2.5 Estimate of Exchange Coefficients	3o
2.6 General Governing Equation	3o
2.7 Initial Conditions	32
2.8 Numerical Solution of Equations	34
CHAPTER 3 EXPERIMENTAL SET UP AND MEASURING TECHNIQUE	41
3.1 Introduction	41
3.2 Experimental Set Up	41
3.3 Calibration Set Up and Results	48
3.4 Experimental Technique	56
3.5 Error analysis	59
CHAPTER 4 PRESENTATION AND DISCUSSION OF AIR FLOW FIELD RESULTS	63
4.1 Effect of Swirl Chamber Geometry on the Turbulence Coefficient C_D	63
4.2 Comparison Between Experimental and Predicted Results	69
4.3 Effect of Swirl Chamber Parameters and Engine Speed on the Flow Field	79
CHAPTER 5 FUEL SPRAY MODELLING	129
5.1 Introduction	129
5.2 Review of Fuel Spray Modelling	132
5.3 Governing Conservation Equations	
CHAPTER 6 ATOMIZATION OF MULTIFUEL	149
6.1 Mechanism of Atomization	149
6.2 Experimental Set Up	155
6.3 Physical Properties of Multifuel	165
6.4 Droplet Size Distribution	172
6.5 Mean Diameter of Spray Droplets	174
6.6 Generalization of droplet Distribution Data	184
6.7 Generalization of Mean Droplet Diameter	19o
CHAPTER 7 CONCLUSIONS	193

SUMMARY

The present project deals with the fuel spray modelling in multifuel engines using the droplet behaviour approach. The analysis given in The First Annual Report showed that the spray is affected by air flow field, heat transfer, fuel atomization, droplet behaviour, fuel evaporation and chemical kinetics . The present work deals with the flow field,spray modelling and fuel atomization inside multifuel engine swirl chambers .

Prediction of the flow field is based on the solution of the finite difference from the governing differential equations for the transport of mass , momentum and energy . The turbulence kinetic energy K and its dissipation rate ε model of turbulence has been used . A special technique has been used to satisfy compressibility, streamline curvature , non-isotropy resulting from the operating conditions and swirl chamber geometry, local continuity and reduction of the mass source at each grid node to zero .

Experiments are performed in a set up that allowed variation of swirl chamber geometry and operating conditions to measure the air velocity components and turbulence fluctuating velocities using a temperature compensated hot wire anemometer . A careful comparison of the air velocity and the predicted values over a wide range of conditions has been included to establish generalized equations for the coefficient of turbulence . Furthermore, results for the effect of engine speed and swirl chamber geometry on the flow velocity and turbulence intensity are obtained and discussed .

A new technique for the measurement of air flow velocity inside reciprocating engines based on the microphone condenser has been established . Experiments are performed on a calibrating set up to clearify the effect of medium density on the velocity measurements . Comparison with the results obtained by hot wire anemometer confirms the accuracy of the microphone condenser anemometer .

Prediction of the air flow field with the suggested model which includes the derived coefficient of turbulence shows a fairly good agreement with the measurements . Reasonable values of the turbulence mixing length at wide range of conditions have been obtained . The solution of the fuel trajectories , size and temperature histories is carried to evaluate the source terms in the gas-phase equation . Experiments have been planed to photograph the spray for various conditions to validate the model .

Analytical and experimental investigation of the atomization quality of multifuel intermittent sprays has been carried out . The effect of fuel properties and operating conditions on size distribution and mean diameter at any instant in the vicinity of the nozzle of a pintle type is studied using an automatic slide sampling technique which is built in a simulating model for multifuel engine combustion chamber . The physical properties of multifuel are firstly determined and expressions for viscosity , surface tension and density are developed .

Droplet size distribution in number fractions has been determined at various conditions . It is found that the distribution is affected by fuel pressure and properties and slightly affected by medium density . Unique comulative distribution curve is obtained . Dimensionless mathematical expressions based on seven of the known statistical distribution functions relating the droplet size distribution and mean droplet diameter with physical properties , nozzle geometry and working conditions are developed and compared. Relations are also determined for different types of mean droplet diameter as well as the maximum diameter .

LIST OF FIGURES

PART 1

		Page
Fig.1	Computational grid	35
Fig.2	Schematic drawing of the experimental set up	43
Fig.3	Scheme of the tested swirl combustion chamber	44
Fig.4	Microphone -condenser electric circuit	46
Fig.5	Condenser microphone measuring probe	47
Fig.6	Calibration set up	49
Fig.7	Hot wire calibration curve	51
Fig.8	Determination of hot wire calibration constant	52
Fig.9	Calibration curve for microphone condenser probe	53
Fig.10	Calibration constants for mic response	54
Fig.11	Calibration curve for fluctuating velocity of microphone condenser	57
Fig.12	Two-positions of hot wire probe during measuring	58
Fig.13	Three positions of condenser microphone probe during measuring	58
Fig.14	Variation of coefficient C_D with radial distance	64
Fig.15	Variation of engine C_D with engine speed	66
Fig.16	Variation of coefficient C_D with ejection port area ratio	67
Fig.17	Variation of coefficient C_D with swirl volume ratio	68
Fig.18	Graphical representation of Eqn 7	70
Fig.19	Comparison of predicted tangential velocity by the suggested and previous methods along the radius with the experimental results at TDC	72
Fig.20	Comparison of predicted tangential velocity by the suggested and previous methods during compression and expansion strokes with the experimental results at radial distance ratio 0.503	73
Fig.21	Comparison of predicted turbulence intensity by the suggested and previous methods along the radius with the experimental results at TDC	74
Fig.22	Predicted and experimental variation of the turbulence intensity during compression and expansion strokes at radial distance ratio 0,503	75
Fig.23	Comparison of predicted radial velocity by the suggested and previous methods along the radius with the experimental results at TDC	77
Fig.24	Comparison of predicted radial velocity by the suggested and previous methods during compression and expansion strokes with the experimental results at radial distance ratio 0.503	78
Fig.25	Predicted ejection velocity and pressure ratio during compression and expansion strokes	80

		Page
Fig.26	Velocity vector plot during compression stroke	81
Fig.27	Velocity vector plot during expansion stroke	82
Fig.28	Predicted and measured tangential velocity during compression and expansion strokes in plane 4 at various radii	83
Fig.29	Predicted and measured tangential velocity in plane 4 at various radii and different crank angles	85
Fig.30	Predicted and measured radial velocity during compression and expansion strokes in plane 4 at various radii	86
Fig.31	Predicted and measured radial velocity in plane 4 and 8 at various crank angles	87
Fig.32	Turbulence intensity contours during compression stroke	88
Fig.33	Turbulence intensity contours during expansion stroke	90
Fig.34	Predicted and measured turbulence intensity during compression and expansion strokes in plane 4 at various radii	91
Fig.35	Predicted and measured turbulence intensity in plane 4 at various radii and different crank angles	92
Fig.36	Velocity vector plot for different port area ratios at 20 degrees BTDC	94
Fig.37	Predicted and measured tangential velocity during compression and expansion strokes in plane 4 for different port area ratios	95
Fig.38	Predicted and measured tangential velocity in plane 4 at TDC and various radii for different port area ratios	96
Fig.39	Predicted and measured radial velocity in plane4 at r/R_s = 0.503 and various crank angles for different port area ratios	97
Fig.40	Turbulence intensity contours for different port area ratios at 20 degree BTDC	98
Fig.41	Predicted and measured turbulence intensity in plane 4 at r/R_s= 0.503 during compression and expansion strokes for different port area ratio	100
Fig.42	Predicted and measured turbulence intensity in plane 4 at TDC and various radii for different port area ratios	101
Fig.43	Velocity vector plot for different swirl volume ratios at 20 degree BTDC	102
Fig.44	Predicted and measured tangential velocity during compression and expansion strokes in plane 4 at r/R_s = 0.503 for different swirl volume ratios	103
Fig.45	Predicted and measured tangential velocity in plane 4 and TDC for various radii and different swirl volume ratios	104

		Page
Fig.46	Predicted and measured radial velocity in plane 4 at r/R_s = 0.503 and various crank angles for different swirl volume ratios	106
Fig.47	Turbulence intensity contours for different swirl volume ratios at 20 degree BTDC	107
Fig.48	Predicted and measured turbulence intensity in plane 4 at TDC and various radii for different swirl volume ratios	108
Fig.49	Predicted and measured turbulence intensity in plane 4 at r/R_s=0.503 during compression and expansion strokes for different swirl volume ratios	109
Fig.50	Velocity vector plot for different engine speeds at 20 degree BTDC	110
Fig.51	Predicted and measured tangential velocity during compression and expansion strokes in plane 4 for r/R_s =0.503 at various engine speeds	111
Fig.52	Predicted and measured tangential velocity in plane 4 at TDC for different engine speeds	112
Fig.53	Predicted and measured radial velocity at plane 4 and r/R_s=0.503 during compression and expansion strokes at various engine speeds	114
Fig.54	Turbulence intensity contours for different engine speeds at 20 degree BTDC	115
Fig.55	Predicted and measured turbulence intensity at r/R_s=0.503 in plane 4 for various crank angles and different engine speeds	116
Fig.56	Predicted and measured turbulence intensity at TDC in plane 4 for different radii and different engine speeds	117

PART 2

		page
Fig.1	Schematic diagram of the spray combustion model of Hiroyasu.	135
Fig.2	The Fuel delivery law and injection law at various engine speeds.	142
Fig.3	The courses of swirl chamber gas pressure, fuel pressure, needle lift and location of TDC.	143
Fig.4	Control volume and introduction location of parcel.	145
Fig.5	Droplet behaviour inside combustion chambers.	145
Fig.6	Trajectory of droplets inside a swirl chamber at injection pressure 110 bar, engine speed 2000RPM, injection angle 60 degree and crankangle 30 degree bTDC.	147
Fig.7	Trajectory of a droplet inside the piston bowl at various injection pressures.	148
Fig.8	Characteristics of the first three regimes of atomization.	149
Fig.9	Air entrainment and division of fuel spray into concentric conical sprays.	150
Fig.10	Effect of Kinematic viscosity of fuel on the break up length for various injection pressures.	154
Fig.11	Schematic drawing of the experimental set up.	157
Fig.12	Pintle nozzle - type DND SD 211 Boxh dim in mm,	159
Fig.13	Slide sampling apparatus	160
Fig.14	Effect of soot layer thickness and droplet weber's number on impression diameter.	162
Fig.15	Samples of droplet photographs.	163
Fig.16	Slide sampling apparatus inside an operating piston.	164
Fig.17	Nature of kinematic viscosity variation for various blend mixtures.	165

page

Fig. 18 Nature of surface tension variation for various blend mixtures. 167

Fig. 19 Nature of density variation for various blend mixtures 168

Fig. 20 Variation of fuel viscosity with temperature rise for clear and multifuel. 170

Fig. 21 Variation of fuel density with temperature rise for clear and multifuel. 171

Fig. 22 Droplet size distribution of clear fuel sprays injected by a pintle type injector with injection pressure 118 bar. 173

Fig. 23 Droplet size distribution of diesel gasolene mixtures. 175

Fig. 24 Droplet size distribution at various medium densities. 176

Fig. 25 Droplet size distribution at various injection pressures. 176

Fig. 26 Droplet size distribution for diesel fuel sprays inside a cold engine model at various injection pressures. 177

Fig. 27 Droplet size distribution for diesel fuel sprays inside a cold engine model for various nozzle diameters. 178

Fig. 28 Variation of Sauter mean diameter with the quantity of diesel fuel in multifuel at various injection pressures. 181

Fig. 29 Effect of injection pressure on Sauter mean diameter for clear and multifuel. 182

Fig. 30 Effect of medium density on Sauter mean diameter for clear fuel at injection pressure 183

Fig. 31 Comparison between Sauter mean diameter D_{32} and other mean diameters. 183

Fig. 32 Comulative frequency distribution of droplet size for multifuel sprays with dimensionless droplet diameter. 185

page

Fig.33 Chi-square distribution curves for different degrees of freedom against experimental values. 187

Fig.34 Comparison of various distribution equations with experimental values. 189

Fig.35 Graphical representation of equation 44. 191

Fig.36 Comparison of calculated and experimental values of Sauter mean diameter. 192

PART 1

NOMENCLATURE

A	Piston area, m^2
A_c	Coefficients of finite-difference equation
A_j	Ejection area, m^2
A_p	Equal to ΣA_c
a	Cell boundary area, m^2
a'	Equal to T_p/T_u
C_{D_o}	Constant appearing in the dissipation term of turbulence model =1.0
C_d	Discharge coefficient
C_p	Constant pressure specific heat
C_{pm}	Mean piston speed, m/s
C's	Coeffecients of the turbulence model
C_v	Velocity coefficient
F	Correction factor depends on the operating conditions
f	Spatial differenceing weighting factors
G	Generation of turbulent kinetic energy
g	Gravitational acceleration, m/s^2
H	Manometer head, mm
h	Total enthalpy, kj/kg
i	Turbulence intensity $=\sqrt{2k/3}/C_{pm}$
K	Turbulent kinetic energy, m^2/s^2
K_2	Constant (equation (4.31))
M	Mass, kg
m	Exponent
N	Engine speed, rev./min.
n	Exponent
P	Pressure; bar
P'	Pressure correction, bar
P_e	Local Peclet number (equation 4.65)
P_o	Ambient pressure, bar
q	Flux through a cell wall
R	Radius, crank radius, m
R_f	Flux Richardson number
R_i	Gradient Richardson number

R_g	Gas constant,kj/kg.k
r	Radial co-ordinate
S_ϕ	Source/Sink term for variable ϕ
S_p, S_u	Coefficients of linearized source term
S_r	Relative swirl chamber volume ratio
T	Temperature,K
T_o	Ambient temperature
T_u	Velocity coefficient
T_ρ	Density coefficient
t	Time,s
U	Instantaneous turbulent velocity at any point=$\sqrt{u^2+v^2}$,m/s
$\bar{U}$	Mean value of U,m/s
$\sqrt{U'^2}$	RMS value of U,m/s
u,v,w	Instantaneous velocities in the θ,r,z directions
$\bar{u},\bar{v},\bar{w}$	Mean values of u,v,w respectively,m/s
$\sqrt{\bar{u}'^2},\sqrt{\bar{v}'^2}\sqrt{\bar{w}'^2}$	RMS valus of u,v,w respectively,m/s
U_j	Ejected air velocity,m/s
u_τ	Friction velocity =$\sqrt{\tau_w/\rho}$,m/s
$\bar{u}$	Velocity vector at any point
u^+	Dimensionless velocity =u/u_τ
V	Hot-wire anemometer reading,mv
V_o	Hot-wire anemometer initial voltage,mv
V_c	Total clearance volume,m^3
V_s	Swirl chamber volume,m^3
V_i	Instantaneous volume,m^3
V_p	Cell volume,m^3
V_h	Swept volume,m^3
X	Criterion = $(p_s/p)^{1/n}$
x,y,z	Cartesian co-ordinates
y^+	Local Reynolds number = $u_\tau y/\nu$

GREEK SYMBOLS

β	Coefficient = $(\partial\rho/\partial p)_T (V_p/\Delta t)^n$
Γ_ϕ	Effective diffusivity coefficient for variable ϕ

Δ	Increment
δ	Increment
ε	Dissipation rate ofturbulent kinetic energy, m^2/s^3
$\bar{\varepsilon}$	Compression ratio
θ	Angular distance co-ordinate
ℓ	Turbulence mixing length,m
κ	Von Karman constant
λ	Turbulence model constant
μ	Viscosity,kg/m.s
ν	Kinematic viscosity $=\mu/\rho, m^2/s$
ρ	Density,kg/m^3
Σ	Summation
σ	Prandtl/Schmidt number
$\sigma_{k,\varepsilon,h}$	Prandtl/Schmidt number for k,ε and h respectively
τ	Shear stress ,N/m^2
ϕ	Arbitrary dependent variable
ψ	Crank angle degree
ω	Vorticity

SUBSCRIPTS

b	External boundary of grid
c	Member of grid cluster
eff	Effective
∞	Pertaining to free stream condition
ℓ	Laminar
N,S,W,E	North,South,West and East neighbouring nodes
n,s,w,e	Northen,Southen,Western,or Eastern wall of cell volume
P	Grid point P
r	Radial
T	Tangential
t	Turbulent
w	Wall
xy,rx,rθ	Direction of the laminar stresses

SUPERSCRIPTS

n	New time level
o	Old time level
$\bar{}$	Mean value
'	Correction
*	Refers to the previous value of the iteration in time
·	Time rate

CHAPTER 1

INTRODUCTION

The development of multifuel engines is required to solve problems arising from the disproportion between consumption and production of diesel fuel and from the use of petroleum products in petrochemical industries. This development can be achieved by improving the combustion characteristics of various types of fuel either clear or mixture. The improvement of combustion characteristics can be achieved by shortening the ignition delay period, increasing air motion and turbulence. Therefore, the air movement in the combustion chamber of diesel engines has a great influence on the improvement of multifuel engine.

A diesel engine with swirl combustion chamber was found to be more suitable for combustion of multifuel due to the induced highly turbulent flow during the compression stroke and the injection period. The induced swirl motion of air carries the atomized fuel away from the Jet and forms a nearly homogeneous mixture with the start of combustion. Thereafter reversal of flow takes place and the gases stream out of the swirl chamber into the main engine cylinder where they continue their burning. The flow velocity and turbulence in the swirl chamber are affected by engine speed, swirl chamber volume ratio and port area ratio.

Prediction and measurement of flow and heat transfer in a motored diesel engine cylinder have been made [5,6,33] using mathematical modelling of turbulent flow field. Few studies [20-22] have been made for the prediction and measurement of flow field in diesel engine swirl chamber. However, the determination of the effect of different factors affecting it have not received detailed study. The flow inside these swirl chambers is governed by the differential conservation equations of energy, mass and momentum for turbulent flow. These governing equations are obtained by decomposing the velocity, pressure, density and enthalpy into a mean and random value. The turbulence diffusion fluxes which appear in the governing equations are modelled using Boussinesq [7] approach in terms of the mean flow gradients and eddy diffusivities. These eddy diffusivities are determined by solving additional differential conservation equations of the kinetic energy of turbulence K and its dissipation rate ε. This approach has been given in detail in the first annual report. In this approach, the values of the turbulence constants have been considered unchanged which may lead to missleading value of the mixing length during the compression stroke and inside the swirl chamber. Actually streamline wall curvature may increase or decrease the intensity of the turbulence mixing depending upon the degree of the wall curvature, and it can strongly affect the skin friction and the heat transfer rates. Bradshow [9] has showed that even very mild streamline curvature can cause significant effects on the turbulent boundary layer.

Suggestions have been made in the new approach to modify the length scale equation for rotating flow inside swirl chambers by making the constant C_1 of the ε - equation a function of the flux Richardson number based on the extra production of lateral fluctuations $\overline{v}^2$ due to the body forces. In the same time the constant C_D in the turbulence kinetic energy equation has been determined for incompressible isotropic flow. Experimental results show that the use of the recommended value can give unreliable results especially for turbulence length scale as it depends upon the local turbulence conditions. The constant C_D is multiplied in this work by a correction function which is a function of the combustion chamber geometry and engine speed to modify the turbulence equation to suit nonisotropic compressible flow.

The aim of the first part of the present work is to develop better modelling of the turbulence flow field in swirl chambers. Moreover, experimental measurements of the random flow velocity have been planned to satisfy careful comparison over a wide range of regimes with the predicted values. This facilitates the determination of reliable expression relating the constants of turbulence model with the engine operating conditions and swirl chamber geometrical parameters. An experimental set up has been built to facilitate measurements of the air velocity components inside the swirl chamber. A swirl chamber has been built up in one cylinder of a two cylinder 4-stroke water cooled diesel engine. The other cylinder has been used for motoring the engine to the required regime. The air velocity components have been measured by two measuring techniques: the microphone-condenser anemometer and temperature compensated hot-wire anemometer. A calibrations set up has been built up to calibrate both probes since their output signals depend upon air pressure and temperature. The output signals have been analysed to determine the mean velocity, random velocity and the derived statistical values. The experimental results facilitate the determination of the turbulence model constants.

The solution of the governing equations for the transport of mass, momentum, energy, kinetic energy of turbulence and its dissipation rate has been done by solving their finite-difference form using digital computer. Comparison have been carried out with the experimental results.

During the past years comprehensive works were carried out at Cairo University about spray modelling. Firstly the spray calculation model was based on the solution of the equation of motion of droplets and air. The interaction between the droplet and air was considered by averaging the over flow processes on a scale smaller than the droplet size and employing typical correlations for the droplet drag, heat and mass transfer. The results of this work which have been reported in several publications [21] were sufficiently encouraging to extend the model to include the prediction of air motion and turbulence interaction between fuel and air. Spray modelling based on the combination of the discrete droplet model with a multidimensional gas flow prediction method is the aim of the second part of the present work. However, this model is

still awaiting sufficiently detailed information about the droplet size distribution and droplet velocity distribution.

The need of the atomization characteristics, which are required for spray modelling, has been a motivating factor for a vast amount of research. It is the purpose of the third part of the present work to illustrate and discuss the problem of atomization and results obtained for clear and multifuel.

The solution of the flow field using the new approach and the measurement of velocity pattern to define the constants of the governing equations have been conducted by Prof.Elkotb, M.M., Dr. Abou-Elleil, M.M. and Eng, Salem, S.

The solution of the droplet behaviour has been conducted by Prof. Elkotb, M.M. and Dr. Abou-Elleil.

The atomization characteristics of multi fuel and the effect of various parameters have been determined experimentally. Generalized expressions have been determined for the calculation of the droplet size distribution and the mean droplet diameter. Prof.Elkotb,M.M. and Eng.Abdalla, M.A. are responsible for this part of the report. The manuscript of this annual report has been written by Prof.Elkotb,M.M. and revised by Dr.Aly, S.L. Experimental set ups for the investigation of droplet behaviour, evaporation rate and chemical rate have been built up. Their details together with the results will be discussed in the third Annual Report.

CHAPTER 2

MATHEMATICAL MODELLING OF FLOW IN SWIRL CHAMBERS OF MULTIFUEL ENGINES

2.1. Inroduction

The development of multifuel engine can be achieved by improving the burning characteristics of fuel by shortening its ignition delay. This could be improved by increasing turbulence inside the combustion chamber. Diesel engines with swirl combustion chambers are more suitable for the burning of different types of fuel due to its ability to evaporate and mix heavy fuels as well as light fuels and to work with high compression ratios | 22 |. Swirl chambers are also characterized by its ability to control combustion of fuel during period of rapid pressure rise and to obtain better burning characteristics. The study of pure phenomena in subclasses will help the solution of the more complex combustion phenomenan resulting from multifuel combustion.

Researches during the last few years show that the air movement in the combustion chamber of diesel engine in general and in swirl chambers in particular has great influence on the problem of controlling the air-fuel mixing and combustion process. Moreover, the mixing process controles combustion which inturn controles the rate of pressure rise, noise and pollutant emissions. | 5 |. It is therefore very important to measure the flow field in the motored diesel engine and to study the effect of engine operating conditions and swirl chamber geometry upon the flow field inside it.

Many researches on the prediction and few measurements of flow have been carried out in a motored diesel engine cylinder. Prediction was carried out using mathematical modelling of the turbulent flow in diesel engine cylinder with assumptions which keep the results far from the actual events when comparing these results with the measured ones. Prediction of flow field was carried out theoretically by numerical solution of the Navier - stokes equation applied to a turbulent flow motion by introducing the time-averaged properties together with statistical correlations involving fluctuating velocities and temperatures in the conservation equations. Since there is no direct way of knowing the magnitude of these terms, approximation or modelling of their effect in terms of quantities which can be determined was used. These modelling terms depend upon the local turbulence conditions especially in swirl chambers which have not received detailed study till now.

2.2. Review of Previous Work

Several theoretical studies and few experimental ones have been made to determine the flow field inside engine combustion chambers and engine main cylinder. These theoretical studies can be divided into three main categories. In the first category flow systems are

treated as being in a quasi-steady state and account being taken of time mean average properties of velocity, pressure temperature and chemical species concentration. Elkotb [18] used this theory in the calculation of the flow field inside the cylinder of two-stroke engine in which he suggested that the central part of the flow underwent a solid vortex motion and the part near cylinder wall underwent a nearly free vortex motion. He also used this theory in calculating the flow field in swirl chambers [20] . The model in this work was based on the equality of the moment of momentum resulting from the ejection velocity to the swirl chamber and the moment of momentum of the rotating air inside the swirl chamber. This model can define the average tangential velocity. Ogasowara [61] and OZ [ ] have used this theory in calculating the trajectory of fuel spray inside a diesel engine combustion chamber. However in many cases of gas motion tangential separation surfaces arise and the flow on either side of this surface is considered a jet. The jet may be moving in the same direction or in opposite directions. The instability of these tangential separation surfaces causes eddies on it, which move in disorderly fashion both along and across the stream. This brings about a transverse transfer of momentum, heat and constituents between neighbouring jets which form a boundary layer of finite thickness with a continueous distribution of velocity, temperature and species concentration. At very low Reynolds numbers, this boundary layer may be laminar. In these works, no account being taken of the turbulence exchange flow which affects the accuracy of the flow field calculations.

At the present time several theories of turbulence are known. Prandtl's old theory of free turbulence in which he arrived at the well known formula $\tau_{xy} = \mu\, \partial u/\partial y$ and for pure turbulent nonviscous motion $\tau_{xy} = -\rho u' v'$ which indicates that the turbulence shear stress is defined by the lateral transfer of the longitudinal component of momentum. He assumed also that the transverse fluctuating velocities v' are proportional to the longitudinal fluctuating velocity u'. The longitudinal fluctuating velocity is determined in turn from the fact that during a transverse displacement of a mol of fluid it preserves its initial velocity u until its transverse displacement ceases, and the change over the distance of a transverse mole length equals $u' = \ell\, |du/dy|$, where ℓ is called Prandtl mixing length. Finally, the prandtl formula of turbulent shearing stress was written in the following form :

$$\tau_{xy} = \pm \rho \ell^2 \frac{\partial u}{\partial y} \left| \frac{\partial u}{\partial y} \right|$$

The mixing length was assumed constant in the transverse direction due to the absence of walls and proportion to a characteristic length in the longitudinal direction ($\ell = cx$). Taylor, after noticing a contradiction in Prandtl's theory of free turbulence, assumed that the turbulent shearing stress in a stream must be determined by the lateral transfer of vorticity and not, as Prandtl assumed, by momentum transfer. For two dimensional flow, the mean velocity is given by

$$\bar{\omega} = \frac{1}{2} \left(\frac{\partial \bar{u}}{\partial y} - \frac{\partial \bar{v}}{\partial x} \right)$$

neglecting $\partial \bar{v}/\partial x$ for axially symmetric flow the mean vorticity is given by

$$\bar{\omega} = \frac{1}{2} \partial u/\partial y$$

If the mean free path of a fluid particle in a turbulent flow equals ℓ_T during a transverse transfer of a particle from one layer to another, then vorticity will be equal to

$$\Delta\bar{\omega} = \ell_T \frac{\partial \bar{\omega}}{\partial y} = \frac{1}{2} \ell_T \frac{\partial^2 u}{\partial y^2}$$

from which the apparent shearing stress is obtained in the following form

$$\tau_{xy} = \pm \frac{1}{2} \rho \ell_T^2 (\partial u/\partial y)^2$$

where , $\ell_T = \ell\sqrt{2}$

Thus, Taylor removed an inconsistency of Prandtl's theory resulting from the neglection of local instantaneous pressure gradients that substantially influence momentum exchange but do not affect vorticity transfer. This hypothesis as Prandtl hypothesis needs one experimental constant for the mixing length.

Both theories gave no more accurate results for the velocity profile especially in cases that involved temperature profiles and heat transmission. This situation forced Prandtl to establish a new theory of free turbulence in which he compared the general expression for turbulent shear $\tau_{xy} = -\overline{\rho u'v'}$ with the formula proposed by Boussinesq in analogy with the Newtonian law of friction in laminar flow,

$\tau_{xy} = \rho\nu_t \partial u/\partial y$, to obtain an expression for ν_t in the following form ;

$$\nu_t = \ell^2 \partial u/\partial y$$

where the constancy of the mixing length ℓ in a transverse cross section of the jet causes the kinematic viscosity along the cross section to vary, becoming zero at the boundaries of the mixing region when $\partial u/\partial y = 0$.

In the second category of mathematical calculation of flow field, the new Prandtl theory has been used. Boni [5] used this theory for the calculation of the velocity profile in a divided-chamber, stratified charge engine using a correlation developed by Ferri ( ) for the turbulent viscosity. Diwkar [15] has also calculated the velocity profile in the cylinder of an engine during the four strokes by numerical solution of the two dimensional inviscid flow field equations. Griffen [35] reported similar calculations for a viscous flow by solving the complete Navier-stokes equations. These studies have been carried out at low Reynolds number.

Prediction of time mean average velocity, pressure, temperature and concentration in turbulent combustion system using stokes-Navier equation can be made provided the turbulent flux tensor τ, the turbulent enthalpy flux vector J_h and the turbulent chemical species flux vector J_j are specified. Turbulent exchange coefficients μ, Γ_h, Γ_j are generally used. The main difficulty in any prediction method is lack of knowledge of these turbulent fluxes and exchange coefficients. Without assuming isotropic turbulence the μ , Γ_h Γ_j associated with the turbulence exchange coefficient require individual specification. Assuming isotropic flow i.e assuming Γ_h and Γ_J to bear constant ratios to the isotropic turbulent viscosity, which gives the Prandtl and Schmidt numbers

$$\sigma_h = \mu/\Gamma_h \quad , \quad \sigma_j = \mu/\Gamma_j$$

will give one unknown μ in the governing equation system. A simple turbulence model for μ would then allow predictions to be made. In Prandtl's mixing length as mentioned before he assumed that the isotropic viscosity μ could be specified in terms of local gradients of mean quantities via a mixing length ℓ and constant mixing length parameter λ i.e. $\ell = \lambda$ times the width of the mixing region where $\lambda = 0.007$ to 0.13.

In the third category of flow field calculations, more recent work on calculating turbulent flows has postulated that the turbulence may be adequately described by the turbulent viscosity $\mu_{rx} = \rho k^{\frac{1}{2}} L$. Therefore, two differential equations are proposed for the kinetic energy K and any other variable $Z = KL$ where L is the turbulence length scale. These two equations for "k" and "Z" are developed by a combination of physical reasoning and intuitive guess work and is called Energy-Length model. Another two differential equations has been reported by Launder and spalding [50] . This two equation model of turbulence is based on the solution of additional partial differential equations for turbulent kinetic energy "k" and its dissipation rate "ε" as follows ;

$$\rho \frac{DK}{Dt} = \frac{\partial}{\partial y} \left(\frac{\mu_t}{\sigma_k} \frac{\partial k}{\partial y} \right) + \mu_t \left(\frac{\partial u}{\partial y} \right)^2 - C_D \rho \varepsilon$$

$$\rho \frac{D\varepsilon}{Dt} = \frac{\partial}{\partial y} \left(\frac{\mu_t}{\sigma_\varepsilon} \frac{\partial \varepsilon}{\partial y} \right) + \varepsilon \left| C_1 \frac{\mu_t}{K} \left(\frac{\partial u}{\partial y} \right) - C_2 \frac{\rho^2 K}{\mu_t} \right|$$

which contain three constants C_D , C_1 and C_2. They suggested that the value of C_D near the wall is determined by the relation :

$$C_D^{\frac{1}{2}} = \tau/\rho k$$

and the other constants from these relations :

$$C_1 = \frac{C_2}{C_D} - \lambda^2/(\sigma_\varepsilon C_D^{\frac{1}{2}})$$

$$C_2 = 2 C_1$$

and on the base of a wide range of experimental data for an

incompressible flow they reported the following recommended values ;

$$C_D = 0.08 \quad , \quad C_1 = 1.44 \quad , \quad C_2 = 0.18, \quad = 0.4$$

Many researchers [32,33,31,28,3] rely on a two equation model of turbulence as reported by Jones and Launder [45] which use new values for the turbulence model constants as ;

$$C_D = 1.0 \quad , \quad C_1 = 1.44 \quad \text{and} \quad C_2 = 1.92$$

They studied the laminar and turbulent flow fields in internal combustion engines using a computer code called RPM (Reciprocating Piston Motion). They compared their results with experimental results obtained by others and showed qualitative agreement during some regimes. No information has been reported about the effect of operating conditions and combustion chamber geometry upon the results.

Ramos et al [67] used the two equation k-ε model of turbulence with the same constants to calculate the flow field in a motored axisymmetric reciprocating internal combustion engine with a centrally located valve which opens and closes instantaneously. They included in their study the compressibility effects upon turbulence. No comparison with experimental data had been reported to validate the model. Elkotb et al [22] have used also the k-ε model of turbulence taking into consideration the compressibility effect to calculate the flow field rotating inside a swirl chamber of a diesel engine. Comparison has been given with experimental results which showed that rotating flow has a strong effect on turbulence.

Various extensions of this theory to flows with swirl have been proposed. This has been done by linking the r-θ shear with the r-x viscosity of the axial equation and allowing for the nonisotropy of the viscosity by taking it proportional to the second invariant of the mean flow of deformation tensor as follows ;

$$\mu_{rx} = \rho \ell^2 \left[(\partial u/\partial r)^2 + \left\{ r \frac{\partial}{\partial r} (W/r) \right\}^2 \right]^{\frac{1}{2}}$$

$$\mu_{r\theta} = \mu_{rx}/\sigma_{r\theta} \quad , \quad \ell = \lambda \, r_{0.05} \quad , \quad \lambda = 0.08(1+\lambda_s s_x)$$

$$S_x = G_\theta \; / \; G_{x, r_{0.01}}$$

$$G_x = \int_0^\alpha \rho u^2 + (P-P_\alpha) r dr$$

$$G_\theta = \int_0^\alpha \rho u \, w r^2 dr$$

The factor $(1+\lambda_s s_x)$ accounts for the change in the length scale due to swirl and is analogous to the Monin-Oboukhov formula

$$\ell = \ell_o (1 - \beta R_i)$$

where,

$$\text{Richardson number } R_i = \frac{(2w/r^2)\ \frac{\partial (rw)}{\partial r}}{(\partial u/\partial r)^2 + \left| r \frac{\partial}{\partial r} (w/r) \right|^2}$$

β is an adjustable parameter.

The above formula is suggested to consider the effect of streamline curvature and centriputal acceleration on mixing length. It is intended in this work to modify the model of turbulence to include the nonisotropy and stream line curvature effects for the calculation of the flow field in swirl chambers.

2.3. Plan of the Present Work

It is clear from the previous discussion that the accuracy of predictions is affected by the isotropy assumption for swirling flow and compressibility of medium as the case of swirl chambers of diesel engines.

Recent studies of the flow prediction inside the cylinder of internal combustion engines were carried out at low Reynolds number and weak swirling flow. Mathematical models have been used to predict the properties of turbulence flow motion using fine grids to render truncation error insignificant. No consideration of the physical properties in combustion chamber is taken, which includes the continuous variation of the medium pressure, temperature and heat transfer during flow. Moreover, the combustion chamber configuration and engine operating conditions affect the streamline curvature and centripetal acceleration which affect directly the turbulence mixing length. Till now the constants in the current k-ε model of turbulence have not been determined for swirling compressible flows or extended to portray nonisotropy. Thus turbulence model await more extensive and complete experimental data before Justifying their use in the prediction of the boundary layer type of flow in swirl chamber of diesel engines.

Since recent works dispute isotropy assumption for swirling flows, it is intended in the present work to predict and measure the flow field in motored diesel engine swirl chamber and to compare the predictions and measurements carefully over a wide range of data to give reliable information about the constants of the turbulence model and their relation with the combustion chamber geometry and engine operating conditions.

Predictions are based on the solution of the finite difference form of the governing differential equations for the transport of mass, momentum and energy as well as the solution of the differential equations of both kinetic energy of turbulence and its dissipation rate. Suggestions have been made to modify the k-ε model of turbulence to include compressibility of medium, nonisotropy for rotating flow, combustion chamber configuration and geometry, and engine operating conditions.

Experimental measurements of the random air velocity are carried out by two different probes : a hot wire and a condenser-microphone anemometers. An experimental set up has been built to facilitate the measurements of air velocity components inside the swirl chamber with

highest possible accuracy. Special calibration set up has also been built up to facilitate the calibration of both hotwire and microphone condenser anemometers and to investigate the effect of air flow temperature and pressure upon their response.

2,4. The Governing Conservation Equations

The flow is governed by the differential conservation equations of mass, momentum and energy. The flow is assumed to be two-dimentional for cylindrical swirl chamber with small width. All equations are time dependent since there is a transient turbulent flow change with the crank angle positions. The effect of turbulence appears in the form of correlations of fluctuating quantities, which are often referred to as turbulent fluxes.

The equations governing the flow in a cylindrical swirl chamber are obtained by decomposing the velocity, pressure, density and enthalpy into a mean and a fluctuating value respectively. Finally, it is assumed that the turbulent fluxes of momentum (i.e. Reynolds stresses) and thermal energy are calculated through scalar eddy diffusivities which are in turn determined by solving additional differential conservation equations for the kinetic energy of turbulence K and its dissipation rate ε.

The turbulent momentum and energy equations differ from the laminar versions only by the appearance of the Reynolds stresses and the temperature-velocity correlations. Both have been modeled using the Boussinesq [7] approach in terms of the mean-flow gradients. The model has been modified to introduce compressibility effect by analogy with laminar stress tensor. The equations governing the turbulent flow field in polar coordinates can be written as follows :

i- Continuity Equation :

$$\frac{\partial \rho}{\partial t} + \frac{1}{r}\frac{\partial}{\partial r}(r\rho v) + \frac{1}{r}\frac{\partial}{\partial \theta}(\rho u) = 0 \qquad (1)$$

ii- Radial Momentum Equation :

$$\frac{\partial}{\partial t}(\rho v) + \frac{1}{r}\frac{\partial}{\partial r}(r\rho vu) + \frac{1}{r}\frac{\partial}{\partial \theta}(\rho uv) - \frac{1}{r}\frac{\partial}{\partial r}\left(r\mu_{eff}\frac{\partial v}{\partial r}\right) -$$

$$- \frac{1}{r^2}\frac{\partial}{\partial \theta}\left(\mu_{eff}\frac{\partial v}{\partial \theta}\right)$$

$$= \frac{-\partial P}{\partial r} + \frac{1}{r}\frac{\partial}{\partial r}\left(r\mu_{eff}\frac{\partial v}{\partial r}\right) + \frac{1}{r}\frac{\partial}{\partial \theta}\left|\mu_{eff}\left(\frac{\partial u}{\partial r} - \frac{u}{r}\right)\right| + \frac{\rho u^2}{r} - 2(\mu_{eff}/r^2)x$$

$$x(V + \frac{\partial u}{\partial \theta}) - \frac{2}{3}\frac{\partial}{\partial r}\left|r(\mu_{eff}.\mathrm{div}.(\vec{u}) + \rho K)\right| \qquad (2)$$

iii- Tangential Momentum Equation :

$$\frac{\partial}{\partial t}(\rho u)+\frac{1}{r}(r\rho vu)+\frac{1}{r}\frac{\partial}{\partial\theta}(\rho uu)-\frac{1}{r}\frac{\partial}{\partial r}(r\mu_{eff}\frac{\partial u}{\partial r})-\frac{1}{r^2}\frac{\partial}{\partial\theta}(\mu_{eff}\frac{\partial u}{\partial\theta})$$

$$=-\frac{1}{r}\frac{\partial P}{\partial\theta}+\frac{1}{r}\frac{\partial}{\partial r}\left|r\mu_{eff}(\frac{1}{r}\frac{\partial v}{\partial\theta}-\frac{u}{r})+\frac{1}{r^2}\frac{\partial}{\partial\theta}\right|\mu_{eff}(\frac{\partial u}{\partial\theta}+2V)\Big|$$

$$+(\mu_{eff}/r)(\frac{1}{r}\frac{\partial v}{\partial\theta}+\frac{\partial u}{\partial r})-\mu_{eff}\frac{u}{r^2}-\rho\frac{uv}{r}-\frac{uv}{r}-\frac{2}{3r}(\mu_{eff}\cdot div(\vec{u})+\rho K) \qquad (3)$$

iv- Energy Equation :

$$\frac{\partial}{\partial t}(\rho h)+\frac{1}{r}\frac{\partial}{\partial r}(r\rho vh)+\frac{1}{r}\frac{\partial}{\partial\theta}(\rho uh)-\frac{1}{r}(r\frac{\mu_{eff}}{\sigma_h}\frac{\partial h}{\partial r})-\frac{1}{r^2}\frac{\partial}{\partial\theta}$$

$$(\frac{\mu_{eff}}{\sigma_n}\frac{\partial h}{\partial\theta})=\frac{\partial p}{\partial t}+v\frac{\partial P}{\partial r}+\frac{u}{r}\frac{\partial P}{\partial\theta}+\text{small terms} \qquad (4)$$

Since no combustion has been considered, the enthalpy, h, is the sensible enthalpy which has been taken equal to :

$$h = C_p T$$

v- Turbulence Kinetic Energy Equation :

The turbulence kinetic energy equation is a modified form of the turbulence kinetic energy equation used by, Launder and Spalding (12) and (13) for incompressible flows. The introduction of compressibility effects has been done by considering terms containing the divergence term, $\nabla.\vec{u}$. The equation for the turbulence Kinetic energy is obtained by multiplying the instantaneous momentum equation by the instantaneous velocity and subtracting the product of the mean velocity times the mean-momentum equations and then taking the average of this result. The final result is obtained in the following form :

$$\frac{\partial}{\partial t}(\rho K)+\frac{1}{r}\frac{\partial}{\partial r}(r\rho vk)+\frac{1}{r}\frac{\partial}{\partial r}(\rho uk)-\frac{1}{r}\frac{\partial}{\partial r}(r\frac{\mu_{eff}}{\sigma_k}\frac{\partial K}{\partial r})-\frac{1}{r^2}$$

$$\frac{\partial}{\partial\theta}(\frac{\mu_{eff}}{\sigma_k}\frac{\partial K}{\partial\theta})=\mu_{eff}\left|2(\frac{1}{r}\frac{\partial u}{\partial\theta}+\frac{v}{r})^2+2(\frac{\partial v}{\partial r})^2+(\frac{1}{r}\frac{\partial v}{\partial\theta}+\frac{\partial u}{\partial\theta}-\frac{u}{r})^2\right|$$

$$-\frac{2}{3}div(\vec{u})(\mu_{eff}\,div(\vec{u})+\rho K)-C_D f\rho\varepsilon \qquad (5)$$

where;

σ_K is the turbulent prandtl/schmidt Number ($\simeq$1.0)

The term before the last one on the right-hand side accounts for the effect of compressibility in the K-equation, namely :

$$- \frac{2}{3} (\mathrm{div}(\vec{u}) . \rho K)$$

The last term, $C_D \rho$, contains the factor f which account for the effect of compressibility mixing length scale resulting from the change of the engine operating conditions and combustion chamber geometry. The constant C_D was suggested by Launder, and spalding (12)for turbulence in the vicinity of a wall, in which convection and diffusion of energy are nearly always negligible; so there is a balance between the production and dissipation energy and obtained the relation :

$$\tau^2 = \left| \mu_t \frac{\partial u}{\partial y} \right|^2 = C_D \rho^2 K^2$$

i,e. $\tau/\rho K = C_D^{\frac{1}{4}}$ or $C_D = (\tau/\rho K)^2$

They recommended a value equal to 0.08 for the constant C_D as a result of wide range comparison between experimental results obtained for incompressible flow and prediction calculations. Experimental results carried out on reciprocating engines show that the use of this value can give unreliable results especially for turbulence length scale as it depends upon the local turbulence condition. A correction of this kind is necessary if the mean velocity is to be predicted correctly with the k- ε model.

vi- Dissipation Rate of Kinetic Energy Equation :

The equation for the dissipation rate of the turbulent kinetic energy in the modified form can be written as follows :

$$\frac{\partial}{\partial t} (\rho\varepsilon) + \frac{1}{r} \frac{\partial}{\partial r} (r \rho v \varepsilon) + \frac{1}{r} \frac{\partial}{\partial \theta} (\rho u \varepsilon) - \frac{1}{r} \frac{\partial}{\partial r} \left(r \frac{\partial}{\partial r} \left(r \frac{\mu_{eff}}{\sigma_\varepsilon} \frac{\partial \varepsilon}{\partial r} \right) \right)$$

$$- \frac{1}{r^2} \frac{\partial}{\partial \theta} \left(\frac{\mu_{eff}}{\sigma_\varepsilon} \frac{\partial \varepsilon}{\partial \theta} \right) = \frac{\varepsilon}{K} (C_1 (1 + C_3 R_i) G - C_2 f \rho \varepsilon) \qquad (6)$$

where :

$$G = \mu_{eff} \left| 2 \left(\frac{1}{r} \frac{\partial u}{\partial \theta} + \frac{v}{r} \right)^2 2 \left(\frac{\partial v}{\partial r} \right)^2 + \left(\frac{1}{r} \frac{\partial v}{\partial \theta} + \frac{\partial u}{\partial r} - \frac{u}{r} \right)^2 \right| -$$

$$- \frac{2}{3} \mathrm{div} (\vec{u}) (\mu_{eff} \mathrm{div} (\vec{u}) + \rho K) \qquad \text{and}$$

σ_ε is the turbulent prandtl/Schmidt Number ($\simeq$ 1.3). The first term on the right hand side in the ε -equation contains the compressibility effect and the part $(1 - C_3 R_i)$ accounting for the effect of streamline curvature and centripetal acceleration on mixing length and allowing for the nonisotropy of the flow. This term was also suggested by Lilly [54] and Launder [52] in their work. Moreover, the second term on the right handside in the ε -equation contains the factor of accounting for the change of engine operating conditions and combustion chamber geometry. The constant C_3 can be determined by optimization considering data for a wide range of flow in engine.

2.5 ESTIMATE OF EXCHANGE COEFFICIENTS

i- Estimate of C_2 from decay of turbulence behined grid :

Behind the grid the decay of turbulence is function only of the streamwise coordinate x :

i.e. $\rho_G u_G \frac{dk}{dx} = - C_D \frac{\rho^2 k^2}{\mu_t} \sim x^{-2}$ (experiment)

and

$$\rho_G u_G \frac{d\varepsilon}{dx} = - C_2 \frac{\rho^2 k\varepsilon}{\mu_t}$$

Hence ; $C_2 = C_D(m - n/2)$

where m and n are the exponents of K and mixing length ℓ in the definition of ε, so for :-

$$\varepsilon = K^{3/2}/\ell \qquad (m = \tfrac{3}{2}, \quad n = -1)$$

$$\therefore \quad C_2 = 2\, C_D$$

where C_D is determined experimentally from the relation

$$C_D = (\tau/\rho k)^2$$

ii- Estimate of C_1 from near-wall turbulence :

As suggested before for turbulent flows near walls :

$$\tau/\rho k = C_D^{\frac{1}{2}} \qquad (7)$$

Launder and spalding [51] measurments near a wall indicated that the mean velocity gradient varies with distance from the wall as follows :

$$\frac{\partial u}{\partial y} = \sqrt{\tau/\rho} \; / \; Ky \qquad (8)$$

where K - constant determined from their experimental data and equal to 0.4 .

Substituting equations (7) and (8) in equation (6) of the dissipation rate of turbulence kinetic energy and simplifying - the following relation can be obtained :

$$C_1 = \frac{C_2}{C_D} - \frac{K^2 n^2}{\sigma_\varepsilon C_D^{\frac{1}{2}}}$$

For $\varepsilon = k^{3/2}/\ell \qquad (m = \tfrac{3}{2}, \quad n = -1)$

2.6 GENERAL GOVERNING EQUATION

Within the above frame work, the complete equation set may be compactly represented in terms of a single general equation for an arbitrary dependent variable ϕ in the following form :-

$$\frac{\partial}{\partial t}(\rho\phi)+\frac{1}{r}\frac{\partial}{\partial r}(r\rho v\phi)+\frac{1}{r}\frac{\partial}{\partial\theta}(\rho u\phi)-\frac{1}{r}\frac{\partial}{\partial r}(r\Gamma_{\phi}\frac{\partial\phi}{\partial r})-\frac{1}{r^2}\frac{\partial}{\partial\theta}(\Gamma_{\phi}\frac{\partial\phi}{\partial\theta})=S_{\phi} \quad (9)$$

where: ϕ : stands for radial velocity v, tangential velocity u, total enthalpy h, K and ε.

t : time
ρ : density
Γ_{ϕ} : the effective diffusivity coefficient.
S_{ϕ} : source/sink terms for variable ϕ.

Equation (9) represents also the continuity equation by replacing ϕ by 1.

The definition of Γ_{ϕ} and S_{ϕ} are given in table (1). The new quantities appearing in this table include the effective viscosity μ_{eff} which is defined as :

$$\mu_{eff} = \mu + \mu_t$$

and the turbulent viscosity μ_t is connected with k and the turbulence energy dissipation rate ε by the following algebriac equation ;

$$\mu_t = C_{\mu}\ \rho\ k^2\ /\varepsilon$$

where $C_{\mu} = 0.09f$

This allows for the nonisotropy of the viscosity in swirling flows for the various combustion chamber geometry and engine operating conditions.

Table 1 Defination of Γ_ϕ and S_ϕ

ϕ	Γ_ϕ	S_ϕ
V	$\mu_{eff.}$	$-\frac{\partial P}{\partial r} + \frac{1}{r}\frac{\partial}{\partial r}(r\mu_{eff}\frac{\partial V}{\partial r}) + \frac{1}{r}\frac{\partial}{\partial \theta}\left[\mu_{eff}(\frac{\partial u}{\partial r} - \frac{u}{r})\right]$ $+ \rho\frac{u^2}{r} - 2(\mu_{eff}/r^2)(V + \frac{\partial u}{\partial \theta} - \frac{2}{3}\frac{\partial}{r\partial r}\left[r(\mu_{eff}\mathrm{div}(\vec{u}) + \rho k\right]$
u	μ_{eff}	$-\frac{1}{r}\frac{\partial P}{\partial \theta} + \frac{1}{r}\frac{\partial}{\partial r}\left[r\mu_{eff}(\frac{1}{r}\frac{\partial V}{\partial \theta} - \frac{u}{r})\right] + \frac{1}{r^2}\frac{\partial}{\partial \theta}\left[\mu_{eff}(\frac{\partial u}{\partial \theta} + 2V)\right]$ $+ (\mu_{eff}/r).(\frac{1}{r}\frac{\partial V}{\partial \theta} + \frac{\partial u}{\partial r}) - \mu_{eff}\frac{u}{r^2} - \frac{2}{3}\frac{\partial}{r\partial \theta}(\mu_{eff}\mathrm{div}(u) +$ $+ \rho k - \frac{\rho u V}{r}$
1	0	0
h	μ_{eff}/σ_n	$\frac{\partial P}{\partial t} + V\frac{\partial P}{\partial r} + \frac{u}{r}\frac{P}{r\theta}$ + small terms
k	$\mu_{eff}./\sigma_k$	$G - C_D f\ \rho\ \varepsilon$
ε	$\mu_{eff}/\sigma_\varepsilon$	$\frac{\varepsilon}{k}(C_1(1+C_3R_i)\ G - C_2 f\ \rho\varepsilon)$
x	$\mu_{eff.}/\sigma_x$	0

where ,

$$\mu_{eff.} = \mu + C_\mu f\ \rho K^2/\varepsilon$$

$$G = \mu_{eff.}\left[2(\frac{1}{r}\frac{\partial \mu}{\partial \theta} + \frac{V}{r})^2 + 2(\frac{\partial V}{\partial r})^2 + (\frac{1}{r}\frac{\partial V}{\partial \theta} + \frac{\partial \mu}{\partial r} - \frac{\mu}{r})^2\right.$$
$$\left. - \frac{2}{3}\mathrm{div}(\vec{\mu})(\mu_{eff.}\ \mathrm{div}\ (\vec{\mu}) + \rho k)\right]$$

2.7 Initial Conditions

At the inlet plane to the swirl chamber the inlet velocity, density and temperature vary with crank angle degree. They are specified by solving an ordinary differential equation for the flow from the main chamber to the swirl chamber, or vise versa, through the tangential port, as reported by Elkotb [20] and can be summarized as follows: By equating the rate of mass transfer obtained from the continuity equation which has the following form :

$$dm = \frac{V_s}{V_o} \left| \rho^{1/n} \, d(V/V_s) + \frac{V/V_s}{n} \, \rho^{(1/n-1)} \, dp \right| \qquad (10)$$

with that obtained from the energy equation, assuming polytropic compressible flow, which has the following form :

$$dm = \frac{30 \, C_d \, A_e}{N} \sqrt{2g \, \frac{n}{n-1} \, R} \sqrt{T_a} \, (\rho/\rho_a)^{\frac{n-1}{2n}} \sqrt{1-(\rho_s-\rho)^{\frac{n-1}{n}}} \, d\phi \qquad (11)$$

an ordinary differential equation of the following form can be obtained :

$$dX/d\phi = \frac{X}{V/V_s} \frac{d(V/V_s)}{d\phi} + \frac{30 \, C_d \, A_e \sqrt{\rho_o V_o}}{\pi \, N \, V_s} \sqrt{29 \frac{n}{n-1}} \left(\frac{X}{V/V_s}\right) (\varepsilon/a_s)^{\frac{n-1}{2}} (X+V/V_s)^{\frac{3-n}{2}} \qquad (12)$$

where,

$$X = (p_s/p)^{\frac{1}{n}} \qquad (13)$$

$$\frac{V_o}{V} = (p/p_o)^{\frac{1}{n}} \qquad (14)$$

$$P = \left(\frac{\varepsilon/a}{X+V/V_s}\right)^n \qquad (15)$$

and ε = compression ratio.

$$a_s = V_s/V_c \qquad (16)$$

V : instantaneous volume.

The solution of this differential equation using Rung-Kutt 4 method gives the instantaneous value of the parameters X, which in turn and with the help of equations (13) and (15) the dimensionless main chamber pressure and the dimensionless swirl chamber pressure at any crank angle position can be determined.

The velocity of air ejected into the swirl chamber is determined from the energy equation when assuming polytropic compressible flow which has the following form ;

$$U_e = C_v \sqrt{p/\rho} \sqrt{2g \left(\frac{n}{n-1}\right) \left(1-\left(\frac{p_s}{p}\right)^{\frac{n-1}{n}}\right)} \qquad (17)$$

and when substituting eqns.(13), (14) and (15) it becomes :

$$U_e = K_2 \left(\frac{\varepsilon/a_s}{X+V/V_s}\right)^{\frac{n-1}{2}} \sqrt{1- X^{n-1}} \qquad (18)$$

where,

$$K_2 = C_v \sqrt{\frac{2gn}{n-1}} \sqrt{p_o V_o} \qquad (19)$$

2.8 Numerical Solution of Equations

The governing set of parabolic equations (eqns 1-6) which are written in a single general equation (g) are solved using a finite difference procedure. The solution allows calculations of unsteady compressible, laminar and turbulent flows with heat transfer. In addition, the calculations of temperature and pressure fields have been made. So the swirl chamber is overlaid with a grid and circles Fig.(1), at which the scalar variables h,k,ε and ρ are stored; while the velocities are located mid-way between the pressures which determine them.

Imaging each variable stands in its own control volume then equation (9) can be integrated over this control volume for a time increment ∂t. The finite difference equations for the governing equations have been derived and can be compactly represented by the following single equation :

$$M_p^o\ (\phi_p^N - \phi_p^o) + \sum_c A_c^n\ (\phi_p^n - \phi_c^n) = S_p\ \phi_p^n + S_u \qquad (20)$$

where, Σ_c denotes summation over the four neighbouring nodes of a typical grid node p.

$$M_p^o = (\rho V)_p^o / \Delta t$$

and

$$A_w = (\rho u\ af)_w \qquad A_s = (\rho\ V\ af)_s$$

$$A_E = -(\rho u\ af)_e \qquad A_N = -(\rho V af)_n$$

$$Sp\ \phi_\rho^n + S_u = \int_{V_p} S\phi\ dV$$

where,

V : is the cell volume

The f's are weighting factors whose specification is determined from the choice of spatial differencing approximation. This in turn influnces both accuracy and computational stability. It follows the following specification :-

$$f_w = \frac{\dot{q}_w}{(\rho a u)_w} \begin{cases} (1+1/\rho_{ew})/2 & , \text{ for } -2 < |\rho_{ew}| < 2 \\ 1 & , \text{ for } |\rho_{ew}| \geq 2 \\ 0 & , \text{ for } |\rho_{ew}| \leq -2 \end{cases}$$

where,

ρ_{ew} : is the local factor number, defined by Runchal as follows,

$$P_{ew} = (\rho u)_w\ \delta x_{pw}/\Gamma_w$$

where,

$$\rho_w = (\rho_w + \rho_p)/2$$

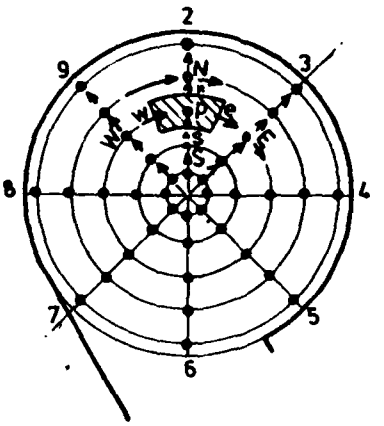

Fig. (1) Computional grid

$$\Gamma_w = (\Gamma_W + \Gamma_p)/2$$

and similar formulae exists for the remaining f's.

Finally equation (20) can be written in the follows form :

$$(A_p + M_p^o - S_p)\ \phi_p^n = \sum_c A_c\ \phi_c^n + M_p^o\ \phi_p^o + S_u \qquad (21)$$

where,

$$A_p = \sum_c A_c$$

and S_ρ is given in table (2), S_p and S_n are coefficients of linearized source terms obtained by integrating S_ϕ. A_c are defined as the influence coefficients which give the combined effect of diffusion and convection.

Table (2) Definition of the Quantity S_p for the individual Variables.

	Sp
u	$(\rho_p - \rho_w)\ (a_e+a_w)/2$
v	$(\rho_p - \rho_s)\ (a_n+a_s)/2$
h	$(M_{pp_p})^n - (M_p p_p)^o$
k	$V_p^n\ (G - \rho_p \varepsilon_p)^n$
ε	$V_p^n \lvert \varepsilon_p (C_1(1 - C_3 Rf)G - C_2 \rho_p\ \varepsilon_p / K_p \rvert^n$

The first step in solving the finite difference equations is to solve the energy equation using the old fields of n,u,v,p and $(\partial p / \partial t)$, to yield the new enthalpy field (h^n) and hence the new temperature field (T^n). At each time step, the solution algorithm proceeds as follows :

With guessed values of pressure, p^{*n}, the momentum equations are solved to determine v^{*n} and u^{*n}. In general these velocities will not satisfy the continuity equation but will produce a net mass source at each grid node. The pressure, density, and velocities are then corrected so as to reduce the mass source at each grid node to zero in the following manner :

$$p^n = p^{*n} + p' \qquad (22)$$

$$\rho^n = \rho^{*n} + \beta\ p' \qquad (23)$$

$$V_p^n = V_p^{*n} + DV\ (P_p' - P_N') \qquad (24)$$

$$u_p^n = u_p^{*n} + Du\ (P_p' - P_E') \qquad (\ )$$

where

* : indicates guessed or preliminary value

p' : pressure correction

β : defined by $(\frac{\partial \rho}{\partial p})_T \quad (\frac{V}{Dr})^n$

D_r and D_u are evaluated from the relavant momentum equation :

$$D_u = u_p^n/(P_p - p_E)$$

$$D_v = v_p^n/(p_p - p_N)$$

Now equations (23) to (25) are substituted in continuity eqn then ;

$$(\frac{\partial \rho}{\partial t}) \text{ vol.} + \Sigma \rho \, u_i A = 0$$

i.e.

$$M_p^n - M_p^o + \Sigma \rho \, u_i A = 0 \qquad (26)$$

which can be written in the following form :

$$(A_p - S_p) p_p' = \sum_c A_c \, p_c' + S_u$$

where,

$$A_p = \sum_c A_c \qquad (27)$$

$$S_u = -(M_p^{*n} - M_p^o + \sum_c m_c^{*n})$$

S_u : is the local continuty imbalance based on u^{*n}, V^{*n} and ρ^{*n}

S_p A_c : coefficients defined as follows :

$$S_p = - V_p \, \beta_\rho / \delta t - \sum_c (\beta_c \, \dot{m}_c^* / \rho_c^{*n})$$

$$A_E = \rho_e^{*n} A_e \, Du_e - 0.5 \, \beta_e \frac{\dot{m}_e^*}{\rho_o^{*n}} \; ;$$

$$A_W = \rho_w^{*n} A_w \, D \, V_w + 0.5 \, \beta_w \, \dot{m}_w^* / \rho_w^{*n}$$

$$A_N = \rho_n^{*n} A_n \, DV_n - 0.5 \, \beta_n \, \dot{m}_n^* / \rho_n^{*n}$$

$$A_S = \rho_s^{*n} A_s \, DV_s + 0.5 \, \beta_s \, \dot{m}_s / \rho_s^{*n}$$

where; subscripts E,W,N,S, and e,w,n,s are neighbouring nodes and corresponding nodes mid-way between both nodes.

Equation (27) is solved to yield the p'field which is required to correct p,v and u fields. The new K and ϵ are then compared from their differential equation (21).

Equation (27) is then a modified form of the pressure correction equation, developed here, giving a fast convergence and reduces the total computational time.

The conservation and local pressure correction equations are solved by using a Gauss-elimination line by-line double sweep technique. While equation (21) converges very fast, equation (27) needs more sweeps and sometimes more than one iteration to reduce the residual mass errors to an acceptable level. The time increment δt which is used in the present programme is $2.2.2 \times 10^{-4}$ which is equivalent to 2^{o} crank angle degree.

In addition to the local pressure correction p', a global pressure correction p' is computed based on overall continuity balance and is added to the existing pressure field before solving the pressure correction equation (27).

The flow diagram for the solution is given below

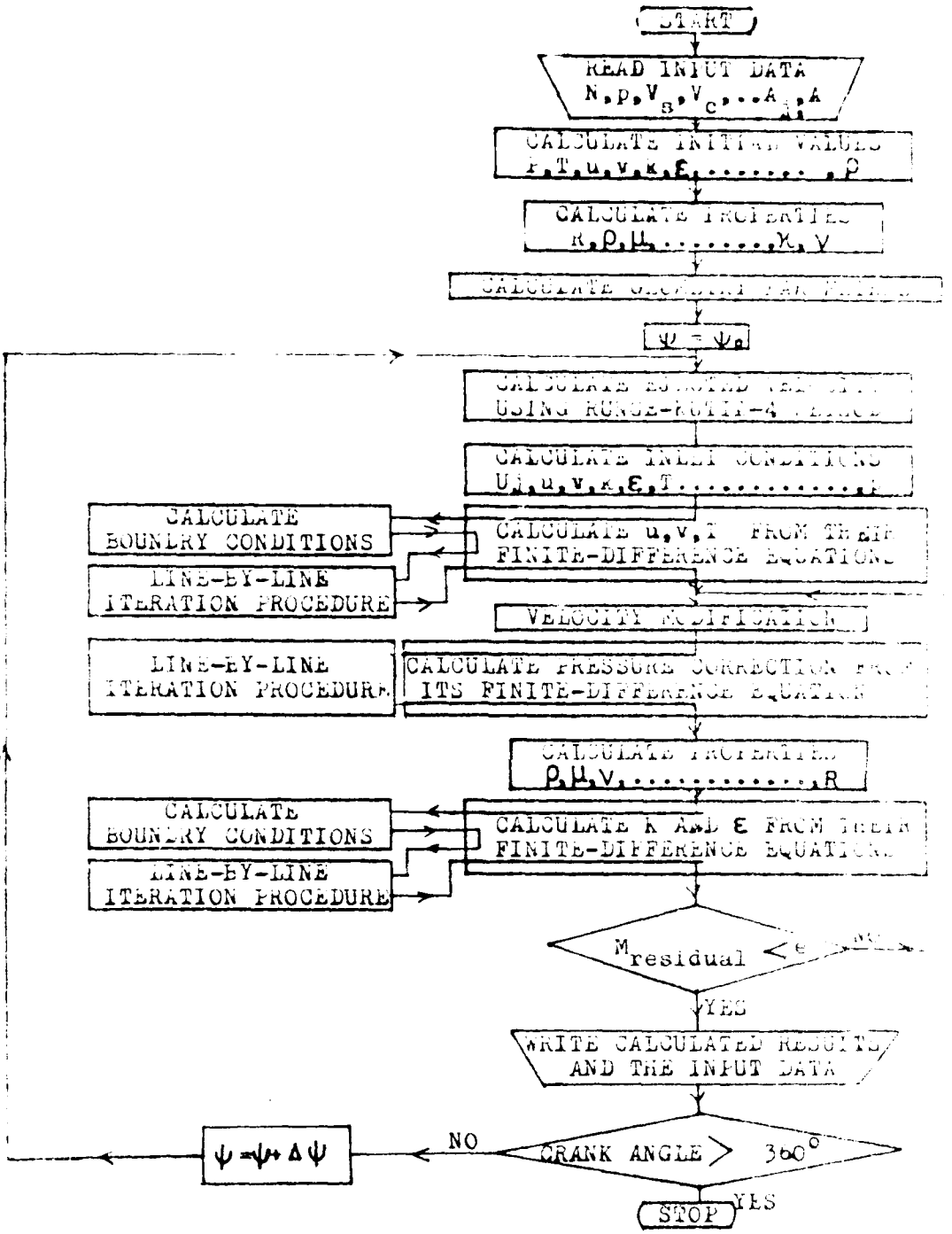

Flow chart of the computer program

CHAPTER 3

EXPERIMENTAL SET UP AND MEASURING TECHNIQUE

3.1. INTRODUCTION

Experimental information about flow inside swirl chambers is limited due to the difficulties involved in measuring turbulent shear flow. Shear layers are formed when two streams are brought together at different velocities. The two streams of fluid are generated from the introduced air through the port and that of the flowing air inside the swirl chamber. The resulting velocity gradients cause shear forces to arise. At high Reynolds number the forces generated are severe enough to cause turbulent flow.

Because of the strong current interest in air flow inside swirl combustion chambers this work is directed to determine the effect of working conditions and combustion chamber parameter on it. This is required for the validation of the suggested mathematical model which leads to better calculation of the fuel spray behaviour.

Therefore, an experimental set up has been built up to facilitate measurements of the air velocity components inside a diesel engine swirl chamber with highest possible accuracy. Two different methods are used to measure the turbulent flowfield inside the swirl chamber. The first one is a constant temperature hot-wire anomometer (DISA 55M system) fitted with a platinum wire probe. The second method is the microphone condenser type which is based on the measurements of the dynamic pressure of the flow. As the flow inside the swirl chamber is unsteady and measuring instruments are affected by the medium pressure, signals of the velocity components detected by the hot wire anemometer and microphone condenser as well as the gas pressure variation have to be recorded with time. It was necessary to record data over a quite sufficient period to obtain better sampling of the flow.

A special calibration set-up has been built to determine the effect of pressure and temperature on the response of the two anemometers.

3.2. EXPERIMENTAL SET-UP

The experimental investigation has been carried out on a 2-cylinder, 4-stroke water cooled medium speed diesel engine, manufactured at the Egyptian Helwan Factory. The data of this engine is given in Appendix -2.

The experimental swirl chamber has been built up in one of the engine cylinder while the other cylinder has been used for motoring the engine to the required regime. The engine is directly coupled with hydraulic dynamometer for speed variation and equipped with various instruments required for measuring the main engine parameters as well as the air velocity components and pressure. The test cylinder head has been modified and a swirl chamber has been constructed and attached instead of the original chamber. The tested swirl chamber

facilitates the variation of the swirl chamber volume ratio and the port area ratio. The intake and exhaust manifolds of the test cylinder are separated from those of the second motoring cylinder.

The following requirments are considered during the design of the set up :

1- Possibility of changing the engine speed.
2- Possibility of changing the port area of channel connecting the main cylinder with the swirl chamber and its inclination.
3- Possibility of changing swirl chamber volume ratio.
4- Control of variables to ensure repeatability.
5- Data recording and processing.

A schamatic drawing of the experimental set up is shown in Fig. ( ). The experimental set up is equipped with the following instruments :

i- X-probe hot wire anemometer,
ii- microphone condenser,
iii- Piezoelectric transducer,
iv- Two magnetic transducers,
v- Oscilloscope
vi- Magnetic tape recorder for recording various signals.

3.2.1. Test Swirl Chamber

The air velocity pattern inside the swirl chamber is affected by the entering inlet moment of momentum of the air [24], which is affected by the swirl chamber relative volume, the connected channel relative area and its inclination. Figure ( ) shows a scheme of the designed swirl chamber which satisfy easy variation of the relative swirl volume ratio, port area ratio and inclination angle.

A cylindrical swirl chamber with swirl chamber volume ratio of 0.772 and diameter of 48.5 cm, has been constructed and built up with compression ratio of 17. The swirl chamber has an optically flat fused quartz window on one of its side. It is also fitted with a cooling jacket supplied with circulating water to control the chamber wall temperature. Two oblique washers are fitted on either sides of the quartz plate to avoid stress concentration. The quartz plate was fastened by a self locking screwed coller to facilitate easy and quick assembly. Connecting ports of different sizes have been constructed in a conically shapped plugs to supply air to the swirl chamber from the main chamber. By these plugs, it is possible to adopt connecting ports with various configurations. Sealing between the plugs and their seat is satisfied by conical fitting. The diameters of the connecting ports have been changed between 8 and 15mm to satisfy variation of moment of momentum.

The swirl chamber is equipped with the hot-wire anemometer probe and the microphone - condenser probe to measure the air velocity components. The radial movement of any of these probes is possible. A piezoelectric pressure transducer is also fitted to the swirl chamber for recording the pressure variation inside the chamber. A ferrous -konstantan thermo couple is fixed to measure the surface temperature.

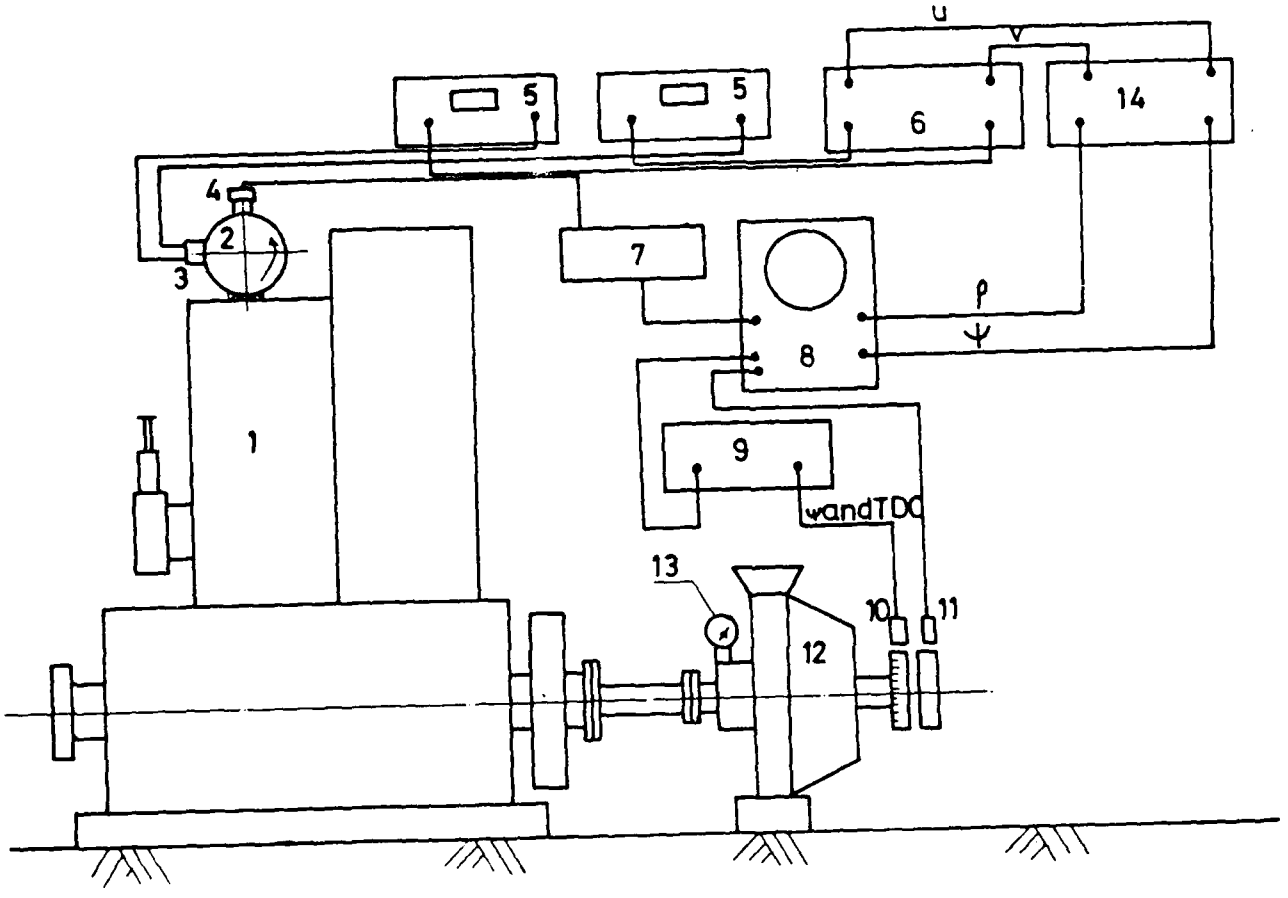

Fig(2)Schematic drawing of the experimental set up.

1_Engine assembly. 2_Swirl chamber. 3_X_Probe hot_wire.
(ormicrophone condenser) probe. 4_Pressure transducer.
5_Balansing system of hot_wire. 6_Subtractor. 7_Preamplifier
8_Cathod ray oscillograph. 9_Degree marker amplifier.
10_Magnetic transducer for ψ and TDC. 11_Magnetic transducer for time.
12_Dynamometer. 13_Tachometer. 14_Magnetic tape recorder.

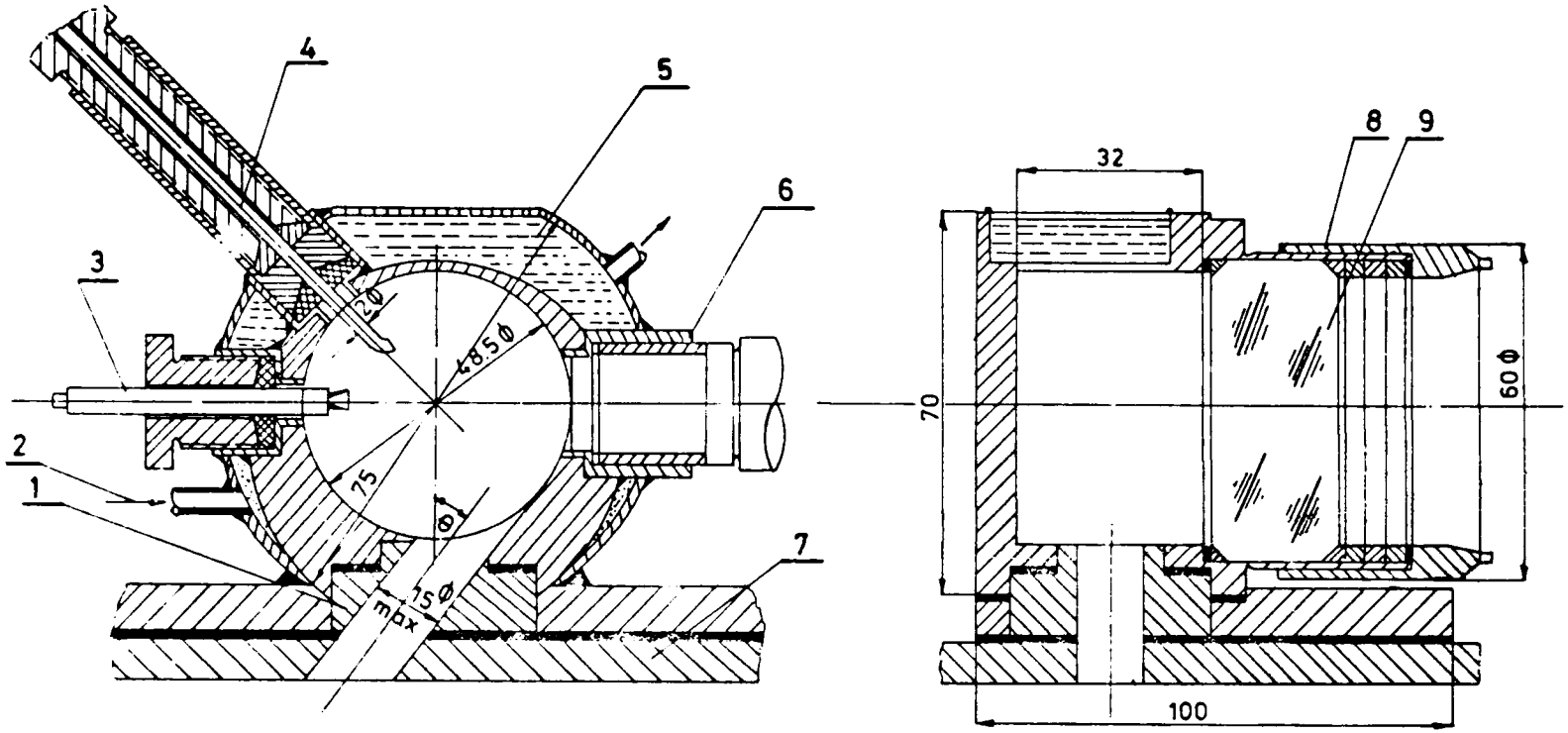

Fig.(3)Scheme of the tested swirl combustion chamber

1_Connecting plug 2_Coolant 3_Hot_wire anemometer
4_Microphone_condenser probe 5_Cooling jacket 6_Pressure transducer
7_Cylinder head 8_Packing cap 9_Quartz window

3.2.2. Measuring Instruments

The accurate determination of experimental results to validate the predicted ones requires sensitive and accurate measuring instruments.

i- Air Velocity Measurements

a- Hot Wire Anemometer

A temperature compensated hot-wire anemometer is employed to measure both the mean and the fluctuating velocity components. The use of hot-wire anemometer is recomended due to its small dimensions, low inertia and small disturbance created by the instrument itself. The theory of the hot-wire anemometer as given in references [38,40,41,19] is based upon the heat transfer between the flow and a constant temperature wire. The constant - temperature hot-wire anemometer type DISA 55M is employed using a platinum wire of 20μ in diameter to withstand mechanical stresses. The platinum wire is able to withstand the effect of dust and oil particles as well as the required higher temperature coefficient.

The variation of the electric current passing through the hot - wire due to air velocity variation is amplified and displayed on the screen of a two channel cathod-ray oscilloscope. A time display unit is used to satisfy the x-motion of the velocity signal. The time display unit, which is fixed on the crankshaft, consists of two discs and two magnetic transducers. The first disc, which is made of steel, is prepared with a slot to define the TDC. The magnetic transducer which is fixed opposite to this disc, generates electrical current corresponding to the crank motion. The slot of the disc is fixed at a position corresponding to the TDC. The TDC , is adjusted within $\pm$ 0.5 degree. The second plastic disc which is prepared with steel liners on the rim correspond to 5,10,....360 degree of the crank angle, together with the magnetic transducer displaying on the second channel of the oscilloscope the time base. The signals of the flow velocity and time are photographed by a movie camera.

b- Microphone-Condenser Anemometer

A microphone - condenser probe is developed to detect both the mean and fluctuating values of velocity. The probe receives pressure fluctuations and transfers them to electrical quantities from which, with suitable assumptions and simplifications, mean velocities and velocity fluctuations u, v, u' and v' can be derived.

The basic electric circuit of the used Microphone condenser is shown in Fig.(4), in which the air pressure affects the condenser diaphragm causing change of its capacity. A variable electric current output proportional to the acting pressure will be obtained. The electric circuit of the Microphone condenser is fed with voltage through a high frequency generator. The frequency of the passing current is chosen not less than 10 times the frequency of the cyclic-flow, resulting from the piston motion.

A water cooled microphone - condenser probe was constructed as shown in Fig.(5) with two different probes; one for the tangential component and the other for the radial one.

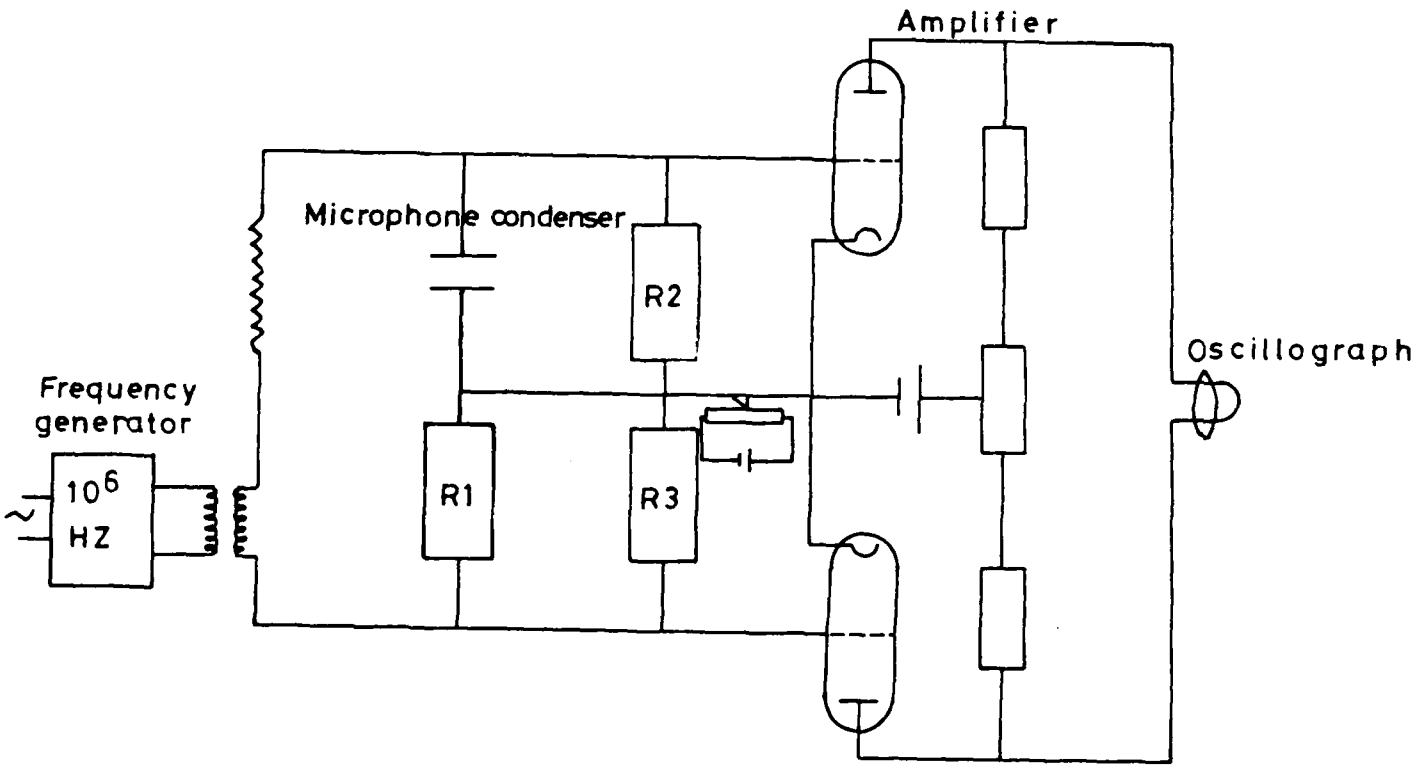

Fig (4)Microphone-Condenser electric circuit

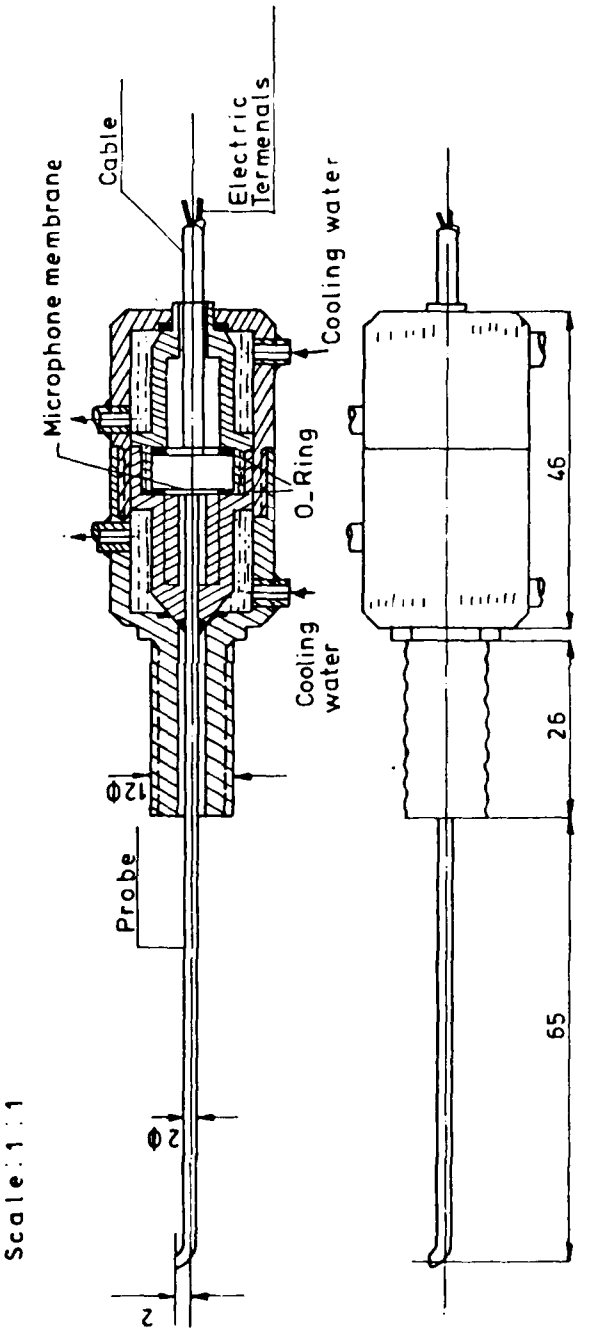

Fig 5.1 Condenser micraphone measuring probe

c- Pressure Measurement

The variation of pressure inside the swirl chamber is measured using piezoelectric transducer and a charge amplifier. The output electrical signals from the transducer and the time display are fed to the oscilloscope at the same time with the recording of the crank angle degree. The transducer has been dynamically calibrated directly on the engine by using a maximum pressure indicator (disindicator instrument). The linear response of the transducer facilitates the calibration.

3.3. CALIBRATION SET-UP AND RESULTS

3.3.1. Calibration Set-Up

The flow in the diesel engine is unsteady resulting in a change in velocity, pressure and temperature. This may affect to a certain extent the response of hot wire and microphone condenser anemometers. Therefor a special calibration set-up has been constructed to calibrate both the hot-wire and microphone - condenser anemometers with the change of pressure, velocity, and temperature.

The general layout of the calibration set-up is shown in Fig. (6). The following requirements have been satisfied during the design of the set-up :

1- Possibility of changing air flow rate (air velocity).
2- Possibility of changing air pressure.
3- Possibility of changing air temperature.
4- Possibility of changing turbulence level.

Compressed air from a reciprocating compressor is supplied to the test section through a pipe of 5 cm diameter. Its velocity can be measured by using a calibrated orifice meter, which is fixed after the heater at a distance of 100 cm from its output section. An electronic anemometer has been used to measure the pressure across the orifice meter. A thermocouple and a pressure gauge are used to measure the air temperature and pressure. The anemometers are fixed at a distance 10 cm from the orifice meter. A wire grid is mounted directly before the orifice meter in order to change the air turbulence level in the test section.

3.3.2. Calibration of Hot-Wire Anemometer

Before starting the calibration procedure of the hot-wire anemometer, it has been rotated to define the normal position of the flow which has been detected by the maximum voltage reading. This reading corresponds to the air velocity and pressure. Several readings have been taken at various pressures keeping the air velocity constant and this has been repeated at several air velocities. During calibration the following parameters have been recorded.

- initial volt of the hot wire anemometer V_o
- Mean voltage of hot wire anemometer V
- Pressure drop across orifice meter ΔP
  from which the mean velocity is obtained by the following relation U = m/s
- Ambient air temperature ^oC t_o
- Air pressure bar P
- RMS of random voltage of hot wire anemometer. v

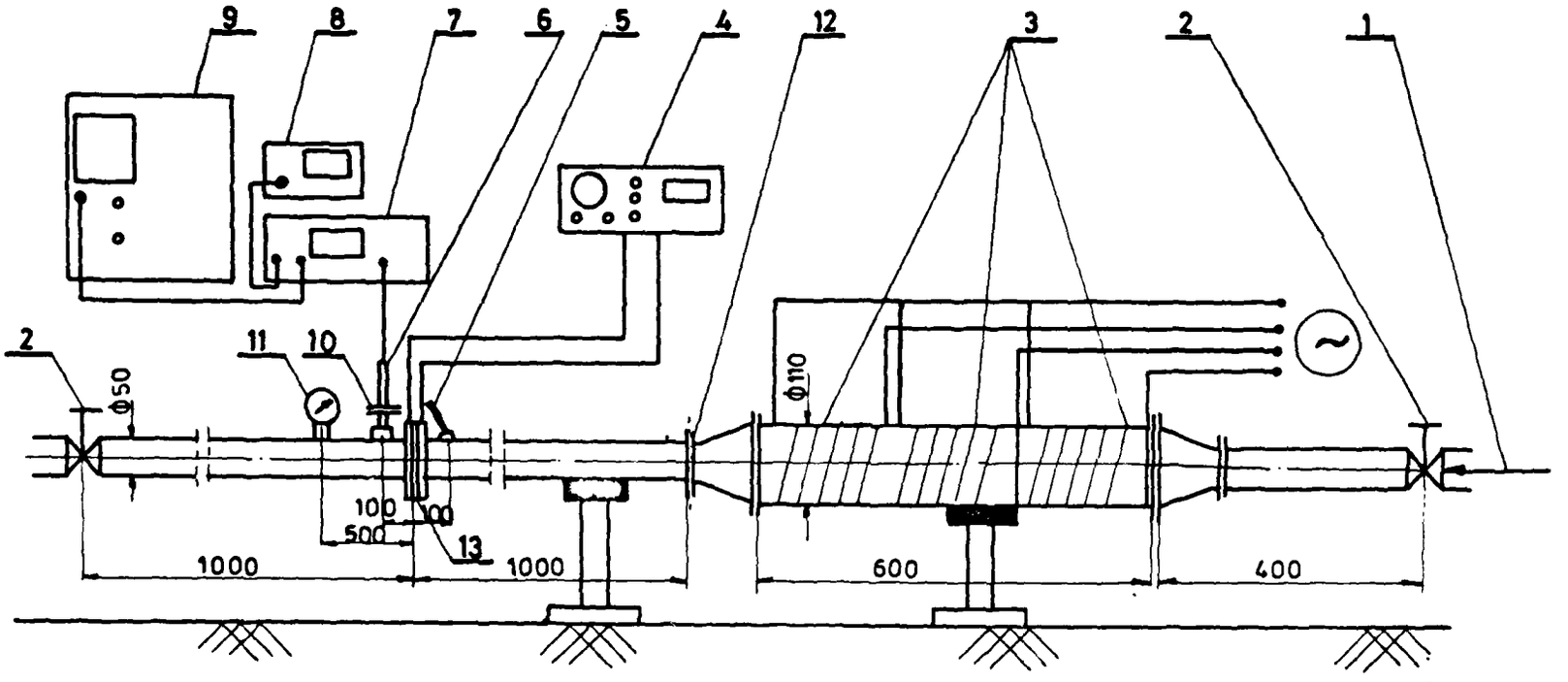

Fig(6) Calibration set-up

Dimension in · mm.

1_Compressed air 2_Gate valve 3_Heater segments 4_Electronic manometer
5_Thermometer 6_Anemometer 7_Balancing system 8_RMS voltmeter
9_Oscilloscope 10_Angle scale 11_Pressure gauge 12_Wire grid 13_Orifice meter

The experimental results have beer illustrated in Fig.(7). The relation between pressure times the velocity as a function of the hot wire anemometer response can be written in the following form ;

$$PU = A(V - V_o)^n$$

where A and n - constants to be determined from experimental results. Therefore, the experimental results are illustrated on a log-log scale as shown in Fig.(8) and the constants have been determined equal to:

$$A = 32 \quad \text{and} \quad n = 1.8$$

This equation is valid for pressures greater than 1 bar. Regarding the turbulence level of the flowing air it is found from the experimental results that the variation of the air pressure and temperature has no effect.

Studying the effect of air temperature on the response of the hot wire anemometer it is found that the change of temperature up to the maximum temperature of air at the end of compression stroke cannot affect its compensation when using platinum wire and compensating ratio.

3.3.3. Calibration of Microphone Condenser Anemometer

It has been found from the experimental results that the response of the microphone - condenser anemometer is affected by both pressure and temperature.

i- Effect of pressure and temperature on mean velocity :

At atmospheric pressure the microphone - condenser is tested at different air velocities for a temperature range of 28°C to 106°C. The change of mean output signal volt for different air velocities is illustrated in Fig.(9) from which it is found that the temperature variation has a negligable effect on the mean velocity response of the microphone - condenser. Keeping the air temperature constant at 28 °C, the microphone - condenser has been calibrated at different air velocities and pressures ranging from 1 to 35 bar. A sample of the results for a pressure 1 baris shown in Fig.(9) which can be represented by the following relation :

$$U = A' (\bar{u})^{n'}$$

where;

$\underline{U}$: air flow velocity m/sec.
$\bar{u}$: mean output from mic (m v)
A',n': calibration constants for Mic.

The constants A',n' have been determined for different air pressures and the results are illustrated in Fig.(10),which can be represented by the following relations :

$$A' = 1.999 - 5.2\times10^{-2}(p) + 4.052\times10^{-4}(p^2)$$
$$n' = 0.6 + 2.95\times10^{-3}(p) - 4.023\times10^{-5}(p^2)$$

where,

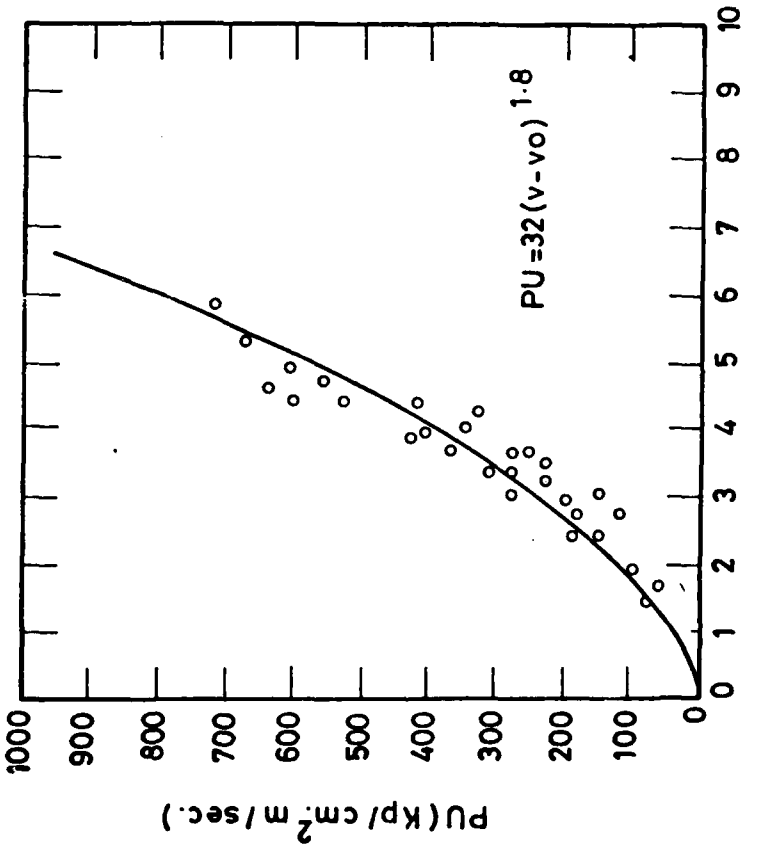

Fig(7) Hot-wire calibration curve

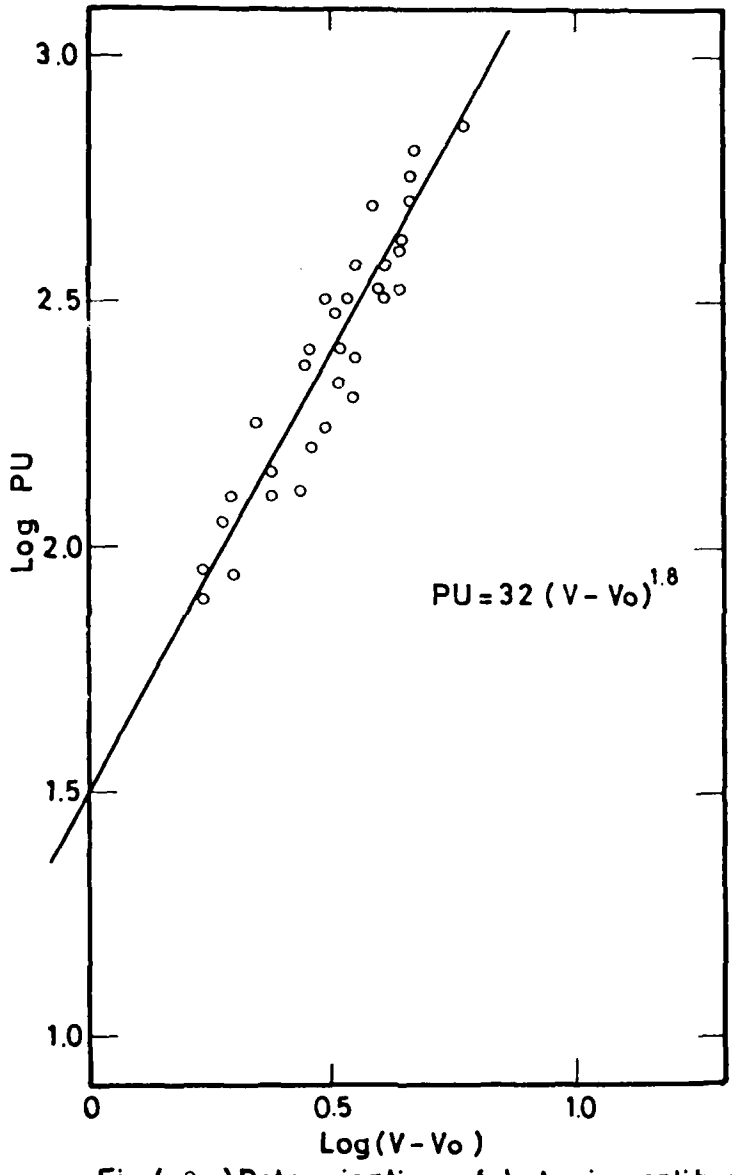

Fig.(8) Determination of hot-wire calibration constants

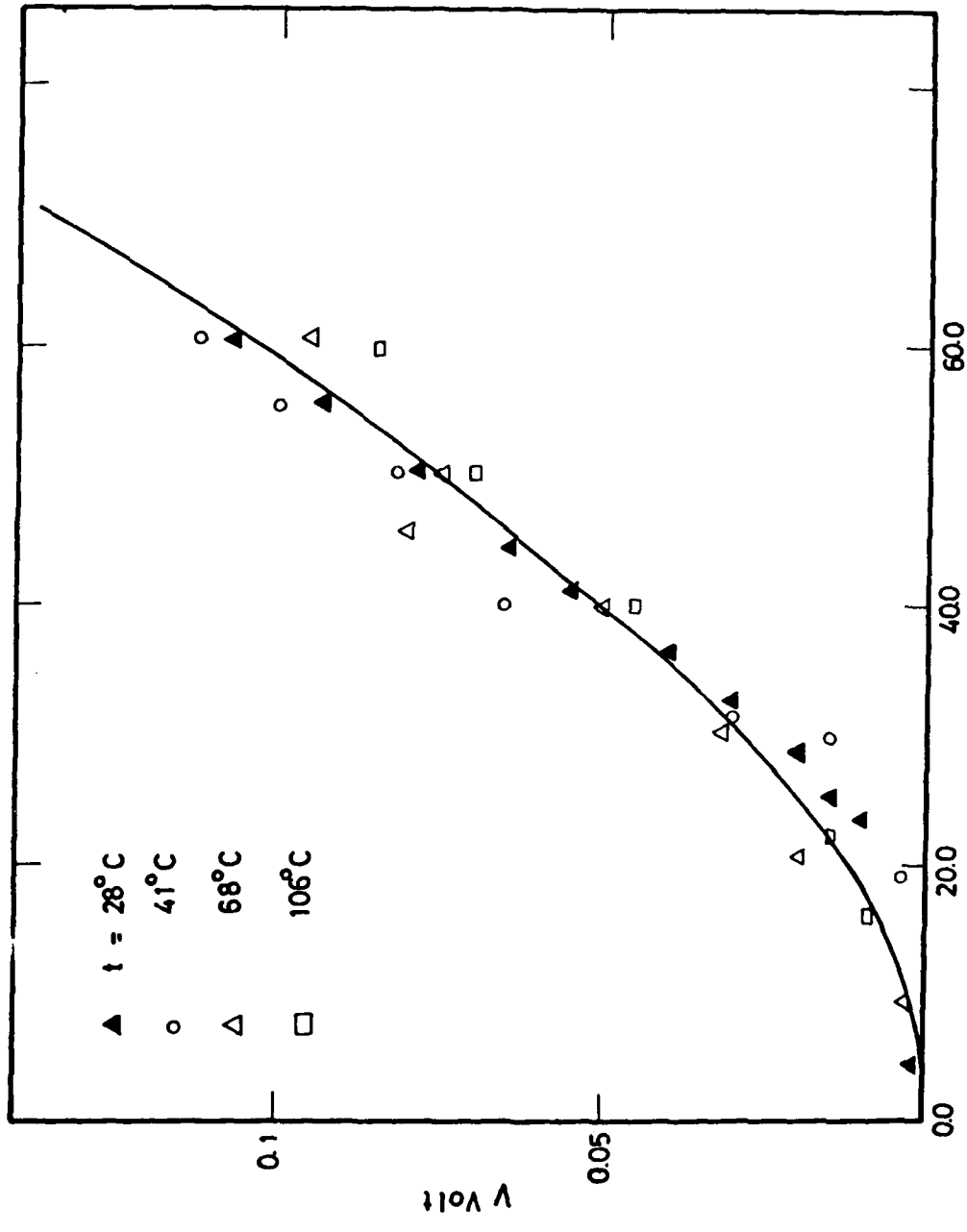

Fig.(9) Calibration curve for microphone condenser probe at atmospheric pressure and different temperatures

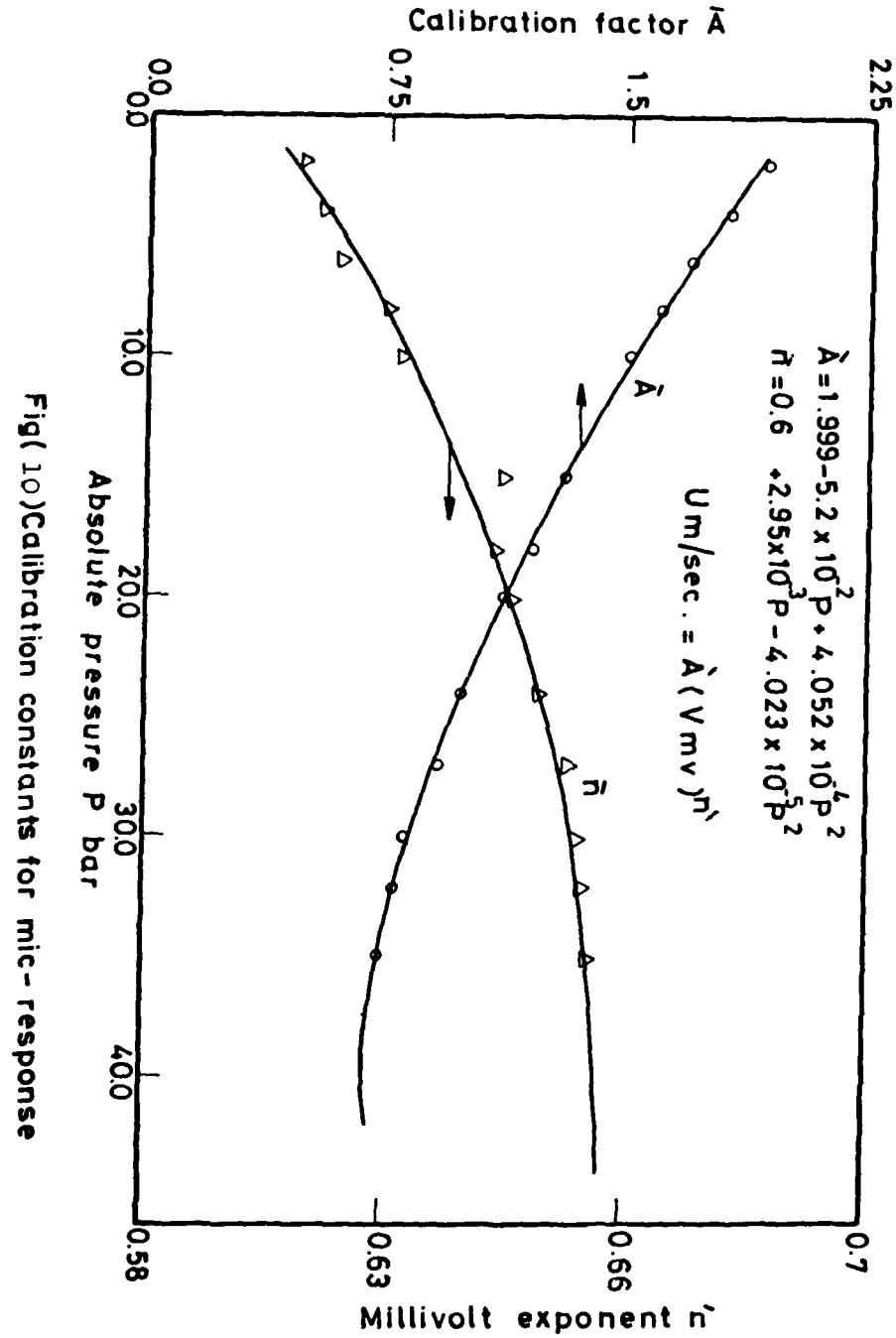

Fig(10)Calibration constants for mic- response

p : the absolute pressure in bar.

b- Effect of Pressure and Temperature on fluctuating Velocity

Mean values of pressure and velocity could be measured as explained before. For fluctuating velocity it was found that both pressure and temperature affect the response of the Microphone condenser.

The principle of the microphone-condenser is based upon the measuring of the velocity fluctuations from the dynamic pressure fluctuations as stated by lenze [53] . The basic equation for the calculation of the velocity fluctuations from their dynamic pressure fluctuations can be written at the inlet to the probe as follows :

$$P_{total} = \bar{P}+P' = \frac{1}{2}\left| (\bar{\rho}+\rho')\{(\bar{u}+u')^2+v'^2+w'^2\}\right| + P_{static} \qquad (1)$$

where,

$\bar{P}$: mean pressure in bar
P': fluctuating pressure in bar
u',v'and w'fluctuating velocity components in polar coordinates r, θ, z.
$\bar{u}$: mean velocity component in radial direction.
$\bar{\rho}$: mean density in Kg/m^3
ρ': fluctuating density in Kg/m^3.

Equation (1) can be written as :

$$\bar{p}+p' = \frac{1}{2}\rho|\bar{u}^2+2\bar{u}u'+u'^2+v'^2+w'^2| + \frac{1}{2}\rho|\bar{u}^2+2\bar{u}u'+u'^2+v'^2+w'^2| + P_{stat.} \qquad (2)$$

Considering the fluctuating velocity u' and neglecting the other two fluctuating velocities and the term $1/2\ \rho' u'^2$, the dynamic pressure can be subdivided into the mean pressure and the fluctuating one in the following forms respectively :

$$\bar{P} = \frac{1}{2}\ \bar{\rho}\ \bar{u}^2 + P_{stat.} \qquad (3)$$

and in the following form :

$$P' = \bar{\rho}\bar{u}\ u' + \frac{1}{2}\ \rho'\bar{u}^2 + \frac{1}{2}\ \bar{\rho}u'^2 + \rho'\bar{u}u' \qquad (5)$$

Rearanging the fluctuating pressure as follows

$$P' = \bar{\rho}\ \bar{u}^2\left(\frac{u'}{\bar{u}} + \frac{\rho'}{2\ \bar{\rho}} + \frac{u'^2}{2\ \bar{u}^2} + \frac{\rho'u'}{\bar{u}\ \bar{\rho}}\right) \qquad (6)$$

Taking the root mean square for both sides of equation (6) and deviding the results by equation (4) the following relation can be deduced

$$T_u = \sqrt{\left(\frac{2+a}{4a+2}\right)^2 + \frac{T_\rho}{2a+1}} - \frac{2+a}{4a+2} \qquad (7)$$

where,

$$a = T_\rho / T_u \qquad (8)$$

$$T_u = \sqrt{\bar{u}'^2}\ /\ \bar{u} \qquad (9)$$

and

$$T_\rho = \sqrt{\rho'^2} / \bar{\rho} \simeq \sqrt{T'^2} / \bar{T} \qquad (10)$$

Equation (7) can be used for the calculation of velocity fluctuations u' ar v' from the corresponding pressure fluctuations if the value of a is determined.

Since

$$a = T_\rho / T_u = \frac{\sqrt{T'^2}}{\bar{T}} / \frac{\sqrt{u'^2}}{\bar{U}} = \frac{\sqrt{T'^2}}{\sqrt{u'^2}} \cdot \frac{\bar{U}}{\bar{T}} \simeq \frac{\bar{U}}{\bar{T}} \qquad (11)$$

then the constant "a" could be obtained using the mean velocity and mean temperature which cauld be easily measured. Calculating the value of "a" along the compression and expansion strokes, it is found that its value ranges between 0.01 and 0.2.

From the measurments of pressure, temperature and velocity, these two extreme values of "a" are constructed in Fig.(11) , and it is noticed that there is a small difference between these two values, which indicates that the change in temperature has a slightly small effect on the value of velocity fluctuations.

3.4. EXPERIMENTAL TECHNIQUE

The aim of the present work is to determine the effect of working conditions and geometrical parameters of the swirl chamber in a diesel engine upon air flow pattern. This is required to modify the mathematical model to correct the turbulence mixing length due to stream line curveture and flow nonisotropy resulting from swirl chamber geometry and operating conditions.

The following experimental data have been determined at various conditions defined by swirl chamber volume ratio, port area ratio, and engine speed :

1- Average and random air velocity components defined by the hot-wire and microphone condenser anemometers.

2- Combustion chamber pressure variation,

3- Maximum swirl chamber pressure.

4- Crank angle degree as a time base,

5- Top dead centre.

6- Engine speed.

The two position technique defined by the x-probe hot-wire an emometer has been used to calculate the radial and tangential components of the instantanous velocity at each location. One of the wires is located in a plane perpendicular to both radial and tangential directions, as shown in Fig.(12.a). In this position the wire response has a superimposed effect of both radial and tangential velocity components. The second wire is located perpendicular to the first wire such that it will be only normal to the radial v - locity component. The hot wire response in this case results only from the radial velocity component. The later wire can determine the radial mean velocity V_r and its fluctuating velocity $V_r'^2$. The

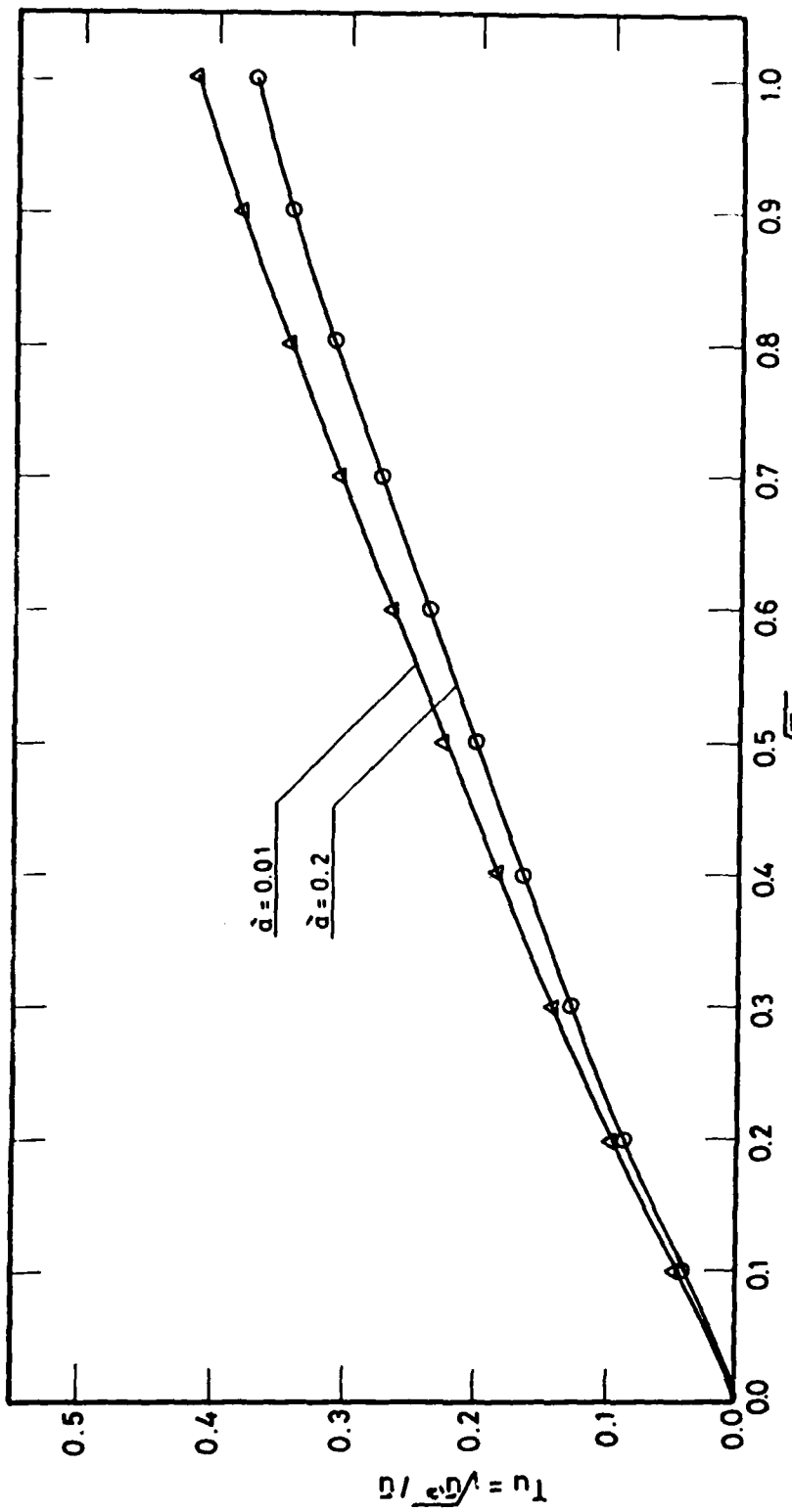

Fig.(11)Calibration curve for fluctuating velocity of microphone condenser.

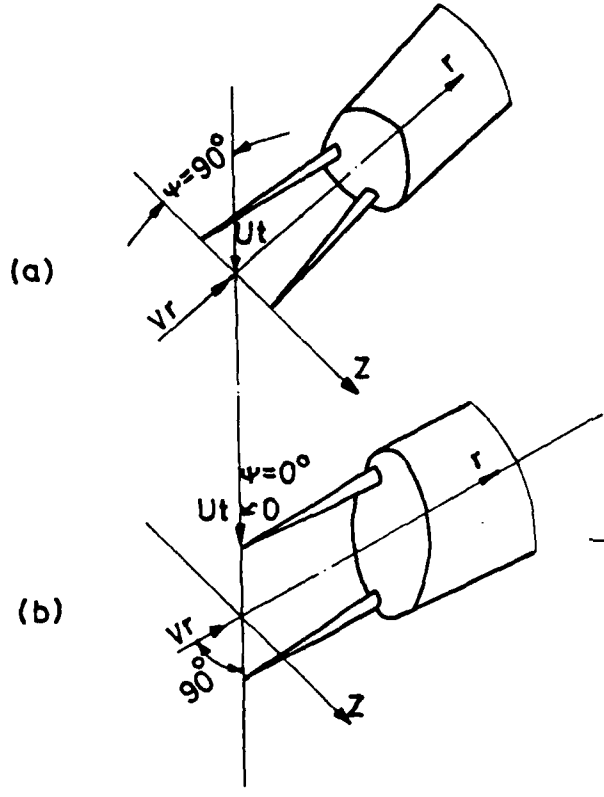

Fig(12) Two- positions of hot-wire probe during measuring.

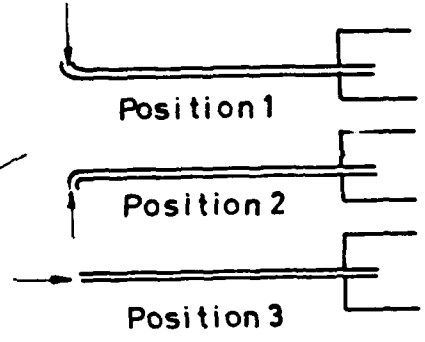

Fig (13) Three positions of condenser microphone probe during measuring.

tangential velocity can be determined by subtracting from the response of the first wire the instantaneous radial velocity. Thereafter the mean tangential velocity and its fluctuation can be determined.

The same technique, which is the two position shown in Fig.(13), has been used by the microphone condenser to determine the mean tangential and radial velocities and their fluctuations.

The experimental work has been carried out at various swirl chamber diameters and tangential part diameters satisfing relative swirl chamber volume ratios and relative port area ratios given in Table (3).

Table (3) Variation of swirl chamber ratio and port area ratio.

Swirl chamber diameter mm	48.5	45.0	41.5	38.0	34.5
Swirl chamber valume ratio	.772	.64	.545	.457	.376

Connected channel diameter mm	8	10	12	14	16
Port area ratio	.0041	.0064	.0092	.0125	.0164

The ergine speed has been changed also between 800 and 1500 RPM. One of the previous parameters has been changed while the other parameters are kept constant within the following values.

Compression ratio	17.0	
Swirl chamber volume ratio	0.772	
Tangential port area ratio	0.009	
Engine speed	1000	rpm

3.5. ERROR ANALYSIS

It is known that the actual value of any measurements can not exactly be obtained. The determination of the possible maximum errors which is expected during the readings of the measured quantity is reported in this section.

3.5.1. Systematic Errors

These kind of errors are created from the imperfection of measuring methods, lack of accuracy and personal errors.

Systematic errors can be calculated as follows :-
Let(G) be any function of $x_1, x_2, \ldots, x_n$

$$G = G(x_1, x_2, \ldots\ldots, x_n) \qquad (12)$$

where, $x_1, x_2, \ldots, x_n$ are independent variables
G may be any one of the measured quantities.

Then the error in any one of the measured quantities can calculated from the following relation ;

$$dG = \sum_{i=1}^{n} \frac{\partial G}{\partial x_i} \, dx_i \qquad (13)$$

applying this equation to the main measured quantities, their error can be evaluated :

1- Flow velocity :-

The pressure drop in the orifice meter of calibration set up has been measured by water manometer of accuracy 1%

$$U = \frac{2gH}{\rho_{air}} \qquad (14)$$

Hence,

$$\frac{\delta U}{U} = \frac{1}{2}\,\frac{\delta H}{H} = \pm\,\frac{1}{2}\,\frac{3}{300} = \pm\ 0.005$$

and the maximum error in velocity U is $\pm$ 0.5%.

2- Error in hot-wire reading :-

$$PU = PU\ (V, V_o)$$

and the error becomes

$$\frac{\delta PU}{PU} = \frac{\delta V}{V} + \frac{\delta V_o}{V_o}$$

$$= \frac{0.093}{10.02} + \frac{0.093}{7.68} = \pm\ 0.0214$$

The maximum error in velocity measurements by hot-wire is $\pm$ 2.14%, which eleminates other errors resulting from cooling effect, corrosion temperature compensation and unhomogeneous distribution on wire.

3- Error in Microphone-condenser reading :-

$$U_{m/s} = U(V_{volt})$$

$$\frac{\delta U}{U} = \frac{\delta V}{V} = \frac{0.0032}{0.112} = \pm\ 0.0285$$

The maximum error in velocity measurements by microphone condenser is $\pm$ 2.85%.

3.5.2. Accidental Errors

It includes the errors originated from accidental unknown causes. Such errors are too complex in nature to be tracted. It can be estimated by the help of theory of probability.

Let $x_1, x_2, \ldots, x_n$ be n observations of a variable x at the same regime then the most probable value of x is given by ;

$$\bar{x} = \frac{x_1 + x_2 + \ldots + x_n}{n} \quad \sum_{i=1}^{n} \frac{x_i}{n} \qquad (15)$$

Hence the mean value of the deviations from x is :-

$$e = \pm \sum_{i=1}^{n} \Delta i^2/n \qquad (16)$$

where,

$$\Delta_i = x_i - x$$

and the most probable error which occurs with probability 50% for a single observation is given by :

$$e_p = \pm 0.67 \sum_{i=1}^{n} \Delta_i^2 / (n-1) \qquad (17)$$

The most probable error of the measured parameters in all tests was calculated from equation (3.30) for 10 observations of the same regime. It was found that the probable error for the swirl chamber maximum pressure and engine speed are $\pm$ 1.81% and $\pm$ 0.6% respectively.

CHAPTER 4

PRESENTATION AND DISCUSSION OF RESULTS

This work locks in the modelling of flowfield inside a motored diesel engine swirl chamber, by developing a mathematical model capable to predict the air velocity inside swirl combustion chamber. For this purpose it is required to investigate experimentally the effect of various geometrical parameters of the swirl chamber and engine working conditions on the flowfield to validate the computational procedure with a wide range of reliable information.

This chapter includes a careful comparison of the air flow velocity and the predicted values over a wide range of experimental data. Generalized dimensionless equations for the coefficient of the turbulence model which depends on the operating conditions of engine and swirl chamber geometry are derived. Furthermore, results for the effect of engine speed and swirl chamber geometry on flow velocity and turbulence intensity are predicted and discussed.

4.1 EFFECT OF SWIRL CHAMBER GEOMETRY ON THE TURBULENCE COEFFICIENT C_D

The value of the turbulence coefficient C_D at various radial distance has been calculated from the experimental results using the following equation :

$$C_D = (\tau/\rho K)^2 \qquad (1)$$

where

$$\tau = \rho u'v'$$

$$K = \tfrac{1}{2}\,(u'^2+v'^2+w'^2)$$

The measurements have been carried out for several operating conditions keeping the reference values constant as mentioned in Table (4) and varying only one parameter.

Table (4) Reference Operating and Geometrical Conditions

Engine speed (r.p.m)	Swirl volume ratio	Ejection port area ratio	Measurement point
1000.0	0.772	0.0092	At T.D.C. plane 4 radius 12.2mm

A sample of the calculation results of the turbulence coefficient C_D, along radius, at engine speed 1000 r.p.m. swirl volume ratio 0.772, ejection port area ratio 0.0092, plane 4, and top dead center, is illustrated in Figure (14). It is clear from the figure that the experimental results fall on a parabolic curve, which can be represented with adequate accuracy by the following relation :

$$C_D = A_1\,(r/R_S)^{n_1} \qquad (2)$$

Plotting the experimental results on a log-log graph the values of A_1 and n_1 have been calculated and equal 1.16 and -0.08 respectively.

The equation of the dimensionless coefficient C_D becomes ;

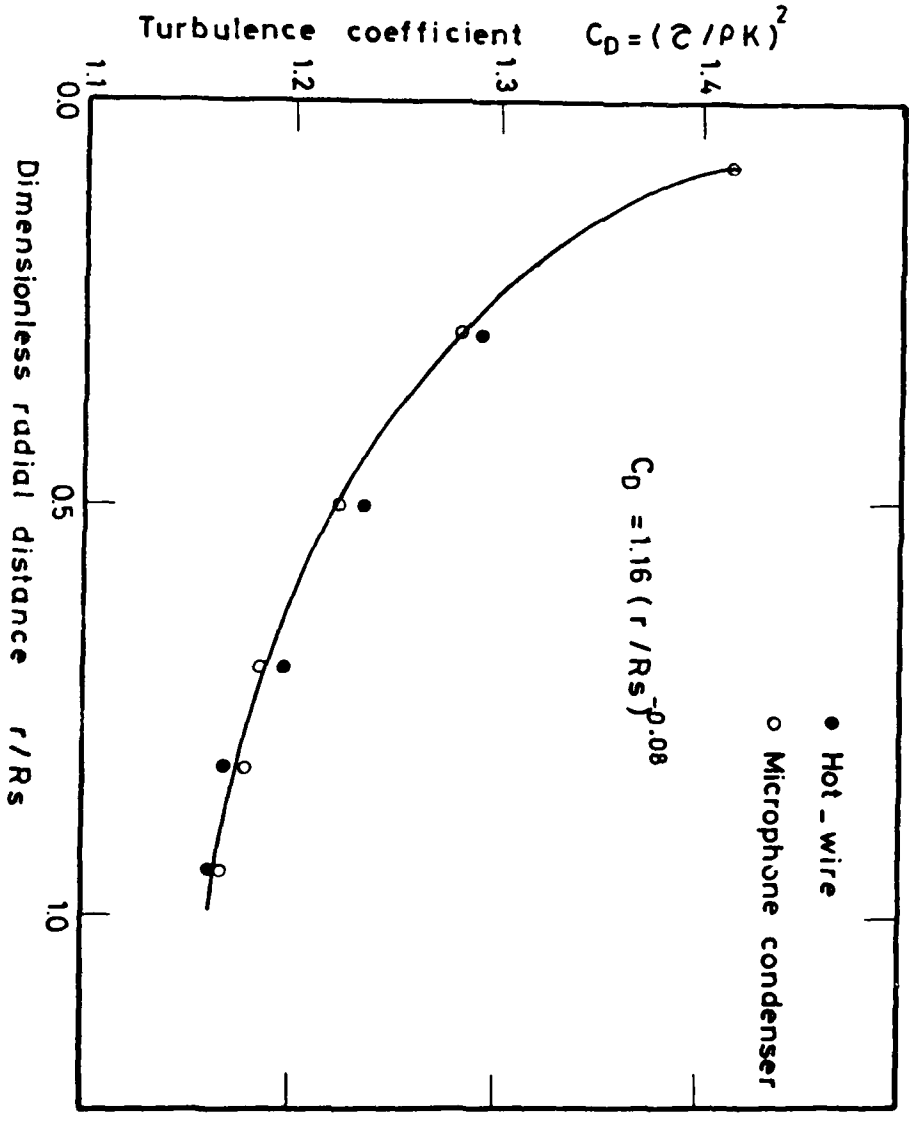

Fig.(14)Variation of coefficient C_D with radial distance.

$$C_D = 1.16\ (r/R_s)^{-0.08} \qquad (3)$$

It is clear from Fig.(14) that the coefficient C_D has different values along the radial distance as it depends upon the local turbulence condition obtained from the variation of the ratio between the turbulence shear stress τand the turbulence generation ρK. The coefficient has a maximum value of about 1.42 near the swirl chamber centre at which the shear stress τ is higher than the turbulence generation ρK and it decreases behind the swirl chamber wall reaching a value of 1.165 due to the effect of chamber wall on the turbulence generation ρK.

Studying the effect of engine speed on the coefficient C_D for the same mentioned parameters at a distance 12.2 mm from the swirl chamber centre, it is found as shown in Fig.(15) that the results fall on a parabolic curve, which can be represented by the following relation:

$$C_D = 1.2255\ (N/N_o)^{-0.88} \qquad (4)$$

It is clear from the figure that the turbulence shear stress τ is higher than the turbulence generation at low speeds than at high speeds. This indicates that the turbulence of flow inside the swirl chamber increases with the increase of engine speed. It is indicated also that the engine speed afects the coefficient C_D significantly while C_D along the radial distance has a smaller variation.
Studying the effect of ejection port area ratio (A_j/A) upon the turbulence coefficient C_D, it was required to calculate it from the experimental results obtained by hot-wire and microphone- condenser anemometers. A sample of results are shown in Fig.(16) where C_d is plotted versus the dimensionless ejection port area ratio. It is clear from the figure that the ejection port area has a strong effect upon the coefficient C_D and that it increases with the increase of ejection port area. This shows that the turbulence shear stress τ is higher than the turbulence generation ρK and therefore the turbulence of the flowfield inside the swirl chamber increases with the increase of ejection port area. Similar to the effect of both radial distance ratio and engine speed ratio, it is found that the experimental results fall in a parabolic curve of the following form :

$$C_D = 33.359\ (A_j/A)^{0.704} \qquad (5)$$

Regarding the effect of swirl chamber volume ratio (V_s/V_c) the results of calculation of the turbulence coefficient are plotted in Fig.(17), from which it is clear that the experimental results fall on a parabolic curve of the following form :

$$C_D = 1.303\ (V_s/V_c)^{0.229} \qquad (6)$$

It is noticed from the figure that the value of the coefficient C_D increases with the increase of the swirl volume ratio, which means that using low swirl chamber volume ratio creates turbulence generation much higher than when using high swirl chamber volume ratio.

The generalized dimensionless equation of the effect of the radial distance, engine speed, ejection port area ratio and swirl chamber volume ratio on the turbulence coefficient can be obtained by plotting $(r/R_s)^{-0.08}(N/N_o)^{-0.88}(Aj/A)^{0.704}(V_s/V_c)^{0.229}$ versus C_D as shown

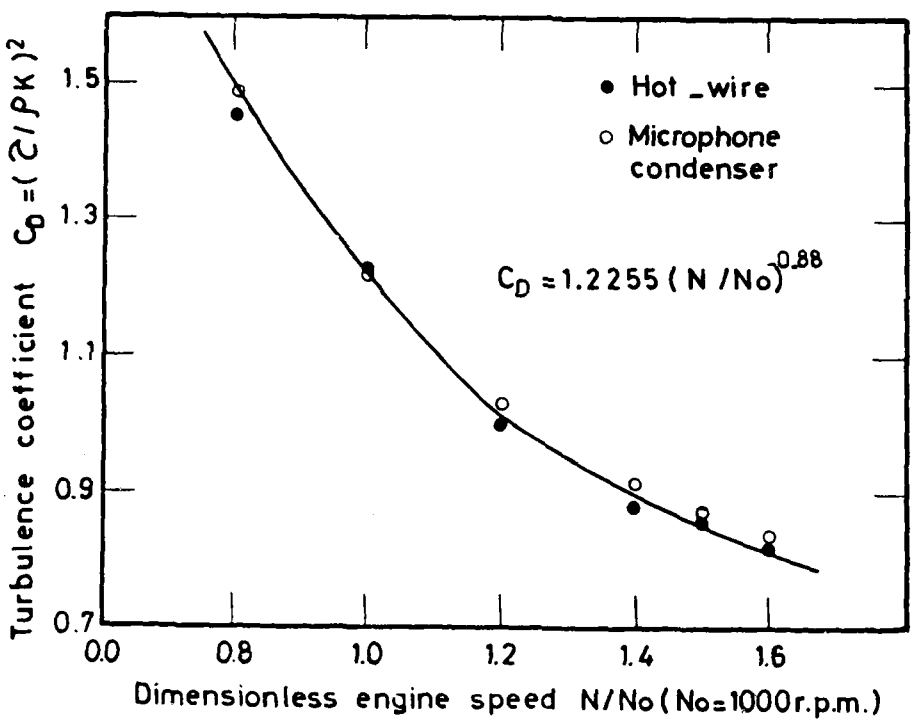

Fig.(15)Variation of coefficier.: C_D with engine speed.

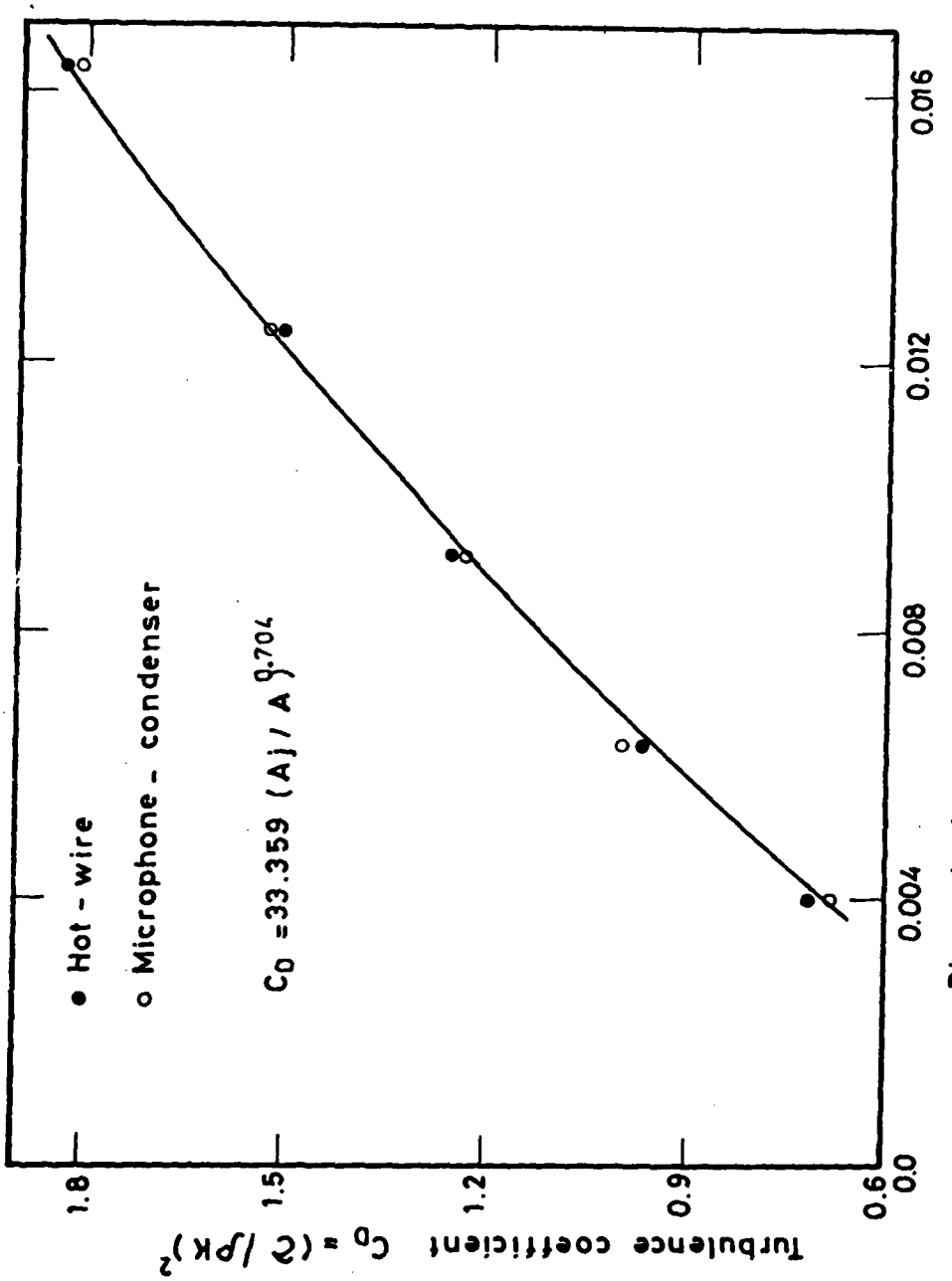

Fig.(16) Variation of coefficient C_D with ejection port area ratio.

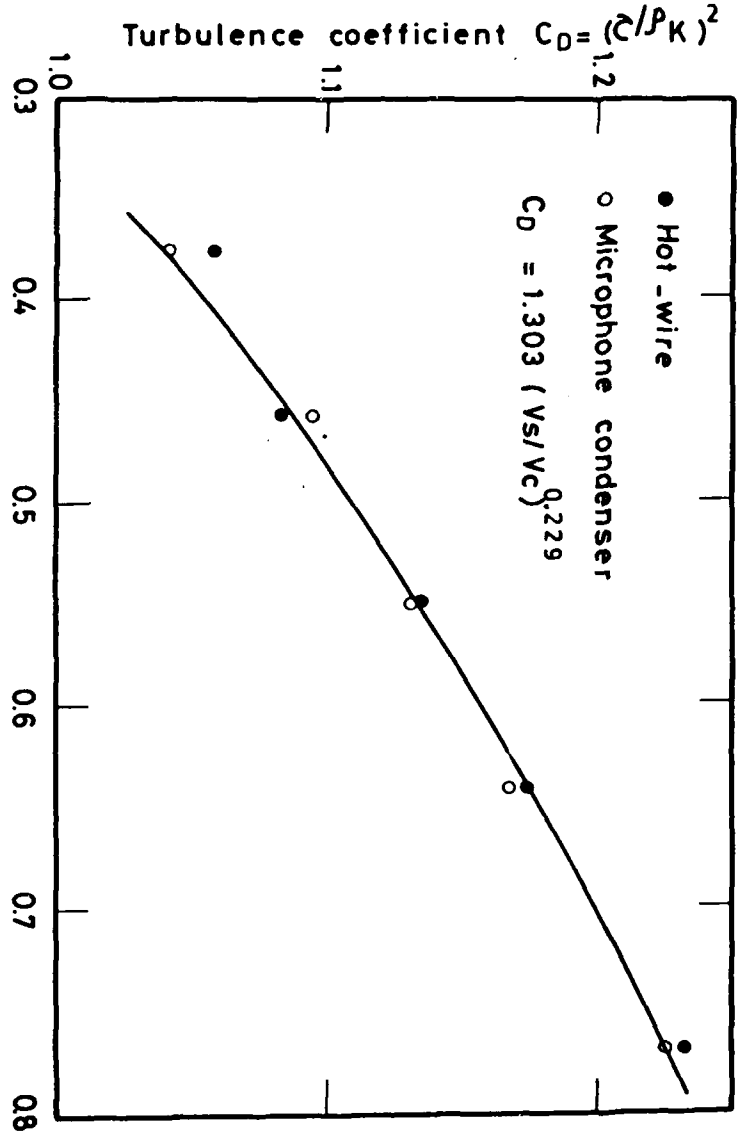

Fig.(17)Variation of coefficient C_D with swirl volume ratio.

in Fig.(18). By means of the least square method, it is found that the following relation fits adequatly the combined effect of the above dimensionless groups on C_D :

$$C_D = 33.47(r/Rs)^{-0.08}(N/No)^{0.88}(A_j/A)^{-0.704}(A_s/A_c)^{0.229} \quad (7)$$

Actually the coefficient C_D could be expressed as a product of the constant value of C_{D_o} (C_{D_o}=1.0) and a factor (F) which depends on the swirl chamber geometry and engine speed as follows :

$$C_D = C_{D_o} \cdot F \quad (8)$$

where, $C_{D_o} = 1.0$

F: correction factor determined from experimental results.

Then the correction factor takes the following form :

$$F= 33.47(r/R_s)^{-0.08}(N/No)^{-0.88}(A_j/A)^{0.704}(V_s/V_c)^{0.229} \quad (9)$$

The coefficients C_D and C_1 were derived for near wall condition while the coefficient C_2 was derived from the decay of turbulence behind a grid. The coefficient C_2 can be written in the following form :

$$C_2 = 2\, C_{D_o}\, F \quad (10)$$

while the coefficient C_1 can be written as follows :

$$C_1 = C_2/C_{D_o}\, F - \lambda^2/\sigma_\varepsilon\, (C_{D_o}\, F)^{\frac{1}{2}} \quad (11)$$

The coefficient C_D depends on the local turbulence and distance and at the same time involves the other two coefficients. Therefore, the coefficient C_D is the adjustable coefficient for the mathematical model to validate the experimental data. The fine adjustment of the model could be obtained by the coefficient C_1 whcih includes the constant λ as it depends on the experimental data and operating conditions |50|.

In order to test the turbulence model incorporating these coefficients calculated from equations (7) through (11) a wide range comparison between predicted and measured results has been carried out in the next paragraph. The comparison has been carried out also with the previously predicted results |22| using the following turbulence constants :

$$C_{D_o} = 1.0 \quad , \quad C_2 = 1.92 \quad \text{and} \quad C_1 = 1.44$$

4.2 COMPARISON BETWEEN EXPERIMENTAL AND PREDICTED RESULTS

The K- and ε - equations incorporating the experimental coefficients together with momentum equation in radial and tangential direction and continuty equations are solved using the finite difference procedure mentioned before. The computation is started at the beginning of the compression stroke. The instantaneous inlet velocities to the swirl chamber are calculated by the previous computational method

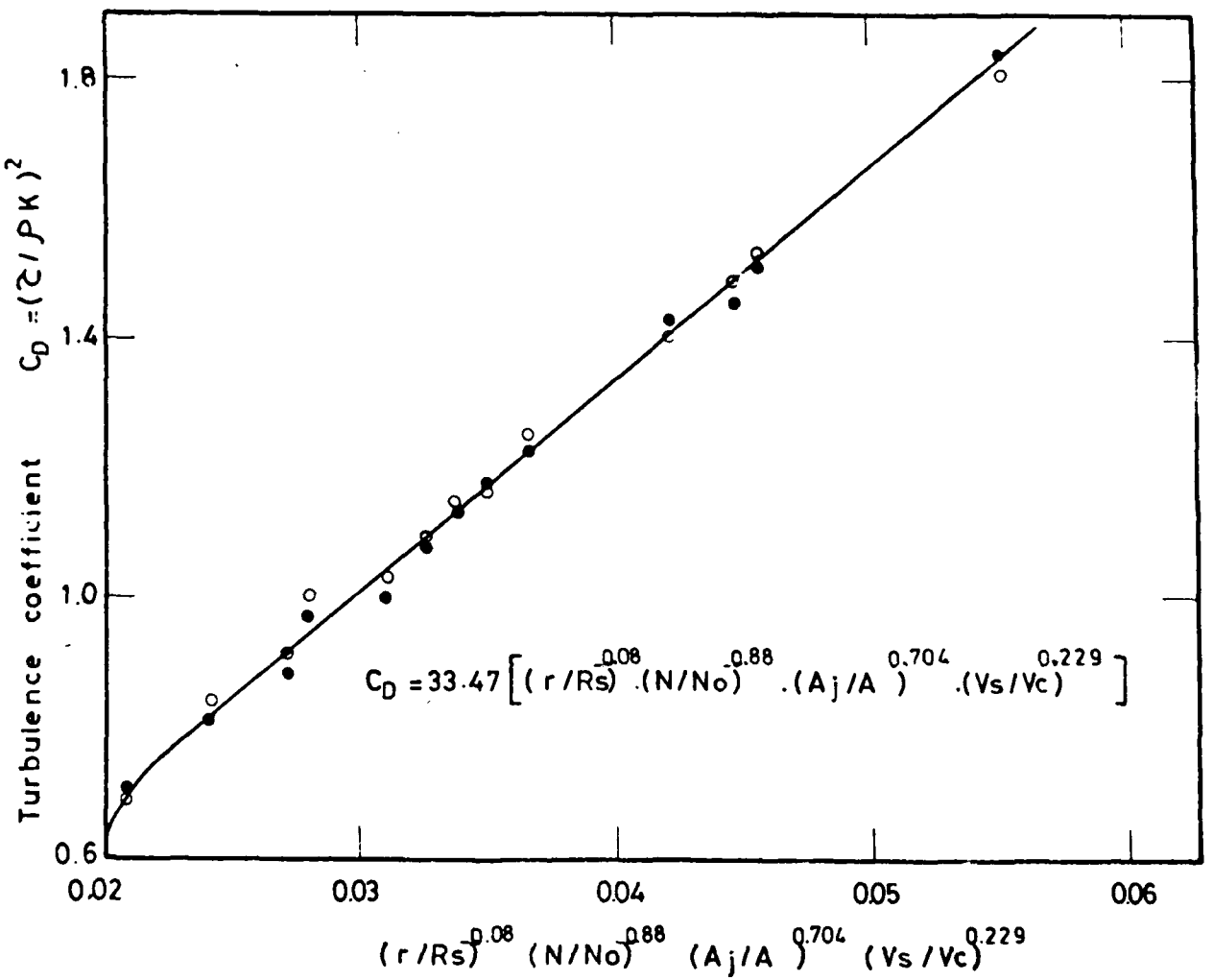

Fig. (18) Graphical representation of equation (7)

discussed in chapter 2. Computations are carried out mainly for a diesel engine having a swirl chamber of 48.5 mm diameter corresponding to a swirl volume ratio of 0.772, tangential port of 12 mm diameter corresponding to an ejection port area ratio of 0.0092, engine speed of 1000 r.p.m., and compression ratio of 17.0. The time step of computations is chosen to be 2^{o} crank angle interval.

A wide range comparison of the present predicted results during the compression and expansion strokes, the predicted results of Ref.[22] and experimental results is shown in Figures (19) through (24) for tangential velocity, turbulence intensity, and radial velocity. The constant C_D has been calculated using equation (4.8) and the experimental results have been determined by the hotwire and microphone-condenser anemometers.

i- Tangential Velocity

The predicted results for the tangential velocity together with the experimental results are determined for the conditions mentioned in the previous paragraph at the top dead centre and plane 4. The results are illustrated in Fig.(19), which shows the variation of tangential velocity with radius at the end of compression stroke. Figure (20) shows also the variation of the tangential velocity for the same conditions with the crank angle during the compression and expansion strokes. It is clear from the results that the tangential velocity along the radius consists of two zones, the solid vortex zone at the centre of the swirl chamber, and the free vortex zone near the swirl chamber wall. A quite sufficient agreement is noticed between the experimental and predicted results by the suggested method especially near the swirl chamber wall. Discrepancy is noticed near the centre with the hot wire results which may be attributed to the error resulting from the determination of the probe inclination and the wire length. A fairly sufficient agreement is noted in the free vortex zone near the swirl chamber wall.

Figure (20) shows the variation of tangential velocity with the crank angle during compression and expansion strokes. A quite sufficient agreement is noticed during the compression stroke between the experimental results and the predicted ones obtained by the suggested model in this work.

ii- Turbulence Intensity

The turbulence intensity has been calculated from the experimental and predicted results by the following relation :

$$i = \sqrt{\frac{2}{3}\ K}/C_{pm}$$

and the results at various radial distances and crank angle degress during compression and expansion strokes are illustrated in Figs. (21) and (22), respectively. A more satisfactory agreement along the radial distance is noted between the experimental and computed results by the suggested model than that obtained by fixed turbulence constants. It is noticed from Fig.(21) that turbulence intensity has a maximum value of about 1.51 near the swirl chamber centre while a minimum turbulence intensity of about 0.9 occurs at a radial distance ratio of $r/R_S = 0.6$. Figure (22) shows the turbulence intensity variation with the crank angle at $r/R_S = 0.503$, from which

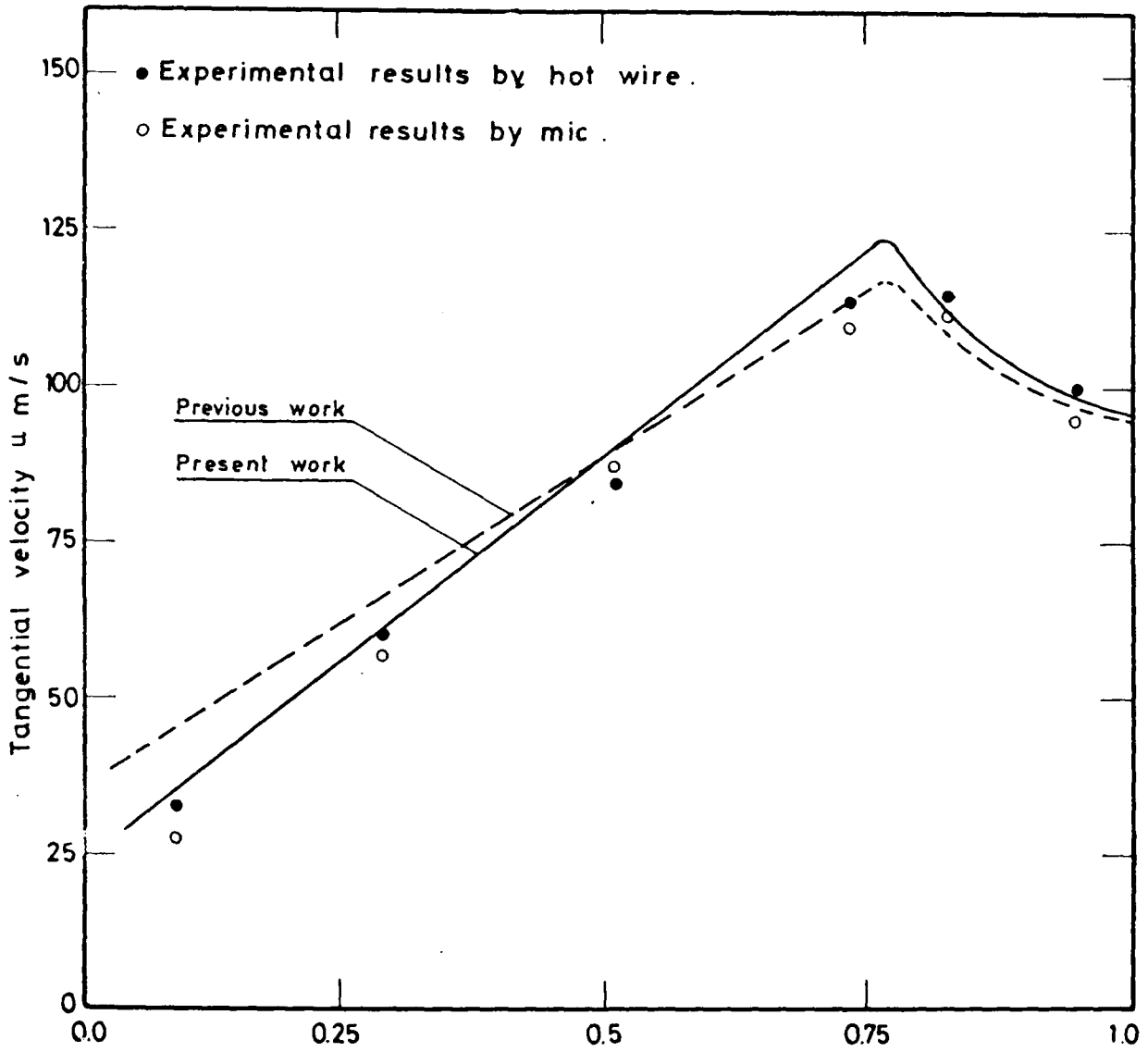

Fig.(19)Comparison of predicted tangential velocity by the suggested and previous method [ ] along the radius with the experimental results at TDC keeping Vs/Vc = 0.772, A_j/A = 0.0092 and N = 1500 r.p.m. constant.

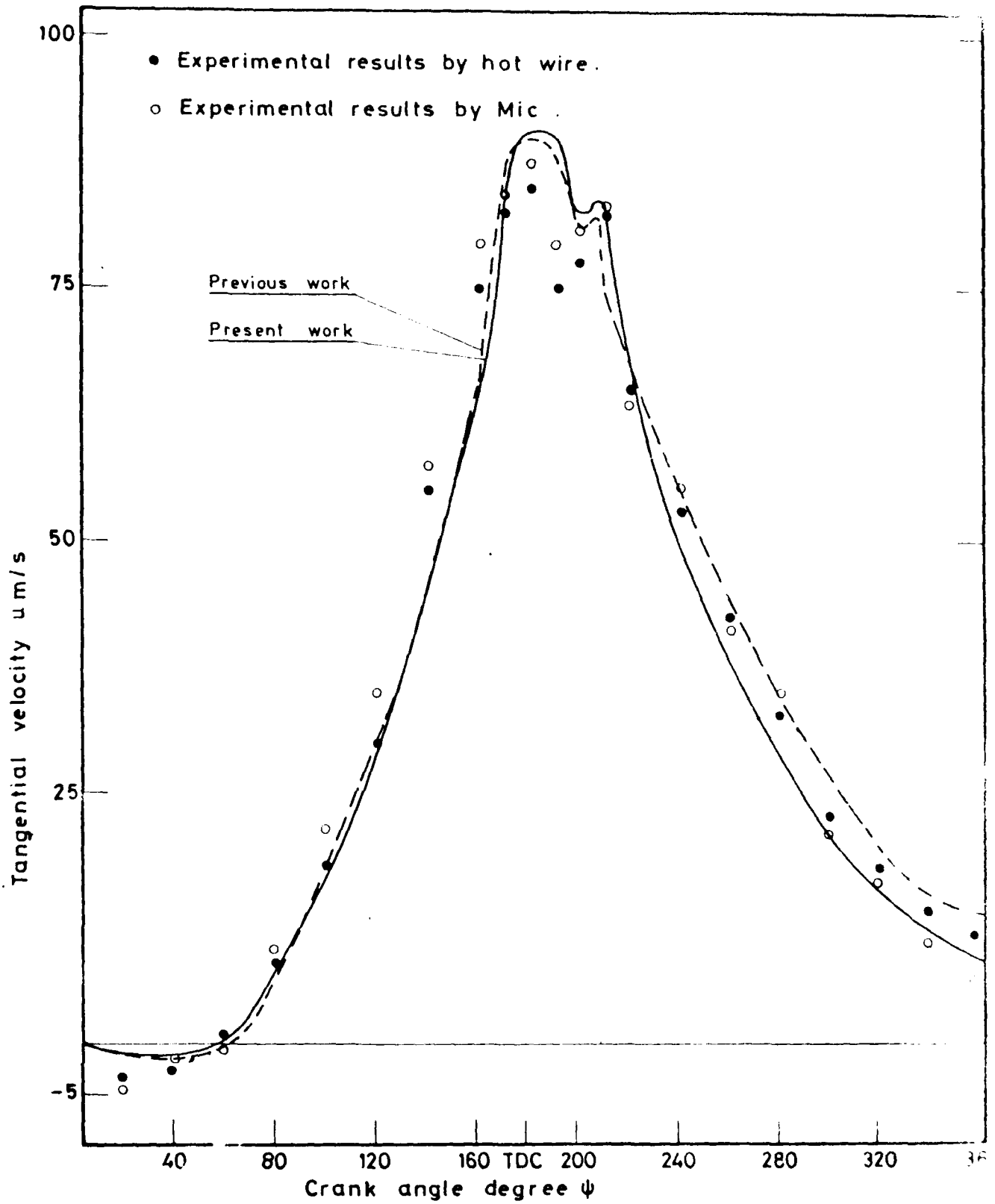

Fig.(20) Comparison of predicted tangential velocity by the suggested and previous method[ ] during compression and expansion strokes with the experimental results at radial distance ratio 0.503 keeping $V_s/V_c = 0.772$, $A_j/A = 0.0092$ and N = 1500 r.p.m. constant.

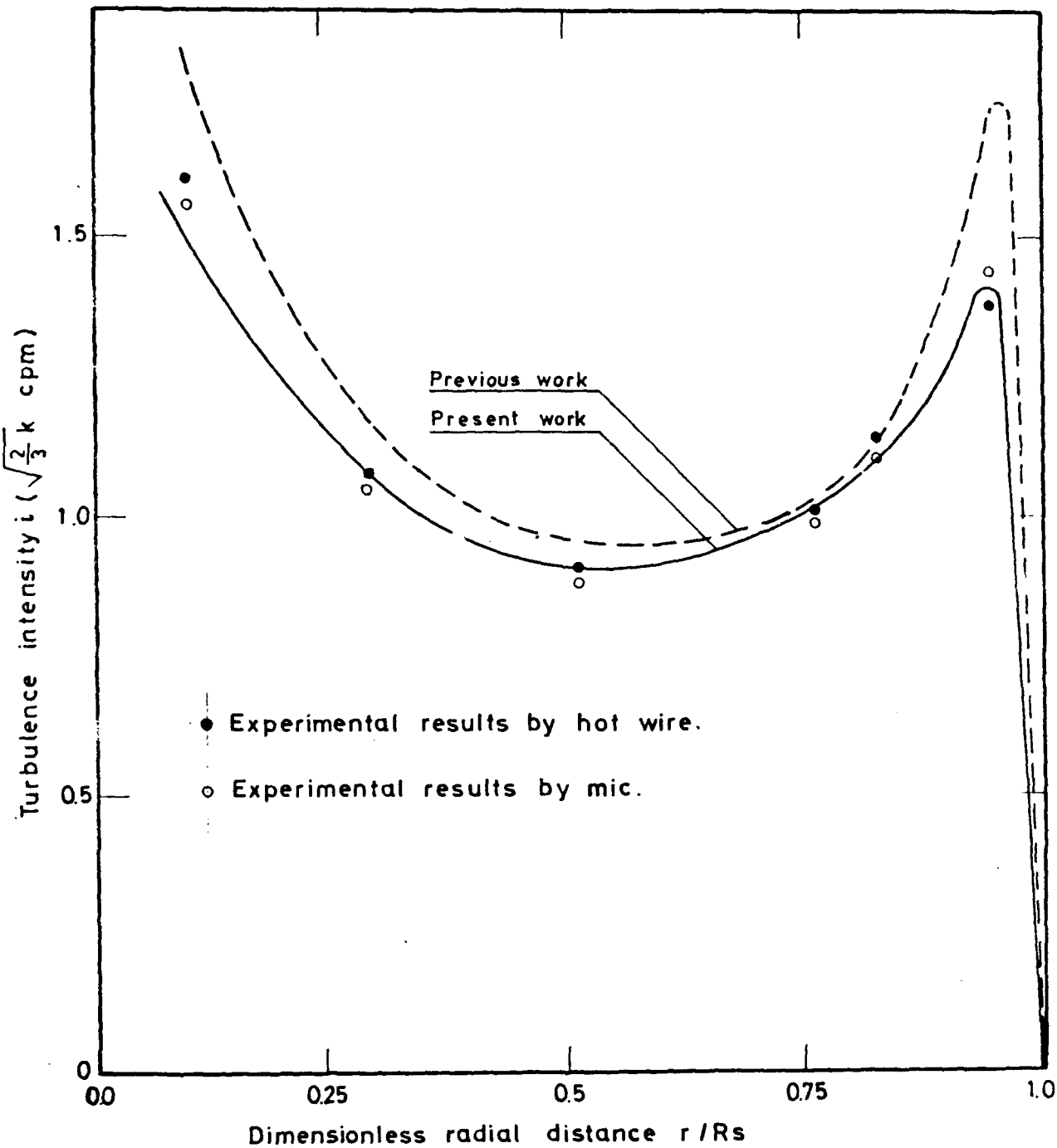

Fig.(21)Comparison of predicted turbulence intensity by the suggested and previous method along the radius with the experimental results at TDC keeping Vs/Vc =0.772, Aj/A= 0.0092 and N = 1500 r.p.m. constant.

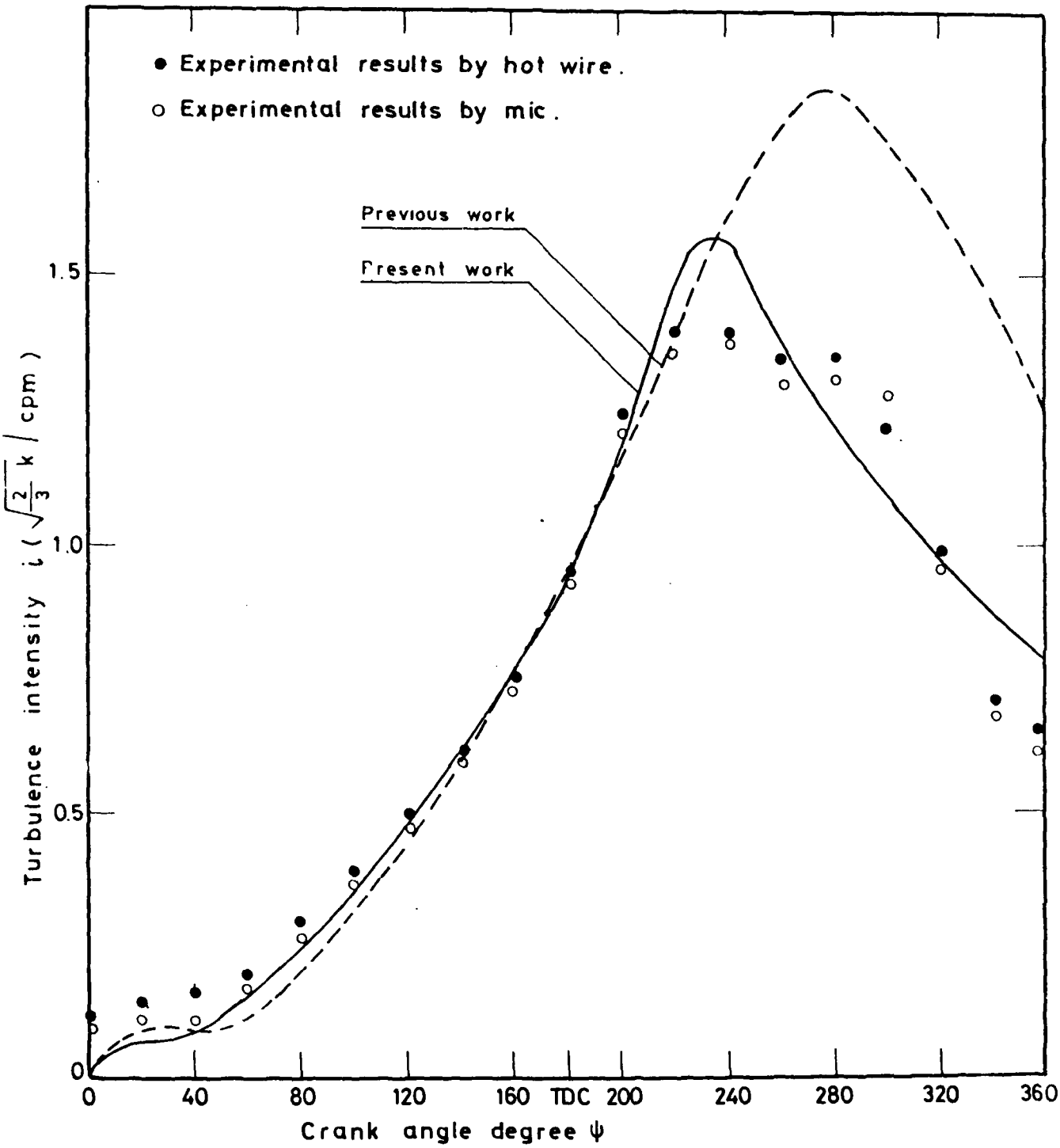

Fig. (22) Predicted and experimental variation of the turbulence intensity during compression and expansion strokes at radial distance ratio 0.503 keeping $V_s / V_c = 0.772$, $A_j / A = 0.0092$ and N = 1500 r.p.m. constant.

it is noted that a quite good agreement is obtained during the compression stroke with the suggested model. Little deviation is noticed during the expansion stroke which may be attributed to the truncation error resulting from the mathematical iteration solution. The turbulence intensity has a very low value at the beginning of compression stroke and increases rapidly during the compression stroke reaching a maximum value of 1.5 at about 100° ATDC. Thereafter it decreases again during the expansion stroke.

iii- Radial Velocity

Figures (23) and (24) show a comparison between the predicted and measured results of the radial velocity at various radial distances and crank angles during compression and expansion strokes respectively. Figure (23) shows the variation of radial velocity at various radial distances at planes 4 and 8 at TDC, good agreement is noticed along the radial distance between the predicted and measured values. There is no discripancy between the predicted results computed with the suggested model and the fixed turbulence constants model, which may be attributed to the lower value of the radial velocity component. The radial velocity has a maximum value of about 8 m/s at about 2 mm from the swirl chamber centre, and decreases slowly with the increase of the radial distance, reaching zero value at the swirl chamber wall. The same behaviour of the radial velocity is noticed at plane 8 where a maximum value of 3.2 m/s is obtained near the centre. This indicates that the presence of a source at the centre causes decay of the radial velocity as it travels towards the chamber wall.

Figure (24) show the variation of the radial velocity during compression and expansion strokes. A quite sufficient agreement is noticed between experimental and predicted results. The change of the turbulence coefficient with the operating condition has a negligble effect due to the small value of the radial velocity. The radial velocity has a low value at the beginning of compression stroke, and increases rapidly with the motion of the piston toward the TDC reaching a maximum value of 11.4m/s at 38° BTDC. Thereafter it decreases with a higher rate than the rate of increase during compression stroke reaching a zero value nearly at 40° ATDC.

From the previous disscussion and analysis of the experimental and predicted results, it can be easily detected that the use of the K-ε turbulence model with coefficients depending on the operating conditions gives better results and satisfactory agreements with the experimental data. Actually the use of the K-ε turbulence model with the empirical values of these constants gives not only deviations from the experimental results but also unlogic values for the turbulence mixing length. However little discripancy is noticed with the experimental results which can be attributed to the errors resulting from the calibration of anemometers and nonisotropy of the flow inside the swirl chamber. Besides uncertainty can exist as a result of the unaccurate determination of the velocity vector inclination angle. The measured values are clearly senstive to this inclination angle.

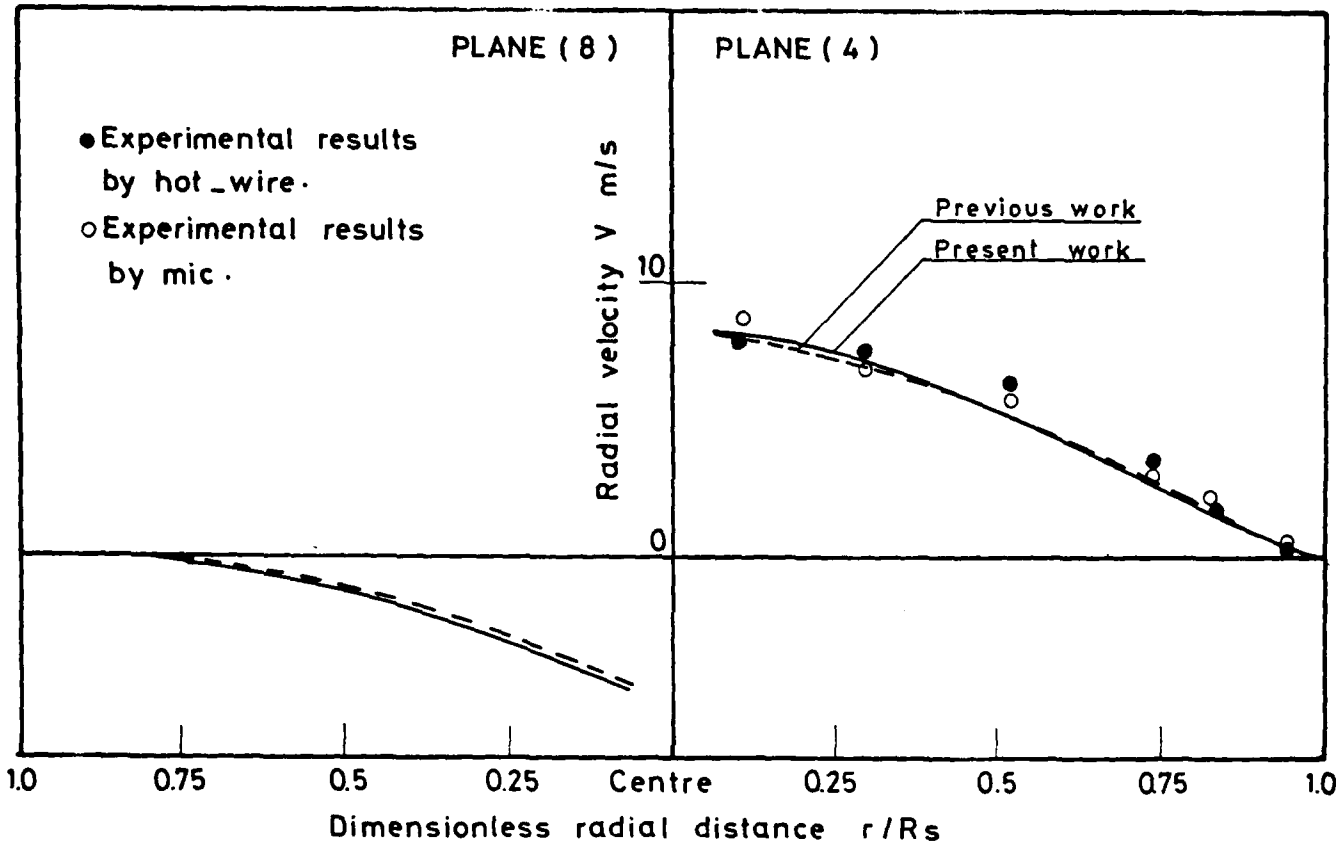

Fig.(23)Comparison of predicted radial velocity by the suggested and previous methods]]along the radius with the experimental results at TDC keeping Vs/Vc =0.772, Aj/A =0.0092 and N =1500 r.p.m. constant.

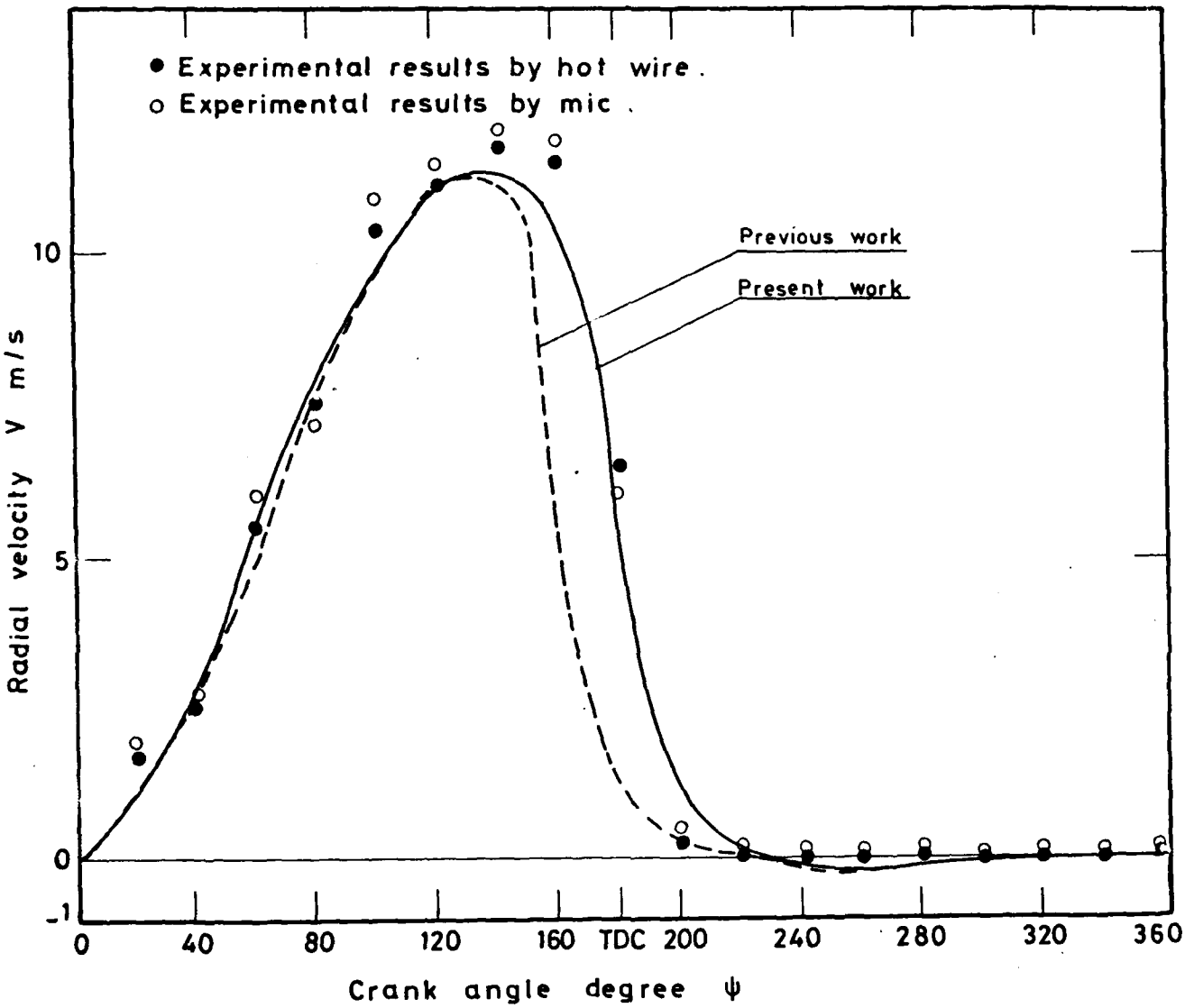

Fig.(24) Comparison of predicted radial velocity by the suggested, and previous method [ ] during compression and expansion strokes with the experimental results at radial distance ratio 0.503 keeping Vs/Vc = 0.772, Aj/A=0.0092 and N = 1500 r. p.m. constant.

4.3. EFFECT OF SWIRL CHAMBER PARAMETERS AND ENGINE SPEED ON THE FLOW FIELD

The flow field inside the swirl chamber is affected by the inlet moment of momentum of the ejecting air from the main cylinder. Consequently,the flow field is affected by the swirl chamber volume ratio, the relative port area, and the engine speed. The study of the effect of these parameters is very important for the spray motion investigation and for the validation of the computational model.

4.3.1. Flow Field During Compression and Expansion Strokes

The air flow field inside the swirl chamber is affected by the inlet moment of momentum of the air entering it, which changes during the compression and expansion strokes. This moment of momentum depends on the pressure ratio between the main cylinder and swirl chamber (P_C/P_S) and consequently on ejected air velocity. Figure (25) shows the variation of the pressure ratio and the ejected velocity versus crank angle during compression and expansion strokes, from which it is clear that the maximum ejected air velocity from the main cylinder occurs at about 22° BTDC. Thereafter the ejected velocity decreases so long as the crank travels towards the TDC. The flow then reversesits direction to be from the swirl chamber to the main cylinder during the expansion stroke. Another maximum velocity is noticed at about 20° ATDC during expansion stroke.

The computation is started at zero time at which the compression stroke starts. The computations are carried out at 2° crank angle intervals, the resulting velocity field computed at various crank angles is shown in Figs.(26) and (27), by way of vectors representing the magnitude and direction of the local fluid motion.

In time sequence, one can observe the features of the flow evolution. At crank angle 20° ABDC, it can be seen that the flow velocities are low, and it almost pure radial flow directed from air jet to the opposite wall surface. After some time, for example at 100° ABDC, the ejected velocity increases and the built up pressure increases causing complete rotational flow in the bulk of the swirl chamber. Before the initiation of the complete rotational flow, for example at 60°, 100°, 140° and 160° ABDC, a vortex is noticed at the right hand side of the tangential port jet. Before the end of the compression stroke the radial pressure gradients strengthen to the point of inducing strong flow recirculation which is observed at 20° BTDC. During expansion stroke the jet velocity at the tangential port begins to reverse its direction from swirl chamber to the main cylinder. At the beginning of the expansion stroke the recirculating flow is unable to reverse its direction to flow through the tangential port inspite of the absence of a jet flow into the swirl chamber, as shown in Figure (27). Before the complete reverse of the flow a vortex is noticed at the opposite side of the port, and low flow velocities can be noticed during the expansion stroke. The recirculating flow begins to reverse its direction at 60 degree ATDC and at 140 degree ATDC it completly changes its direction to rush out from the tangential port.

The predicted and measured tangential velocity versus crank angle degree during compression and expansion strokes at radial distances of 2.2, 7.0, 12.2, and 17.7mm from the swirl chamber centre are shown in Fig.(28). The solid lines represent the predicted results and the back signs represent the experimental results obtained by hot-wire

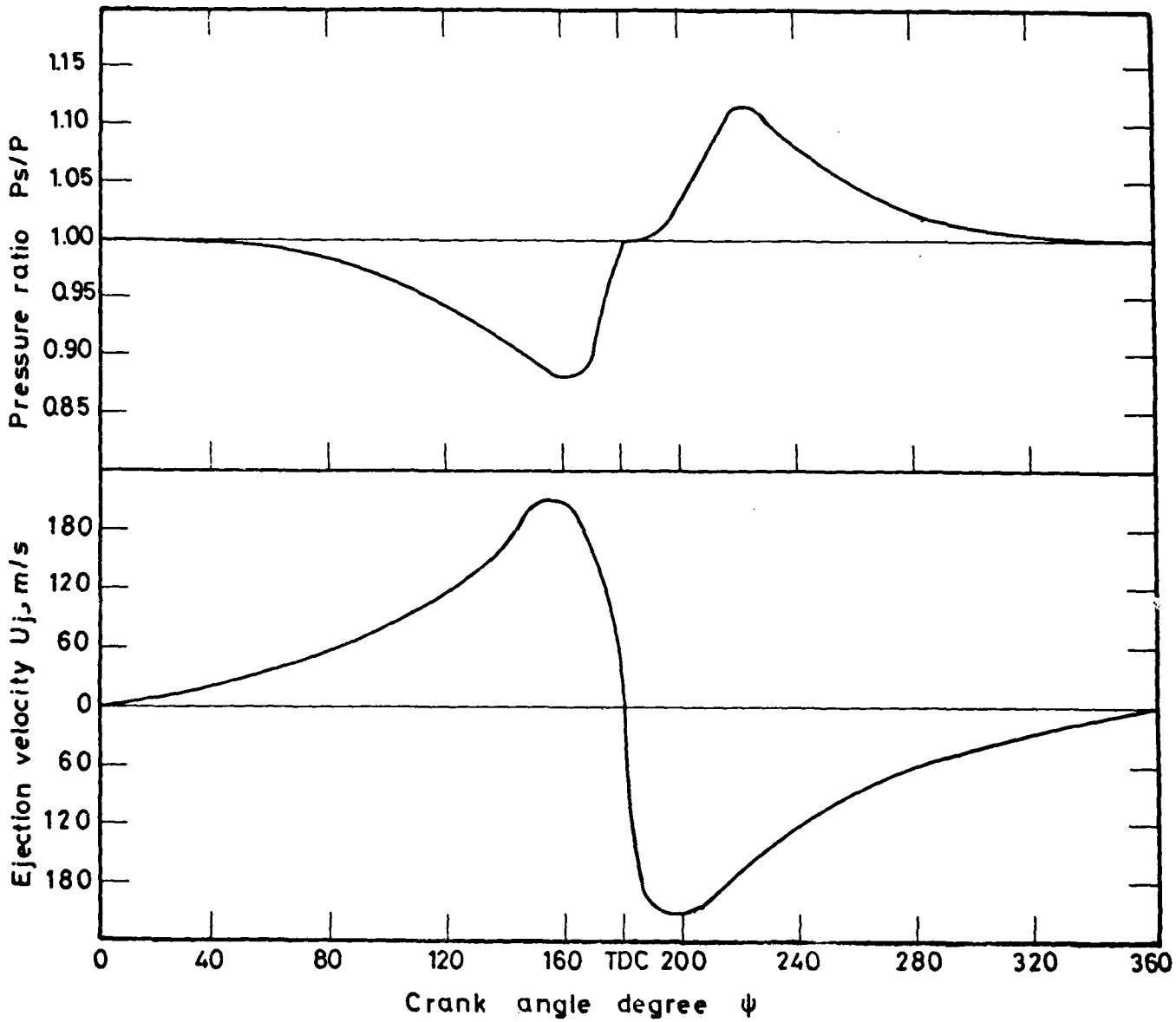

Fig.(25) Predicted ejection velocity and pressure ratio during compression and expansion strokes for $A_j/A = 0.0092$, $Vs/Vc = 0.772$ and $N = 1000$ r.p.m.

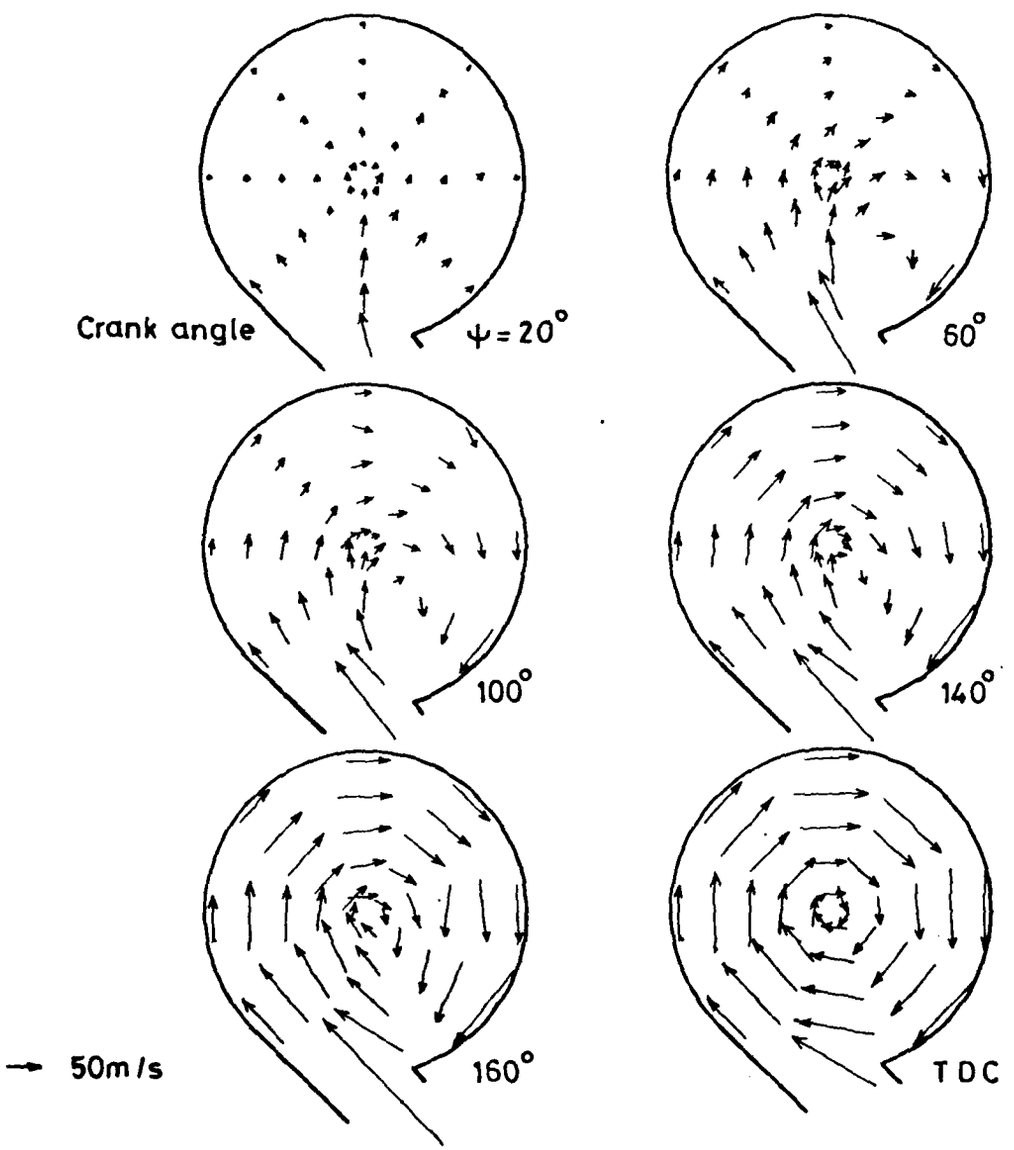

Fig (26) Velocity vector plot during compression stroke for Vs/Vc=0.772, N=1000 r.p.m and Aj/A = 0.0092

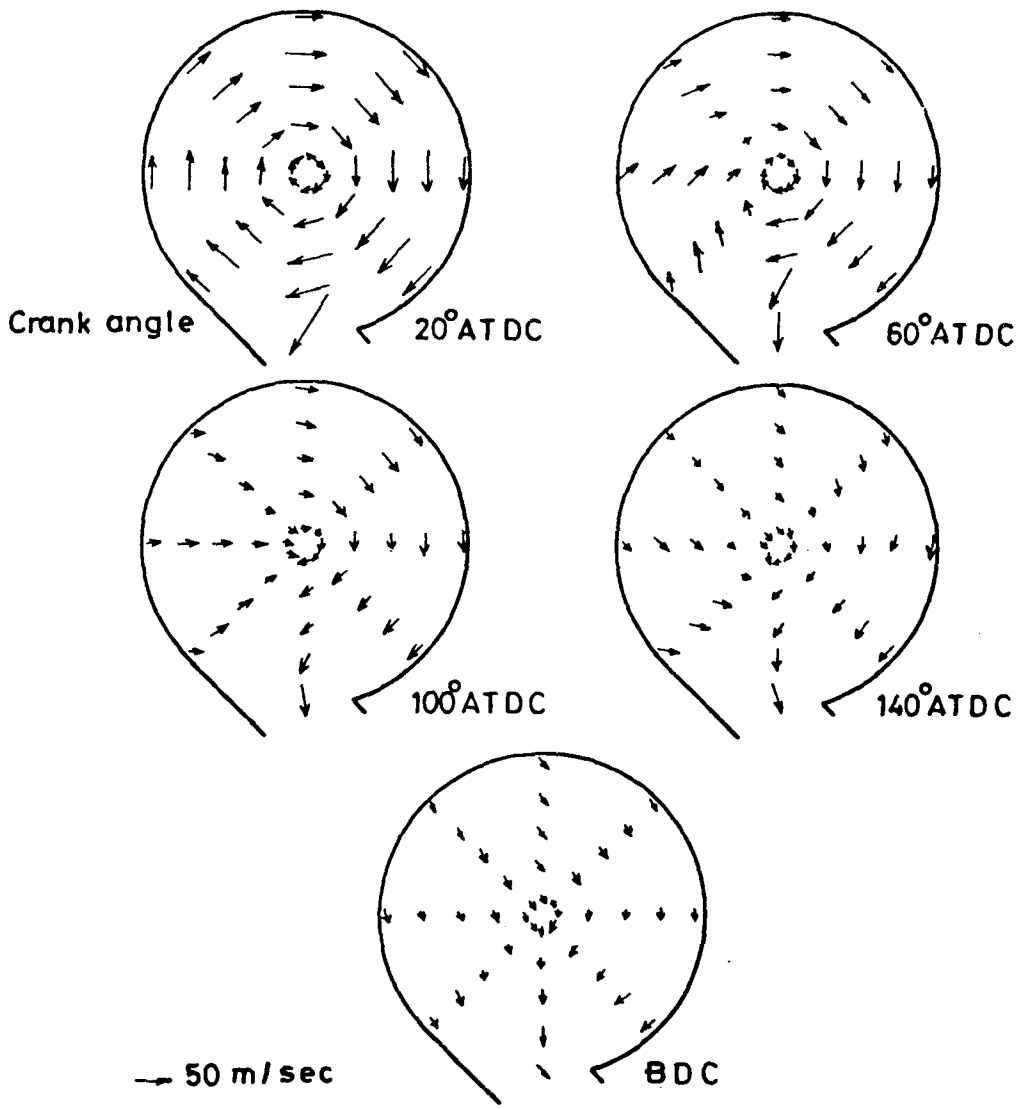

Fig(27) Velocity vector plot during expansion stroke for Vs/Vc=0.772, N=1000r.p.m and Aj/A = 0.0092

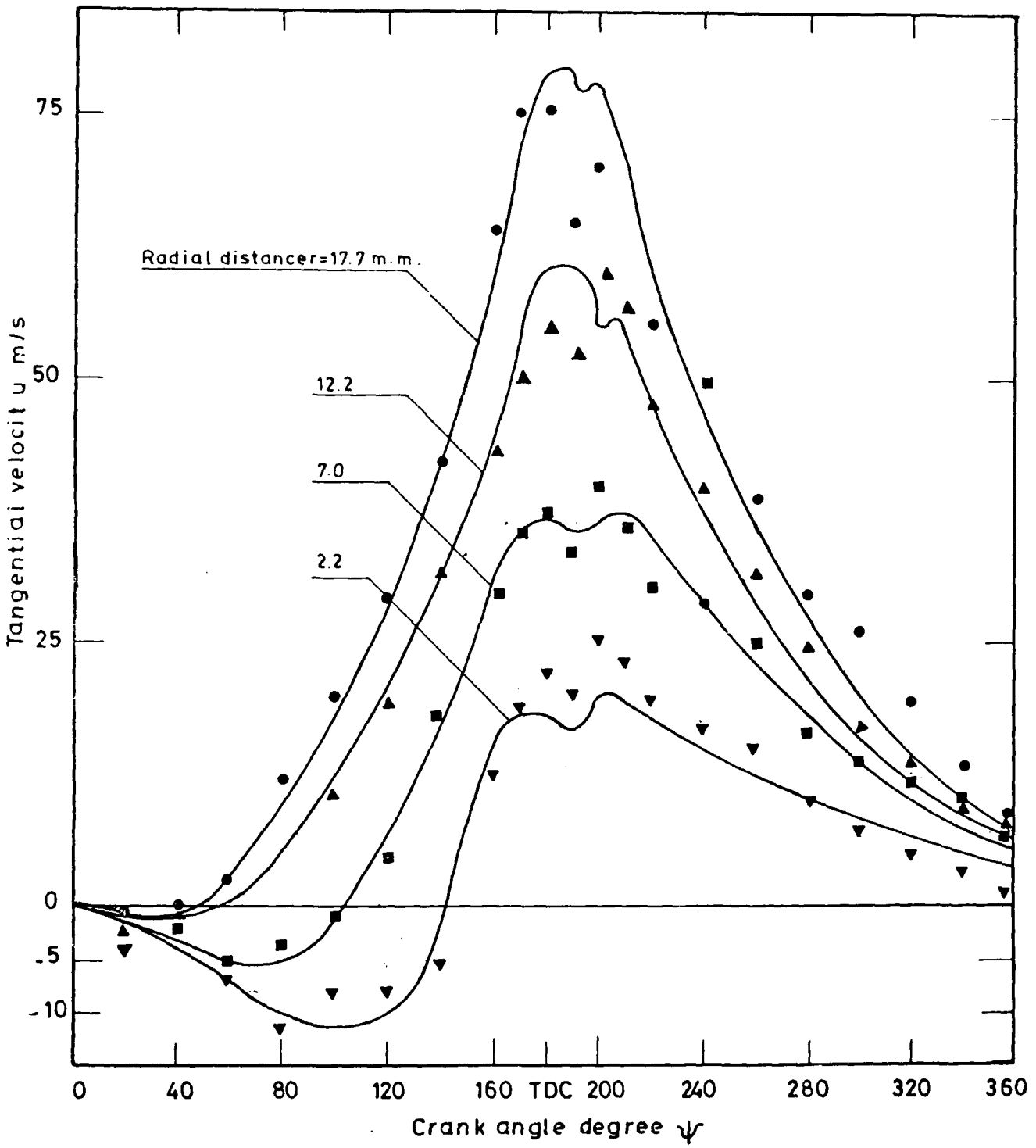

Fig(28)Predicted and measured tangential velocity during compression and expansion strokes in plane 4 at various radii keeping Vs/Vc=0.772, Aj/A = 0.0092 and N = 1000 r.p.m constant.

anemometer.

At the beginning of the compression stroke, it is noticed that the tangential velocity component has a negative sign due to the anticlockwise flow direction which continues for several crank angles. As the crank angle increases during the compression stroke, the tangential velocity increases in the clockwise direction, reaching its maximum value at about 2^{o} BTDC, and then a slight decrease of the tangential velocity occurs at about 10^{o} ATDC. This may be attributed to the continuous decrease of the ejected velocity till zero value at TDC resulting from the decrease of the pressure gradient across the port as shown in Fig. (25). A maximum tangential velocity during expansion stroke can be noticed in Fig.(28) at about 22^{o} ATDC. This differs from the angle at which the maximum ejected velocity occurs during the expansion stroke. The same behaviour is obtained during the compression stroke where the maximum tangential velocity occurs at about 2^{o} BTDC while the maximum ejected air flow velocity from the main cylinder to the swirl chamber occurs at about 22^{o} BTDC. The maximum value of the tangential velocity changes from plane to plane through the swirl chamber.

The predicted and measured tangential velocity versus the radial distance at different crank angle degrees during compression and expansion strokes are shown in Fig. (29). The tangential velocity can be noticed to be rather small along the radial distance at 20^{o} ABDC, and then begins to increase at higher crank angles during compression stroke. For example at 80^{o} BTDC ($\theta = 100^{o}$) the tangential velocity has a negative value (anticlockwise direction) near the swirl chamber centre and a closkwise direction near the swirl chamber wall as the complete circulating flow is not reached at all locations. Before the end of compression stroke the tangential velocity distribution along the radial distance decomposes to a solid vortex motion and a nearly free vortex motion near the swirl chamber wall. The free vortex motion region increases as the crank travels towards the TDC as shown in Fig.(29), and then begins to decrease as the crank travels towards the BDC during the expansion stroke as shown at 80^{o} ATDC and 160^{o} ATDC.

The distribution of the radial velocity versus the crank angle degree during the compression and expansion strokes at different radial distances is shown in Fig. (30). The radial velocity distribution versus radial distance for different crank angles is shown also in Fig. (31). The radial velocity has a low value at the beginning of compression stroke, and increases slightly with the travel of the crank towards the TDC and a maximum value can be noticed at 20^{o} BTDC at a radial distance of 2.2mm. Thereafter, a rapid decrease occurs during the expansion stroke. The radial velocity diminishes also near the swirl chamber wall where the velocity is purely tangential. It is noted from Fig. (31) that a source is created at the centre resulting from the vorticies existing at the swirl chamber centre with high shear stress.

The contours of the dimensionless turbulence intensity distribution, defined by the ratio $\sqrt{2K/3}/C_{pm}$, during compression stroke are shown in Fig.(32) It is clear from the figure that the turbulence levels at the beginning of the compression stroke are very low, and have a maximum value of 0.082 in the centre at 20^{o} ABDC. During the compression stroke the inflow to the swirl chamber becomes much stronger and begins to separate near the tangential port to form two eddies on either sides of the port. For example, at 100^{o} ABDC the turbulence

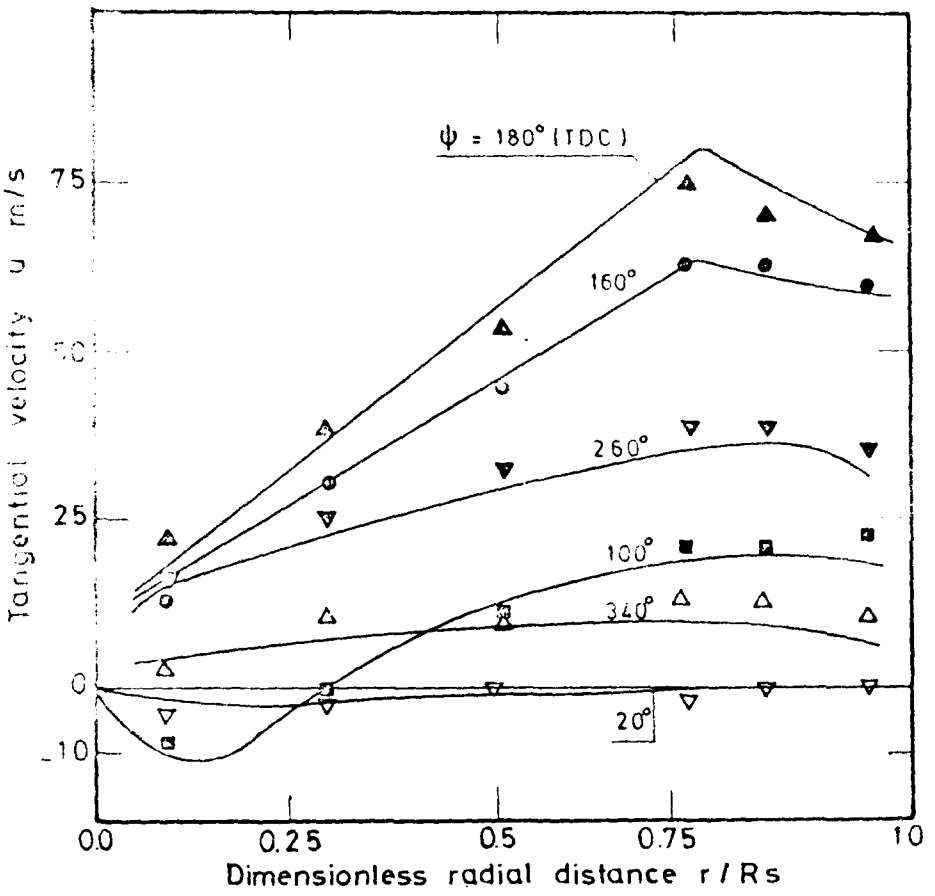

Fig.(29) Predicted and measured tangential velocity in plane 4 at various radii at different crank angles, keeping Vs/Vc=0.772, Aj/A=0.0092 and N=1000 r.p.m. constant.

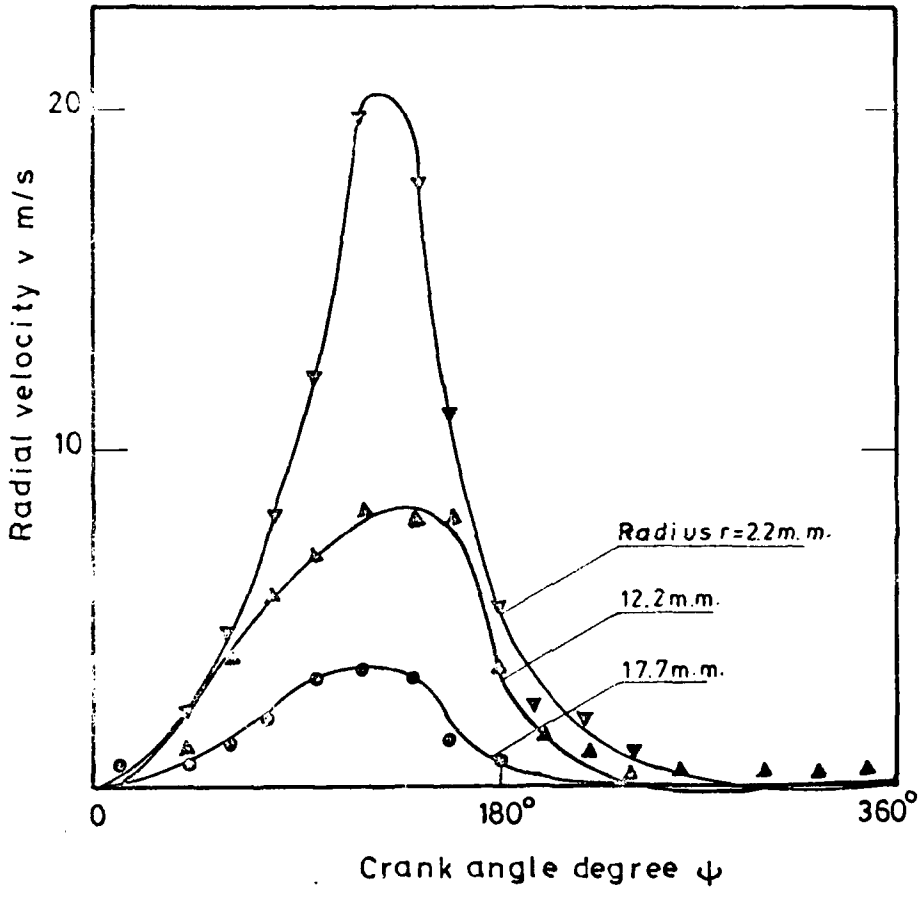

Fig(30)Predicted and measured radial velocity during compression and expansion strokes in plane 4 at various radii, keeping Vs/Vc = 0.772, Aj/A=0.0092 and N=1000 r.p.m. constant.

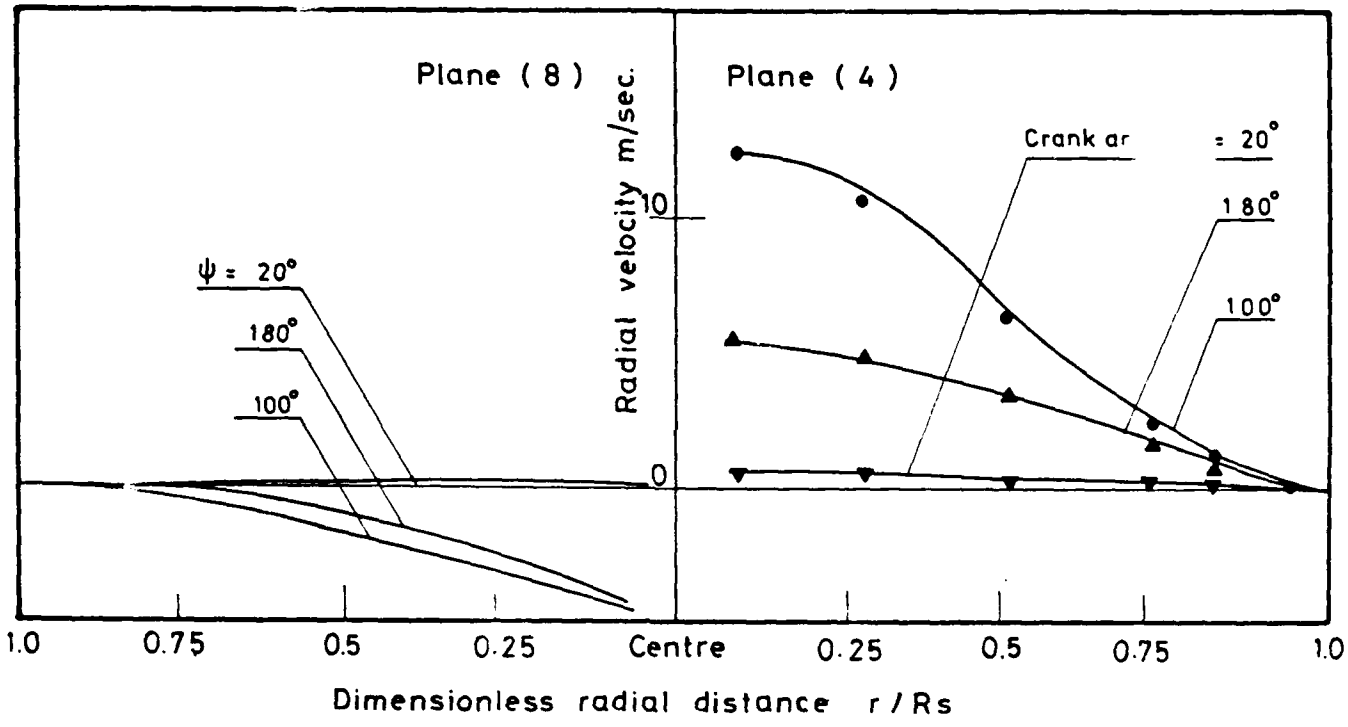

Fig.(31) Predicted and measured radial velocity in plane 4 and 8 at various crank angles, keeping Vs/Vc = 0.772, Aj/A = 0.0092 and N = 1000 r.p.m. constant.

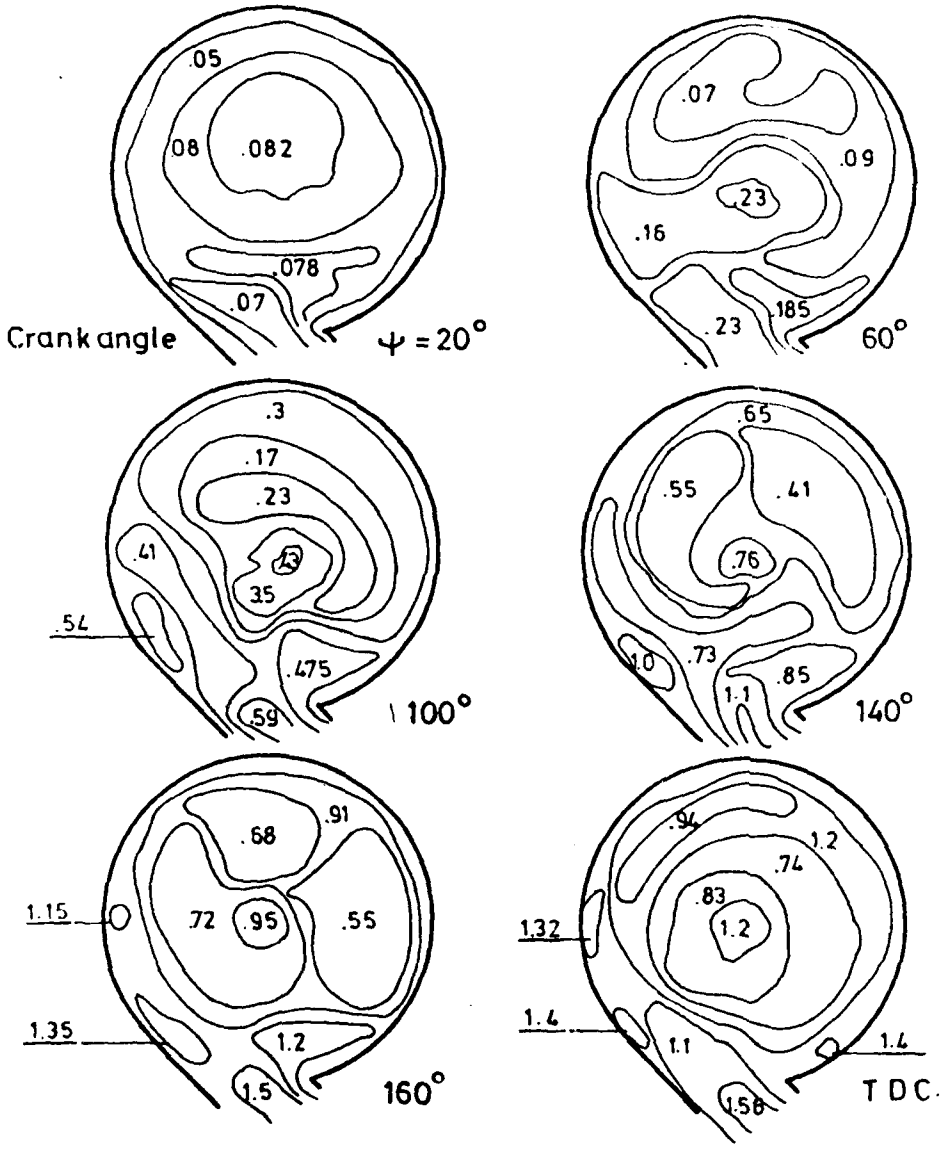

Fig.(32) Turbulence intensity contours during compression stroke keeping Vs/Vc=0.772, Aj/A=0.0092 and N=1000 r.p.m constant.

intensity has a value of 0.475 at the right side of the port and 0.54 at the left side. The magnitude of these turbulence intensities generated during the compression stroke due to the high shear stress and pressure gradient on both sides of the port increases so long as the crank travels towards the TDC. This is due to the combined action of fluid inertia, pressure gradients and wall shear. The normal stresses produced at the swirl chamber centre causes significant turbulence intensity increase until the expansion stroke begins, Fig. (33). At TDC it is noticed that the turbulence generation is particularly strong in the shear layers along the port and has a value of 1.56 adjacent to the entry lip. In addition there are significant turbulence intensities in the swirl chamber which have been built up during the compression stroke. Near the chamber walls the turbulence intensity is low due to the influence of the damping factor. The turbulence generated during compression stroke reaches a maximum value of 1.4 near the port entry at TDC. This value of turbulence intensity begins to decrease during the expansion stroke and has a value of 1.23 at 20^{o} ATDC. The vorticies which have been generated during the compression stroke begin to disappear in the expansion stroke, as shown in Figure (33), although a high turbulence intensity exists at the centre having a maximum value of 1.8 at 60^{o} ATDC. Thereafter it begins to diminishes during the crank travel towards BDC where small vorticies appear, and their values decay due to the decrease of the shear stress.

Figure (34) shows the variation of the turbulence intensity with the crank angle degree during compression and expansion strokes at plane 4. It is clear from the figure that the turbulence intensity is very low at the beginning of the compression stroke, reaching a maximum value at about 20^{o} ATDC where the outflow from the swirl chamber to the main cylinder is maximum. Thereafter the turbulence intensity decreases again during the expansion stroke. High value of turbulence intensity obtained near the chamber centre (r=2.2 mm) with a value of about 1.84.

Variation of turbulence intensity versus radial distance in plane 4 at different crank angles is shown in Fig.(35). It is noticed from the figure that the turbulence intensity has a low values along the radial distance at 20^{o} ABDC and begin to increase at 100^{o} ABDC. A maximum value can be noticed near the chamber wall and centre due to high shear stresses generated in these regions. At TDC ($\psi = 180^{o}$) a maximum turbulence intensity of about 1.35 occurs near chamber wall and centre and a minimum value of about 0.74 occurs at a radial distance of about 12 mm. At 80^{o} ATDC a maximum value of turbulence intensity of 1.55 is noticed near the chamber wall ($r/Rs = 0.74$) and a manimum value of about 1.15 is noticed at a radial distance ratio of about 0.25. It can be concluded that a significant change of the turbulence intensities along the radial distance specially at TDC, at which a highly difference exists between the maximum values occuring at chamber wall and centre. The minimum value occurs at, nearly the midway between chamber wall and centre.

4.3.2. Effect of Port Area Ratio on the Flow Field

The air flow field inside the swirl chamber is affected by the port area ratio as defined by the ratio of the port cross-sectional area (A_p) to the piston area (A). Therefore the investigation of the influence of the port area ratio on the flow field and consequently

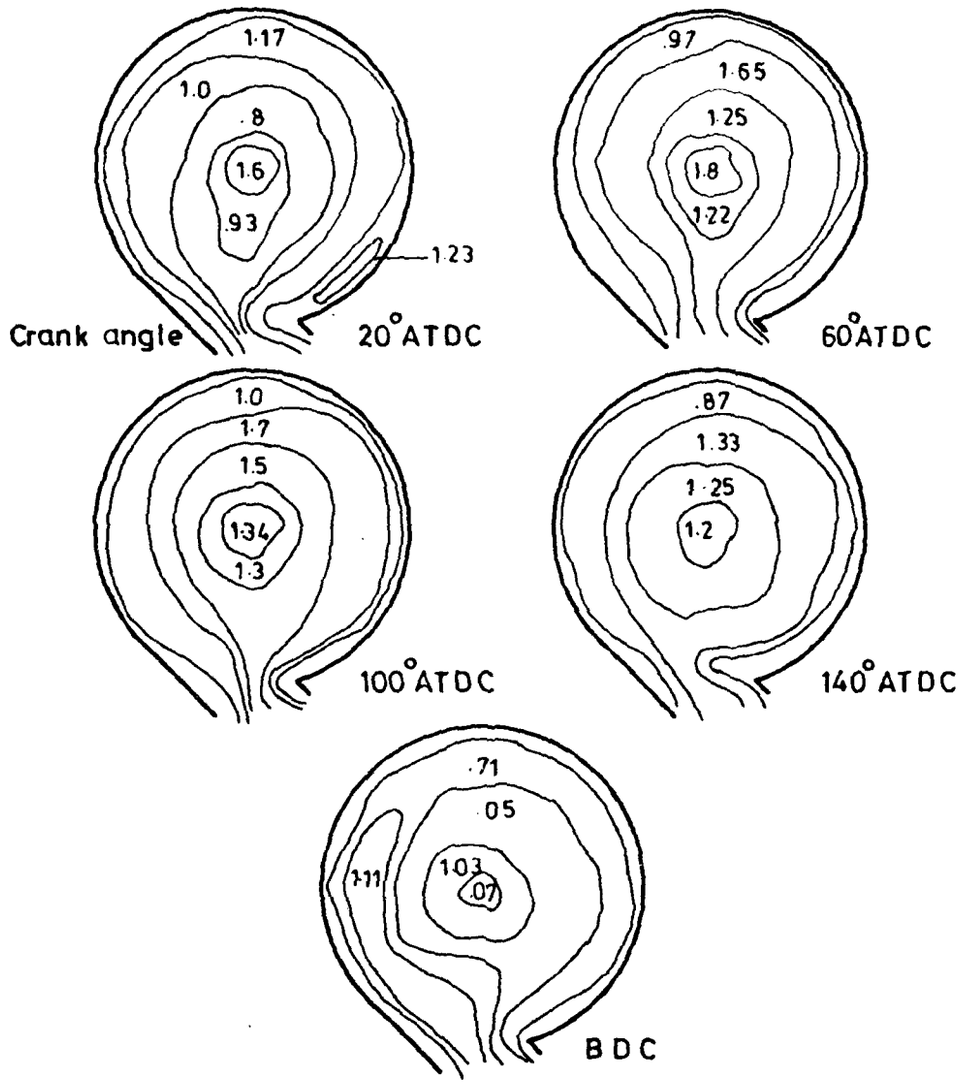

Fig(33)Turbulence intensity contours
during expansion stroke keeping
Vs/Vc=0.772,Aj/A=0.0092 and N=1000r. p.m constant.

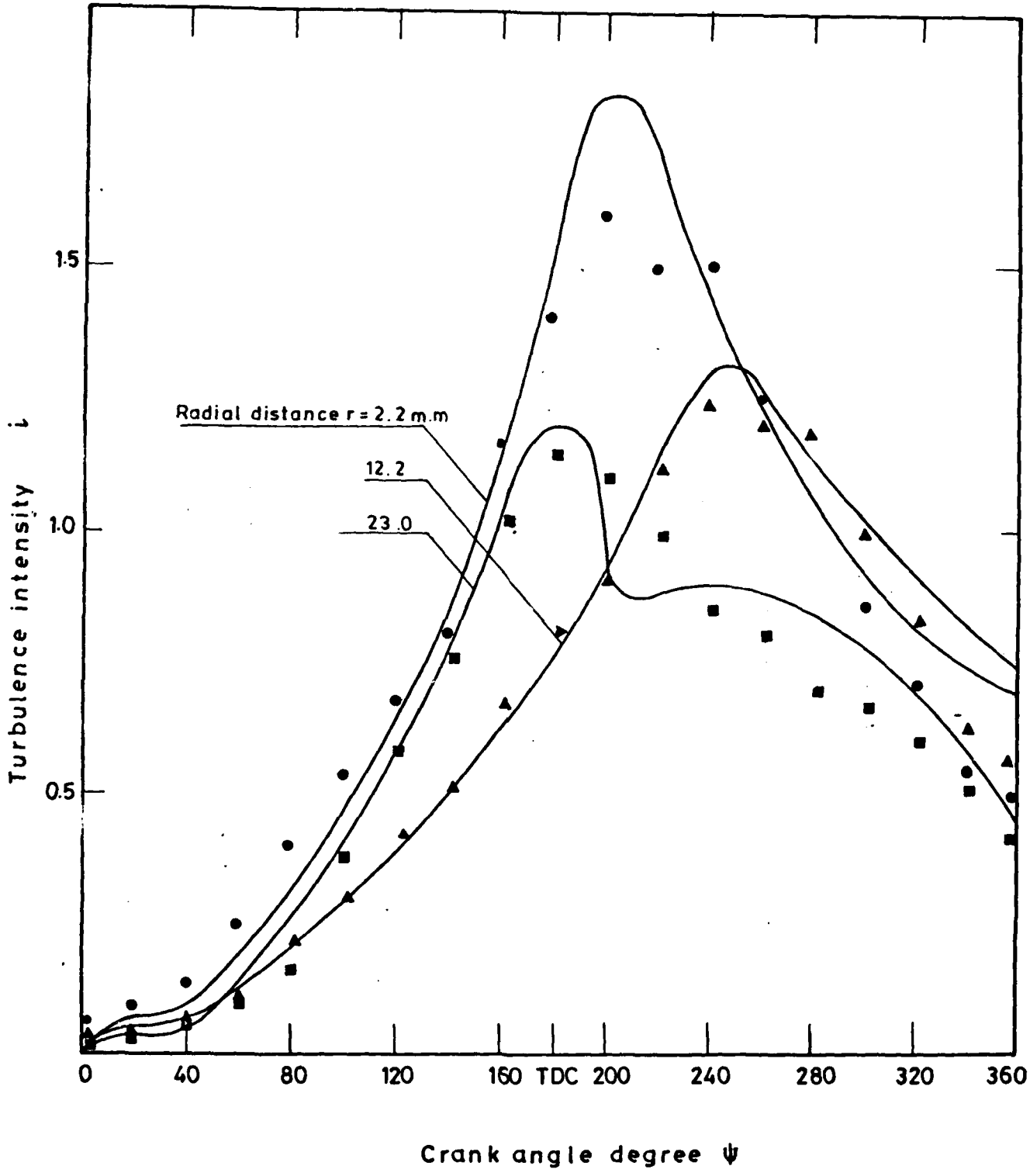

Fig(34)Predicted and measured turbulence intensity during compression and expansion strokes in plane 4 at various radil keeping Vs/Vc=0.772 Aj/A = 0.0092 and N = 1000 r.p.m. constant.

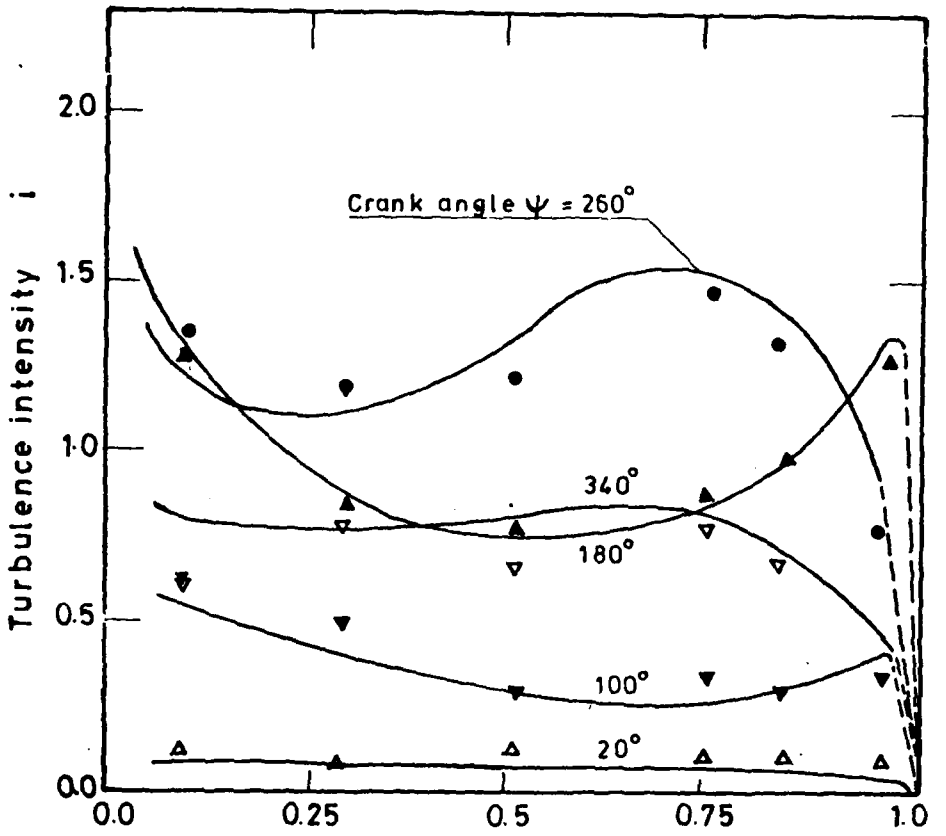

Fig (35)Predicted and measured turbulence intensity in plane 4 at various radii and different crank angles keeping Vs/Vc = 0.772, Aj / A = 0.0092 and N=1000 r.p.m. constant.

on the turbulence model coefficients is required to validate the prediction model.

The calculation shows that the decrease of the relative port area ratio will give a remarkable increase of the ejected air velocity through the port, consequently an increase of the flow velocities inside the swirl chamber is obtained.

The effect of the relative port area ratio (A_j/A) on the flow field velocities inside the swirl chamber is shown in Fig.(36). A remarkable decrease of the flow velocities can be noticed with the increase of the port area ratio. In addition the two eddies which had been formed during the compression stroke on both sides of the port decrease with the increase of the relative port area ratio. A strong flow recirculation at low relative port area ratio is shown in the figure. This may be attributed to the existance of significant radial pressure gradients when using low port area ratio. The strong recirculating flow generates a large tangential velocity as shown in Figs. (37) and (38). In both figures it is clear that the port area has no effect on the crank angle or the radius at which the maximum tangential velocity occurs.

Figure (37) shows the experimental and predicted results of the effect of the port area ratio (A_j/A) on the tangential velocity during compression and expansion strokes at engine speed of 1000 r.p.m. It is clear that with the decrease of the port area ratio a remarkable increase in the tangential velocity component is noticed, reaching a value of about 102 m/s with port area ratio of 0.0041 at 2^o ATDC. It then decreases again during expansion stroke. Another maximum velocity is obtained during expansion stroke which can be noticed at about 26^o ATDC and has a maximum value of about 97 m/s at port area area ratio of 0.0041. The slight decrease of the tangential velocity at this instances is obtained due to the reverse of the flow direction.

Figure (38) shows the effect of the port area ratio on the distribution of the tangential velocity component along the radial distance of plane 4. It is noticed that both the solid and free vortices which are built up at the end of compression stroke (TDC), have larger values at lower port area ratio. A strong free vortex near the chamber wall is noticed at port area ratio of 0.0041.

The effect of the relative port area ratio on the radial velocity distribution during compression and expansion strokes is shown in Fig. (39), which indicates lower values of the radial velocity as compared to the values of the tangential one.

Figure (40)shows the predicted turbulence intensity contours at different port area ratio of 0.0041, 0.0064, 0.0092, 0.0125 and 0.0164, at 20^o BTDC and at engine speed of 1000 r.p.m. The increase of the ejected air velocity from the main cylinder with the decrease of the port area ratio has a great effect on the creation of a strong turbulence intensity field in the swirl chamber which is clearly evident in Fig.(40). Regions of intensive turbulence are noticed near the lip of the connected port due to the high flow shear stresses produced with the inlet ejected flow. The turbulence level has a maximum value of about 2.4 near the port at port area ratio of 0.0041. An increase of the turbulence intensity, which is formed in the central zone of the swirl chamber, takes place when the port area ratio decreases.

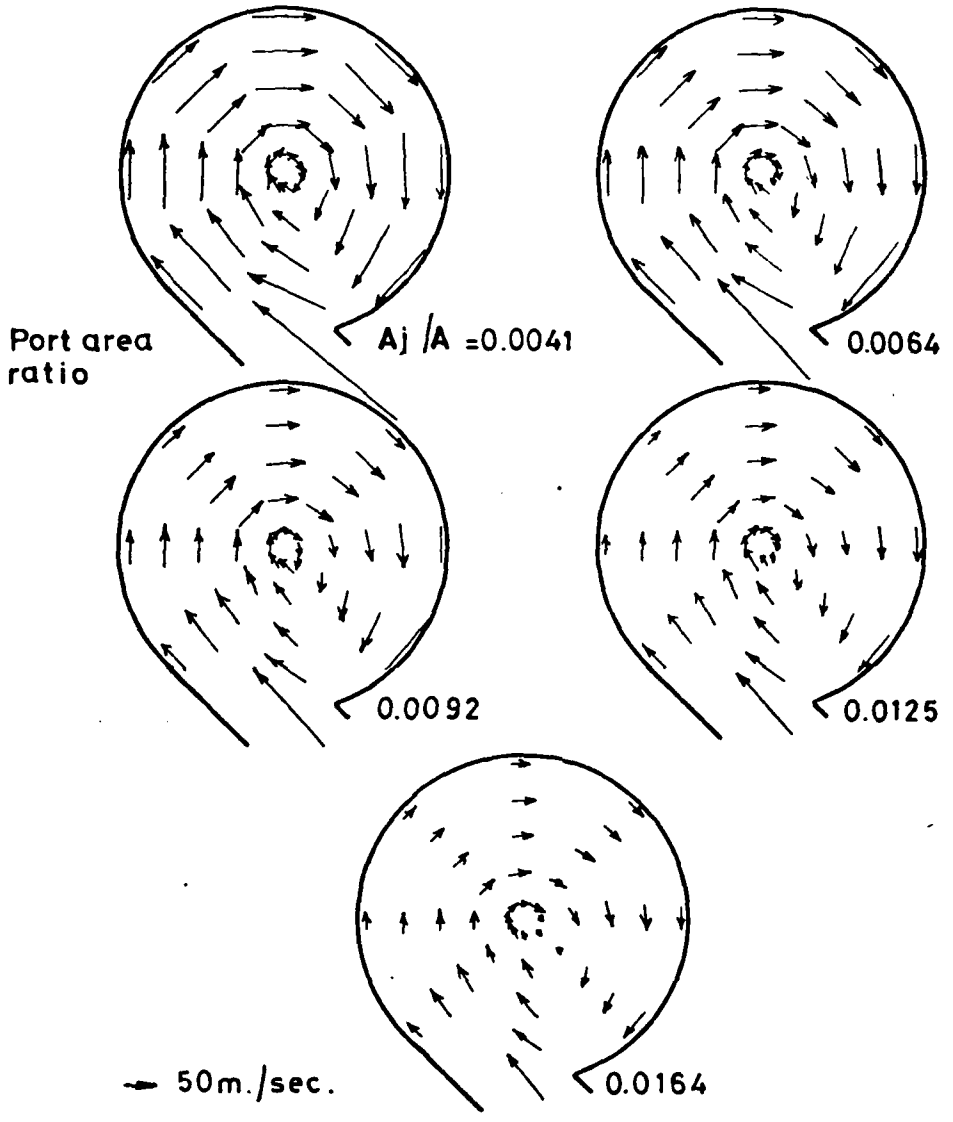

Fig.([36])Velocity vector plot for different port area ratios at 20° BTDC keeping Vs/Vc=0.772 and N=1000 r.p.m constant.

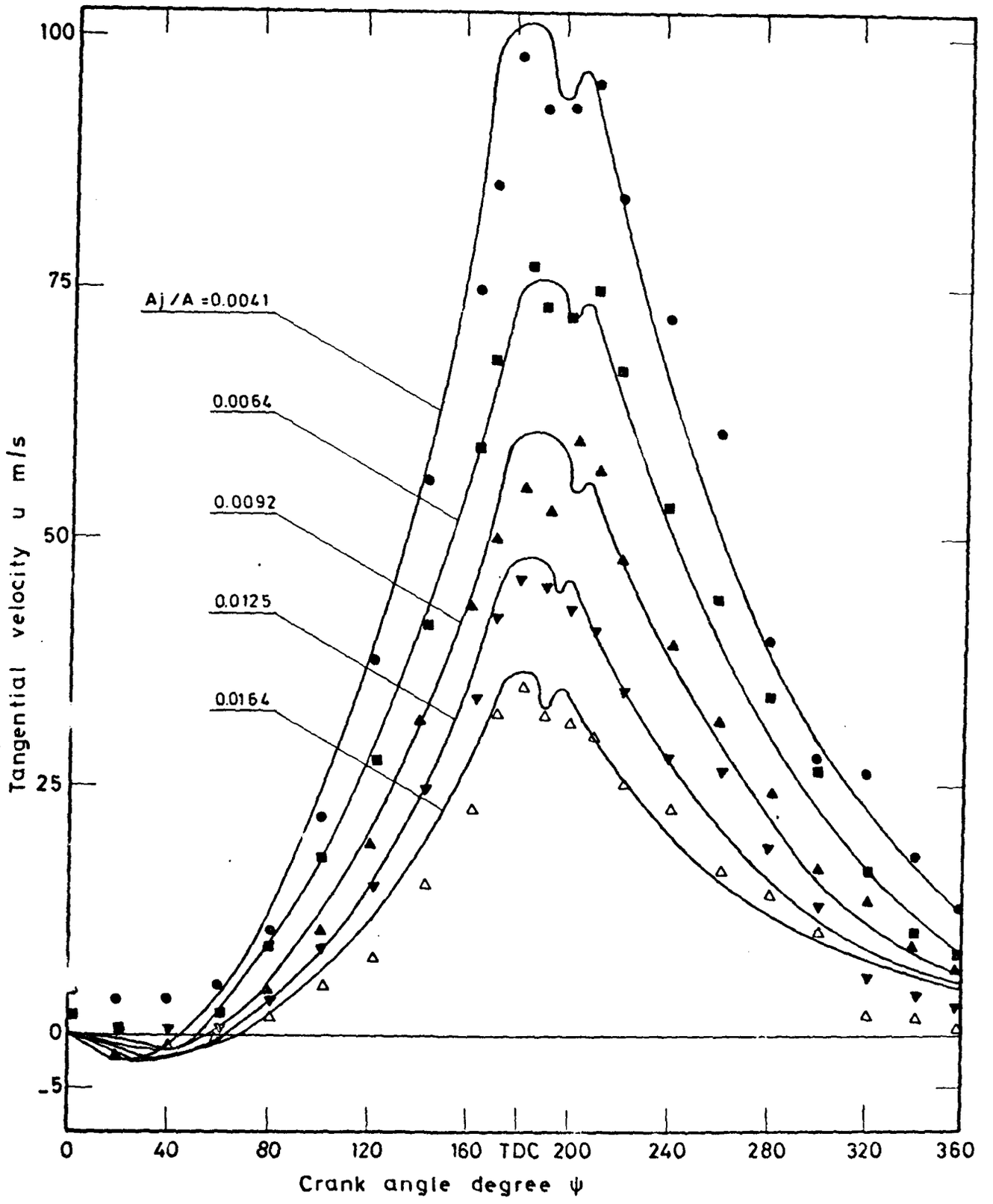

Fig.(37)Predicted and measured tangential velocity during compressior and expansion strokes in plane 4 for different port area ratioskeeping Vs/Vc=0.772 and N=1000r.p.m. constant.

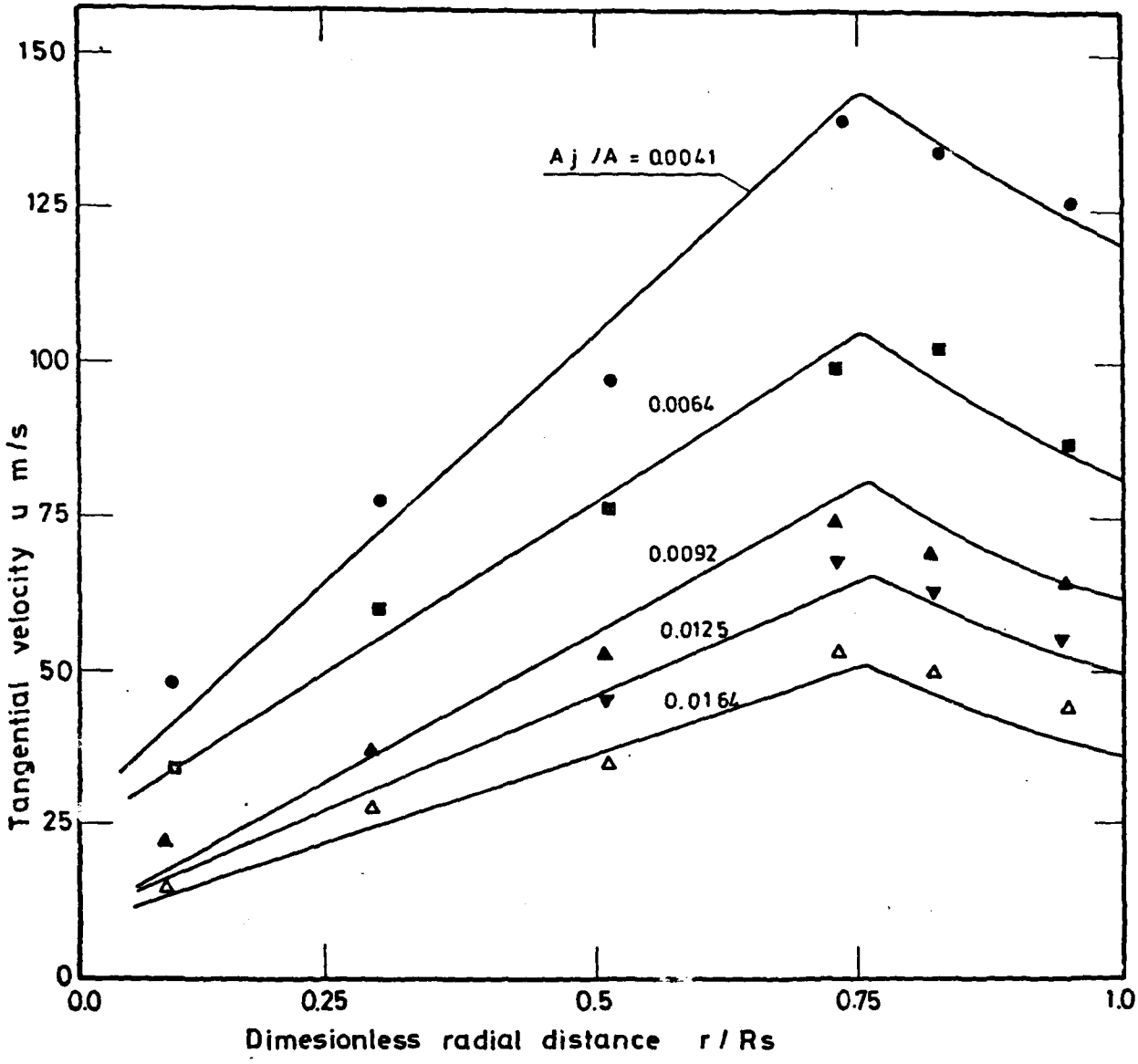

Fig.(38)Predicted and measured tangential velocity in plane 4 at TDC and various radii for different port area ratios keeping Vs/Vc =0.772 and N= 1000 r.p.m. constant.

AD-A116 818 CAIRO CENTER FOR COMBUSTION (EGYPT) F/G 21/5
SPRAY MODELLING FOR MULTIFUEL ENGINES.(U)
JUL 82 M M ELKOT8 DA-ERO-79-G-0017
UNCLASSIFIED NL

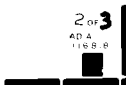

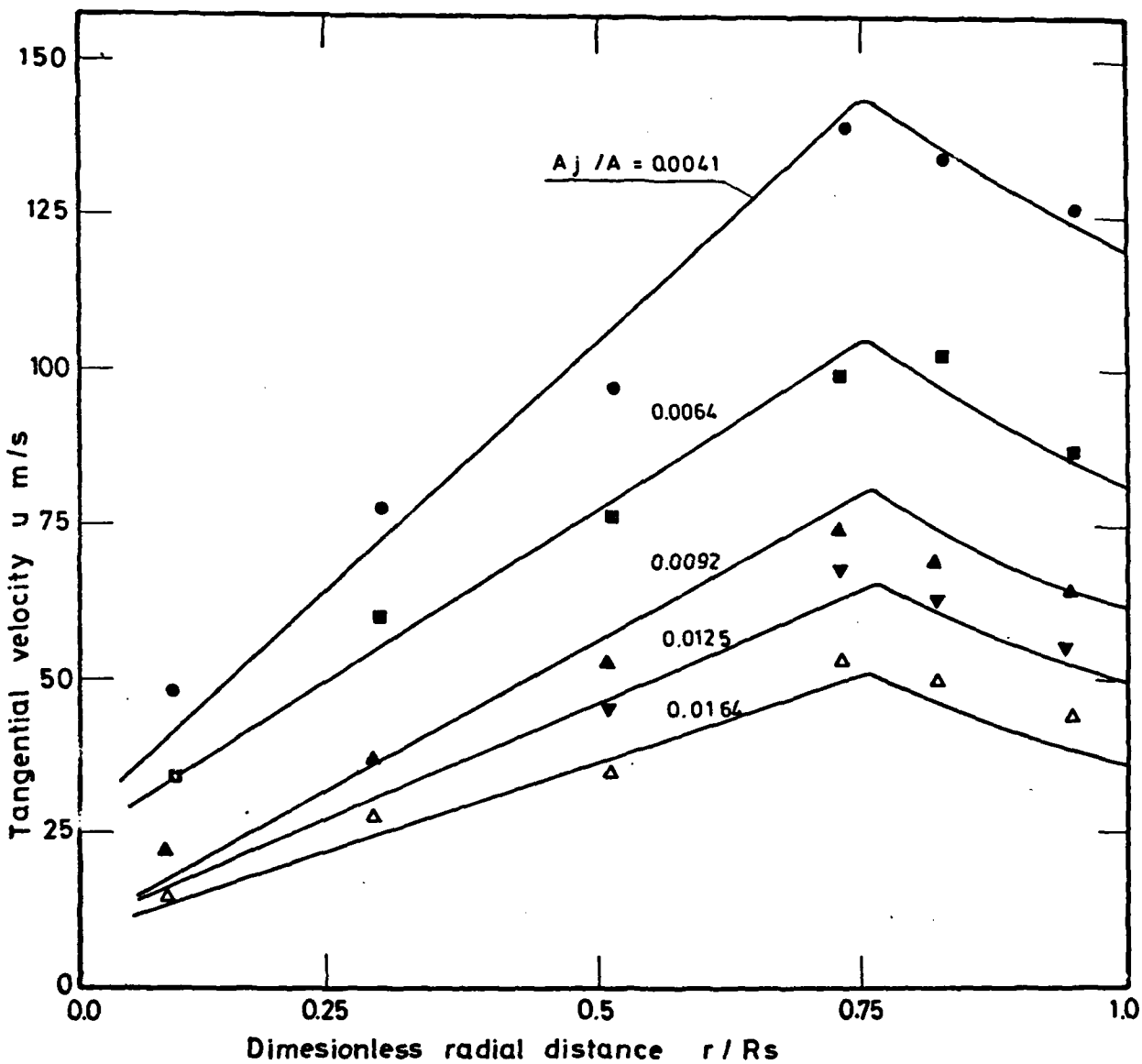

Fig.(38)Predicted and measured tangential velocity in plane 4 at TDC and various radii for different port area ratios keeping Vs/Vc =0.772 and N= 1000 r.p.m. constant.

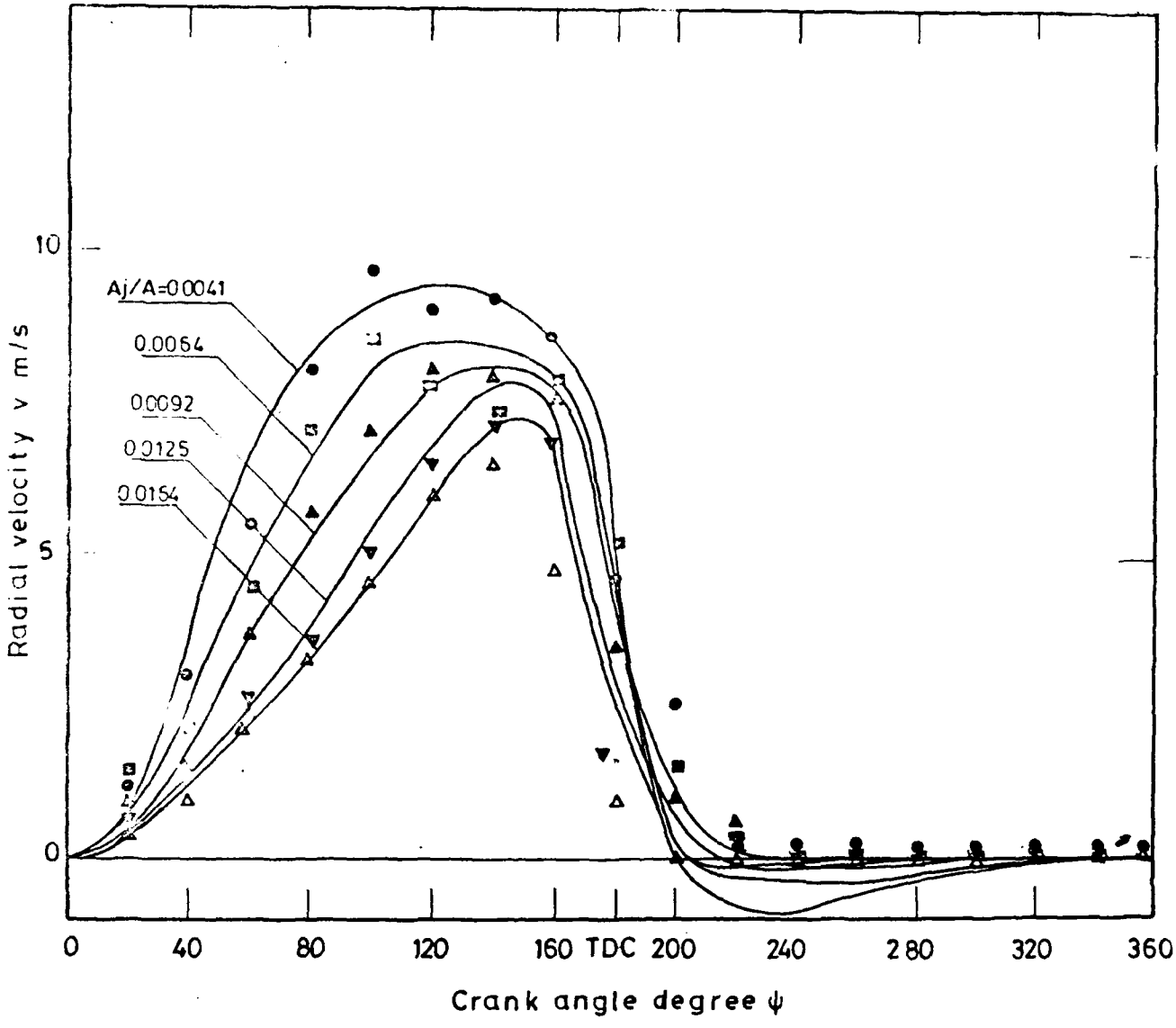

Fig (39) Predicted and measured radial velocity in plane 4 at r/ Rs=0.503 and various crank angle for different port area ratios, keeping Vs/Vc= 0.772 and N = 1000 r. p. m. constant.

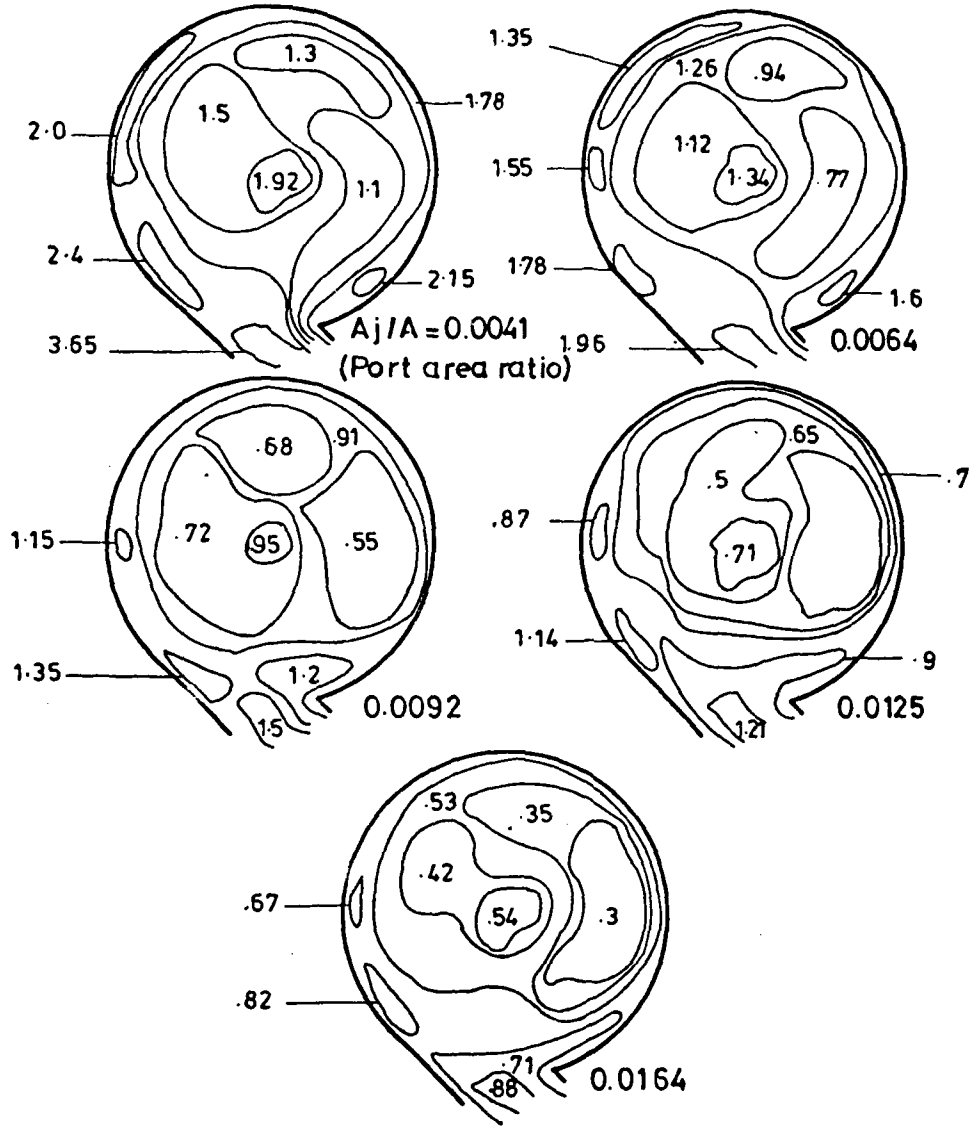

Fig (40) Turbulence intensity contours for different part area ratios at 20° BTDC keeping Vs/Vc = 0.772 and N = 1000 r.p.m constant

However the turbulence intensities elsewhere in the swirl chamber have larger values at low port area ratio. It has a value of 0.7 near the swirl chamber wall at port area ratio of 0.0125 and increases to a value of 1.78 at port area ratio of 0.0041.

The effect of the port area ratio on the turbulence intensity distribution during compression and expansion strokes is shown in Fig. (41). It is clear from the Figure that the turbulence intensity has a maximum value reaches about 3.0 with port area ratio of 0.0041 at about 60° ATDC. The increase of the turbulence intensity during compression and expansion strokes with the decrease of port area ratio may be attributed to the produced air flow jet from or to the swirl chamber. The experimental results in Fig. (41) show that the crank angle at which the maximum turblence intensity occurs (ψ = 60° ATDC) is independent of the port area ratio. The predicted results show a slight deviation from the experimental ones at high port area ratio.

Figure (42) shows the effect of the port area ratio on the turbulence intensity distribution along the radial distance. It is clear from the figure that for all ratios of port area the maximum turbulence intensity exists near the chamber centre due to the double effect of both shear stresses and flow inertia generated during compression stroke which forms a strong recirculation zone. Another maximum turbulence intensity appears near the chamber wall for all port area ratios due to high shear stresses resulting from the expansion of the air jet. The minimum value of the turbulence intensity is 0.35 occuring at a port area ratio of 0.0164 and a radial distance of about 12.6 mm.

4.3.3. Effect of Swirl Volume Ratio on the Flow Field

The effect of swirl chamber volume ratio as defined by the ratio of swirl chamber volume (V_s) to the total clearance volume (V_c) is studied for five swirl chamber volume ratios of 0.772, 0.54, 0.545, 0.457 and 0.376, and at engine speed of 1000 r.p.m., constant compression ratio of 17.0, and port area ratio of 0.0092, to investigate its effect on both flow velocities and turbulence intensity. The study indicates that by increasing the swirl volume ratio (V_s/V_c) the ejected flow velocity and consequently the flow field velocities and turbulence intensity increase.

Figure (43) shows the predicted results of the effect of the swirl volume ratio (V_s/V_c) on the flow field velicities. It is clear that the velocities decrease with the decrease of the swirl volume ratio, and consequently a corresponding decrease of the two eddies formed on both sides of the connected port is obtained. It is clear also that the swirl volume ratio has a higher effect on the flow field velocities than the port area ratio. This effect can be noticed by comparing the results illustrated in Figs. (44) and (37). This comparison shows that a maximum tangential velocity of 102 m/s is reached when using a port area ratio of 0.0041, while a maximum tangential velocity of 60 m/s is reached when using a swirl volume ratio of 0.772. The same results is obtained when comparing the results illustrated in Figs. (45) and (38) for the tangential velocity distribution along the radial distance .

The experimental and predicted results indicate also that the radial distance ratio at which the maximum tangential velocity occurs (about r/Rs= 0.75) is independent of the relative swirl chamber volume ratio.

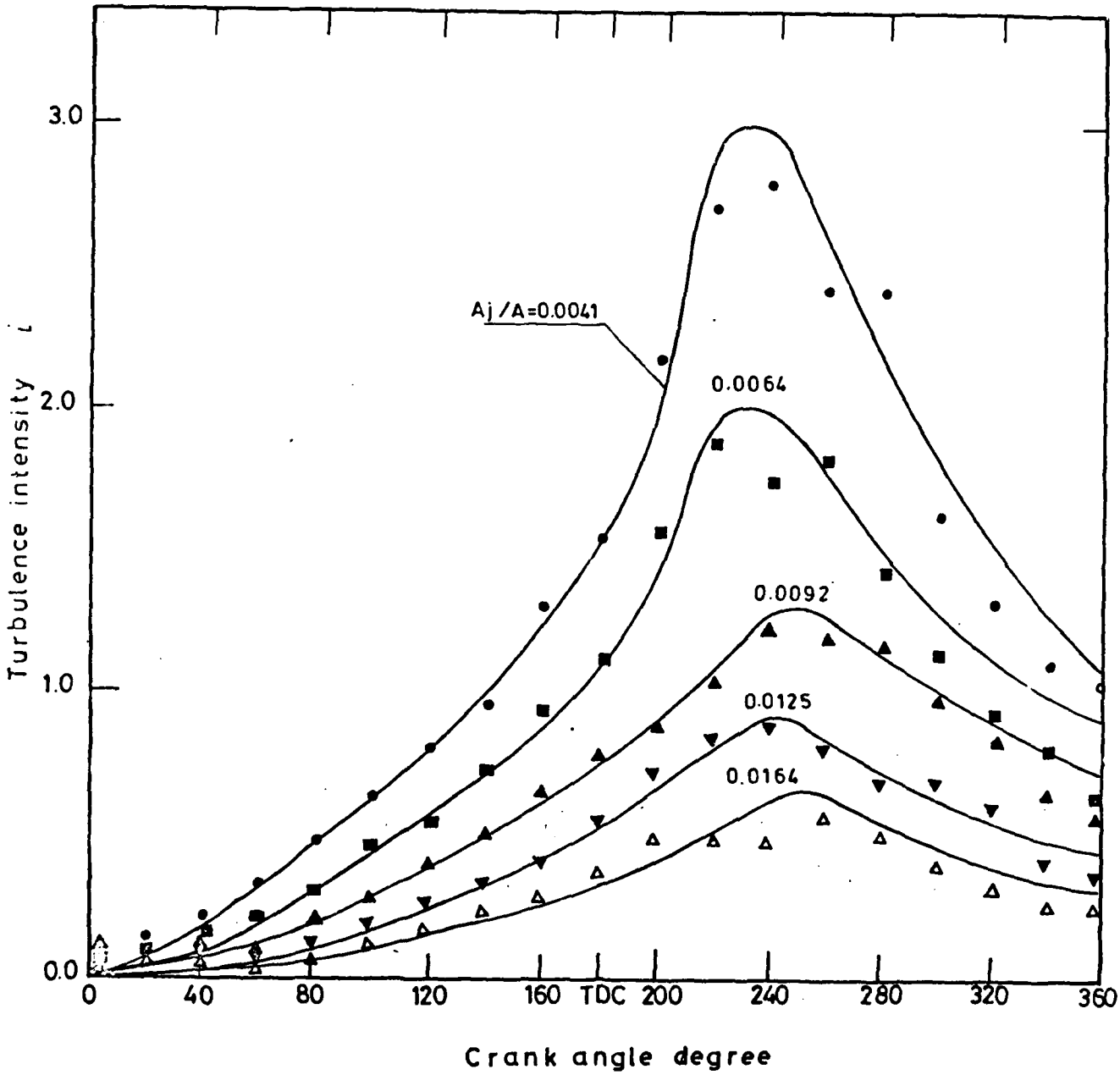

Fig (41) Predicted and measured turbulence intensity in plane 4 at r/Rs = 0.503 during compression and expansion strokes for different port area ratio keeping Vs/Vc = 0.772 and N = 1000 r.p.m. constant.

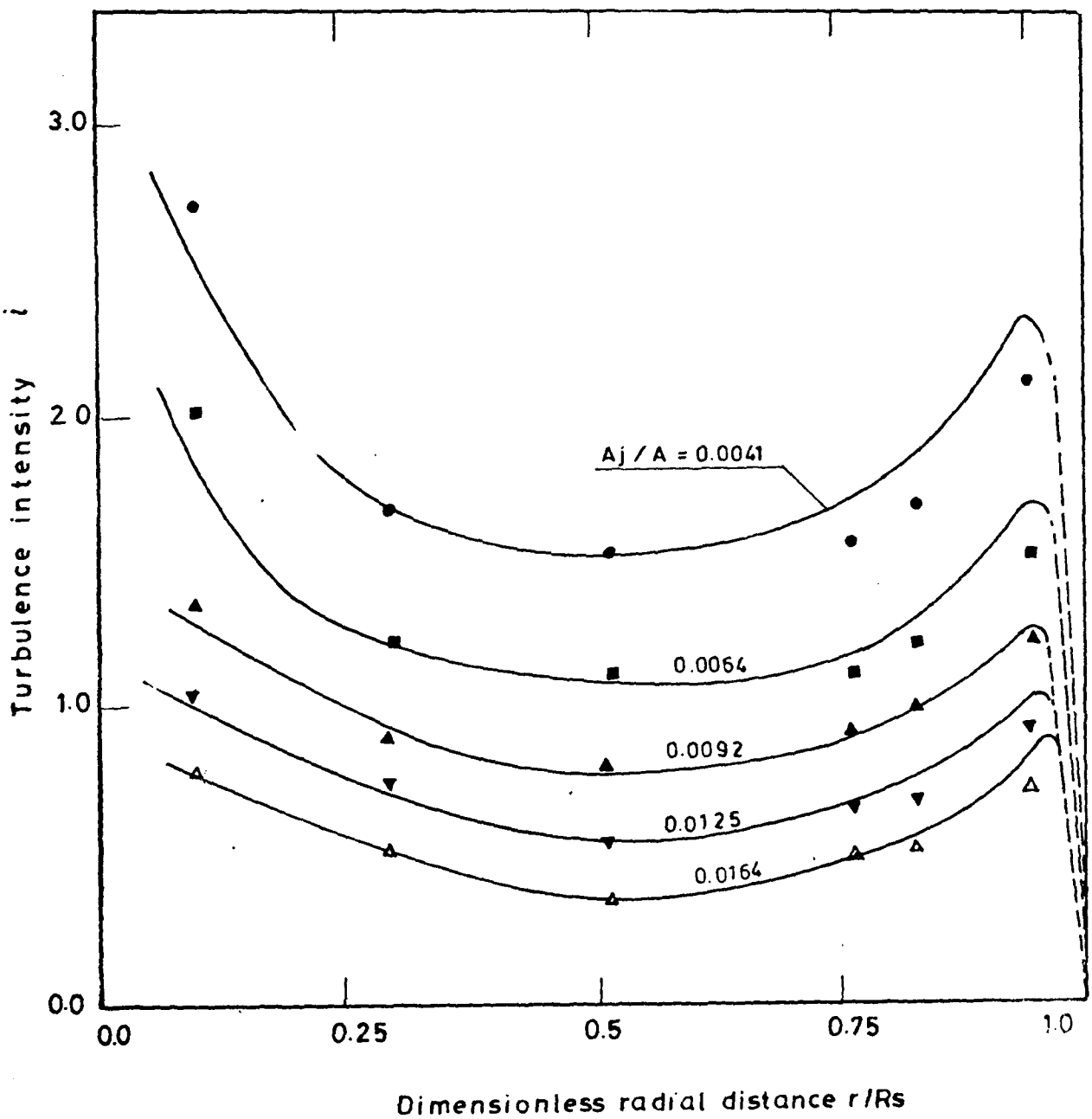

Fig(42)Predicted and measured turbulence intesity in plane4 at TDC and vaious radii for different port area ratios keeping Vs/Vc=0.772 and N= 1000 r.p.m constant.

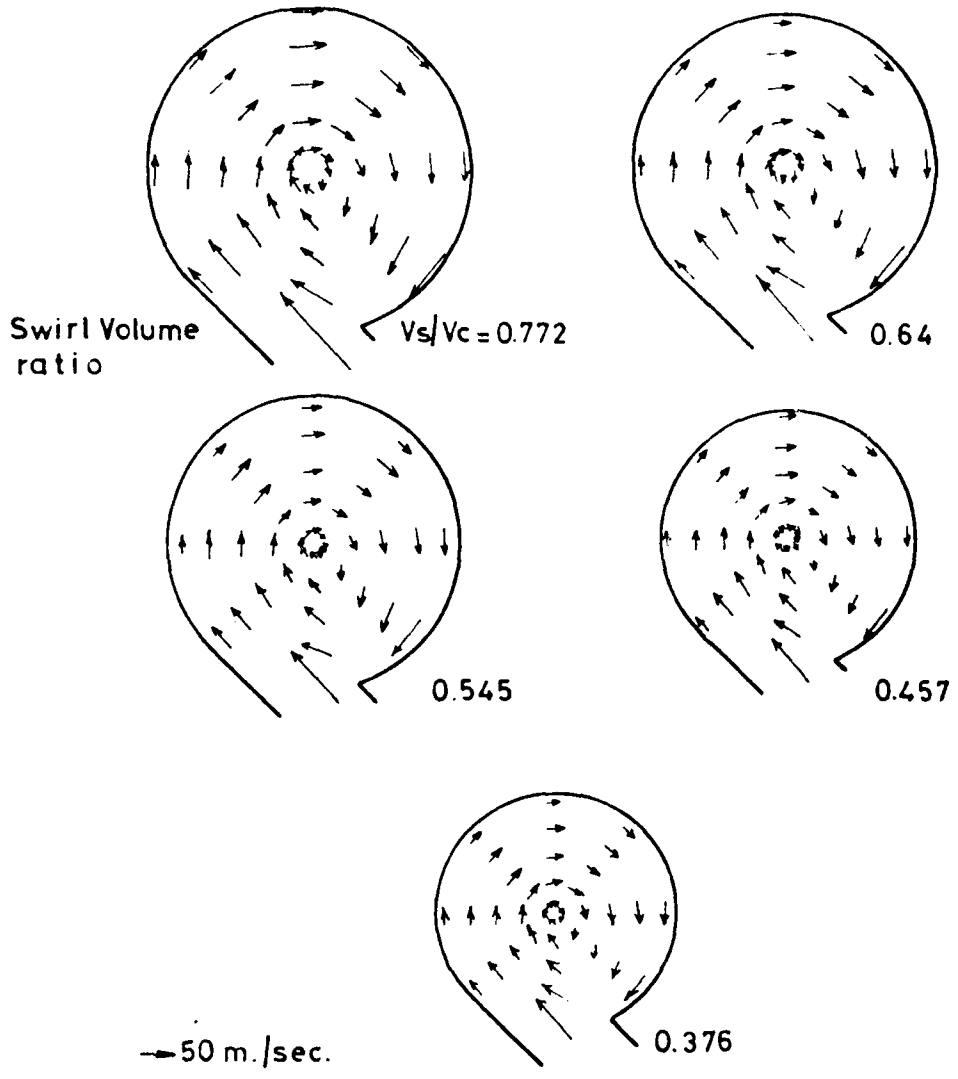

Fig.(43)Velocity vector plot for different swirl volume ratiosat 20°BTDC keeping Aj/A=0.0092and N=1000r.p.m constant.

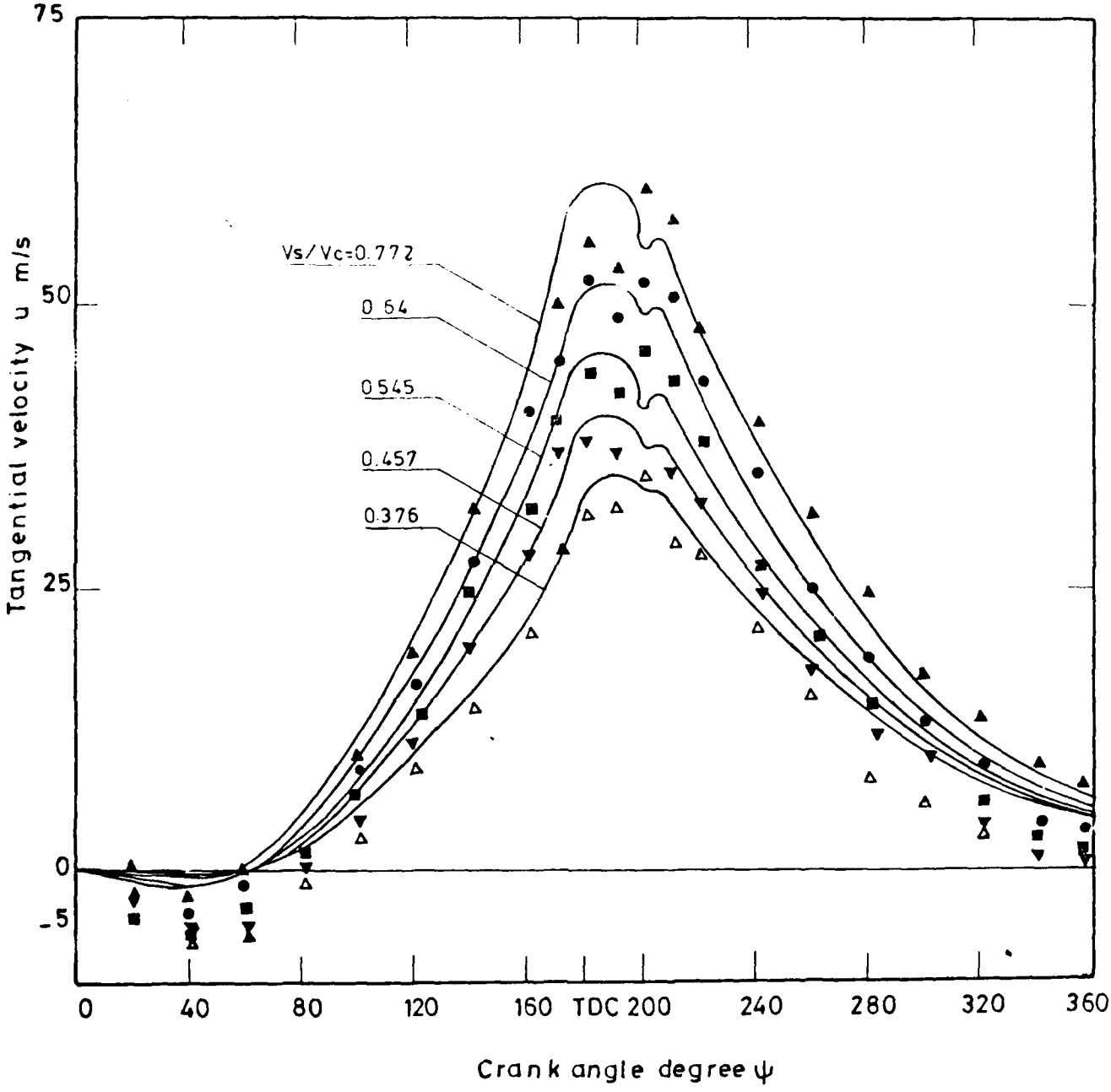

Fig.(44)Predicted and measured tangential velocity during compression and expansion strokes in plane 4 at r/Rs = 0.503 for different swirl volume ratios keeping Aj/A = 0.0092 and N = 1000 r.p.m. constant.

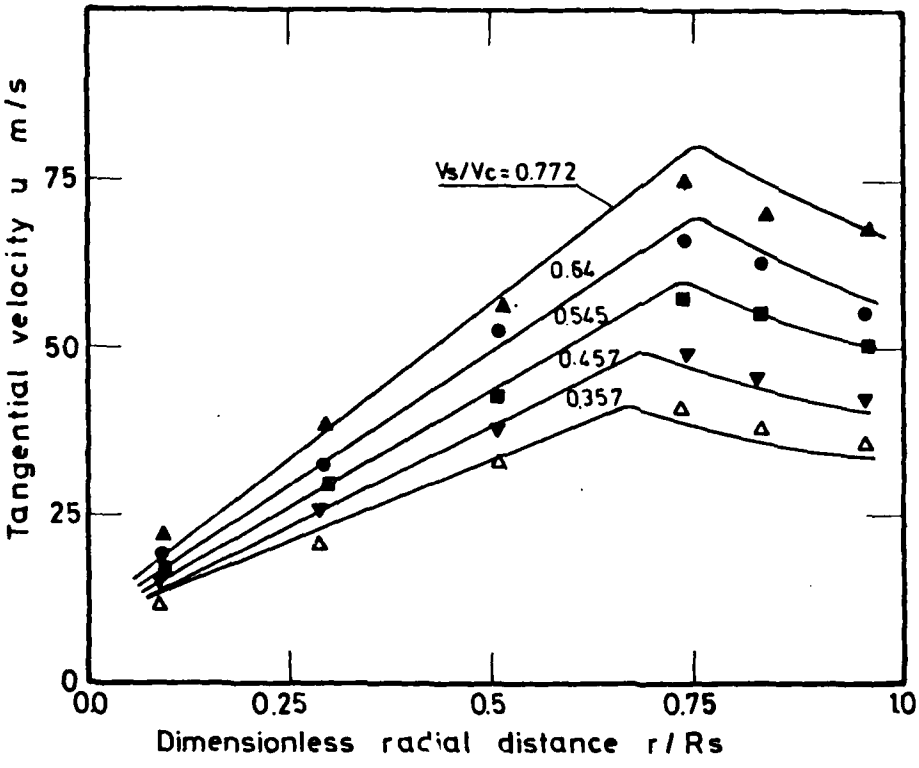

Fig. (45) Predicted and measured tangential velocity in plane 4 and TDC for various radii and different swirl volume ratioskeeping Aj/A= 0.0092 and N= 1000 r.p.m. constant.

The effect of the swirl chamber volume ratio (V_s/V_c) on the radial velocity distribution during compression and expansion strokes is shown in Fig.(46), from which it can be seen that the effect of swirl chamber volume ratio on the radial velocity component is smaller than that of the port area ratio.

Figure (47) shows the predicted turbulence intensity for various relative swirl chamber volume ratios. It is clear from the figure that the turbulence intensity increases in all swirl chamber space with the increase of the swirl chamber volume ratio, taking into consideration that the compression ratio has a constant value of 17.0 for all relative swirl chamber volume ratios. A slight increase of the turbulence intensity value near the swirl chamber wall is noticed with the increase of the swirl chamber volume. Values of about 0.7 and 0.91 are obtained at 0.545 and 0.772 swirl volume ratio respectively.

The two eddies generated at both sides of the port begin to decrease and spread around the inlet port and the right-hand side eddy has a value of about 0.75 at a swirl chamber volume ratio of 0.457. It is clear from Fig.(47) also that the maximum turbulence value is obtained near the centre of the chamber with high shear stress, Figure (48) illustrates the effect of the swirl chamber volume ratio on the turbulence intensity distribution along the radial distance of plane 4 at BTDC. It is clear from this figure that the maximum turbulence intensity of 1.35 occurs near the centre when using a swirl chamber volume ratio of 0.772. A minimum turbulence intensity of 0.485 occurs at about 0.65 radial distance ratio when using 0.357 swirl volume ratio.

Figure (49) shows the effect of the swirl chamber volume ratio on the turbulence intensity distribution during compression and expansion strokes in plane 4 at 12.2 mm radial distance and 1000 r.p.m. engine speed. It is clear from this figure that the turbulence intensity generated during the compression stroke increases with the increase of the swirl chamber volume ratio, and takes on a maximum value at about 60° ATDC.

4.3.4. Effect of Engine Speed on the Flow Field

The effect of engine speed on the flow field in the swirl chamber has been studied by varying the engine speed from 800 to 1500 r.p.m while keeping all other factors constant. Figure (50) shows the effect of engine speed on the flow field inside the swirl chamber. It is clear from the figure that the velocities at each point increases with the increase of the engine speed, and the eddies generated in both sides of the port are strongly increased with the increase of the engine speed.

The effect of the engine speed on the tangential velocity distribution at various crank angles during compression and expansion strokes, and at various radial distances is shown in Figs.(51) and (52) respectively. It is clear from Fig.(51) that the tangential velocity increases with the increase of engine speed during both compression and expansion strokes. The decrease of the tangential velocity occuring during the reverse of flow of the ejecting air to the main cylinder increases with the increase of engine speed. The second maximum tangential velocity occuring at about 22° ATDC is independent on engine speed. The maximum tangential velocity component has a value of about 92 m/s at 1500 r.p.m.

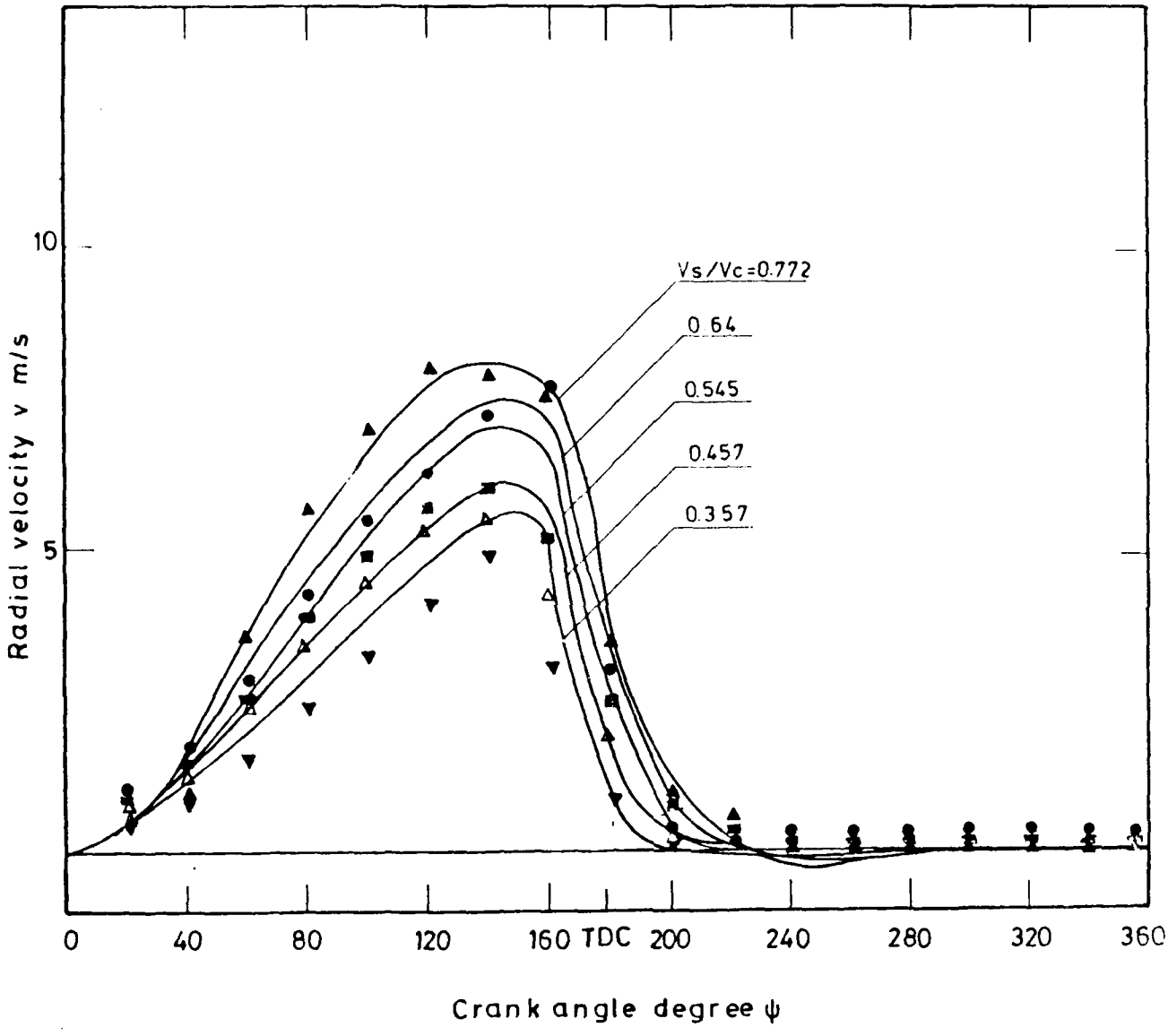

Fig(46) Predicted and measured radial velocity in plane 4 at r/Rs=0.503 and various crank angles for different swirl volume ratios keeping Aj / A = 0.0092 and N = 1000 r.p.m constant.

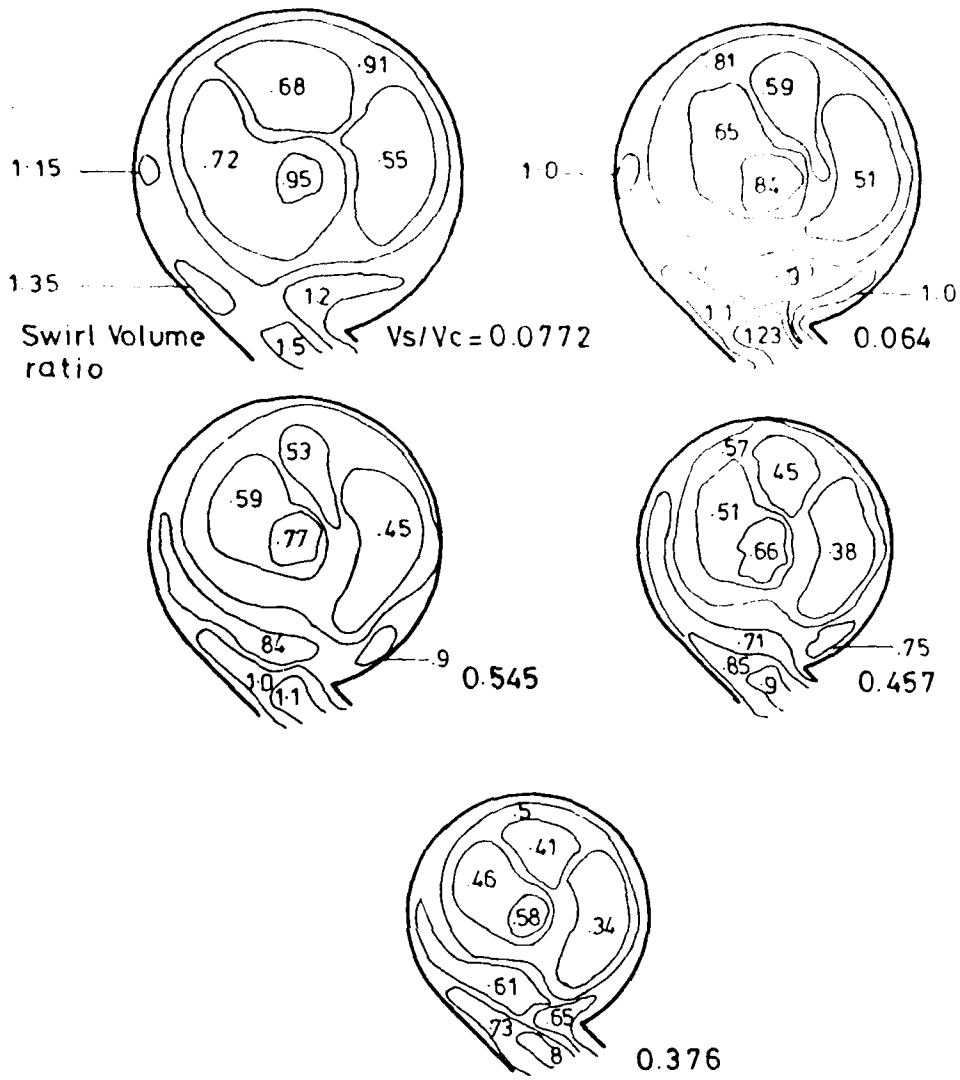

Fig.(47)Turbulence intensity contours for different swirl volume ratiosat 20° BTDC keeping Aj/A = 0.0092 and N = 1000 r.p.m constant.

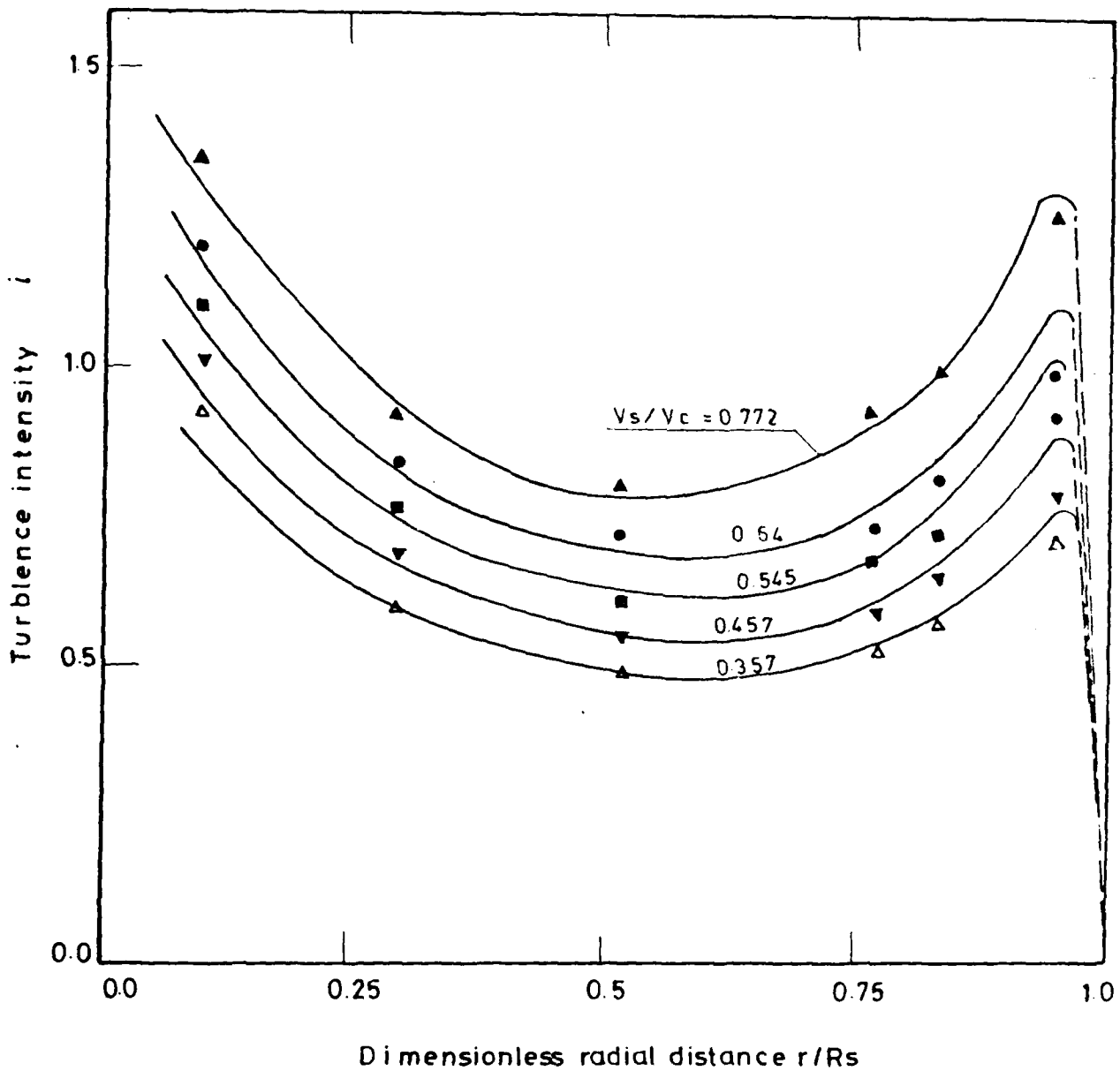

Fig.(48) Predicted and measured turbulence intensity in plan 4 at TDC and various radii for different swirl volume ratios keeping Aj/A = 0.0092 and N = 1000 r.p.m. constant.

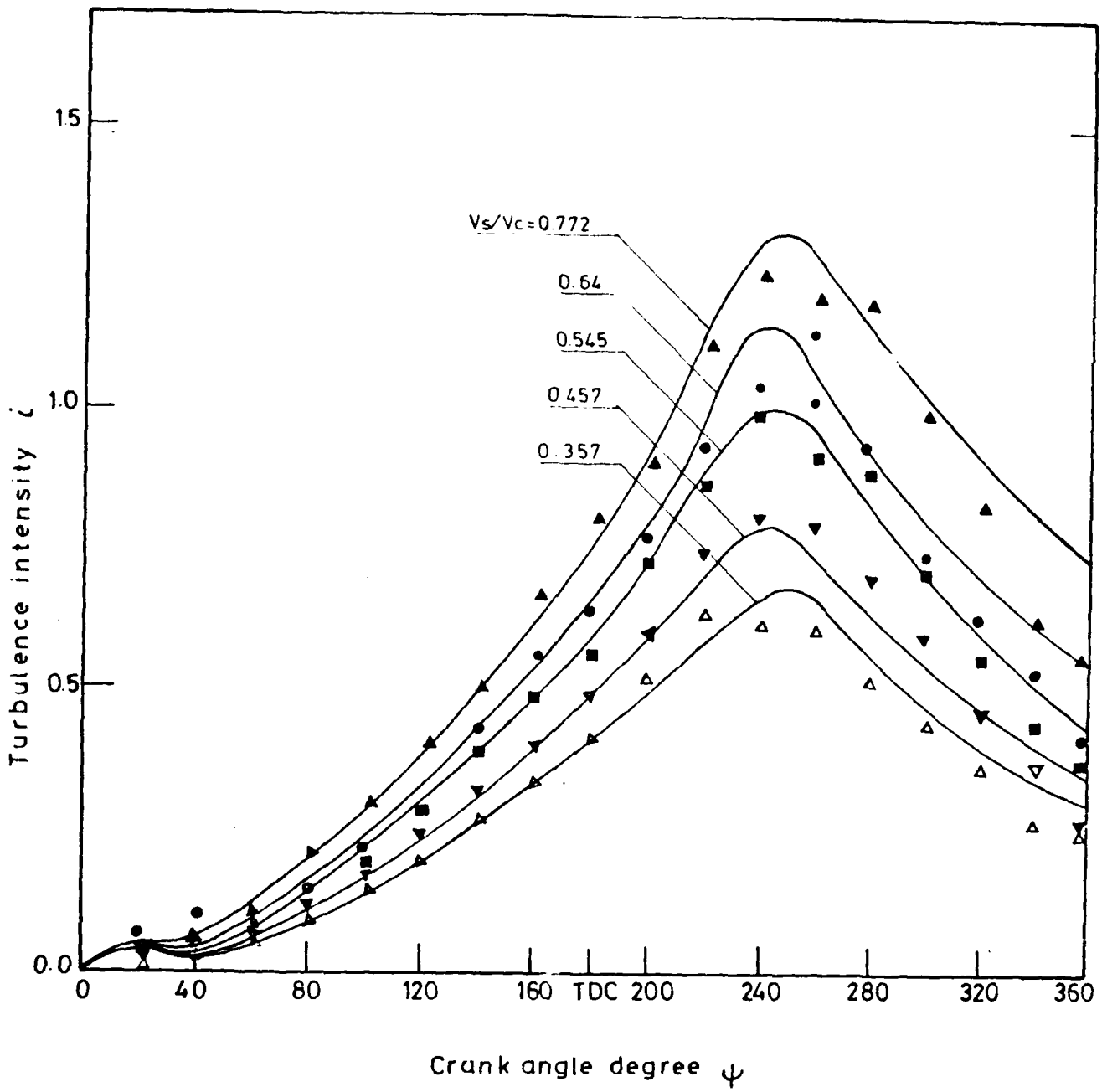

Fig (49) Predicted and measured turbulence intensty in plane 4 at r/Rs=0.503 during compression and expansion strokes for different swirl volume ratioskeeping Aj/A=0.0092 and N=1000 r.p.m. constant.

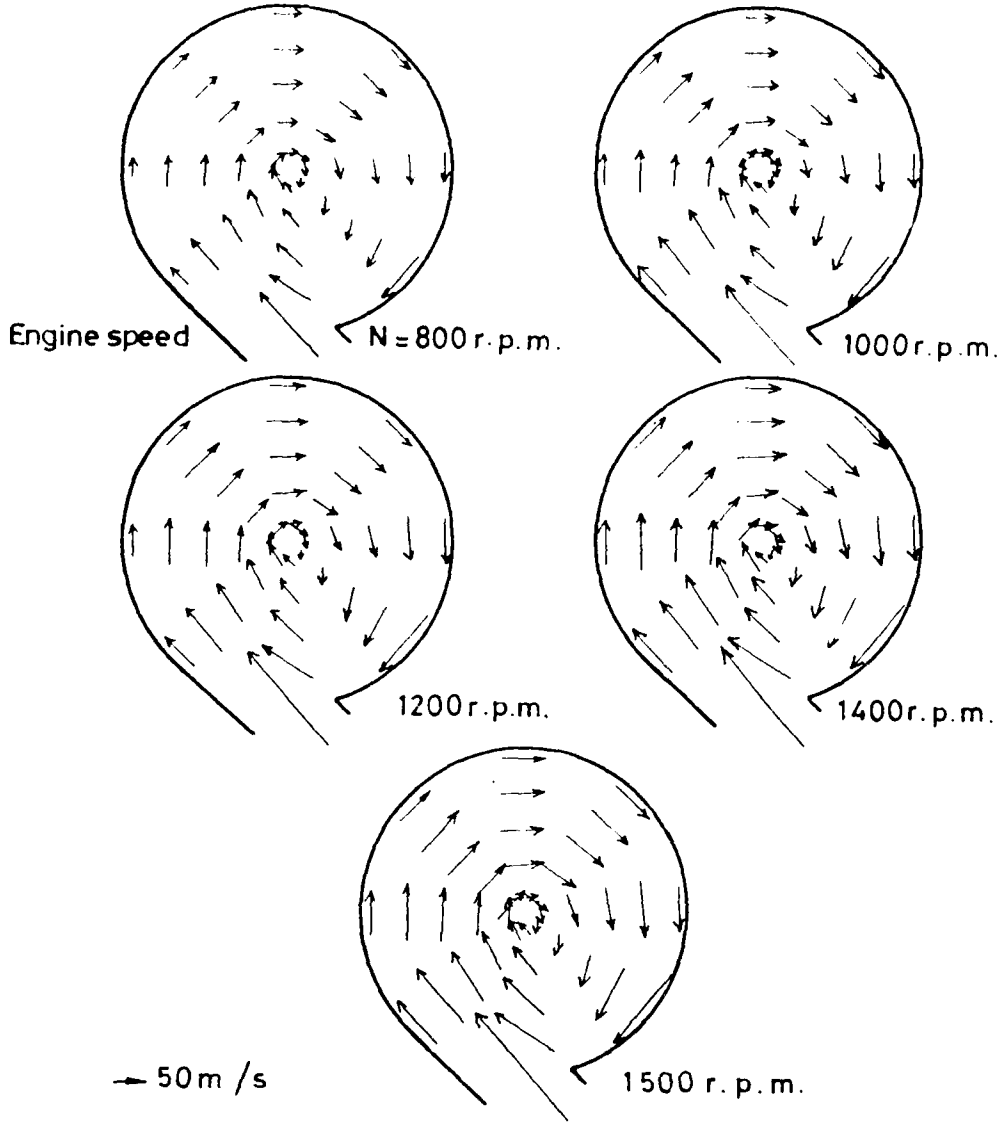

Fig(50)Velocity vector plot for different engine speed at 20° B T D C keeping Vs/Vc=0.772 And Aj/A =0.0092 constant.

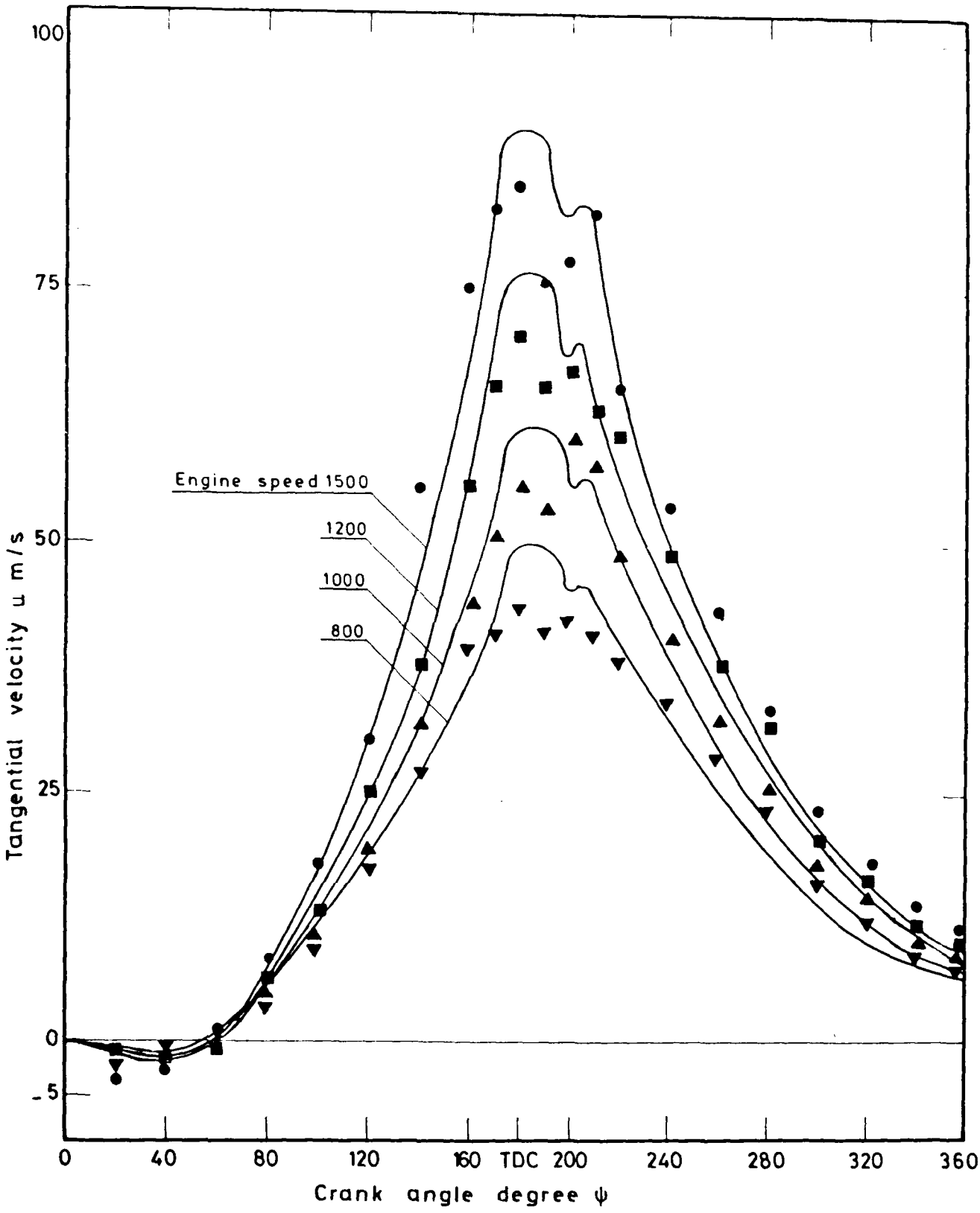

Fig.(51)Predicted and measured tangential velocity during compression and expansion strokes in plane 4 for r/Rs = 0.503 at various engine speeds keeping Vs/Vc = 0.772 and Aj/A = 0.0092 constant.

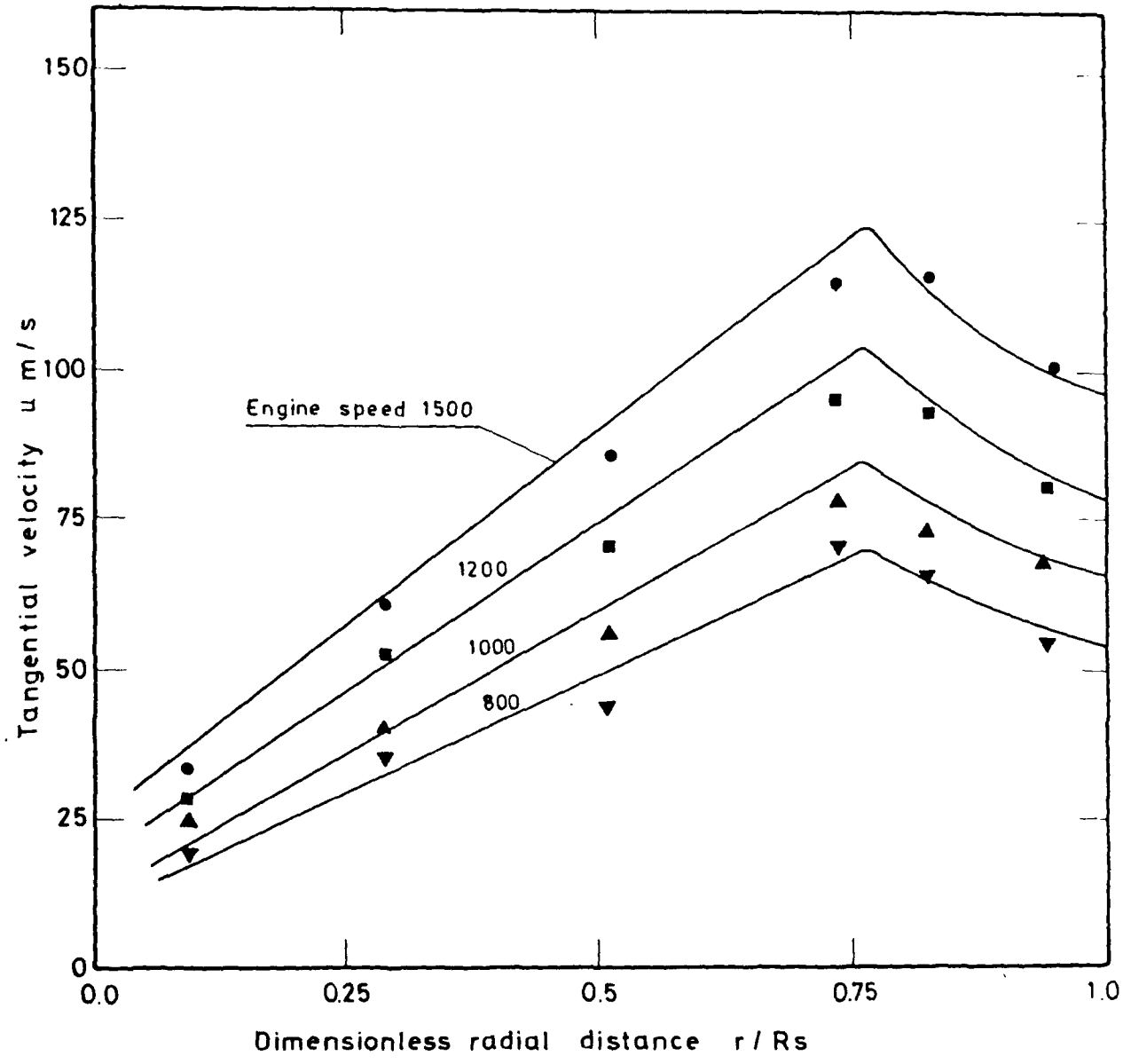

Fig.(52) Predicted and measured tangential velocity in plane 4 at TDC for different engine speeds keeping Vs/Vc = 0.772 and Aj/A = 0.0092 constant.

Figure (52) shows also that the tangential velocity increases with the increase of the engine speed along the radial distance, and that the position of the maximum value is independent on the engine speed. It has a value of about 123 m/s for 1500 r.p.m. engine speed at about 0.75 radial distance ratio (r/R_s). It is noticed that at this crank angle (TDC) all tangential velocities for all engine speeds are decomposed into two regions, solid vortex region near the chamber centre, and free vortex one near the chamber wall. These two regions are strenthened with the increase of engine speed.

The effect of the engine speed variation on the radial velocity during compression and expansion strokes is shown in Fig.(53). It is clear from the figure that the radial velocity increases with the the increase of engine speed reaching a maximum value of about 11.3 m/s at 1500 r.p.m. at about 40^{o} BTDC. and then decreases again to zero at the end of the expansion stroke (BDC).

Figure (54) shows the effect of engine speed on the turbulence intensity field inside the swirl chamber. It is clear that the engine speed has slightly lower effect on the turbulence intensity than the effect of relative port area ratio, and relative swirl volume ratio. The two eddies which are formed on both sides of the port change from a value of about 1.2 at engine speed of 800 r.p.m. to about 1.1 at engine speed of 1000 r.p.m. This small effect of the engine speed on the turbulence intensity is attributed to the effect of engine speed on the kinetic energy of turbulence K and the mean piston speed C_{pm} determining the turbulence intensity. The effect of engine speed on the turbulence intensity distribution with crank angle degree and radial distance is shown in Figs (55) and (56) respectively.

Figure (55) shows the effect of engine speed on the turbulence intensity distribution during compression and expansion strokes for different engine speeds at TDC in plane 4, from which it is clear that the engine speed has a very low effect on the turbulence intensity.

Figure (56) shows the effect of engine speed on the turbulence intensity distribution along radial distance of plane 4, from which the slight increase of turbulence intensity with the increase of engine speed is clear. It is clear also from the near wall results that the turbulence intensity values are independent on the engine speed, while an appreciable increase of the turbulence intensity appears near swirl chamber centre. A value of about 1.51 at engine speed of 1500 r.p.m. is reached. The minimum value of the turbulence intensity is obtained at about $r/R_s = 0.51$ and has a value of about 0.71 at engine speed of 800 r.p.m., its location is independent on the engine speed.

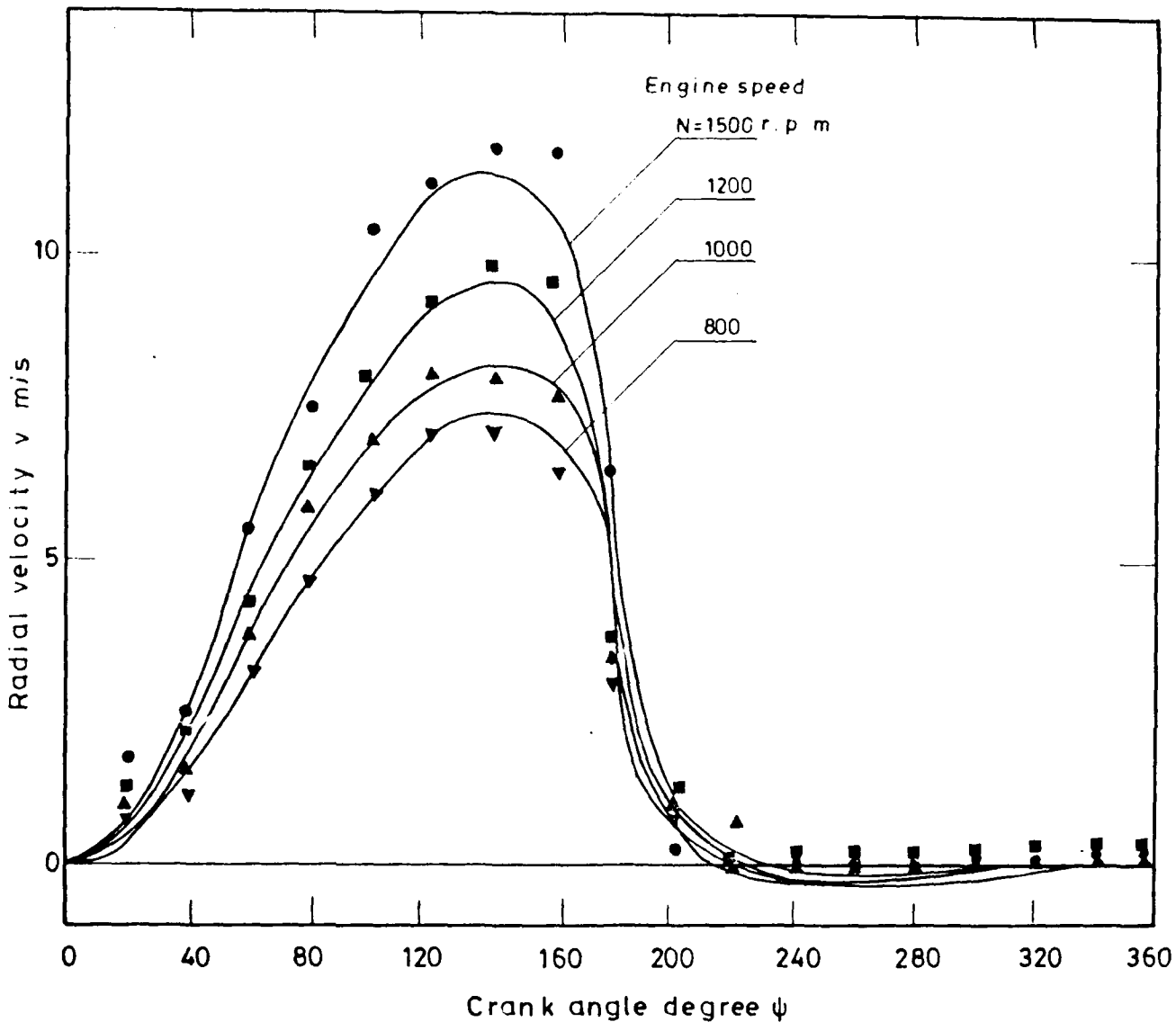

Fig (53) Predicted and measured radial velocity at plane 4 and r/Rs = 0.503 during compression and expansion strokes at various engine speeds keeping Vs/Vc = 0.772 and Aj/A = 0.0092 constant.

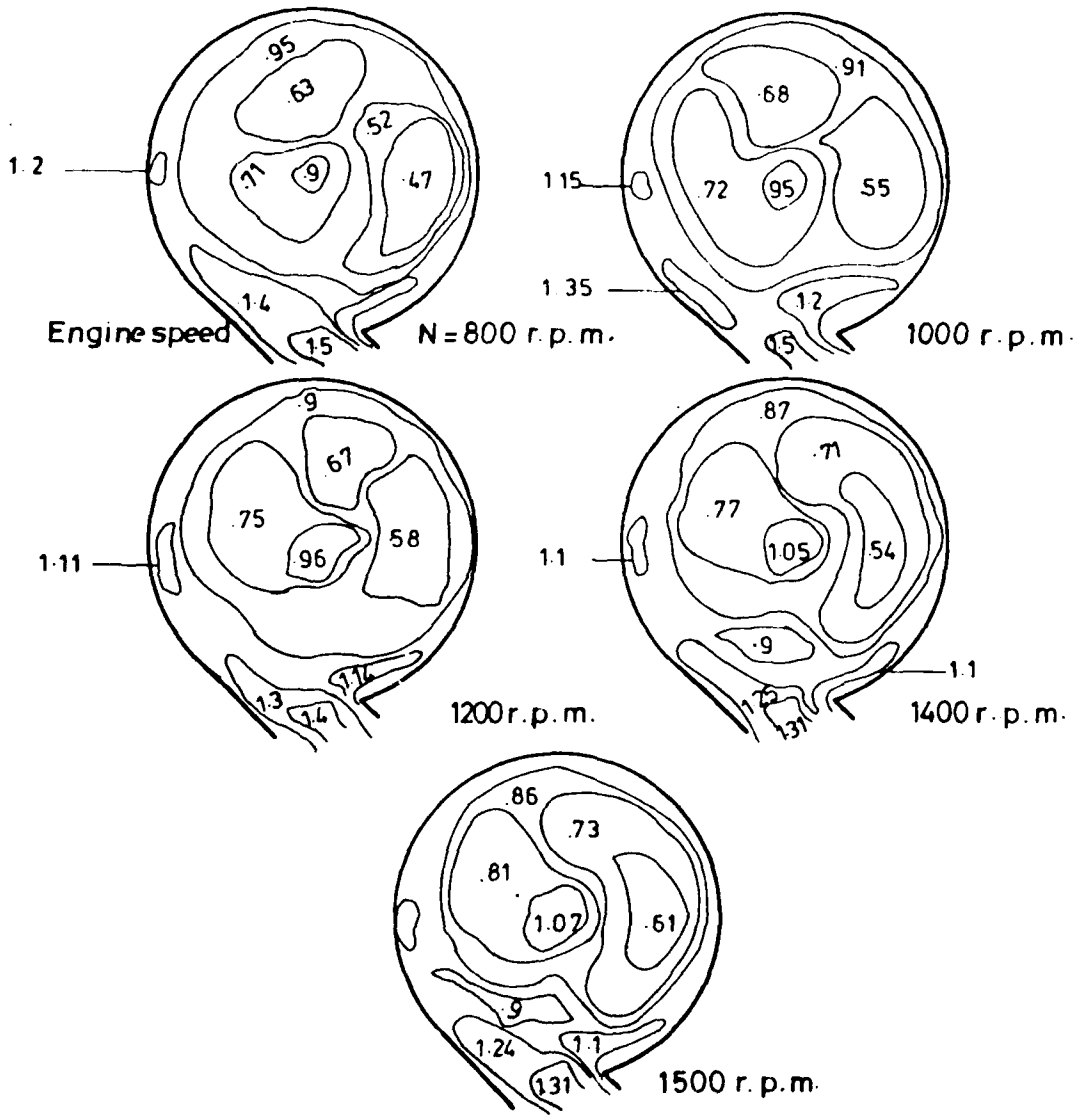

Fig (54) Tur bulence intensity contours for different engine speeds at 20° BTDC keeping Vs/Vc = 0.772 And Aj/A = 0.0092 constant.

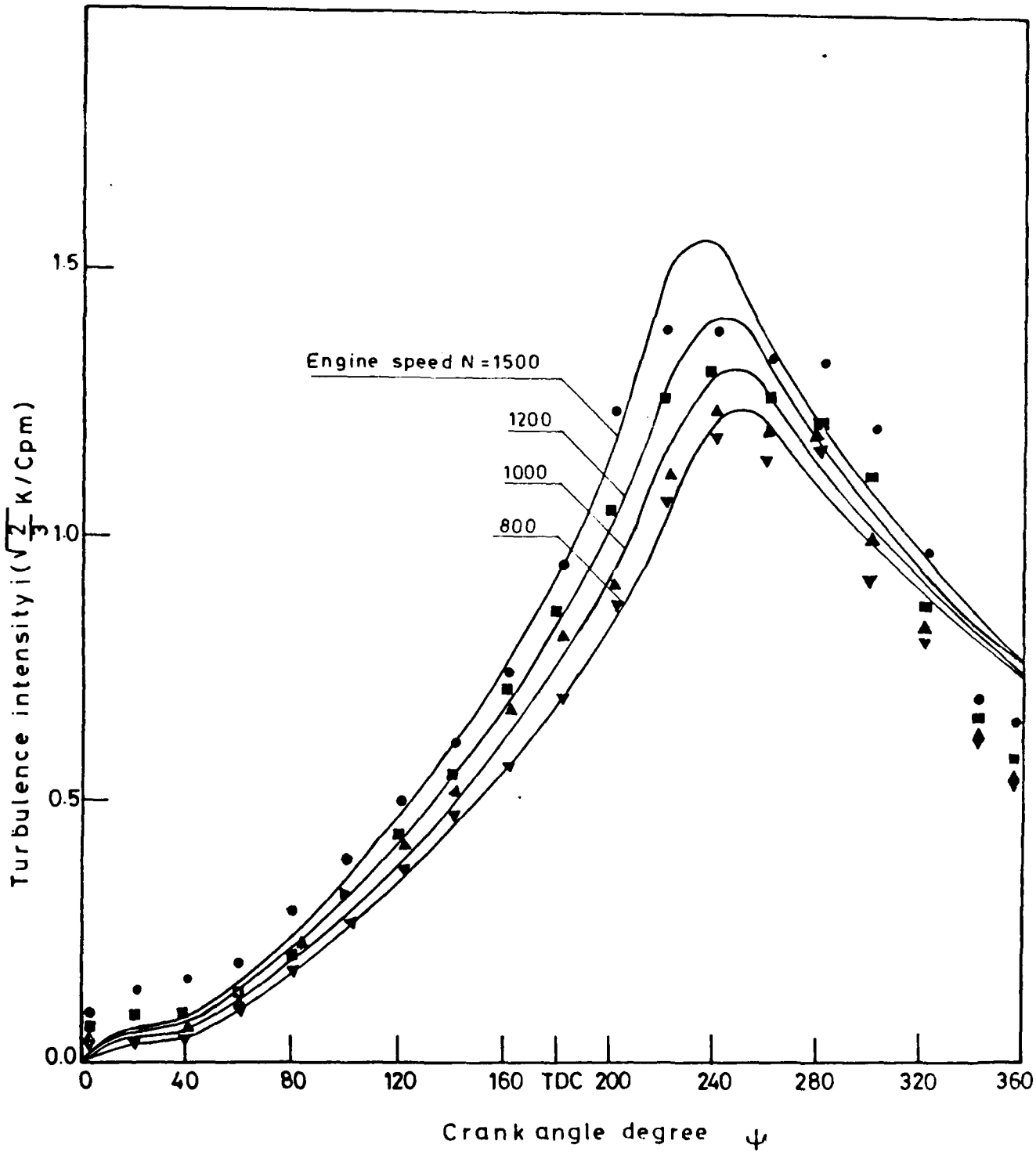

Fig(55) Predicted and measured turbulence intensity at r/Rs = 0.503 in plane 4 for various crank angles and different engine speeds keeping Vs/Vc = 0.772 and Aj/A = 0.0092 constant

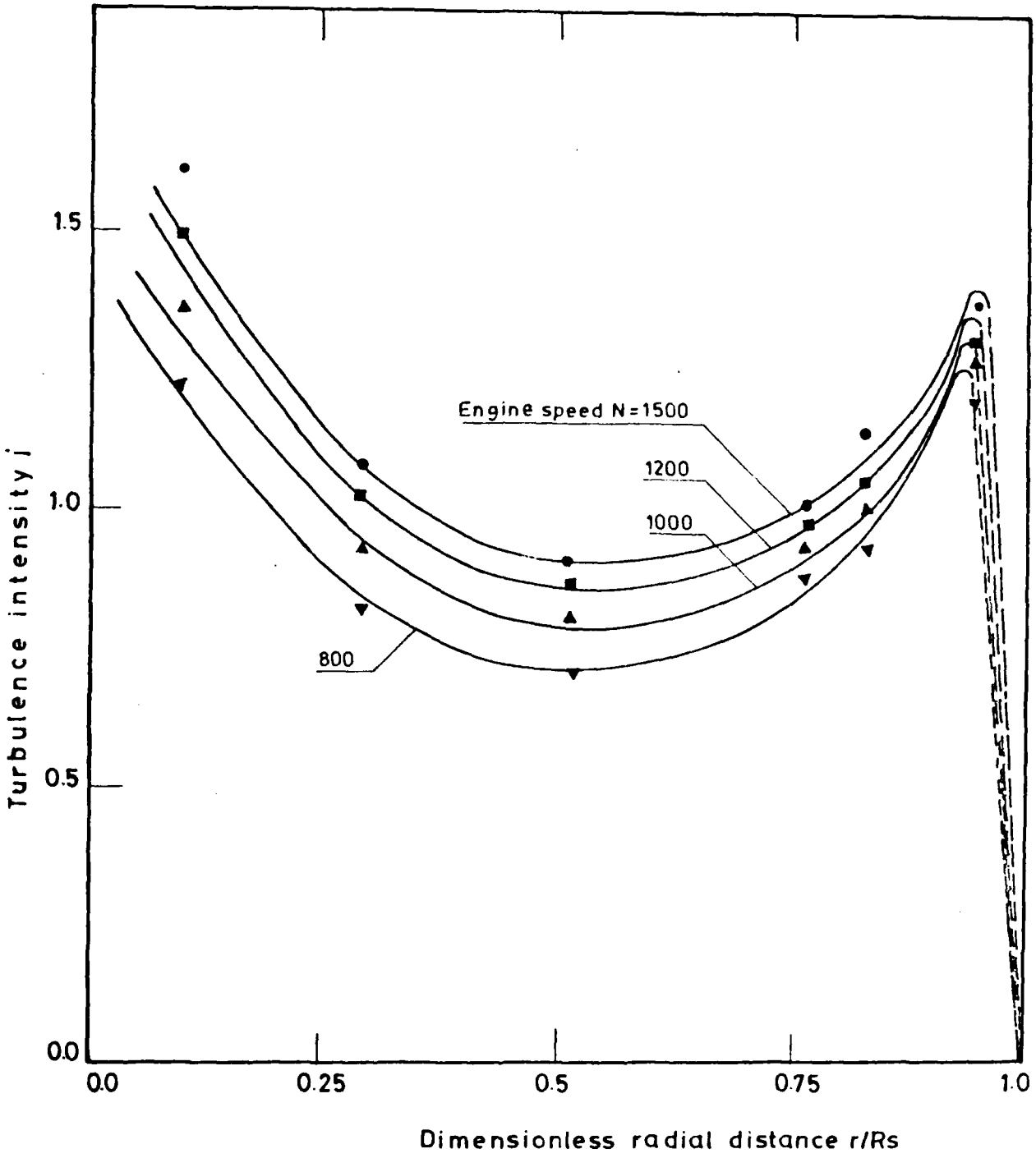

Fig(56)Predicted and measured turbulence intensity at TDC in plane 4 for different radii and different engine speeds keeping Vs/Vc = 0.772 and Aj/A = 0.0092 constant.

BIBLIOGRAPHY

1- Beer,J.M. and Chigier, N.A.,"Combustion Aerodynamics", Applied Science Publishers LTD, London (1974).

2- Bellan,J.R. and Sirignano,W.A.,"A Theory of turbulent Flame Development and Nitric Oxide Formation in Stratified Charge Internal Combustion Engines", Comb.Science and Tech.,vol.8, pp.51-68,(1973).

3- Bellan,J.R. and Sirignano,W.A.,"Combustion and No Formation in a Stratified Charge Engine: a Two Turbulent Equations Model", Comb. Science and Tech., vol.12,pp.75-104, (1976).

4- Bendat,J.S. and Piersol, A.G.,"Measurement and Analysis of Random Data", Wiley, New York (1967).

5- Boni,A.A., Chapman,M.,Cook,J.L. and Schneyer G.P., "Computer Simulation of Combustion Processes in a Divided Chamber Stratified Charge Engine", Presented at the 5th Int. Colloquium on Gasdynamics of Explosions and Reactive Systems, Bourges, France, Sep.(1975). Also, Acta Astronautica, vol.3,-4,pp. 281-292, March- April (1976).

6- Bpmo.A.A., Chapman,M., Cook,J.L. and Schneyer, G.P., "Computer Simulation of Combustion in a Stratified Charge Engine", Sixteenth Int. Symposium on Combustion, August (1976).

7- Boussinesq, J., "Theorie de l'ecoulement tourbillant", Mem.Pre. div.Sav. 23, Paris (1877).

8- Bracco, F.V.,"Two Phase, Two-Dimensional, Unsteady Combustion in Internal Combustion Engines: Preliminary Theoretical-Experimental Results", Paper Pressented at the Automotive Exposition, Detroit, Detroit, Michigan, SAE paper No.760114, Feb.(1976).

9- Bradshaw, P.,"The Analogy Between Streamline Curvature and Buoyancy in Turbulent Shear Flow", Journal of Fluid Mechanics, 36,pp.177-191, (1969).

10- Bradshaw, P. "Effects of Streamline Curvature on Turbulent Flow", AGARD graph No.169, (1973).

11- Carnahan,B.,"Applied Numerical Methods", John Wiley and Sons, Inc. New York (1969).

12- Chong, M.S., Milkins, E.E. and Watson, H.C.,"The Prediction of Heat and Mass Transfer During Compression and Expansion in I.C. Engines", SAE paper No.760761, October (1976).

13- Chorlin, A.J., "Numerical Solution of the Navier-Stokes Equations", Math.Comp., vol. 22,p. 745, (1968).

14- Dent,J.C. and Derham, J.A.,"Air Motion in a Four-Stroke Direct-Injection Diesel", Proc.Instn. Mech. Engrs.,vol.18800/74,(1974).

15- Diwakar,R.,Anderson,J.D.,Griffin,M.D. and Jones,E., "Inviscid Solutions of the Flow Field in an Internal Combustion Engine", AIAA Journal, vol.14,No.12, pp.1667-1668,Dec.(1976).

16- Eckert and Drake,"Heat and Mass Transfer", McGraw-Hill Book Co-Inc, (1960).

17- Eickhoff,H.,"Statischer Druck und Turbulenz in drehsymmetrischen Freistrahlen und Freistrahlflammen", Thesis,Universitat Karlsruhe (1968).

18- Elkotb,M.M.,"Investigation of the Air Pattern in the Cylinder of a Uniflow-Scavenging Two Stroke Engine",Ph.D.Dissertation, Moscow (1964).

19- Elkotb,M.M.,"Fine Measurements in Gas Dynamics and Combustion", Faculty of Engng- Cairo, (1976).

20- Elkotb,M.M.,El-Sabiligi,M., Diab,M.R. "Theoretical Investigation of velocity Air Pattern Inside the Swirl Chamber", Bull. of the Faculty of Engng, Cairo University, paper 17, (1976).

21- Elkotb,M.M., El-Sabiligi,M. and Diab,R.,"Spray Behaviour Inside a Swirl Chamber of a Diesel Engine", Proc. of the 1st Conference of Mech. Power Engng, Cairo, Feb, (1977).

22- Elkotb,M.M., "Spray Modelling for Multifuel Engines" First Annual Technical Report, Cairo, July (1980).

23- Eskinazi,S. and Yeh,H.,"An Investigation of Fully Developed Turbulent Flow in a Curved Channel", Journal of the Aeronautical Science, vol.23,pp.23-34,(1956).

24- Fedatenko,F.S.,"The Effect of Swirl Chamber Volume on the Work or 4-Stroke Self-Ignition Engines", NAMU,vol.69, (1953).

25- Fitzgeorge,D.and Allison,J.L.,"Air Swirl in a Road Vehicle Diesel Engine", Proc. Intstn. Mech Engrs., (A.D.) No.4, (1962-63).

26- Gosman,A.D.,PUN,W.M.,Runchal,A.K., Spalding,D.B. and Wolfshtein, M.,Heat and Mass Transfer in Recirculating Flows", Academic press, London, (1969).

27- Gosman,A.D. and Watkins,A.P. "A Calculation Procedure for Flow and Heat Transfer in Piston/Cylinder Assemblies", Imperial College Mech.Eng.Dept. Report, (1975).

28- Gosman,A.D. and Watkins,A.P.,"Simulation of Flow and Heat Transfer During a Four-Stroke Motored Engine Cycle", Imperial College of Science and Technology, Preliminary Version, March (1976).

29- Gosman,A.D. and Ideriah,F.J.K.,"TEACH-T: A General Computer Program for Two-Dimensional, Turbulent, Recirculating Flows",Imperial College of Science and Technology, June (1976).

30- Gosman,A.D. and Watkins,A.P.,"Calculations of Turbulent Heat Transfer in a Closed Piston/Cylinder System", Imperial College,Mech. Eng.Dept. Report, March (1976).

31- Gosman,A.D., Melling,A., Watkins, A.P.,"Axisymmetric Laminar Motion in a Motored Reciprocating Engine", Imperial College of Science and Technology, Internal CHT/77/3, Feb.(1977).

32- Gosman,A.D. and Watkins, A.P.,"A Computer Prediction Method for Turbulent Flow and Heat Transfer in Piston/Cylinder Assemblies", Paper Presented at the Symposium of Turbulent Shear Flows,April (1977).

33- Gosman,A.D. and Johns,R.J.R.,"Development of a Predictive Tool for In-cylinder Gas Motion in Engines" SAE,No.780315, March (1978).

34- Gosman, A.D., Melling,A., Watkins, A.P. and Whitelow, J.H. " "Axisymmetric Flow in a Motored Reciprocating Engine" Proceedings of the Inst. of Mechanical Engineers,vol.192,No.11,pp.213-223,(1978).

35- Griffin,M.D., Anderson,J.D. and Diwaker,R.,"Navier-Stokes Solution of the Flow Field in an Internal Combustion Engine", AIAA paper, No. 76-403, July (1976). Also,AIAA Journal,vol.14,No.12,pp.1665-1666, Dec. (1976).

36- Griffin,M.D., and Diwaker,R. "Computational Fluid Dynamics Applied to Flows in an Internal Combustion Engine", AIAA paper 78-57. Also AIAA 16th Aerospace Science Meeting, Huntsville, Alabama, Jan.16-18 , (1978).

37- Heldt, P.M., "High Speed Diesel Engines", Chilton Co., Text-Book.

38- Hinze, J.O.,"Turbulence", Mc Graw-Hill, New York (1959).

39- Hirt, C.W., Amsden, A.A. and Cook,J.L., "An Arbitrary Lagrangian Eulerian Computing Method for all Flow Speeds", Journal of Computational Physics, vol.14, No.3,pp.227-253, March (1974).

40- Horvatin,M.and Hussmann,A.W.,"Measurement of Air Movements in Internal Combustion Engine Cylindera" DISA Information No.8,(1969).

41- "Horvatin,M.,"Some Problems Concerning the Analytical Evaluation of the Characteristics of Hot-wires Immersed in a Fluid of Variable Pressures and Temperatures", DISA Information No.8, (1969).

42- Hutchinson,P.,"Velocity Measurements in Motored Engines for Engine Research", Internal Report AERE-R 8972, AERE Harwell , Oxford shire, January (1978).

43- Johns,R.J.R.,"The Generation of Curvilinear-Orthogonal Grids for the Solution of Problems in Fluid Mechanics",Imprial College,Mech, Eng.Dept. Report, Nov. (1977).

44- Johns, R.J.R., Gosman, A.D., Tipler, W. and Watkins, A.P. "Computer Simulation of In-cylinder Flow, Heat Transfer and Combustion", A Progress Report, Imperial College of Sc. , and Tech., Mech.Eng. Dept., (1979).

45- Jones,W.P. and Launder,B.E.,"The Prediction of Laminarization with a Two Equation Model of Turbulence", Int. Jour. of Heat and Mass Transfer, 15,pp. 301-314, (1972).

46- Khofax,M.C.,"Investigation of Mixture Creation in Engines with Divided Swirl Combustion Chamber", Proceeding of the Science Technology Conference, Academy of Science USSR, Moscow (1960).

47- Kolmogrov,A.N., "Equations of Turbulent Motion of an Incompressible Turbulent Fluid", Izv.Akad.Nauk SSR Ser Phys.VI,No.1-2,56,(1942).

48- Lancaster,D.R; Krieger,R.B.;Sorenson,S.C. and Hull,W.L.,"Effect of Turbulence on Spark-Ignition Combustion",General Motors Research Laboratory Report,GMR-2061 R,(1976).

49- Lancaster,D.R.,"The Effects of Engine Variables on Turbulence in a Spark- Ignition Engine", General Motors Research Publication, GMR-2062 R, Feb. (1976).

50- Launder, B.E. and Spalding, D.B.,"Mathematical Models of Turbulence", Academic Press, London (1972).

51- Launder, B.E. and Spalding, D.B.,"The Numerical Computation of Turbulent Flows", Computer Methods Applied Mechanics and Engineering 2,pp. 269-289, (1974).

52- Launder, B.E.; Priddin,C.H. and Sharma,B.I.,"The Calculation of Turbulent Boundary Layers on Spinning and Curved Surfaces",Journal Fluids Engineering ASME, (1977).

53- Lenze,B.,"Turbulenzverhalten und Ungemischtheit von Straholen Und Strahlflammen", Thesis, Universitat Karlsruhe, (1971).

54- Lilley,D.G.,"Prediction of Streamline Curvature on Turbulent Flow", AGARDO Graph No.169, (1973).

55- Lilley, D.G.,"Prediction of Inert Turbulent Swirl Flows", AIAA paper No.7, vol.11, July (1973).

56- Lilley,D.G.,"Modeling of Combustor Swirl Flows", ACTA,vol.1,pp. 11[illegible]-1147, (1974).

57- Maccormack,R.W.,"The Effect of Viscosity in Hypervelocity Impact Cratering", AIAA paper No.69-354, (1969).

58- Melling,A.,"Axisymmetric Turbulent Flow in a Motored Reciprocating Engine", Imperial College, Mech.Eng. Dept. Report, CHT/77/1(1977).

59- Naslt,J.F.,"The Calculation of Three-Dimensional Turbulent Boundary Layers in Compressible Flow", J. Fluid Mech.37, 625, (1969).

60- Obert,E.F.,"Internal Combustion Engine Processes and Air Pollution", Intext Educational Publishers, New York (1973).

61- Ogasawara, and Sami,A study on the Behaviour of a Fuel Droplet Injection into Combustion of a Diesel Engine", SAE.No.670468. USA (1973).

62- Patanker,S.V. and Spalding.D.B.,"A Calculation Procedure for Heat, Mass and Momentum Transfer in Three-Dimensional Parabolic Flows", Int.J.Heat and Mass Transfer, vol.15,pp.1787-1806, (1972).

63- Pischinger,F.F. and Kolocker,J.J., "Single Cylinder Study of Stratified Charg Process with Prechamber Injection", SAE paper No. (1974).

64- Prandtl,L.,"Uber cin Neues Formelsystem fur die ausgebildete Turbulenz", Nachichten Von der Akad, der Wissen schaft in Gottingen, (1945).

65- Ramos,J.I.,"Laminar Flow Calculations in Internal Combustion Engines", MAE Report 1409, Princeton University, Princeton, N.J.,(1978).

66- Ramos,J.I.,"Turbulent Flow Colculations in Internal Combustion Engines", MAE Report 1410, Princeton University, Princeton,N.J.(1978).

67- Ramos,J.I.,Humphrey, J.A.C. and Sirignano, W.A., "Numerical Prediction of Axisymmetric Laminar and Turbulent Flows in Motored Reciprocating Intenal Combustion Engines", SAE paper No.790356,(1980).

68- Reynolds,A.J.,"The Variation of Turbulent Prandtl and Schmidt Numbers in Wakes and Jets", J.Heat Mass Transfer, vol.19,pp.757-761, (1976).

69- Roache,P.J.,"Computational Fluid Mechanics", Hermosa Publishers, Albuquerque, N.M., 87108, (1972).

70- Rodi,W."Influence of Buoyancy and Rotation on Equations for the Turbulent Length Scale", Symposium of Turbulent Shear Flow,(1980).

71- Salvadori,M.G. and Baron,M.L.,"Numerical Methods in Engineering", Academic Press, New Delhi,(1966).

72- Schlchting,H.,"Boundary Layer Theory",New York, Mcgraw Hill Book Co. Inc.,(1955).

73- Shivaprasad,B.G. and Ramaprian, B.R.,"Turbulence Measurements in Boundary Layers Along Mildly Curved Surfaces, Journal of Fluids Engineering, vol.100. March (1978).

74- Sirignano,W.A.,"One -Dimensional Analysis of Combustion in a Spark-Ignition Engine", Comb. Science and Tech.,vol.7,pp.99-108,(1973).

75- So,R.M.C. and Mellor,G.L.,"An Experimental Investigation of Turbulent Boundary Layers Along Curved Surfaces",NASA CR 1940.(1972).

76- So,R.M.C. and Mellor,G.L.,"Experiments on Convex Curvature Effects in Turbulent Boundary Layers", Journal of Fluid Mech.,vol.50,pp. 43-62,(1973).

77- So,R.M.C.and Mellor,G.L.,"Experiments on Turbulent Boundary Layer on a Concave Wall", Aeronautical Quarterly,vol.XXVI,pp.55-40,(1975).

78- Stephenson,P.L.,"A Theoretical Study of Heat Transfer in Two-Dimensional Turbulent Flow in a Circular Pipe and Between Parallel and Diverging Plates", Int.J. Heat Mass Transfer.,vol.19,pp.413-423, (1976).

79- Temple,R.W. and Pediani,"Fuel Drop Vaporization Under Pressure on a Hot Surface", Inst. Mech. Eng., 184(I),677, (1969).

80- Townsend,A.A.,"The Structure of Turbulent Shear Flows", Cambridge University Press, Cambridge, England (1953).

81- Voiculescu ,I.A. and Borman,G.L.,"An Experimental Study of Diesel Engine Cylinder-Averaged No Histories", SAE paper No.780228,(1978).

82- Watkins,A.P.,"Calculation of Flow and Heat Transfer in the Combustion Chamber of a Reciprocating Engine", M.Sc. Thesis, University of London, (1973).

83- Watkins,A.P.,"Flow and Heat Transfer in Piston-C linder Assemblies", Ph.D. Thesis, Univ. of London, (1977).

84- Witze, P.O.,"Preliminary Hot-Wire Measurements in a Motored Engine with an Axisymmetric Cylinder Geometry",Private Communication, July (1977).

85- Wu,J.C. and Sugavanam,A.,"Method for the Numerical Solution of Turbulent Flow Problems, J.AIAA,vol.16, No.9,(1978).

PART 2

NOMENCLATURE

a,b	constants in Tanasaw-Tesima Eqn. (4)
A	area, m^2
b_v	mass transfer coefficient
C_D	discharge coefficient.
C_1C_2,C_μ	constants of the turbulence model
C	absolute velocity of fuel droplet, m/s.
d	nozzle diameter, m
d_J	ligament diameter, m.
D	droplet diameter, m
D_c	diffusion coefficient.
d_J	diameter of fuel ligament, m
D_{qp}	relevant mean diameter depending on values of p and q such as D_{10} -linear mean diameter, D_{32}- Sauter mean diameter, μm.
E	energy lost in forming new ligament J.
E_{act}	activation energy
f	degree of freedom for chi-square distributions
F	percentage by volume of diesel fuel in the mixture.
h	heat transfer coefficient, W/m^2 hr C
H	total enthalpy, W.
$K_1K_2K_3$	constants of rate Eqn. (1,2) and Eqn. (32).
k	kinetic energy of turbulence
K	thermal conductivity, W/m C.
ℓ	spray penetration, m.
ℓ_n	length of fuel nozzle, m.
L	latent heat of fuel, J/Kg fuel.
L_o	theoretical quantity of air needed for complete combustion of fuel, Kg/Kg fuel.
m	mass, Kg.
m_1	index in rate Eqn. (1)
M	Ohnesorse Number, dimensionless value $\mu_\ell / (\rho_\ell \, d \, \sigma_\ell)$
M_i	total mass of fuel injected, Kg.
M_u	total mass of unprepared fuel,Kg.
n	number of fuel droplets.

N	engine speed, RPM
Nu	Nusselt number, hD/K, dimensionless
p	pressure, bar
Δp	pressure drop across fuel nozzle, bar,
p_d	normalized chamber density $(\rho_a/\rho_{ac})\ p_o$, bar.
p	preparation rate.
p_{o2}	partial pressure of oxygen, bar.
p_r	prandtle number, $\mu\ c_p\ /K$, dimensionless
Q	normalized fuel quantity per cycle, dimensionless.
r	radius,m.
R	Universal gas constant.
R_i	instantaneous heat release rate or reaction rate.
R-R	Rosin-Rammler.
Re	Reynolds number, $CD\rho/\mu$, dimensionless
R_v	gas constant of fuel vapour, J/Kg ^oC.
R_s	source vector of Eqn. (7).
S_Φ	volumetric source rate of Φ arising from gas
$S_{\Phi\ell}$	volumetric source rate of Φ arising from fuel
Sc	Schmidt number, droplet, dimensionless,
Sh	Sherwood number, dimensionless
t	time, S.
T	absolute temperature, ^oK
T-T	Tanasawa-Tesima
u	tangential velocity of air, m/s.
v	cumulative volume of droplets less than a given size D,m^3.
V	radial velocity of air, m/s.
dv	incremental value of drops within the size range D,D+dD, m^3
W	relative velocity of droplet, m/s.
We	Weber number
x	index in rate Eqn. (1).
$\dot{x},\dot{y}$	droplet velocity in x and y direction .
$\ddot{x},\ddot{y}$	accelaration of droplet in x and y direction.
α	excess air factor, $\dot{m}_a/(L_c\dot{m})$, dimensionless.
α , β	constants of T-T Eqn.(41).
β_J	optimum length/diameter of ligament
$\Gamma(K)$	Gamma tunction $\Gamma(K) = \int_o^\infty x^{k-1}\ e^{-x}dx$.

Γ_ϕ	eddy duffusivity for Φ.
δ	inclination of droplet relative velocity to x-axis.
ε	dissipation rate of kinetic energy of turbulence.
θ	angular position
Φ	crankangle, degree, arbitrary dependent variable.
ψ	injection angle, degree
μ	dynamic viscosity, kg s/m^2.
ν	Kinematic viscosity, m^2/s.
$\bar{\rho}$	density, kg/m^3
σ	surface tension, N/m.
$\sigma_h, \sigma_k, \sigma_\psi$	constants of turbulence model for enthalpy, kinetic energy dissipation rate and concentration.

Subscripts

a	air
c	chamber
f	surface
i	arbitrary value
in	inlet to control volume
ℓ	liquid fuel
o	initial
out	outlet to control volume.
p	piston cavity
r	radius
s	saturation
v	vapour
x	x-direction
y	y-direction
α	free streem.

CHAPTER 5

FUEL SPRAY MODELLING

5.1 INTRODUCTION

The fuel-air mixture creation prior to as well as after autoignition is important in diesel engines. It controls the rate of heat release and consequently rate of pressure rise, noise, and pollutants formation. The mixing process depends upon the kinetic energy of both fuel and air. In open combustion chambers, since the air motion is small the fuel is injected under high pressure through a nozzle with one or several holes to ensure adequate mixing of fuel and air. Increasing the air motion during the suction stroke by a mask valve, tangential port or swirl inlet manifold assists in decreasing the fuel pressure. The air motion in quiescent combustion chambers can be created also during the compression stroke by using bowl piston. The energy of mixture formation in swirl chambers is mainly generated by the kinetic energy of the air swirl motion during the compression and expansion strokes. The energy of the fuel spray has rather smaller effects on mixture formation in these chambers.

The mixing process now includes transport of fuel from the jet by swirling air flow, deflection of the jet, impingement of the jet on the combustion chamber wall. Besides, the impinged jet is spread on the walls of the combustion chamber forming a film of very small thickness. This film takes its required heat of evaporation from the walls and surrounding gases by convection. The injection and mixing of fuel with air in the combustion chamber needs to be achieved very rapidly if the engine is to be efficient. Many investigators have studied the problem of mixture formation and combustion in diesel engines, but most of them treated the problem either in general, or by formulating empirical relations for the individual processes.

The use of modern computers makes possible the calculations of more realistic and complex engine cycles , and these in turn require mathematical formulation of the combustion process. A major purpose of early studies was to calculate the cylinder pressure diagram using a predetermined heat release pattern obtained by analysing experimental cylinder pressure diagram of similar engines. The cycle calculations involve adding energy to the cylinder contents using small steps and considering uniform cylinder conditions of composition, pressure and temperature. This method of combustion modelling is called single-zone model. It suffers from severe limitations if the effect of various factors on combustion process are to be investigated. Modifications were proposed to include the fuel-air mixture preparation by Austen and Lyn[1,2] in which the fuel injection process is divided into a number of steps. The fuel injected during one step is calculated according to a simple mathematical formula. Summing all such steps would then give the preparation rate diagram. However, the used formulae neglect oxygen availability. Whitehouse et al[3,4] suggested semi-empirical formulae for the preparation and combustion rate of fuel. The rate of preparation was assumed depenendent upon the total surface area of the droplets forming the fuel spray. Considering homogeneous droplet size distribution of size equal to the mean droplet diameter the preparation rate is represented by

$$p = K_1 M_i^{(1-x)} M_u P_{O_2}^{m_1} \qquad (1)$$

and the reaction rate is calculated by the following equation

$$R_1 = \frac{K_2 P_{O_2}}{N \sqrt{T}} \text{Exp}(-E_{act}/RT) \int (P - R_i) \, d\phi \qquad (2)$$

Inaccurate results are obtained when applying this method to quiescent combustion chambers where jet entrainment is of major performance. In this case the single zone model cannot estimate the effect of number of orifices in the nozzle. It cannot

indicate the lack of air and production of polluting subtances which are dependent on local temperature and chemical concentration.

A two-zone model has been developed to improve the previous model. In this model the combustion chamber contents are divided into two parts, the burning and the nonburning zone. Formulae of preparation and combustion rate of the single zone model are used in the burning zone and the combustion products are assumed ideal gases. The nonburning zone consists of pure air which is treated as a perfect gas. Such two-zone model has been developed for both quiescent[5] and swirl[6] combustion chambers. The burning zone has been assumed as a cone jet of known cone angle whose development is determined from the fuel spray penetration data. The development of the jet of fuel plus air prior to impingement on the walls has been investigated by numerous research workers[7-12] and simple formulae for the penetrated spray are suggested. Once the jet has struck the combustion chamber wall it is treated as wall jet[13-15] . Such model does not deal with the motion of either the air or fuel jet.

The major problem in the aforementioned models is to estimate the rate of mixing of the gas outside the burning zone with the gases inside this zone. Empirical or semi-empirical estimates are used. High speed photography of the spray shows that when the gas flows perpendicular to the fuel spray, the spray deflects in the direction of the gas flow and loses its symmetry. Assuming same drop size distribution and mean droplet diameter for every increment of fuel in the injection process, some investigators[16-20] attempted to use spalding's single-droplet results to predict burning rates in an engine. The concept of a finite spray burning rate based on single droplet was also proposed[21-22] assuming no interaction between droplets. However, Shipinski[23-24] evaluated these models and concluded that the overall performance of the engine is highly dependent on the burning rate. Recently, few investigators[25-30] have tried to formulate more fundamental methods for predicting mixing and turbulent flow. Some of these models divided the fuel spray into a lot of small packages and no mixing among them was assumed[27]. Others tried to solve the equations governing the droplet motion to define the spray development. However, data for the droplet size distribution and the effect of various factors upon it are required for the development of these models.

Itis the aim of the present work to review the fuel spray models and to develop a new spray model for the calculation of fuel spray trajectory in a swirl chamber diesel engine based on the combination of the discrete droplet model with a multi-dimensional gas flow prediction method . The model includes turbulence interaction between fuel and air , variation of fuel droplet diameter and consiquently drag force and heat transfer to the fuel droplet .

5.2 REVIEW OF FUEL SPRAY MODELLING

Overpenetration of fuel spray in quiescent chamber would lead to impingment upon a cold surface giving consequent fuel wastage. Early studies of fuel penetration were mainly based on the correlations of the experimental data. Along this line many investigators have carried out experimental measurements of the penetration of a single spray injection into air using different techniques [30-34]. Hay[11] surveyed these penetration formulae and concluded that Dent's expression of the following form:

$$\ell = 0.865 \left| (\Delta P/\rho_a)^{\frac{1}{2}} t\, d \right|^{\frac{1}{2}} \left(\frac{530}{T_a}\right)^{1/4} \qquad (3)$$

can be recommended for small densities. However, spray penetration in diesel combustion chambers varies with the operating parameters and geometrical design of injectors. Therefore, these correlations are limited in their applications and a theoretical calculation approach of the fuel spray is needed.

Riehm , Triebnigg and Sitkei[35-37] were the first who attempted to calculate the spray penetration. They treated the spray motion as constant radius spheres leaving the injection nozzle under aerodynamic resistance forces. They applied the law of conservation of energy. Mehlig[38] analysed the experimental results of

Trieb.igg and assumed that the lateral motion of the spray results from turbulence which depends on the injection system only. This leads to that the radial velocity of the spray does not depend on the back pressure. He deduced an expression for spray penetration from the geometrical relations.

Hakki OZ[39] calculated the spray penetration using the differential equation of free jet and considering the influence of turbulent friction force alone. Making use of the available experimental data he proposed the following formula for the spray penetration :

$$\frac{\ell}{\sqrt{C}} = 4.85 \; e^{-0.04 \, P_d} \qquad (4)$$

Ogasawara and Sami[25] have attempted to investigate theoretically the behaviour of a single droplet representing the mean droplet diameter and moving at the spray tip. The equation of motion of the droplet and the equation of heat balance have been derived during the delay period assuming that the droplet diameter was constant and that the air velocity had no effect. A closed form integration of the equation was obtained giving the trajectory of the droplet during the delay period in the following form :

$$\frac{\ell}{C_o \rho_\ell d^2/\mu_o} = \frac{10}{3\beta_v \, Re_\ell} \ln\left|1+\frac{Re_\ell}{125}\right| \{1-\exp(-37.5\,\beta_v N_t)\} \qquad (5)$$

where, $N_t = t/\rho_\ell \, d^2/\mu_a$, $Re_\ell = C_o \, d/\nu_a$

β_v = constant = 0.85

Considerable discrepancy appeared between the theoretical and experimental results for kerosene flame. This resulted from neglecting relative velocity. Air motion contributes to the magnitude of Reynolds number and thus affects the droplet behaviour and the heat transfer to the droplet. Therefore,it is necessary to take the air motion to formulate a mathematical model based on the droplet behaviour. Hiroyasi and Kadota[27] developed models for combustion and formation of nitric oxide and soot in direct

injection diesel engines. In this model, the spray injected into a combustion chamber from an injection nozzle is divided into a lot of small packages. Each package experiences its own history of temperature, pressure, and equivalence ratio, which govern the chemical kinetics. The processes occuring in the package are shown in Fig.(1). The package, immediately after the fuel injection, involves a lot of fine droplets and a small volume of air. During the package motion, the air entrains into it and fuel droplets evaporate. Therefore, the small packages consist of liquid fuel, vaporized fuel and air. Shortly after the start of injection ignition occurs in the gaseous mixture and a sudden expansion of the package takes place. Thereafter, the fuel droplets evaporate and fresh air entrains into the package. Vaporized fuel mixes with fresh air and combustion products and spray continues to burn. All fuel-air packages are assumed to burn at the stoichiometric condition. The effect of air motion and the interaction of neighbouring droplets have not been taken into account in this analysis.

The only studies of spray injection into gaseous flow fields which are based on continuum mechanics are those of Wakuri et al[40] and Cotton et al[41]. These studies enable us to calculate the spray penetration, but neither the evaporation rate nor the mixing field details, such as velocity, temperature and concentration distribution, can be calculated with these methods. Adler and Lyn[42] developed a theoretical model based on the continuum mechanics basis using the classical differential equations of continuity, momentum energy and diffusion. A differential volume element having a mass equivalent to the total mass of air, liquid droplets and evaporated liquid contained in the element was used. The element is, therefore, characterized by its concentration and evaporation functions.They treated the transient phenomenon on a steady state basis by taking the elemental section of the spray as a quasi - solid body under equilibrium of the inertia and drag forces in the flow field. The cross section of the

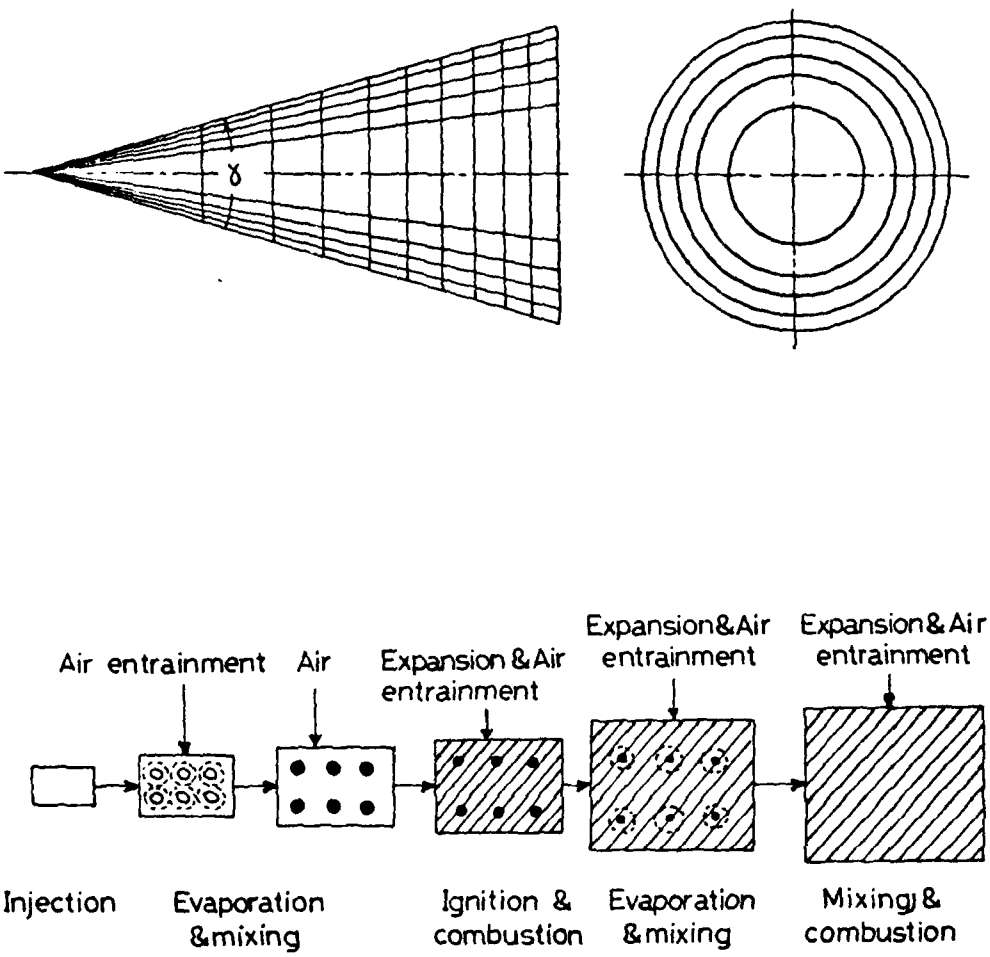

Fig (1) Schematic diagram of the spray combustion model of Hiroyasu

spray was replaced by a rectangular cross section with constant height/width ratio to formulate a two dimensional model. An integral method was used to replace the partial differential equation by a set of ordinary differential equations which was then solved to determine the spray centre line. Thereafter, the velocity, concentration, temperature and density structures are built on this framework. Such a model cannot determine the exact values of the local concentration especially when there is interference from neighbouring sprays. It can however be generalized for all types of combustion chambers.

Spray modelling based on the combination of the discrete droplet model with a multidimensional gas flow prediction method was developed for the prediction of turbulent combustion of liquid fuels in steady flow combustors[43] and in direct injection engines[44]. However, these models are still awaiting sufficiently detailed information about the droplet size distribution and droplet velocity distribution.

During the past seven years comprehensive works were done at Cairo University about spray modelling. Firstly the spray calculation model was based on the solution of the equation of motion of droplets and air. The interaction between the droplet and air was considered by averaging the over flow processes on a scale smaller than the droplet size and employing typical correlations for the droplet drag, heat and mass transfer. The results of this work, which have been reported in several publications[15,28,29,45,46] were sufficiently encouraging to extend the model to include the prediction of air motion and turbulence interaction between fuel and air.

THE GOVERNING CONSERVATION EQUATIONS

i- Gas Motion and Mixing

The flow inside diesel engine swirl chambers is a transient, turbulent, two dimensional flow. The flow is, thus, governed by the differential conservation equations of energy, mass and momentum. The equations governing the flow in a cylindrical swirl chamber of a diesel engine are obtained by decomposing the velocity, pressure, density and enthalpy into a mean and a fluctuating value respectively. The turbulent diffusion fluxes which appear in the governing equations are modelled using Boussinesq approach in terms of the mean flow gradients and eddy diffusivities. These eddy diffusivities are determined by solving additional differential conservation equations for the time averaged kinetic energy of turbulence K and its dissipation rate ε taking into consideration compressibility effects.

Within the above framework, the governing set of equations may be represented in terms of a single equation for an arbitrary dependent variable Φ , as mentioned in chapter 2 , as follows :

$$\frac{\partial}{\partial t}(\rho\Phi)+\frac{1}{r}\frac{\partial}{\partial r}(r\rho v\Phi)+\frac{1}{r}\frac{\partial}{\partial\theta}(\rho u\Phi)-\frac{1}{r}\frac{\partial}{\partial r}\left(r\Gamma_\Phi\frac{\partial\Phi}{\partial r}\right)$$

$$-\frac{1}{r^2}\frac{\partial}{\partial\theta}\left(\Gamma_\Phi\frac{\partial\Phi}{\partial\theta}\right)=S_\Phi+S_{\Phi\ell} \qquad (6)$$

where Φ stands for radial velocity V, tangential velocity u, total enthalpy h, kinetic energy k and dissipation rate of the kinetic energy of turbulence ε .

The equation represents also the continuity equation by replacing Φ by 1. The definition of Γ_Φ and S_Φ are given in Table (1).

ii- Droplet Trajectory

The solution of the fuel droplet trajectories, size and temperature histories is necessary for the evaluation of the

source terms in the gas-phase flow equations. The droplet is subjected during its motion to the effect of the air velocity and therefore the equation of motion of a droplet is given by :

$$\frac{d}{dt}\,(m_\ell C_\ell) = \frac{1}{2}\,C_D\,A_\ell\,\frac{\rho_a}{\rho_\ell}\,W_\ell^2 + R_s \qquad (7)$$

The source vector R_s contains terms involving the pressure gradient, Basset, Magnus and gravity forces. The pressure gradient and Basset terms are neglected as they are very small quantities. The Saffman lift and Magnus forces are also neglected because the droplets are not in a high shear region of the gas flow. Substituting for the mass and area of droplet the equation of motion is described by the following two equations :

$$\begin{aligned} r_\ell\,\ddot{x} &= -3\,C_{\ell x}\,\frac{dr_\ell}{dt} - \frac{3}{8}\,C_D\,W_\ell^2\,\frac{\rho_a}{\rho_\ell}\cos\delta \\ r_\ell\,\ddot{y} &= -3\,C_{\ell y}\,\frac{dr_\ell}{dt} - \frac{3}{8}\,C_D\,W_\ell^2\,\frac{\rho_a}{\rho_\ell}\sin\delta \end{aligned} \qquad (8)$$

where ;

$$\delta = \tan^{-1} W_{\ell y}/W_{\ell x}$$

$$W_{\ell x} = C_{\ell x} - u_x = \dot{x} - u_x$$

$$W_{\ell y} = C_{\ell y} - u_y = \dot{y} - u_y$$

and

$$u_x = u\cos\theta - V\sin\theta$$

$$u_y = u\sin\theta + V\cos\theta$$

where $\theta = \tan^{-1}\dfrac{x}{r_c - y}$

The drag coefficient can be represented reasonably well by Ingebo's equation[47] multiplied by a correction coefficient $\beta_D = 0.85$ as it was derived for a non-evaporating droplet:

$$C_D = 0.85 \times 27/Re^{0.84} \qquad (9)$$

The rate of decrease of droplet mass during the evaporation period is given by :

2.3 THE GOVERNING CONSERVATION EQUATIONS

2.3.1- Gas Motion and Mixing

The flow inside diesel engine swirl chambers is a transient, turbulent, two dimensional flow. The flow is, thus, governed by the differential conservation equations of energy, mass and momentum. The equations governing the flow in a cylindrical swirl chamber of a diesel engine are obtained by decomposing the velocity, pressure, density and enthalpy into a mean and a fluctuating value respectively. The turbulent diffusion fluxes which appear in the governing equations are modelled using Boussinesq approach in terms of the mean flow gradients and eddy diffusivities. These eddy diffusivities are determined by solving additional differential conservation equations for the time averaged kinetic energy of turbulence K and its dissipation rate ε taking into consideration compressibility effects.

Within the above framework, the governing set of equations may be represented in terms of a single equation for an arbitrary dependent variable Φ , as mentioned in chapter 2 , as follows :

$$\frac{\partial}{\partial t}(\rho\Phi)+\frac{1}{r}\frac{\partial}{\partial r}(r\rho v\Phi)+\frac{1}{r}\frac{\partial}{\partial\theta}(\rho u\Phi)-\frac{1}{r}\frac{\partial}{\partial r}\left(r\Gamma_\Phi\frac{\partial\Phi}{\partial r}\right)$$
$$-\frac{1}{r^2}\frac{\partial}{\partial\theta}\left(\Gamma_\Phi\frac{\partial\Phi}{\partial\theta}\right)=S_\Phi+S_{\Phi P} \qquad (6)$$

where Φ stands for radial velocity V, tangential velocity u, total enthalpy h, kinetic energy k and dissipation rate of the kinetic energy of turbulence ε .

The equation represents also the continuity equation by replacing Φ by 1. The definition of Γ_Φ and S_Φ are given in Table (1).

2.3.2- Droplet Trajectory

The solution of the fuel droplet trajectories, size and temperature histories is necessary for the evaluation of the

$$\frac{-dm_\ell}{dt} = 4\pi r_\ell^2 b_V(P_s - P_\infty) = -4\pi r_\ell^2 \rho_\ell \frac{dr_\ell}{dt} \qquad (10)$$

where P_s is the mass fraction of vapour at the droplet surface and P_∞ the mass fraction of vapour in the free stream. The mass transfer coefficient is calculated from the Ranz - Marshall equation[41]:

$$b_V = \frac{Sh\ D_c}{2\ r_\ell} \qquad (11)$$

where ;

$$D_c = D_o(T_s/T_o)\ (P_o/P_a)$$

The Sherwood number is augemented due to convection as Bird et al suggested[42] by the following expression ;

$$Sh = 2 + 0.6\ Re^{\frac{1}{2}}\ Sc^{1/3} \qquad (12)$$

Using the above equations and taking into consideration that the partial pressure of vapour at the surface is equal to the saturation pressure corresponding to the temperature of the droplet, the rate of change of droplet radius can be written as ;

$$\frac{dr_\ell}{dt} = \frac{-Sh\ D_c}{2\ r_\ell \rho_\ell} \frac{P_s}{R_V\ T_s}$$

where ;

$$p_s = 2.39 \times 10^9\ Exp\ (-6065/T_s)$$

$$T_{s,T_a} = 462\ p_a^{0.043} + 0.06\ (T_a - 673);\ 350 < T_a < 600\ ^oC$$

The heat balance equation for the droplet is :

$$\frac{4}{3}\pi r_\ell^3 \rho_\ell c_{p\ell} \frac{dT_\ell}{dt} = 4\pi r_\ell^2\ h(T_a - T_\ell) + 4\pi r_\ell^2 \rho_\ell L \frac{dr_\ell}{dt} \qquad (14)$$

Thus, the rate of temperature increase can be written as :

$$\frac{dT_\ell}{dt} = \frac{3}{r_\ell c_{p\ell}} \left| \frac{h}{\rho_\ell} (T_g - T_\ell) - \frac{L\ Sh\ D_c}{2\ r_\ell\ \rho_\ell} \frac{P_s}{R_V\ T_s} \right| \qquad (15)$$

The last term of the equation is equal to zero during the sensible heating period. The Nusselt number is obtained from the

following correlations[50, 51] multiplied by a correction factor $\beta = z/e^{z}-1$ which considers the effect of mass transfer[49] :

$$Nu = 0.54\ Re^{\frac{1}{2}} \qquad 100 < Re < 100000$$
$$Nu = 2 + 0.6\ Re^{\frac{1}{2}}\ P_r^{\frac{1}{3}} ; \quad 100 < Re \tag{16}$$

where,

$$z = -(c_{pv}\frac{dm}{dT}) / dKNu$$

The duration of the sensible heating period can be determined from the following relation ;

$$t_s = \frac{1}{3} r_{\ell o} \rho_\ell c_{p\ell} \int_{T_o}^{T_s} \frac{d T_\ell}{h(T_a - T_\ell)} \tag{17}$$

substituting for the rate of change of droplet radius from equation (13), the equation of motion (8) can be written in the following form.

a - For the sensible heating period :

$$r_\ell \ddot{x} = \frac{-8.6}{Re^{0.84}} (\rho_a/\rho_\ell)\ A^{\frac{1}{2}}\ B \tag{18}$$
$$r_\ell \ddot{y} = \frac{-8.6}{Re^{0.84}} (\rho_a/\rho_\ell)\ A^{\frac{1}{2}}\ C$$

b - For the evaporation period :

$$r_\ell \ddot{x} = 3\dot{x} \frac{Sh\ D}{2r_\ell \rho_\ell} c \frac{p_s}{R_v T_s} - \frac{8.6}{Re^{0.84}} \frac{\rho_a}{\rho_\ell} A^{\frac{1}{2}}\ B$$
$$r_\ell \ddot{y} = 3\dot{y} \frac{Sh\ D}{2r_\ell \rho_\ell} c \frac{p_s}{R_v T_s} - \frac{8.6}{Re^{0.84}} \frac{\rho_a}{\rho_\ell} A^{\frac{1}{2}} C \tag{19}$$

where :

$$A = B^2 + C^2$$
$$B = (\dot{x} - u \frac{r_p - y}{K} + v \frac{x}{k'})$$
$$C = (\dot{y} - u \frac{x}{k} - v(r_p - y)/K')$$

$$K' = x^2 + (r_p - y)^2$$

Equations (15,18 & 19) are used to determine the droplet positions and temperatures along the trajectory.

iii- Source Term

When the fuel is injected into the combustion chamber, a liquid jet is formed and breaks up into fine droplets after a certain period. The break up length depends on various factors which will be discussed below.

In this model, the spray which is injected into a combustion chamber from an injection nozzle is divided into five introudction locations. The injection rate diagram shown in Fig. (2) was correlated for various factors and an empirical relation is given in the following form[52]

$$Q^* = 0.9\ \Phi^* + 1.3\ \Phi^{*2} - 1.2\ \Phi^{*3} \qquad (20)$$

where,

$Q^* = Q_f/Q$, normalized fuel quantity=cumulative fuel quantity/quantity of fuel per cycle.

$\Phi^* = \Phi/\Phi_{max}$ normalized injection crank angle=injection angle calculated from start of injection/injection period.

The injection period is discretised into a number of equal intervals equal to 1^ocrank angle. The quantity of fuel injected during this period is calculated from a detailed atomization model. Dividing the total number of droplets equally on the five introduction locations and using the droplet size distribution it is possible to identify the number of droplets for each size. In the absence of a detailed model for the droplet velocity it is possible to assume the same distribution for the velocity taking into consideration the variation of the exit velocity due to the variation of the fuel and combustion chamber pressures as shown in Fig.(3). Thus, every droplet is assigned different initial conditions of location, size and velocity. The droplet size range is covered with several sizes of increment 10 μm covering the

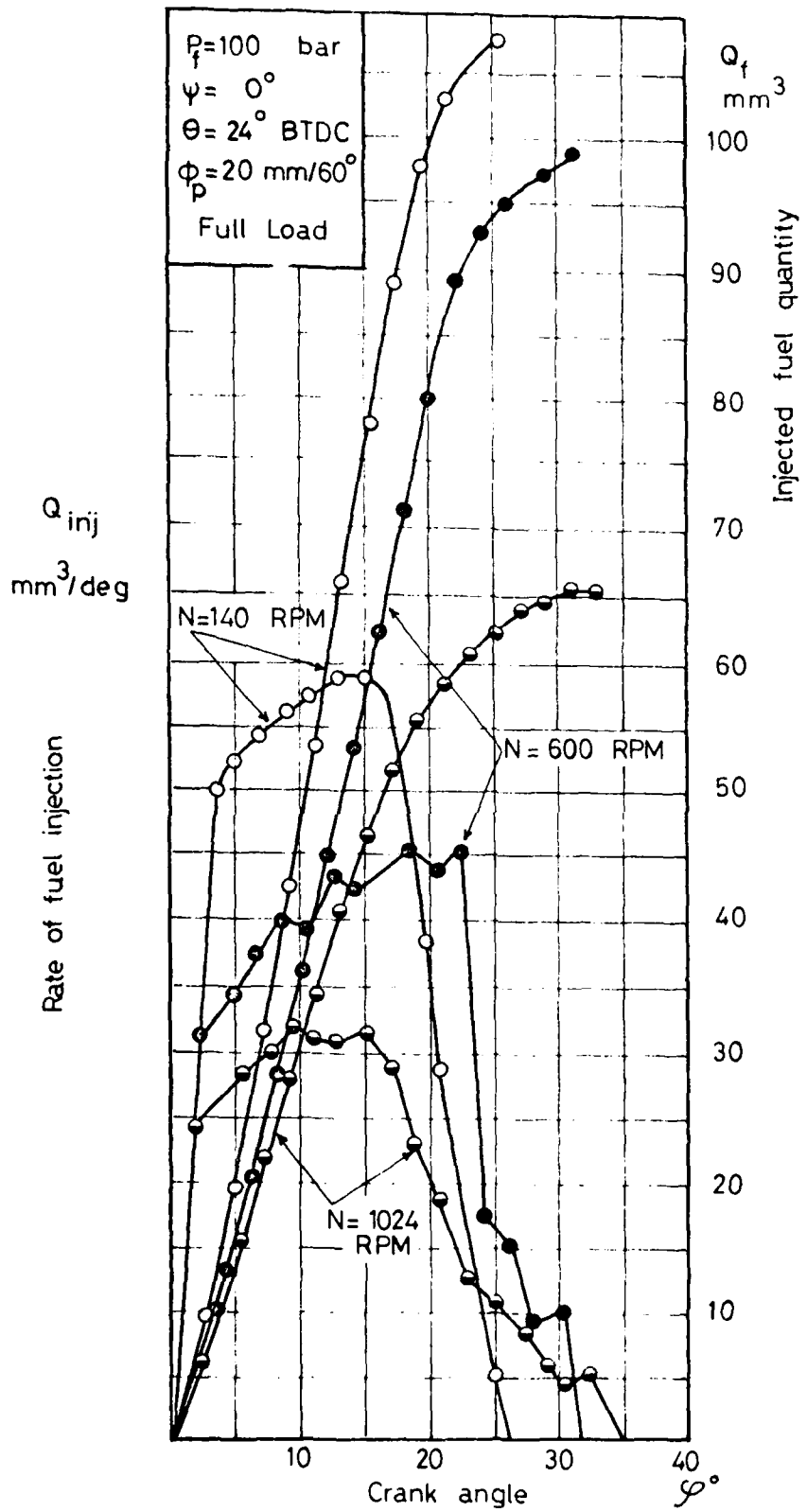

Fig(2) The fuel delivery law and injection law at various engine speeds

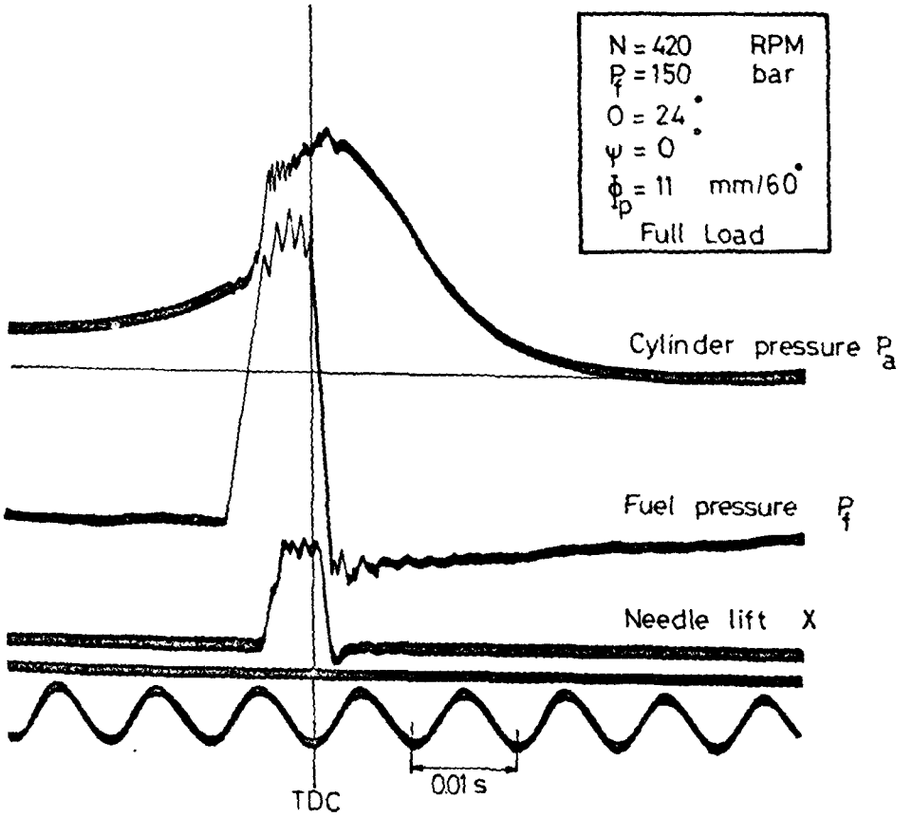

Fig (3) The courses of swirl chamber gas pressure , fuel pressure , needle lift and location of TDC .

range till the maximum droplet diameter according to the predefined conditions.

The flow field of combustion chamber is subdivided into grids as shown in Fig.(4) and each grid is treated as a control volume. The net efflux rate of droplet mass from a computational grid which is the source term in the continuity equation is obtained by assumming overall trajectories traversing that grid and is given by :

$$(\Delta \dot{m}_{\ell}) = n_r (m_{\ell out} - m_{\ell in}) \qquad (21)$$

where,

$$m_{\ell_r} = \sum^{i} n_r (n_i) \frac{\pi}{6} \rho_{\ell} D_i^3$$

At any instant of time, t, the ϕ field of the variables is assumed and the predictions for a time increment Δt are then obtained by solving the gas flow equations, by a marching integration algorithm. In this way the solution is marched forward in time until the desired period has been covered. More details on the solution procedure can be found in Ref[53]. Once the solution of the gas flow equations are solved at any time then the fuel concentration can be calculated to determine the spray contours as follows :

The mass of air in the grid at this moment is given by , Fig. (5) :

$$m_{a_r} = r \, d\theta \, dr.t \frac{\rho_{\theta,r} + \rho_{\theta+\Delta\theta} \, r}{2} \qquad (22)$$

and

$$\alpha = \frac{m_{ar}}{L_o \, \Delta m_{\ell r}} \qquad (23)$$

Some results of the calculations of the fuel droplet trajectories in swirl and open combustion chambers are given in Figs. (6) and (7) respectively.

It is seen from the suggested model that the characteristics of the mixing process and consequently the combustion process are mainly a function of the droplet size distribution . Therefore, comprehensive work is required to obtain fundamental knowledge for transient characteristics of the droplet size distribution in clear and multifuel .

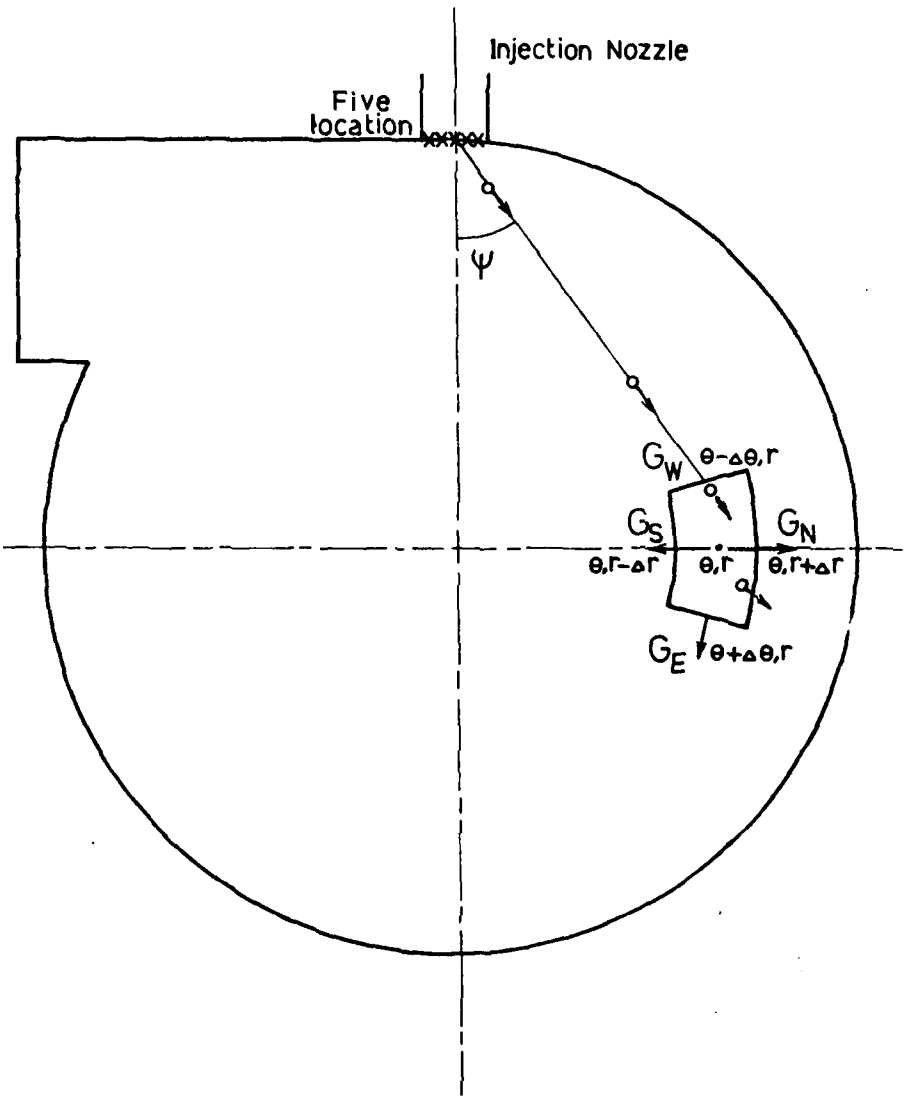

Fig(4) Control volume and introduction location of parcel .

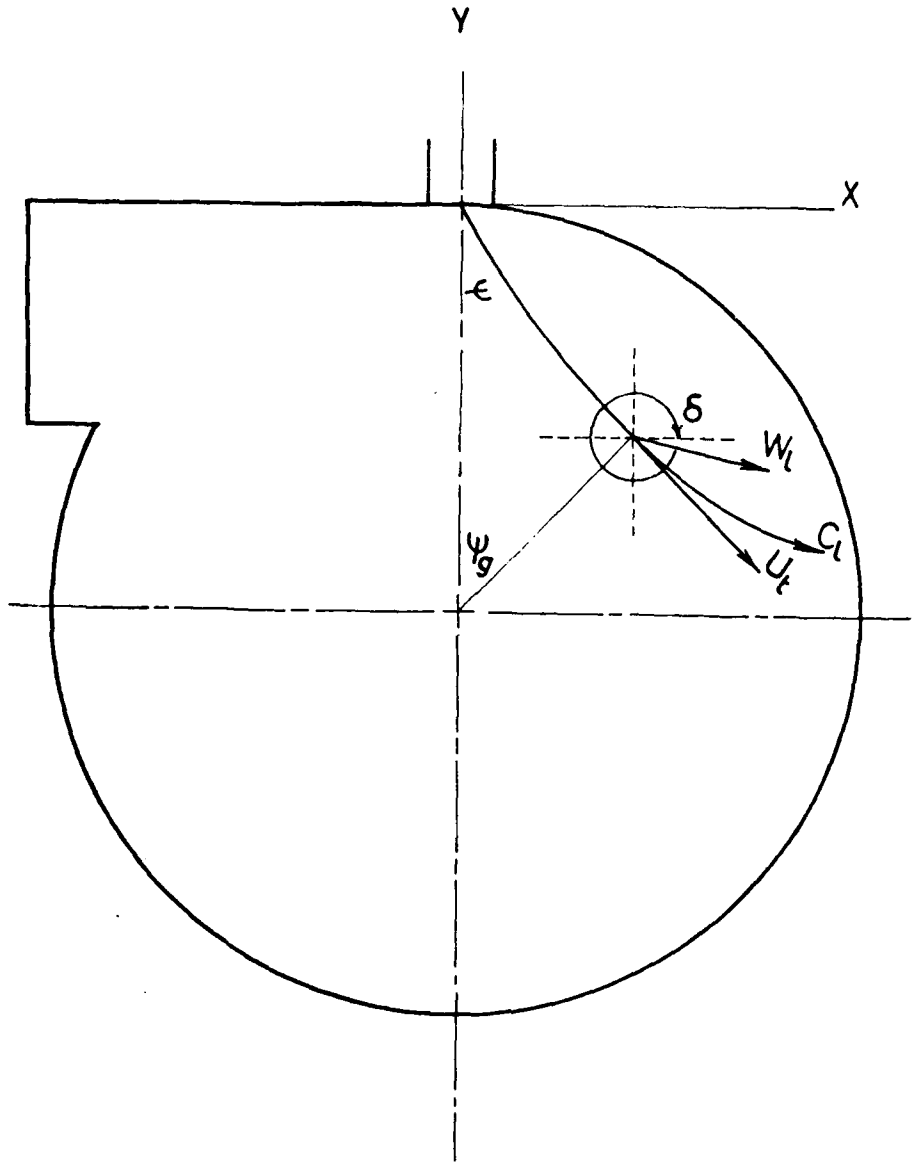

Fig(5) Droplet behaviour inside combustion chambers

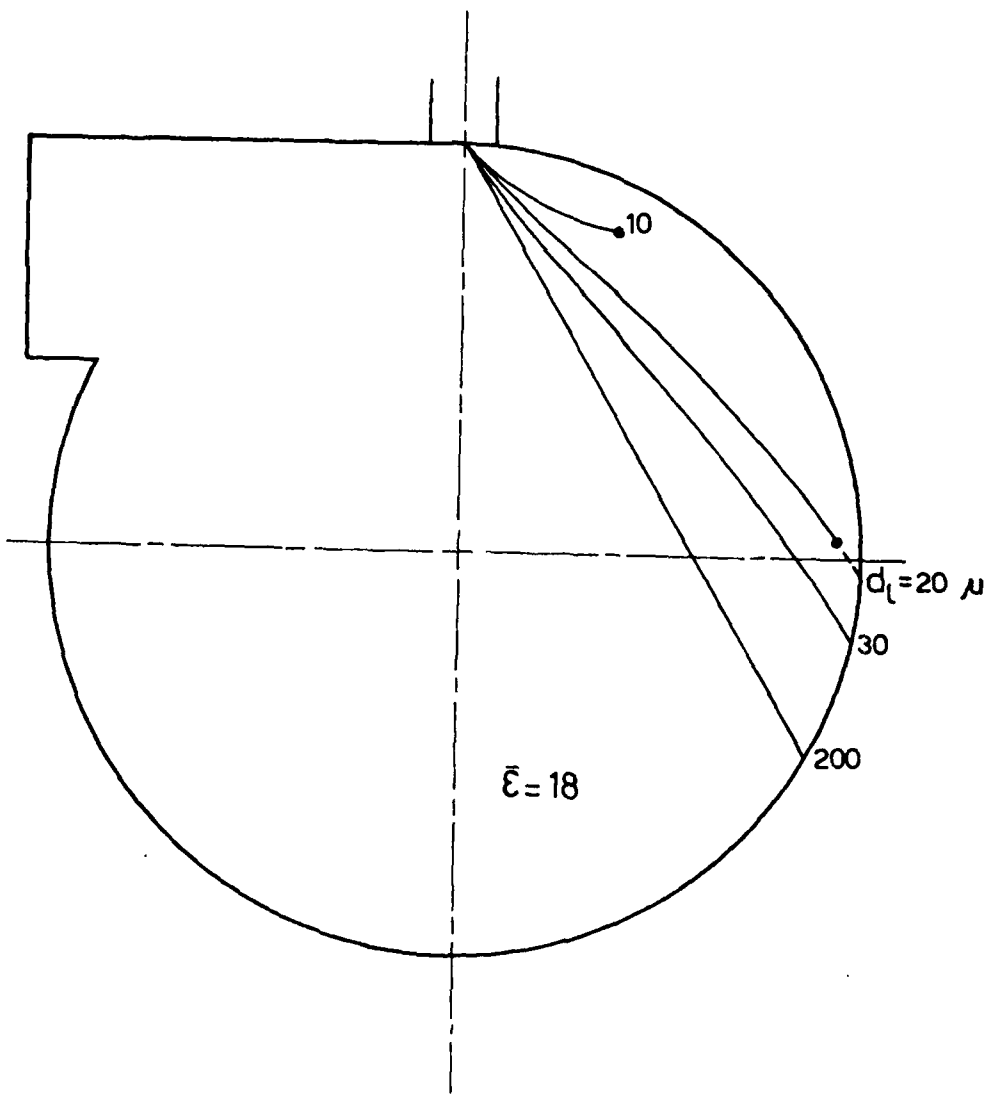

Fig(6) Trajectory of droplets inside a swirl chamber at injection pressure 110 bar, engine speed 2000 rpm , injection angle 60 degree and crank-angle 30 degree .

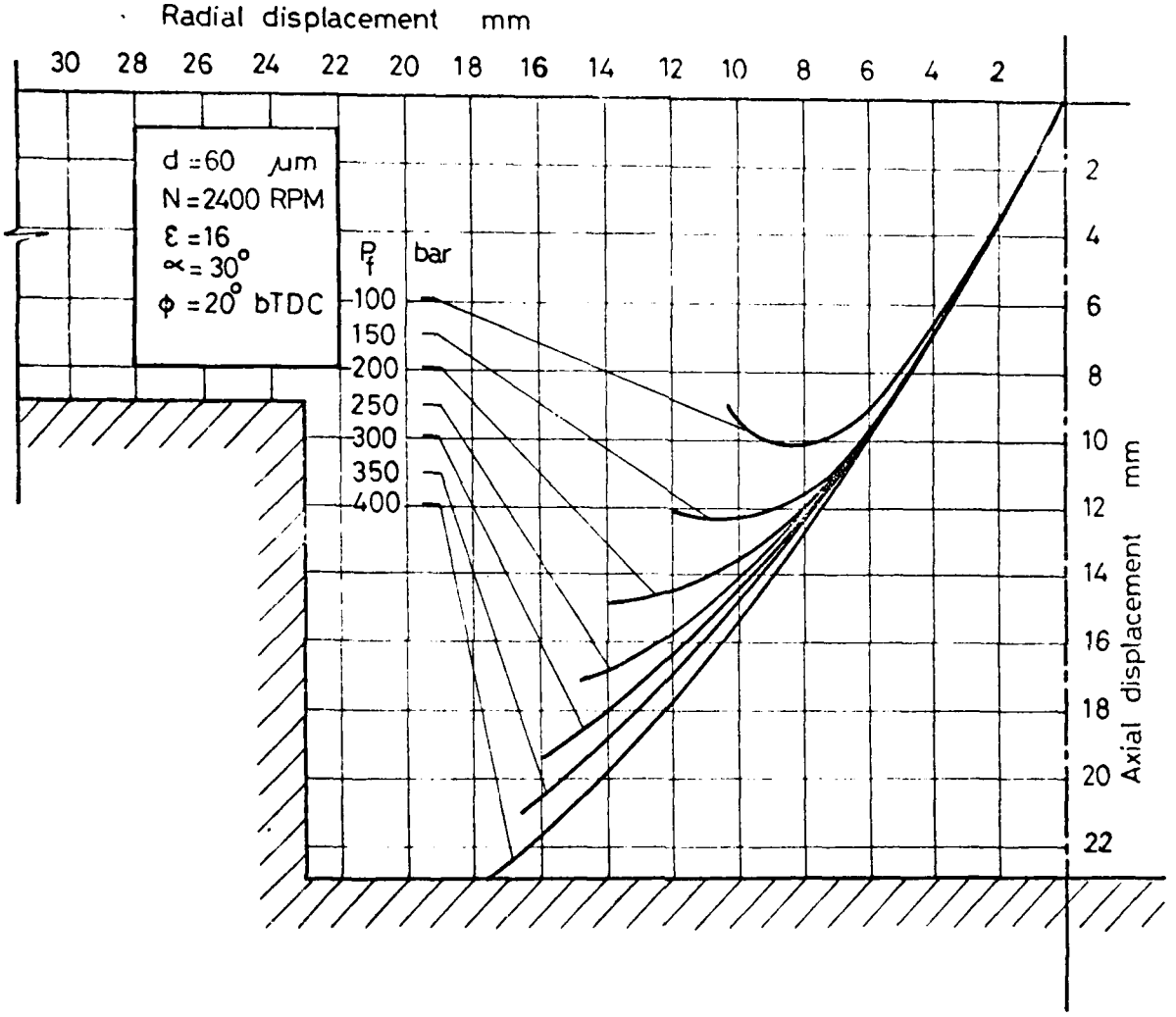

Fig(7) Trajectory of a droplet inside the piston bowl at various injection pressures .

CHAPTER 6

ATOMIZATION OF MULTIFUEL

6.1 MECHANISM OF ATOMIZATION

The efficiency of combustion systems which use liquid fuels depends on the process of liquid atomization as an essential intermediate stage between injection and combustion. A spray of fuel is obtained inside the combustion chamber either by an atomizer or an injector. The injectors introduce the fuel spray into the combustion chamber with high velocity creating suffient turbulence inside the fuel spray jet to satisfy better dispersion of fuel droplets. The atomizers disintegrate the fuel either internally by spreading the fuel on the surface of swirl chamber or by internal blast fluid or externally by external blast fluid and then disperse the resulting droplets in the combustion chamber space. Experimental investigation showed that when a fuel is injected through a smooth circular orifice into a chamber of quiescent gas, four main regimes of jet disintegration are observed:

i- Atomization of fuel with small exit velocity without aerodynamic resistance force, Fig.(8,a),

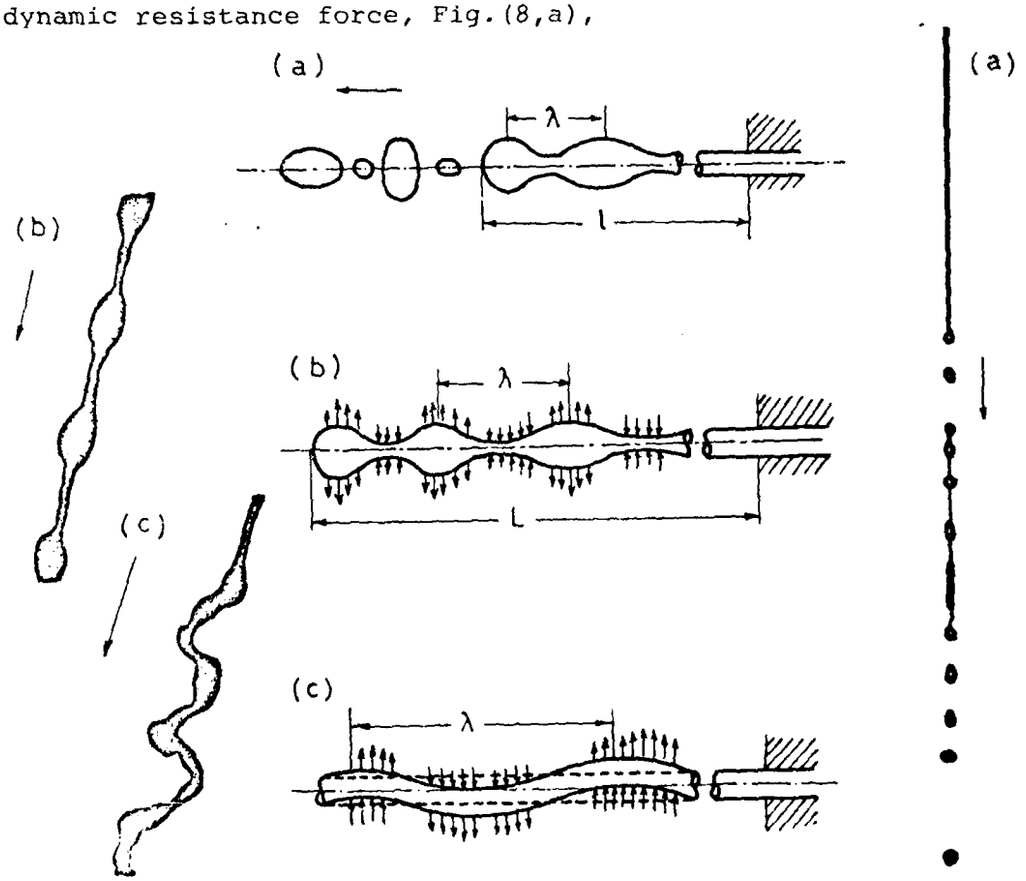

Fig. (8) Characteristics of the first three regimes of atomization .

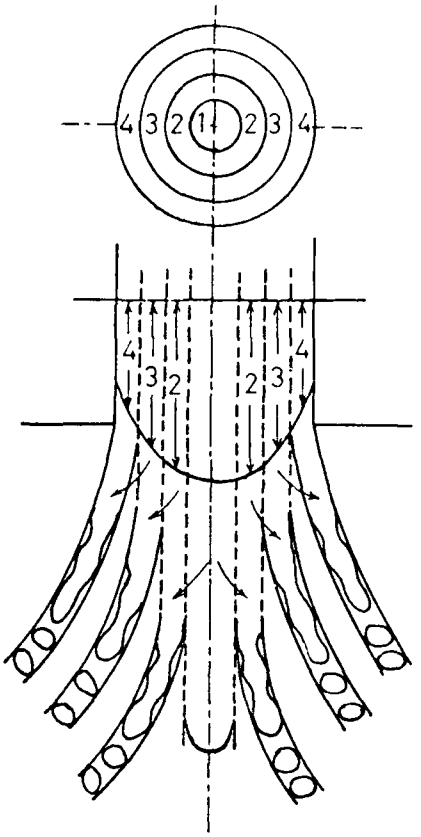

Fig(9) Air entrainment and division of fuel spray into concentric conical sprays .

ii- Atomization of fuel with higher exit velocity and aerodynamic resistance force, Fig.(8,b),

iii- Atomization of fuel with still higher exit velocity and initial turbulence resulting from resisting air force, Fig. (8,c).

iv- Atomization regime.

These four regimes of breakup are encountered as the injection velocity is progressively increased. The mechanisms controlling the breakup of liquid jets in the first three of these regimes are reasonably well understood. However, the breakup mechanism for the jets in the fourth regime, which is called atomization regime, is currently unknown. Several researchers have proposed mechanisms ascribing the breakup process to aerodynamic effects, liquid turbulence, cavitation phenomena, velocity profile and fuel pressure oscillations.

On the bases of the large number of experiments and theoretical studies carried out on the plain jet injectors which are dealt with in this work, one may consider that the atomization of liquid fuels goes through the following stages :

1- Spreading of fuel jet into a cone with a cone angle depending on the fuel velocity.

2- Entrainment of air and division of fuel spray into concentric conical sprays, as shown in Fig.(9), with various velocities. The central spray has a velocity greater than the outer one. Therefore, radial velocities are created from the central ligament causing the deceleration of the outer ligaments.

3- Occurance of small waves in the liquid surface as a result of internal turbulence.

4- Tearing of the surface into fine ligaments as a result of drag, surface tension and viscous forces.

5- Breaking-up of fine ligaments into droplets due to the above mentioned forces.

6- Further breaking up of these droplets by secondary atomization.

7- Agglomoration of droplets by collision,

The relative importance of these six stages changes according to the type of injector, relative velocity between the air and fuel, fuel properties, air pressure and temperature and air-fuel ratio. The radial velocity creates radial turbulence forming ligaments of a thickness depending upon the magnitude of its wave length.

The theoretical analysis of the jet disintegration is based on Lord Rayleigh's studies[55] who considered the growth of initially small disturbances. He showed that ideally the wavelength which governed the disintegration was that for which the rate of growth was maximum. He found that the required wave length was given by :

$$\lambda = 4.5 \; d_J \tag{24}$$

Thus, if the volume of the spherical droplets is equal to the velocity of the cylindrical ligament of length equal to the wave length and radius equal to the jet radius, the droplet diameter is given by :

$$\frac{1}{6}\pi \; D^3 = \frac{\pi}{4} d^2 \; \lambda$$

or

$$D = 1.89 \; d \tag{25}$$

In practice, Rayleigh's breakup of a plain jet occurs only if the relative velocity is low and the surface tension is adequate. In the more general case, drag forces tend to tear the surface of the turbulent liquid jet into fine ligaments of wave length λ . These ligaments become spheres of diameter D under the action of surface tension. Hence, the drop size predicted by Rayleigh represents the upper limit of possible sizes.

A similar analysis of breakage of a liquid column, which takes both the viscosity and surface tension into account has been made by Weber[56]. The time required for a column of diameter d_j to break up is given by ;

$$t = C \left| \left(\frac{8\rho_\ell}{\sigma_\ell}\right)^{\frac{1}{2}} d_J^{3/2} + 6\mu/\sigma_\ell \, d_J \right| \qquad (26)$$

and the optimum length to diameter ratio β for breakage is also given by :

$$\beta = \sqrt{2}\,\pi \left| 1 + \frac{2\,\mu_\ell^2}{\sigma_\ell\,\rho_\ell d_J} \right|^{\frac{1}{2}} \qquad (27)$$

However, the fuel atomization is affected by the spray turbulence in the fuel nozzle, which depends mainly on the construction of the fuel nozzle and Reynolds number. The effect of kinematic viscosity on the solid spray length for various injection pressures was determined experimentally[57] and the results are given in Fig.(10). The solid length can also be calculated using the following formula :

$$\ell_s = 372\, d\, M^{0.308}\, We_{max}^{-0.71}\, \rho^{-1.2}.$$

The relation of length-diameter ratio of the diesel engine nozzles must be less than 3/4 and therefore the Reynolds number may not characterize the spray motion completely.

York et al[58] had developed an approach to study the process of atomization in which they indicated that the ligaments are subjected to internal disturbances which finally produce Rayleigh's break-up of the unstable film when :

$$We = \frac{\rho_a |\vec{C}_\ell - \vec{V}_a|^2 d_J}{2\,\sigma_\ell} \quad \frac{\rho a}{\rho_\ell} \qquad (28)$$

Droplets may thereafter breakup during their motion inside the combustion chamber, which is defined by secondary atomization, as a result of drag, inertia, viscous and surface tension forces. The aerodynamic forces imposed on the droplets

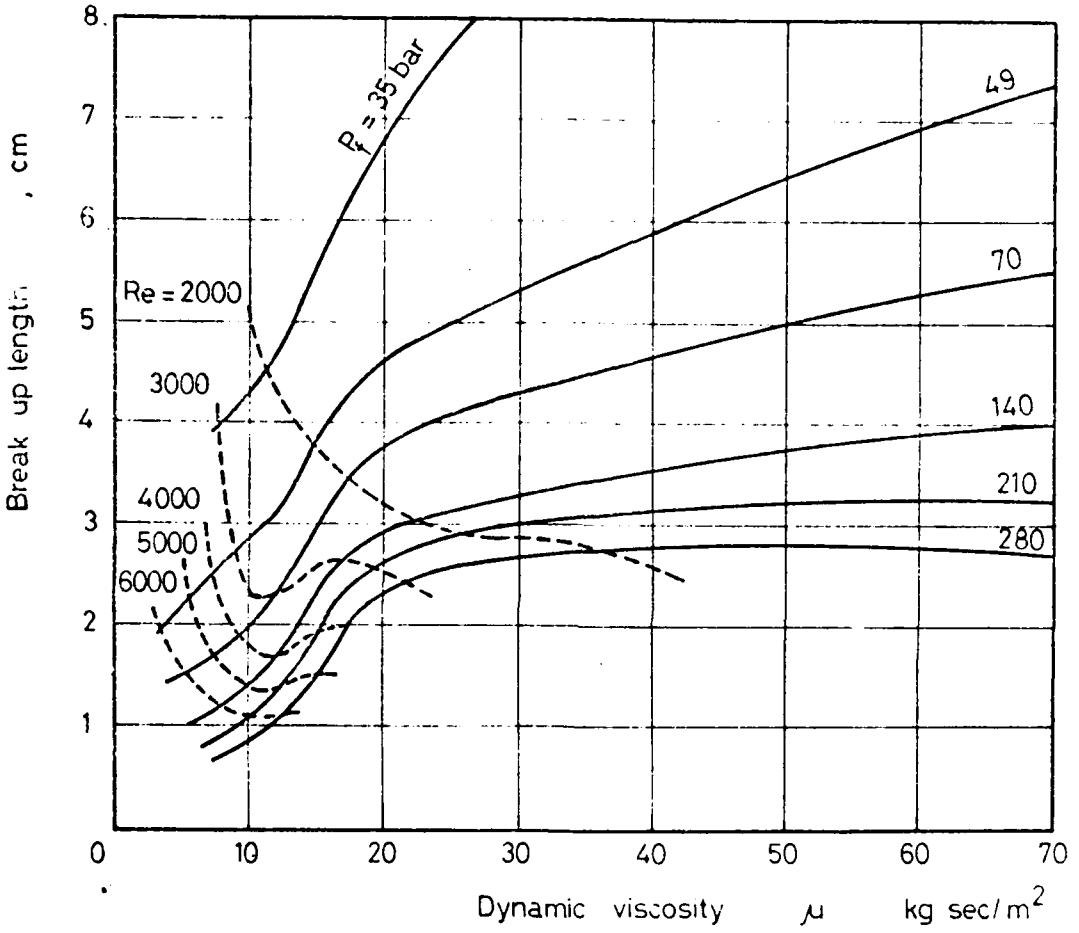

Fig(10) Effect of kinematic viscosity of fuel on the break up length for various injection pressures .

during its motion may cause deformation of their shape and eventually overcoming the droplet cohesive forces and may in some cases break them into smaller fragments. Rabine et al[59] showed that droplet break up is associated with a critical value of the Weber number after which secondary atomization may be expected. This occurs when :

$$We = \frac{\rho_a (v - v_a)^2 D}{2 \sigma} > Re^{\frac{1}{2}} \qquad (29)$$

Critical Weber number after which secondary atomization may be expected is given by Borstein et al[60] as equal to 100 and by Lambrisis et al[61] as equal to 65.

Finally, the atomization of fuel injected in diesel engine combustors depends on the external aerodynamic resisting force, surface tension force, internal binding force which depends on its viscosity, and the internal turbulent force resulting from the initial turbulence created during the fuel motion. The external aerodynamic resisting force increases with the increase of the injected fuel velocity, relative velocity, medium density and the surface area of the spray. The complete theoretical calculation of the droplet size distribution is not developed till now and recourse is taken to experiments for its determination.

6.2 Experimental Set Up

Several experimental methods have been used for measurement of the droplet size. These methods are photographic thermal, electric, optical methods based on scattering or absorption of light as well as physico-chemical technique and slide sampling technique. A review of the published techniques for drop size measurement has been carried out by Azzopardi[62].

McCreath and Beer[63] pointed out that for sprays from liquid fuel atomizers in furnaces, drop size frequency and spatial distribution control fundamental flame characteristics such as radiant heat transfer, flame length, flame stabilisation, smoke

formation, carbon carry over and formation of oxides of nitrogen. Droplet size distribution is required also for the calculation of the spray concentration. The photographic method is most suitable for the study of a single droplet, because of its small depth of focus, or sprays of small cone angles. Both the molten-wax method and the frozen spray method are not suitable for measuring the droplet size distribution at high air temperatures and pressures, since the progressive development of the fuel spray inside the combustion is not reflected in the results.

Amongst the other techniques it seems that the optical ones show most promise. If an overall distribution is required then the diffraction technique, particularly as described by Swithenbank et al[64] appears to possess admirable sensitivity to changes in both the peak value and the width of the distribution. The Laser-Doppler approach using visibility[65,66] is still limited to very small particles and work is needed to extend its range. Since the drop size frequency is required to be determined at high pressures and temperatures simulating the combustion chamber environment, the slide sampling method is the most suitable until the development of other techniques reaches a stage where they could be applied freely. In this method a slide with thinly coated soot deposited from a candle flame is introduced into the fuel spray for a short time. Arrangements are provided to prevent interfering of the spray, to satisfy suitable moving velocity of the slide preventing the soot layer distortion, and to adopt suitable layer thickness minimizing the flattening coefficient of Crater size. The impression left by the impinging droplets in the soot layer are photographed under microscope.

The experimental set up is shown in Fig.(11). It consists of a pressure chamber of diameter 150 mm and height 180 mm. The pintle type injector, Bosch DNO SD 211 with a nozzle diameter 1 mm and pin diameter 0.55 mm, is fitted on the top of the chamber, Fig.(12). The fuel is pumped to the injector by a fuel pump driven by an

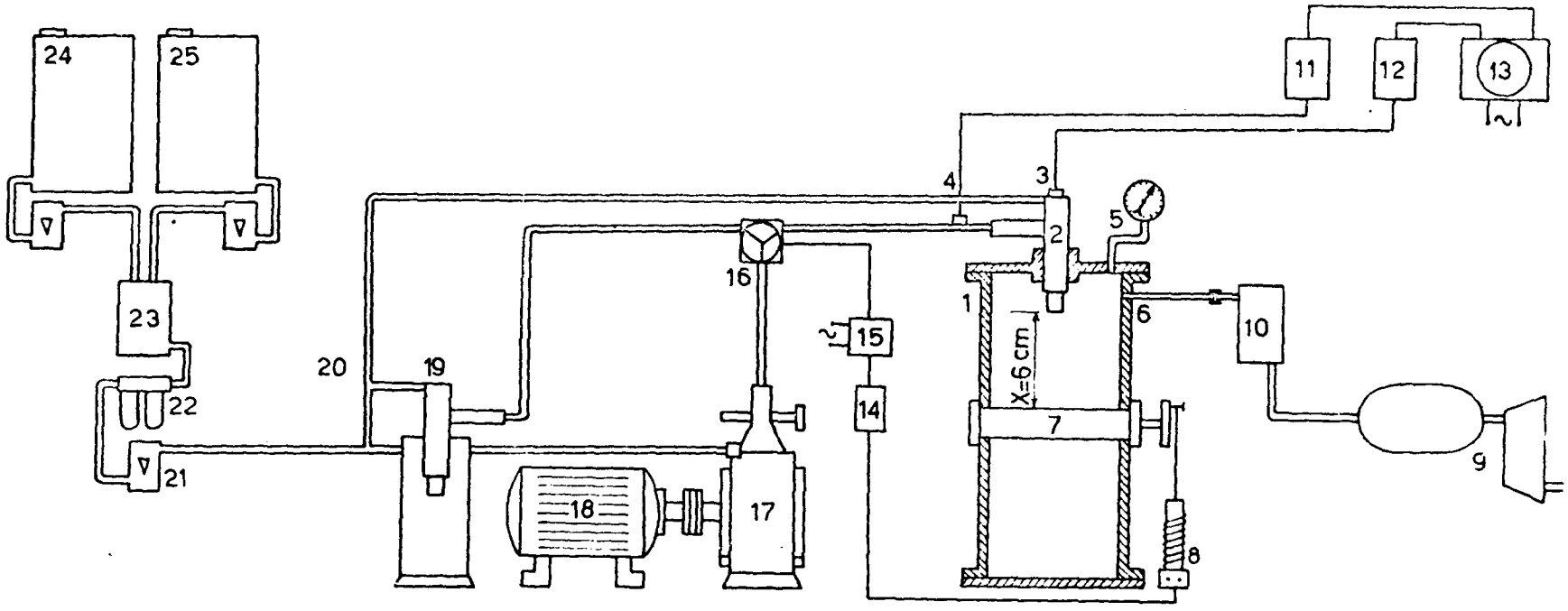

1	Main cylinder	9	Compressor	17	Injection pump
2	Main injector	10	Heater	18	Motor
3	Inductive transducer	11	Pre-amplifier	19	Dummy injector
4	Piezo electric transducer	12	Balance bridge	20	Residual fuel
5	Pressure gauge	13	Oscillograph	21	Flowmeter
6	Air inlet	14	Time relay	22	Fine filter
7	Slide sampling apparatus	15	Switch	23	Mixing tank
8	Solenoid	16	Electromagnetic three way valve	24-25	Fuel tanks

Fig (11) Schematic drawing of the experimental set up .

electrical motor using a gear chain system with a reduction ratio 1:2. The rack of the fuel pump is adjusted by a [illegible] moving system to determine accurately the active stroke of the plunger and consequently the quantity of delivered fuel. The fuel is fed to the pump from a reservoir through a filter and a flow meter to determine the rate of flow of fuel. A dummy injector is used for intermittent operation of the working injector by means of an electromagentic three way valve. The fuel pressure at the inlet of the injector is picked by a piezoelectric transducer and the needle lift by an inductive pick up. Both signals together with a signal indicating the moving moment of the slide sampling apparatus are displayed on an oscillograph. The pressure chamber, which is fitted with a pressure manometer, is fed with compressed air from a high pressure reservoir through a heater and a pressure regulating valve. The flowing air is heated by a methane torch capable of heating the incoming air up to about 500 ^{o}C. The air temperature is measured by a Cu-Co thermocouple connected to a potentiometer.

A special sampling apparatus mounted in the pressure chamber at a distance 60 mm from the injector is used for measuring the droplet size, Fig.(13). It consists of a cylindrical tube of a 30 mm outer diameter prepared with a rim slot of 2.5 mm width. A cylindrical core of 23 mm outer diameter having a rim slot is mounted inside the cylindrical tube. The glass slide is inserted inside it. A lever ratchet tension spring system is connected to the core axis to rotate it.

Fuel sprays injected from the injector and passing from the slots of the fixed cylindrical tube are collected on the glass slide, when the slot of the cylindrical core faces that of the cylindrical tube during its rotation as shown in Fig.(13.b). The rotation of the cylindrical core is satisfied at a specified moment after the injection by an electrical system. Connecting this circuit by the main switch, the electrical current passes to both electromagnetic three way valve and a time relay. The

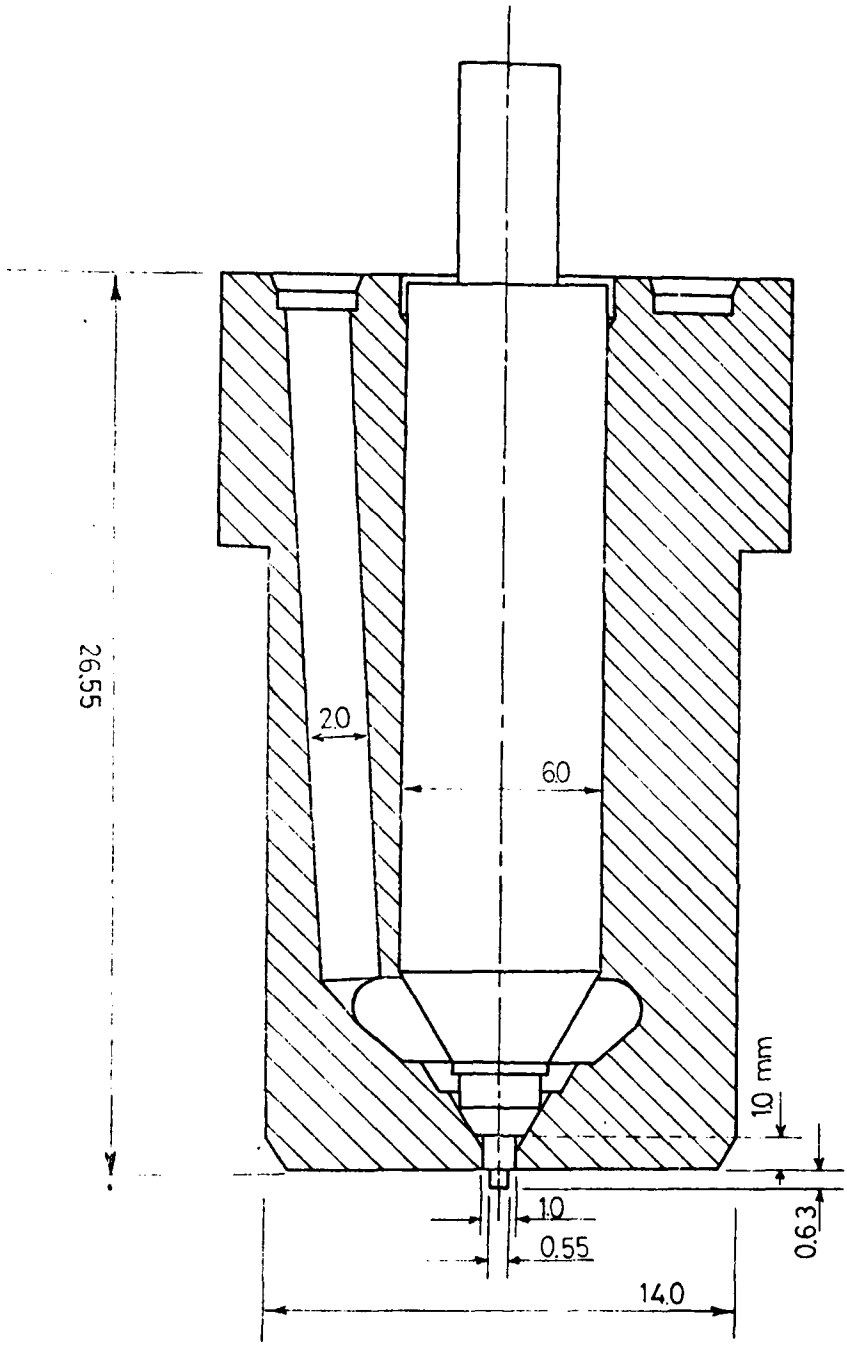

Fig(12) Pintle nozzle - Type DNO SD 211 Bosch
DIM. IN MM

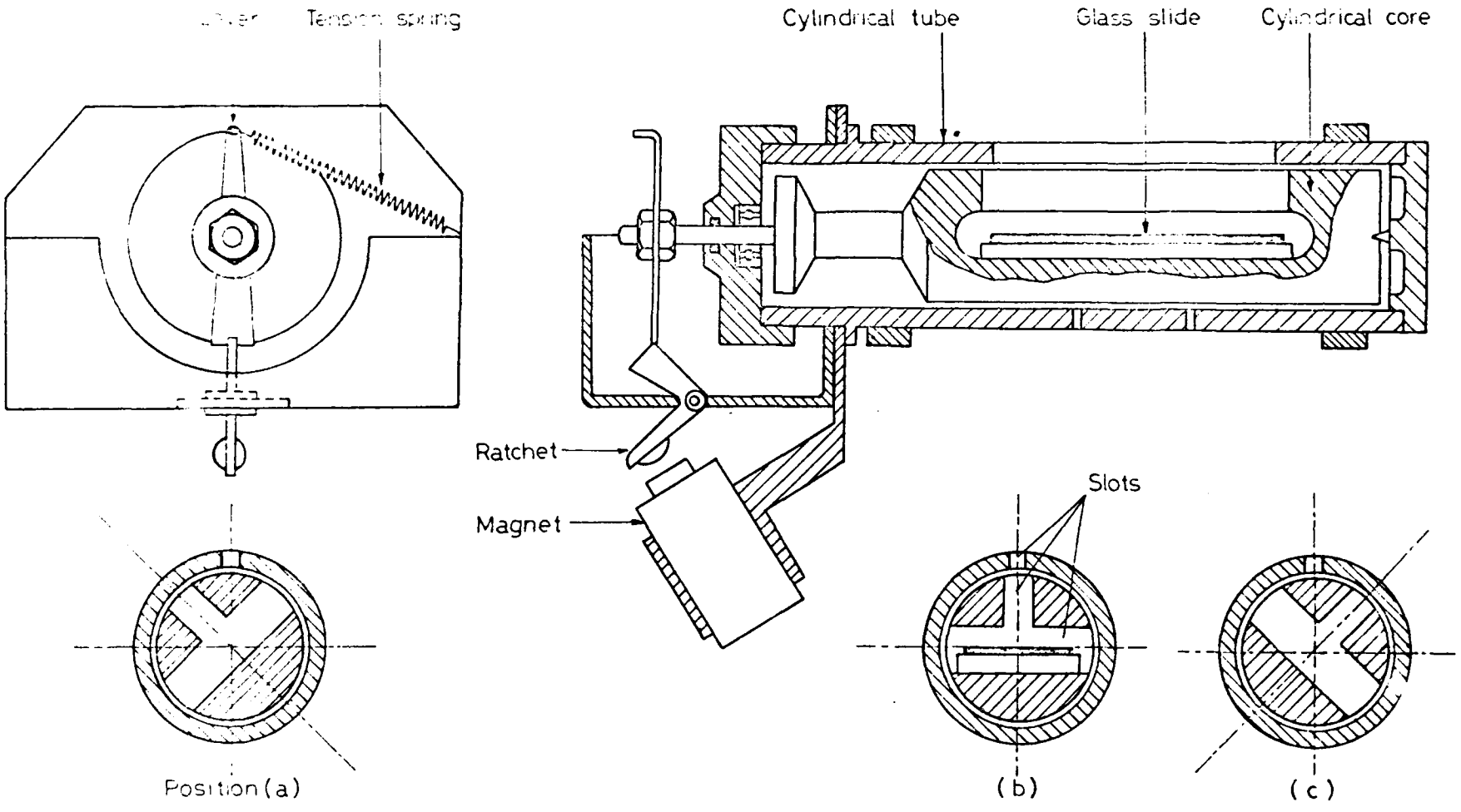

Fig(13) Slide sampling apparatus .

magnetic valve changes the fuel flow from the dummy to the active injector, while the time relay lasts the current of the solenoid valve by 0.5 sec. Such delay period permits the injector to inject six sprays before the introduction of the glass slide in the spray to achieve steady state conditions. A vibrating switch which operates at maximum needle lift position is used to close the solenoid circuit and consequently rotate the cylindrical core only at this position. A uniform soot layer is deposited on the glass slide from a kerosene flame. The soot layer thickness is determined from the relation between the droplet Weber's number and the impression diameter[67] in the order of 1.5:3.5 of maximum droplet diameter. The soot layer thickness is taken equal to 350 μm for diesel fuel and 120 μm for gasolene. The average value of the soot layer thickness is measured by a travelling microscope.

The impinging fuel droplets leave impressions on the soot layer. These impressions are magnified 60 times under an electronic microscope, where representative photographs are taken at different radial distances from the centre of the spray. These photographs are then remagnified ten times on a screen by a projector to satisfy total magnification of 600. The number and diameter of these impressions after correction from Fig. (14) are determined with a scale graduated in 0.5 mm and classified into groups with size intervals 10 μm. Each group of impressions represents a part of the fuel spray at a specified radial distance. The total summation of these groups gives the total droplet size distribution. The accuracy of the measurement of impression is about $\pm$ 3 μm. Samples of these droplet photographs are shown in Fig.(15).

The same technique is used to measure the droplet size distribution inside an operating motored diesel engine. Fuel spray injected from the nozzle is collected on a slide sampling apparatus, which is fitted in the space between the two discs that are fixed over the piston crown Fig.(16). The glass slide, which has

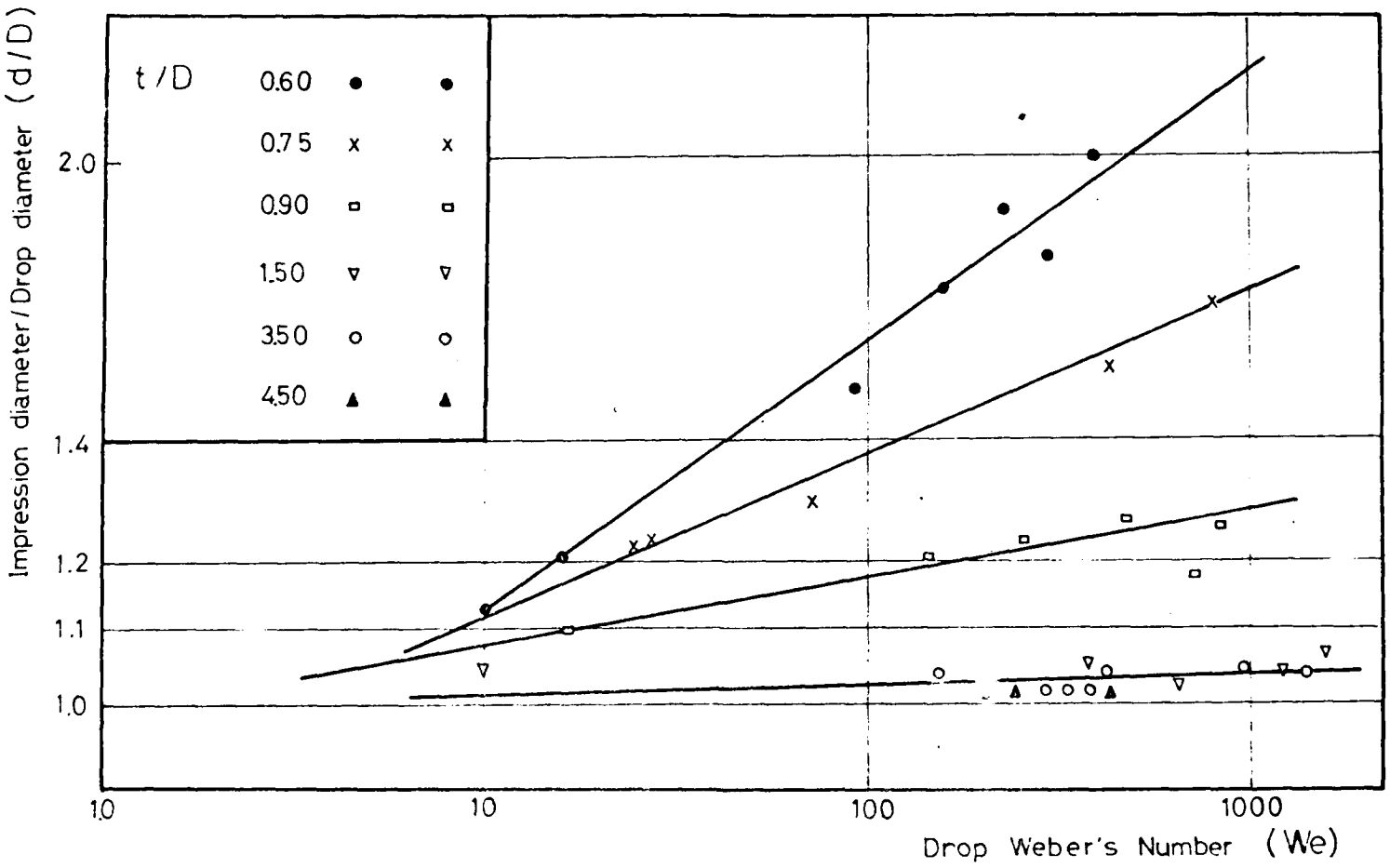

Fig(14) Effect of soot layer thickness and droplet Weber number on impression diameter .

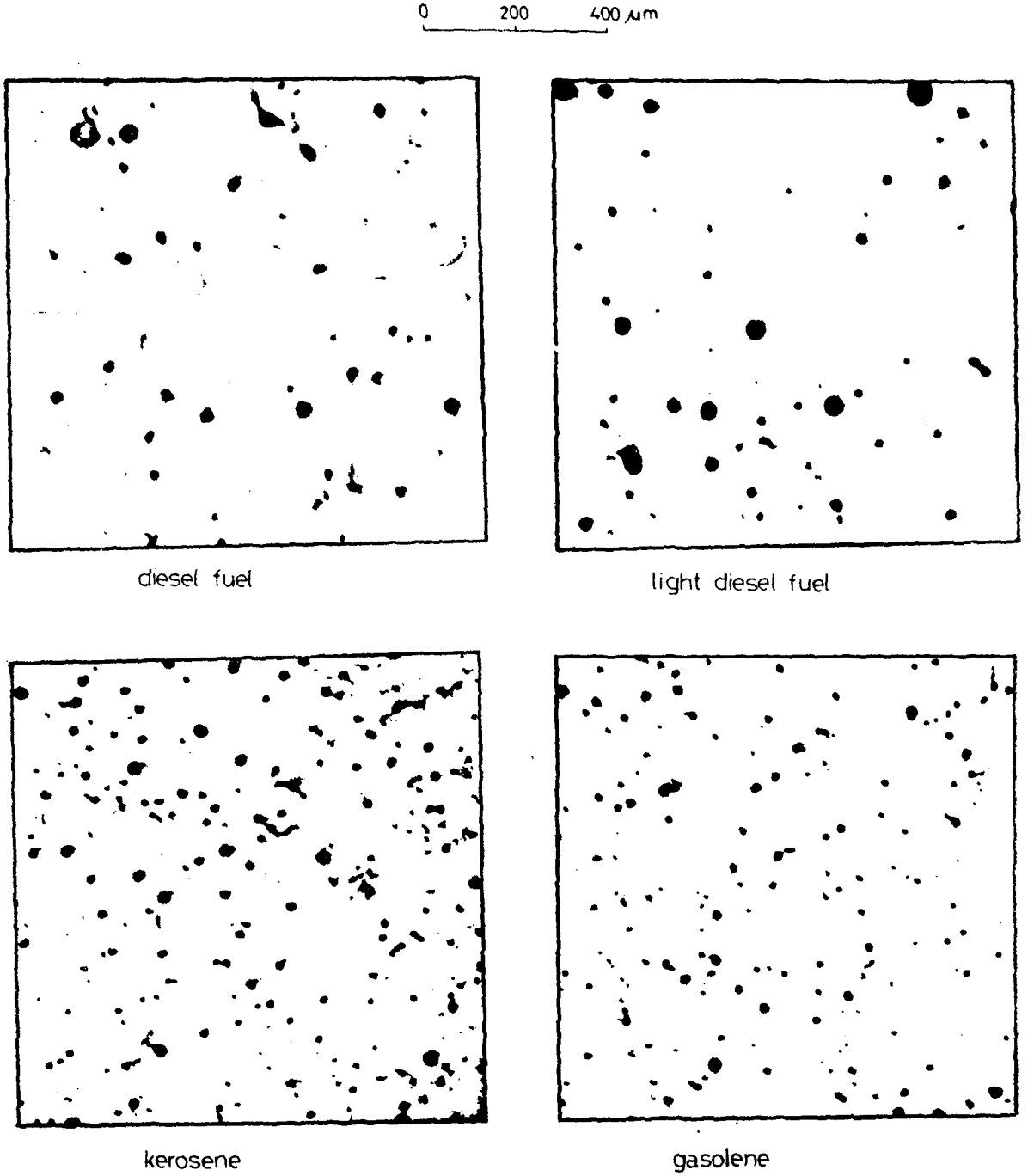

Fig(15) The photographed impressions of clear fuel sprays
P_i = 118 bar , X = 60 mm , N = 700 rpm
ρ_a = 1.2 kg/m , R = 3.0 mm T_a = 293 °K

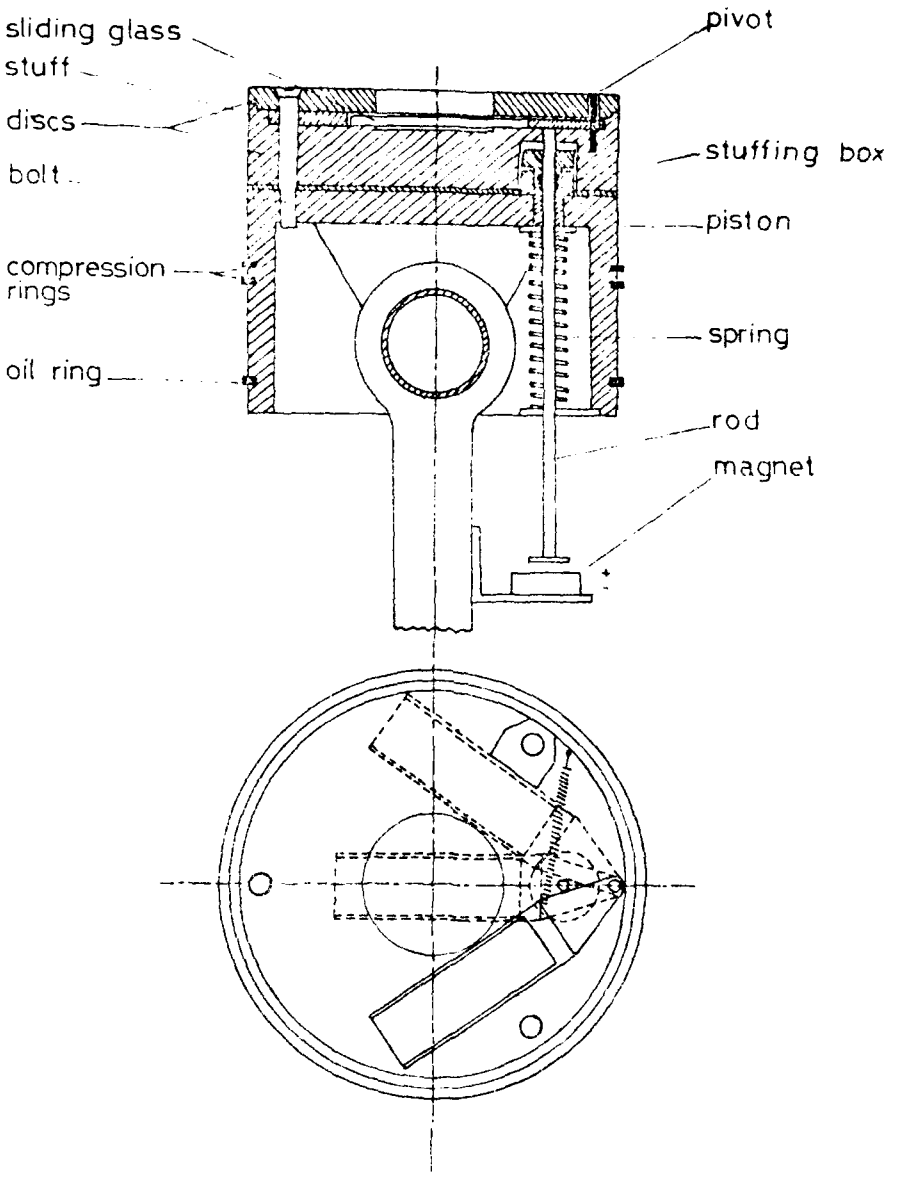

Fig(16) Slide sampling apparatus inside an operating piston .

a dimension of 70x20 mm is allowed to rotate around a pivot fixed in the piston crown under the effect of the tension spring whenever the stopper moves. The stopper is allowed to move under the effect of an attraction force created by a solenoid valve. This valve can be actuated at a difinite controlled angle by a push button which is closed by a cam fixed on the pump shaft. More details of the apparatus and results are given in Ref [68].

6.3 Physical Properties of Multifuel

The main physical properties which affect the atomization process are viscosity, surface tension and density. The viscosity of fuel affects the spray form together with the atomization quality. High viscosity causes a large droplet size, i.e. low and poor atomization, and a high spray jet penetration. Such droplets evaporate with a slow rate forming a hetrogeneous mixture with imperfect combustion. Droplet size depends also on the surface tension of the injected fuel as the surface tension force opposes the distortion of the fuel surface. The fuel density affects spray penetration as the kinetic energy of fuel issuing from a nozzle is one of the main factors determining spray behaviour.

Studying the behaviour of the previously mentioned properties, fuel mixtures of diesel fuel and another fuel as light diesel fuel, kerosene or gasolene are tested. Diesel fuel is used as a basic fuel and the other fuel is blended with it in intervals of 10% by volume. In addition, fuel preheating up to 70 ^{o}C is applied to all these tested fuels as their properties are known to vary considerably with temperature.

Kinematic viscosity, surface tension and density of the tested fuels vary from 8.553×10^{-6} m^2/S, 27.5×10^{-3} N/m and 847 Kg/m^3 respectively for diesel fuel to 8.08×10^{-7} m^2/S, 20.4×10^{-3} N/m and 732 Kg/m^3 for gasolene at 20 ^{o}C as shown in Figs. (17) (18) and (19). It is clear from these figures that the viscosity of

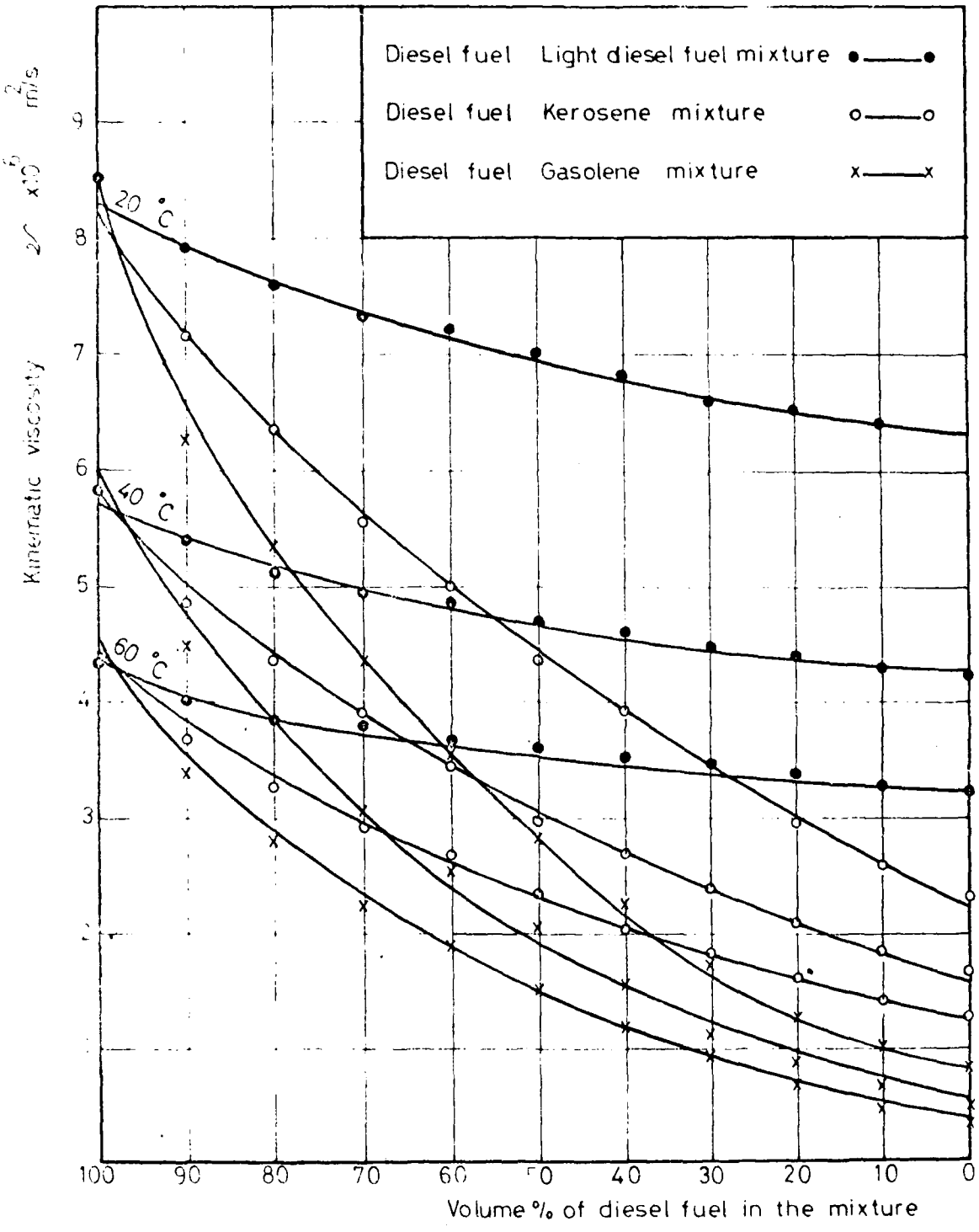

Fig(17) Nature of kinematic viscosity variation for various blend mixtures .

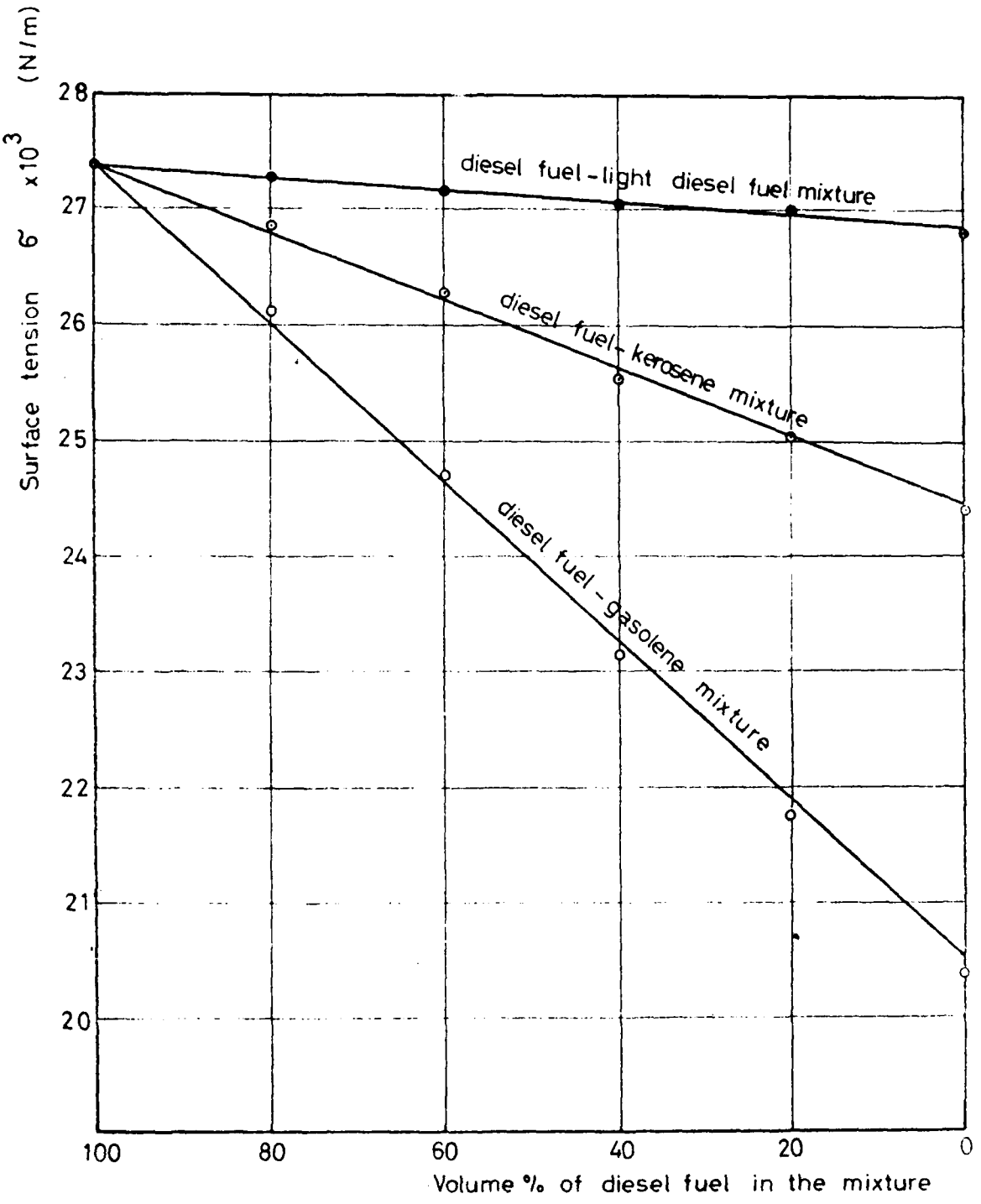

Fig(18) Nature of surface tension variation for various blend mixtures .

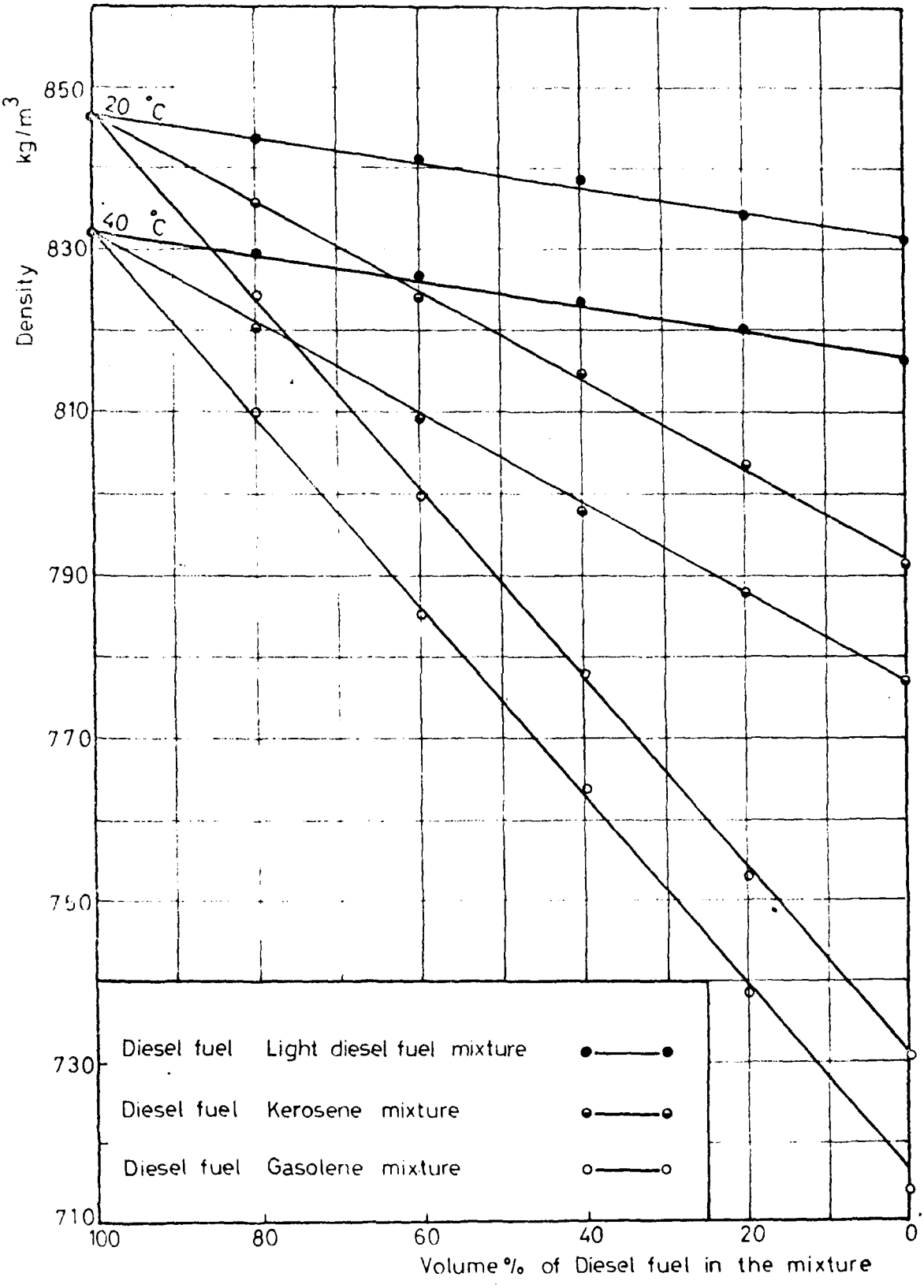

Fig(19) Nature of density variation for various blend mixtures .

diesel fuel is about 11 times greater than that of gasolene while the surface tension and density are about 1.4 and 1.2 times greater than that of gasolene. The kinematic viscosity of diesel fuel is sharply reduced when blended with gasolene as compared with blending with kerosene or light diesel fuel. Similar behaviour can be deduced for both surface tension and density. It is found also that the physical properties of the fuel are quite sensitive to temperature. The variation of kinematic viscosity and density with temperature of the tested fuel is shown in Figs.(20&21). It is clear from the results that the kinematic viscosity of heavy grade fuels such as diesel fuel and light diesel fuel decreases sharply with the temperature increase. A lower decreasing rate is noticed in light fuels such as gasolene and kerosene. Correlations of the experimental data give the following empirical relations for the kinematic viscosity, surface tension and density :

$$\nu_\ell = A\,(T + 30)^{-b}\, e^{cF}$$

$$\sigma_\ell = (1-9\times10^{-4}T)(a_1F + K_1)10^{-3} \qquad (30)$$

$$\rho_\ell = (1-9\times10^{-4}T)(K_2+a_2F)$$

where the constants are given in table 2.

Table 2: Constants of Equation 30

	diesel fuel-light diesel fuel	diesel fuel-kerosene	diesel fuel-gasolene
A	5.55×10^{-4}	1.66×10^{-4}	6.15×10^{-5}
a_1	0.51	3.0	7.1
a_2	16.0	56.0	17.0
b	1.14	1.09	1.1
c	0.274	1.266	2.33
K_1	27.4	24.9	20.8
K_2	846.0	806.0	745.0

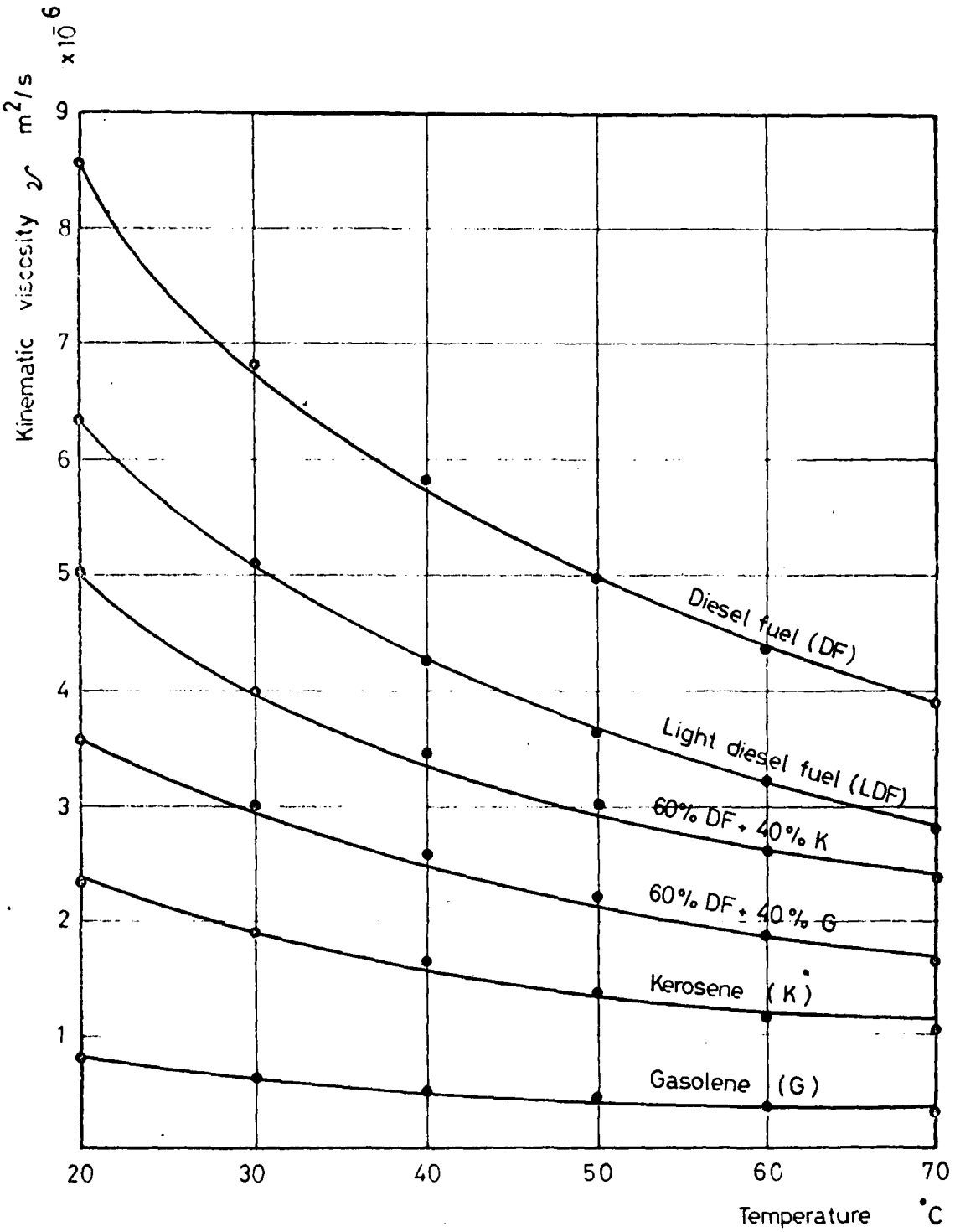

Fig (20) Variation of fuel viscosity with temperature rise for clear and multifuel .

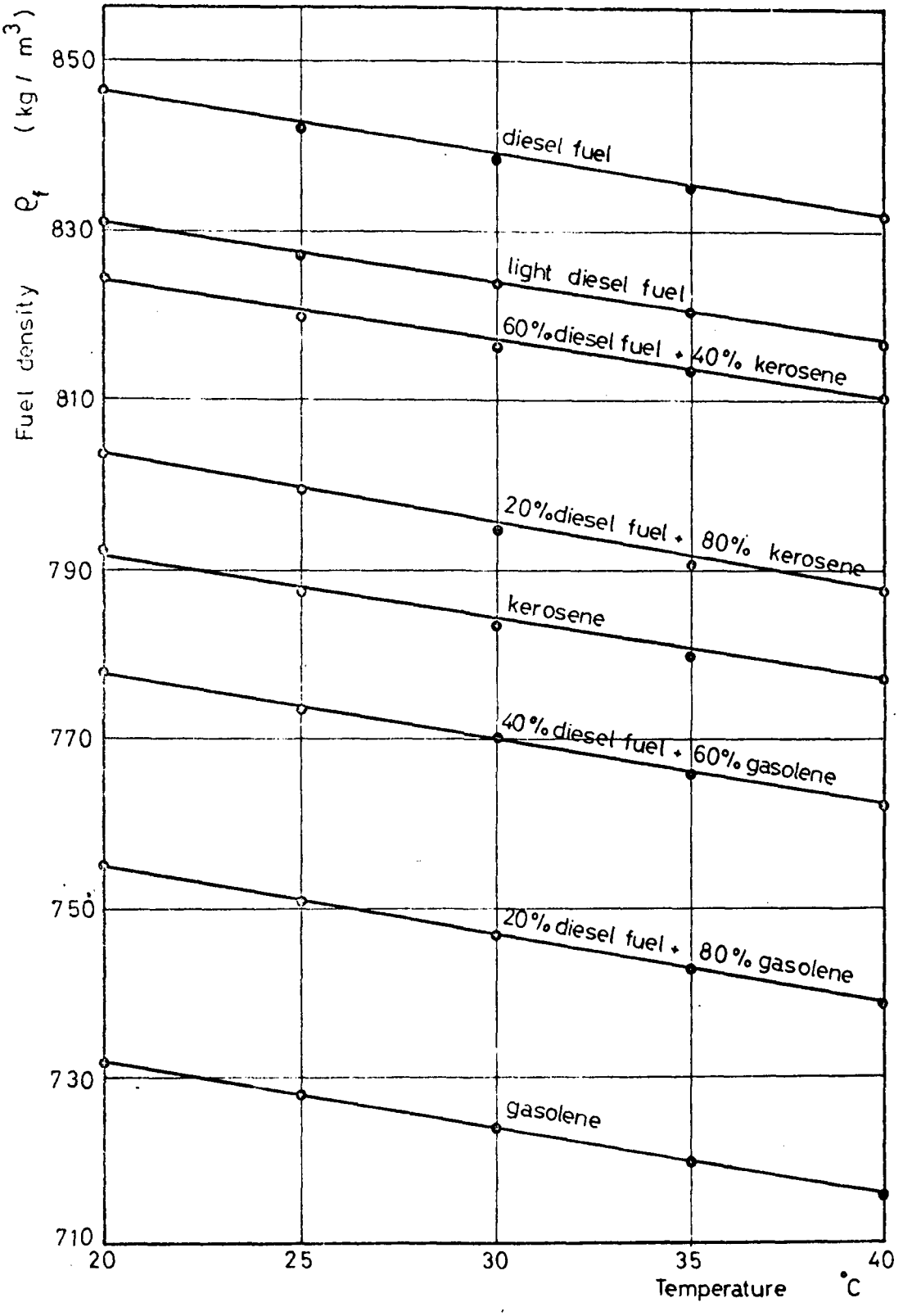

Fig(21) Variation of fuel density with temperature rise for clear and multifuel .

6.4 Droplet Size Distribution for Injectors

The atomization quality of fuel sprays depends to a great extent upon fuel properties. The atomization of fuel sprays issued from injectors has been studied by many authors. Most of the previous experiments were carried out to determine the Sauter mean diameter in atmospheric conditions. In reciprocating engines, however, fuels are injected in high compressed air. Moreover, the droplet size distribution of fuel injected in such compressed air is required for the computational model of fuel-air flow field. Some authors[69,70] reported the droplet size distribution under the same conditions of diesel engines. The liquid immersion technique consisting of collecting a sample of spray in a cell filled with immersion liquid, was employed. The cell was located at a high distance 650 mm from the injector to prevent break up of large droplets on the cell and flow of small droplets with the air stream resulting from the motion of the slit plate. However, the droplet size distribution in this case, can not represent that in the vicinity of the injector which is required for the computational model due to secondary atomization and recombination of droplets. Moreover, the droplet size might not be always constant during the injection period but fluctuates rapidly during the injection period due to the variation of the injection pressure and nozzle needle lift. The transient characteristics of the droplet size distribution was reported by Hiroyasi and Kodata[70] using the liquid impersion technique. The cell was located at high distance 160 mm from the injector. Moreover, the used immersion liquid can be used only for kerosene.

Therefore, the objective of the present work is to obtain the droplet size distribution of multifuel for various injection pressures, back pressures, and sampling positions. Some examples of the droplet size distribution are exhibited in Figs.(22) to (25). These are the frequency distribution diagrams of droplet number. More details of the results can be found in[71,68]. The variation of the frequency distribution diagram of droplet number for various fuels is shown in Fig.(22) for a pintle type injector, Fig12)

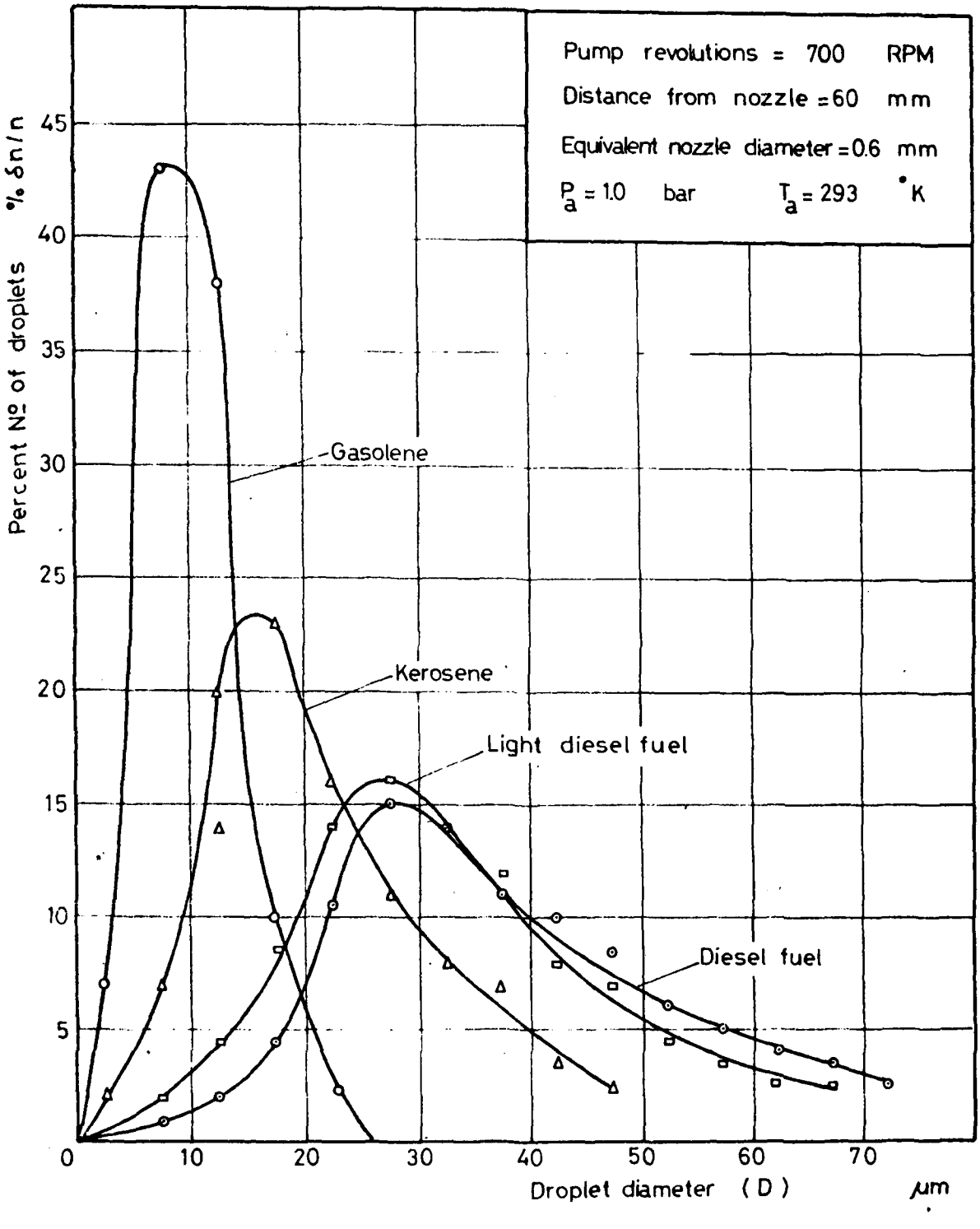

Fig (22) Droplet size distribution of clear fuel sprays injected by a pintle type injector with injection pressure 118 bar .

The samples are taken during the period from 0 to 0.5 ms from the start of injection. It can be noticed that the curve has a sharp and high peak at small diameter droplets for gasolene fuel. The curve has rather gentle slope for diesel fuel and the curves of kerosene and light diesel fuel are in between. This means that large droplet diameters are obtained with diesel fuel. The droplet size distribution of sprays obtained by a pintle type injector for various diesel-gasolene mixtures is given in Fig. (23). It can be noticed that the curves acquire a sharp and high peak from the basic distribution of pure diesel fuel at the small size range of droplet diameters with increasing the gasolene percentage in the mixture. This behaviour may be attributed to the decrease of viscosity, surface tension and density with the increase of gasolene percentage in fuel.

The effect of medium pressure and injection pressure on the frequency diagram of the number of droplet of multifuel sprays is studied. The distribution curves are found to be shifted towards the large size range with the increase of medium pressure and decrease of injection pressure as shown in Figs. (24 & 25).

The influence of various factors such as injection pressure, nozzle diameter, fuel quantity, injection angle and distance from the injector is studied also inside the cold engine model. Some examples of the frequency distribution diagrams are shown in Figs. (26) and (27). The fuel droplets are collected on the slide at 20 degree b TDC. The results show that the size distribution curve is shifted towards the small size of droplet diameters as the nozzle diameter decreases and also as the fuel quantity increases. This is believed to be due to the formation of small ligament with small nozzle diameter.

2.5 Mean Diameter of Spray Droplets

The droplet size distribution is evaluated by the relevant mean diameter D_{qp} defined by

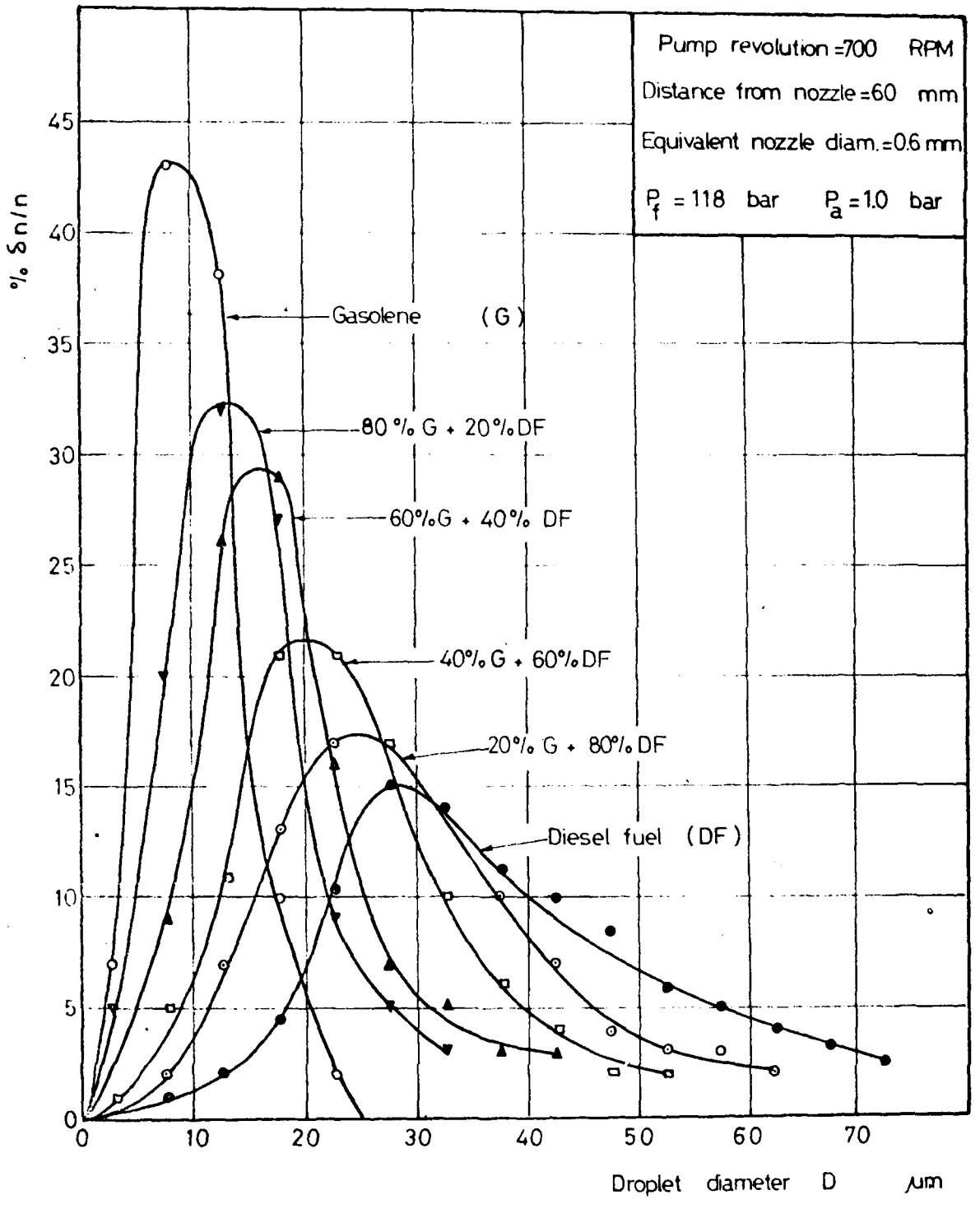

Fig(23) Droplet size distribution of diesel-gasolene mixtures .

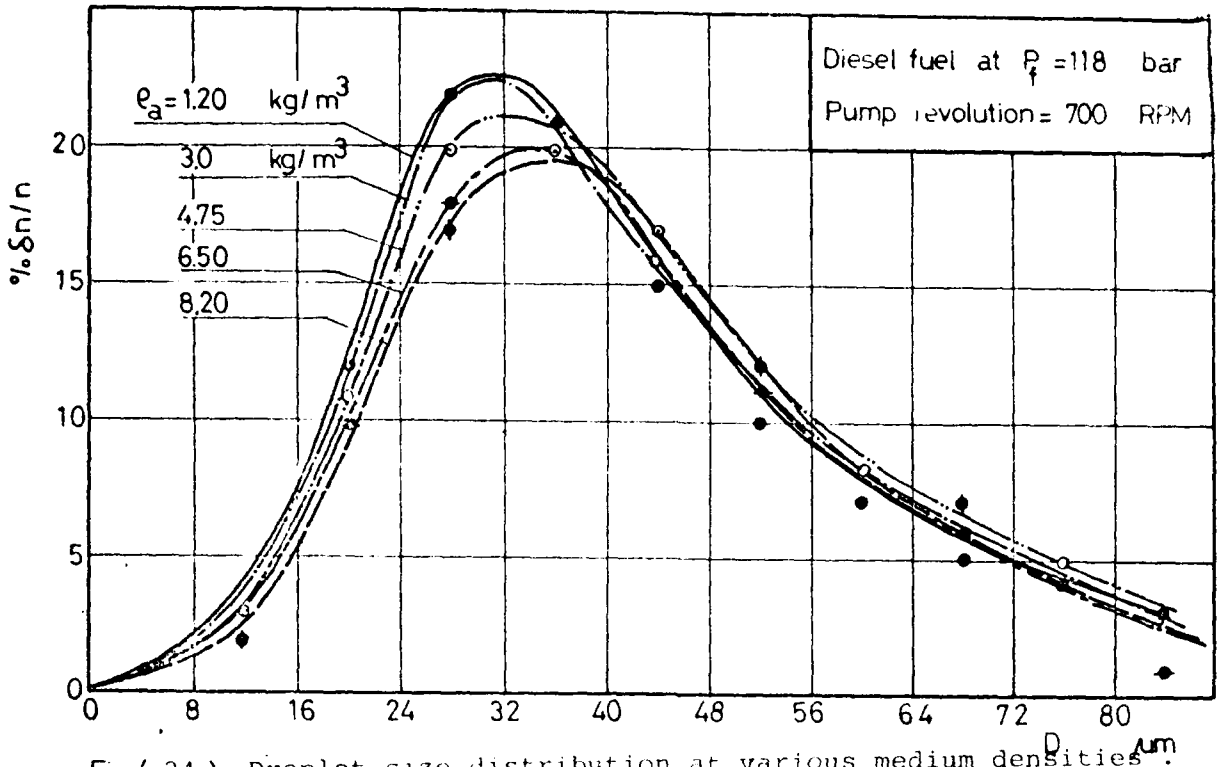

Fig (24) Droplet size distribution at various medium densities .

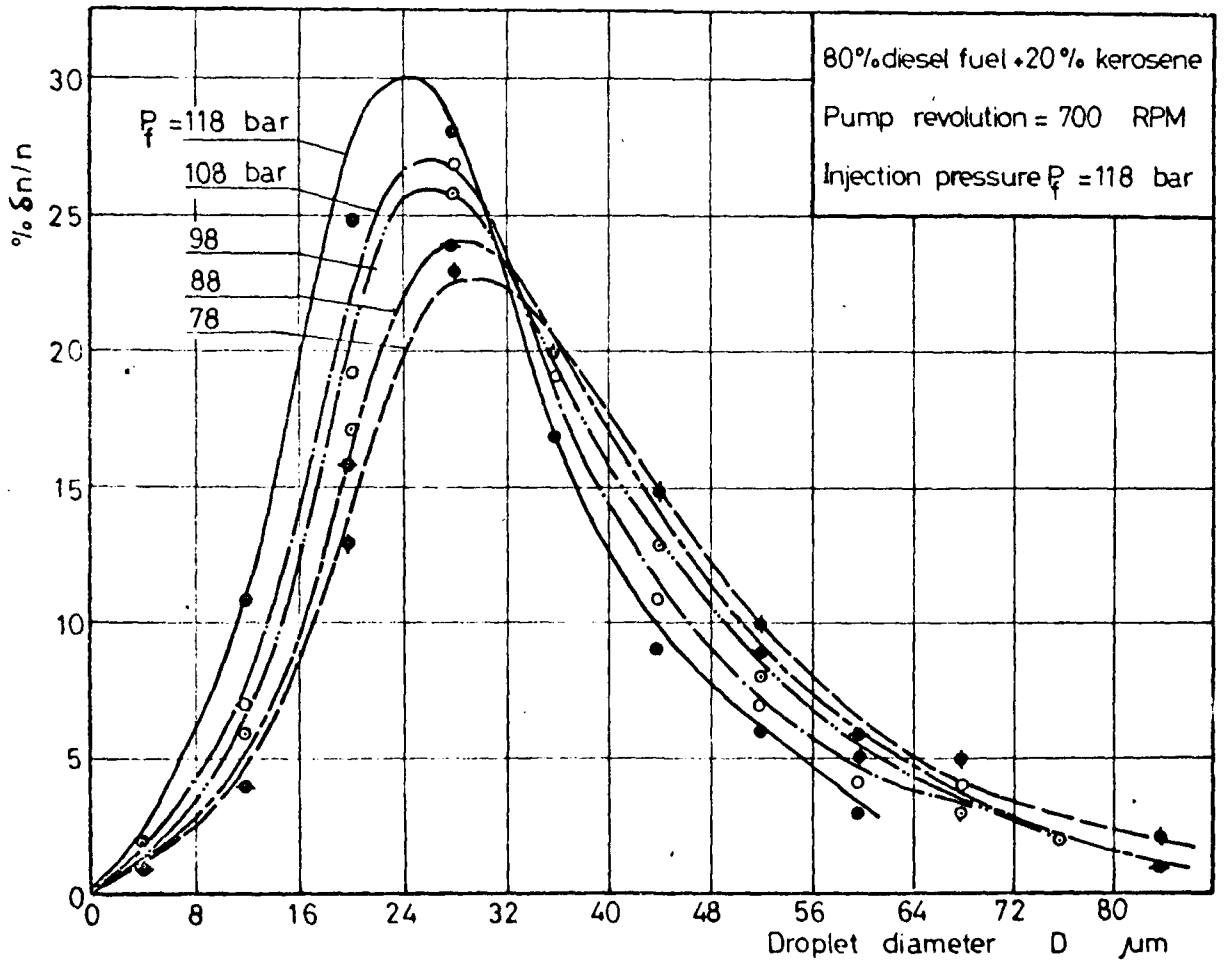

Fig(25) Droplet size distribution at various injection pressures .

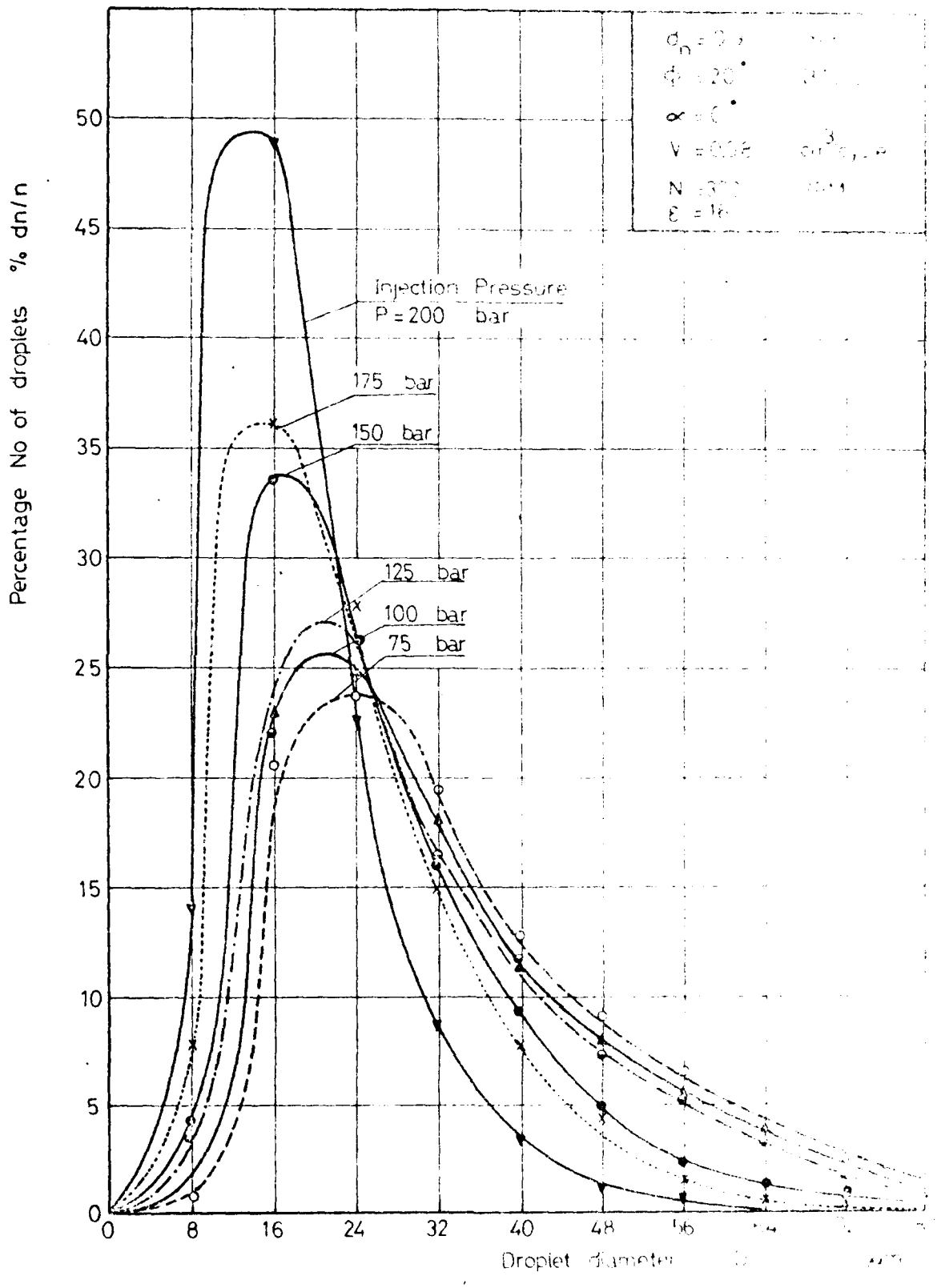

Fig(26) Droplet size distribution [illegible]
inside a cold engine model [illegible]

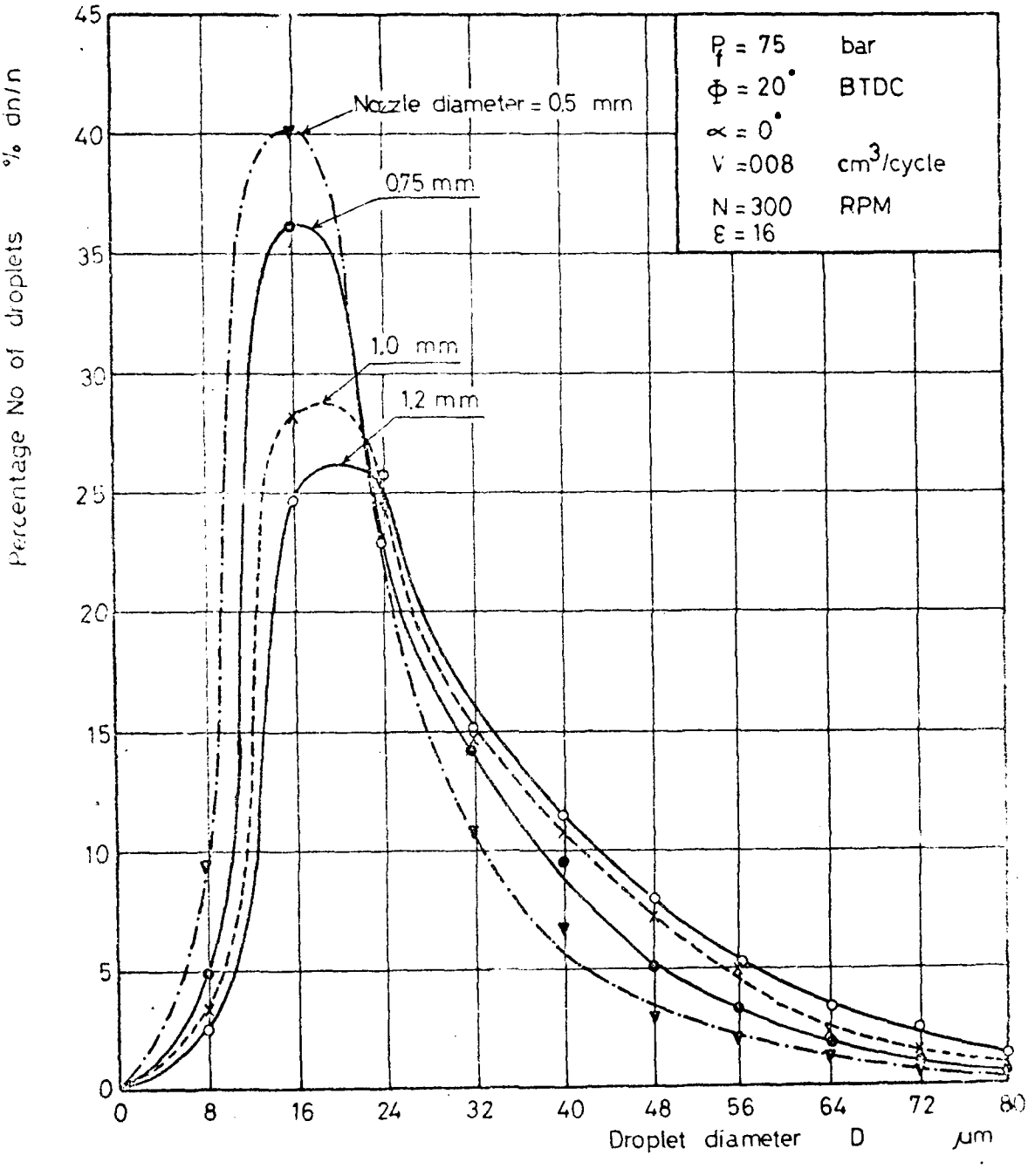

Fig(27) Droplet size distribution for diesel fuel sprays inside a cold engine model for various nozzle diameters.

$$D_{qp} = \left[\frac{\int_{D_{min}}^{D_{max}} D^q \frac{dn}{dD}\, dD}{\int_{D_{min}}^{D_{max}} D^p \frac{dn}{dD}\, dD} \right]^{1/(q-p)} \qquad (31)$$

The mean diameter of spray droplets is used to describe the quality of atomization, trajectory and penetration of the spray and to facilitate correlation with physical parameters. There are at least six mean diameters which may be used to repesent. the spray distribution and therefore, the values of p and q depend on the field of application[72]. Consider the Langmuir's equation, which is commonly used for describing the evaporation rate of spherical particles in still air, a necessary prerequisite is to known the relevant average diameter of the fuel spray droplets. For number of droplets having different diameters the equation is

$$\frac{d \Sigma (m_i n_i)}{dt} = -K_3 \Sigma D_i n_i$$

dividing by Σn_i, it becomes

$$\frac{dm_\ell}{dt} = -K_3 \frac{\Sigma D_i n_i}{\Sigma n_i} = -K_3 D_{10} \qquad (32)$$

where ,

D_{10} is the linear mean diameter.

Also considering the efficiency of an atomizing operation, in which a fraction of energy "E" lost in pressure drop ΔP_i is used in forming new ligament, the equation may be expressed for the entire spray as follows :

$$E \Delta P_i \Sigma D_i^3 n_i = 6 \sigma \Sigma D_i^2 n_i \qquad (33)$$

which can be arranged in the following form ;

$$\frac{E \Delta P_i \Sigma D_i^3 n_i}{\Sigma D_i^2 n_i} = 6 \sigma$$

$$E \Delta P_i D_{32} = 6 \sigma \qquad (34)$$

$$E \quad \Delta P_i \quad D_{32} \quad = \quad 6 \sigma_l \tag{34}$$

where, D_{32} is the Sauter mean diameter.

It is seen thus that the evaporation law holds for D_{10} and the atomizing efficiency for D_{32}.

The Sauter mean diameter D_{32} is thus used for the mass transfer and combustion problems since the surface area and the volume of droplet are of primary importance for evaporation and combustion. The Sauter mean diameter can be defined as the diameter of a droplet that has the same surface to volume ratio as that of the total spray. It is calculated from the formula

$$D_{32} = \Sigma n_i D_i^3 / \Sigma n_i D_i^2 \tag{35}$$

The influence of various factors on the Sauter mean diameter for various multifuel spray is studied, sprays of the four main types, diesel, light diesel, kerosene and gasolene are tested with the same injection pressure. The rack of the fuel pump is adjusted to its maximum position. Some of these results are shown in Figs.(28 - 30). It is clear from Fig.(28) that the mean droplet diameter decreases slightly with the increase of light diesel fuel quantity. The rate of decrease of the mean droplet diameter increases with the increase of kerosene and gasolene quantity. This may be attributed to the decrease of viscosity and surface tension of the mixture. It is found also that the mean droplet diameter decreases with the increase of fuel pressure due to the increase of the available atomization energy affecting the initial disturbance and entrainment as shown in Fig.(29). The effect of medium density is illustrated in Fig.(30) which indicates that the Sauter mean diameter increases with increasing the medium density. This is believed to be due to the decrease of the entrained air, and consequently increase of ligament diameter, resulting from the increase of air viscosity. It can also be attributed to the agglomeration of droplets due to small penetration of spray in a denser medium. It is clear also from the figure that the increase of Sauter mean diameter with the increase of medium density in case of gasolene

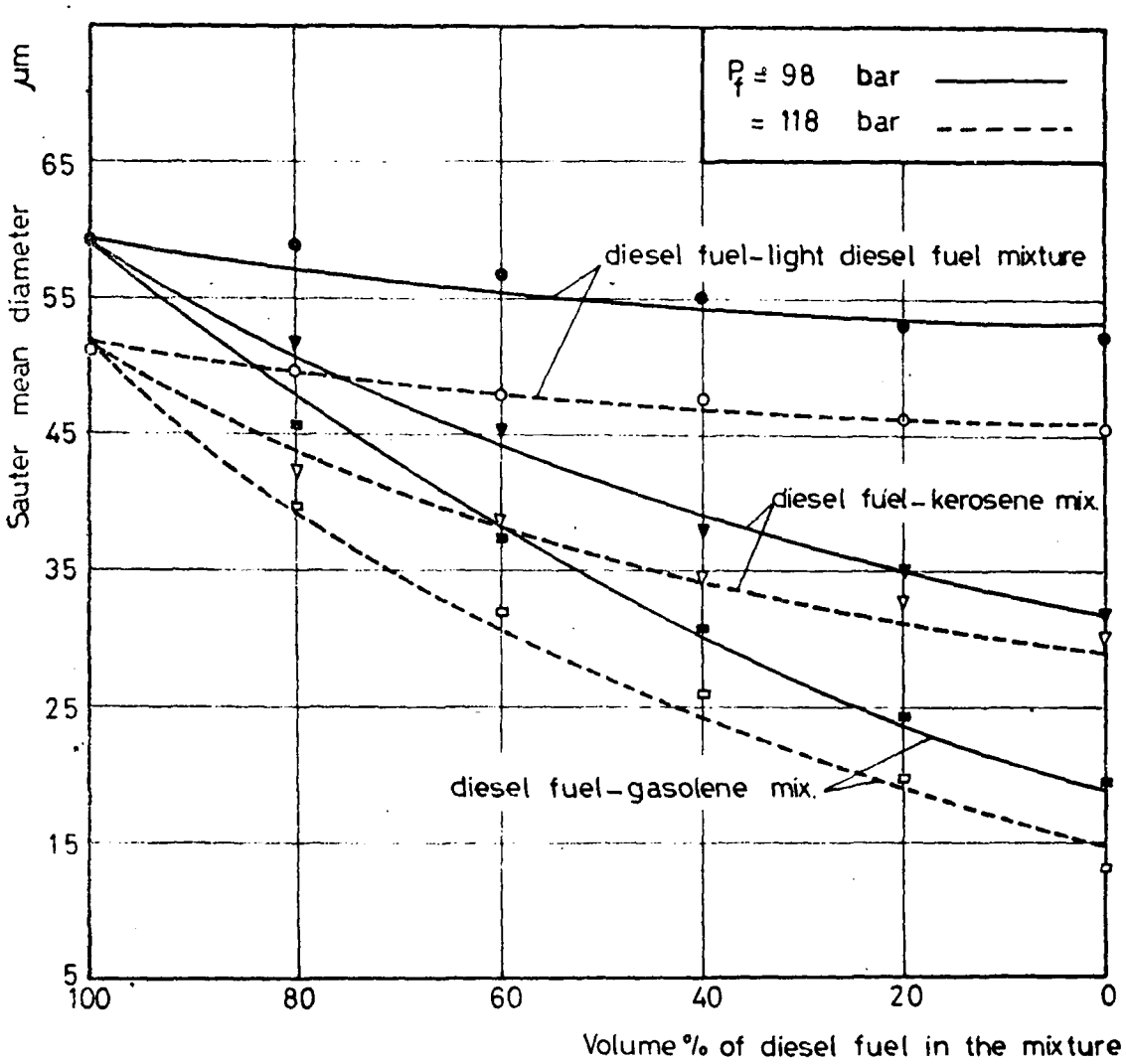

Fig(28) Variation of Sauter mean diameter with the quantity of diesel fuel in multifuel at various injection pressures .

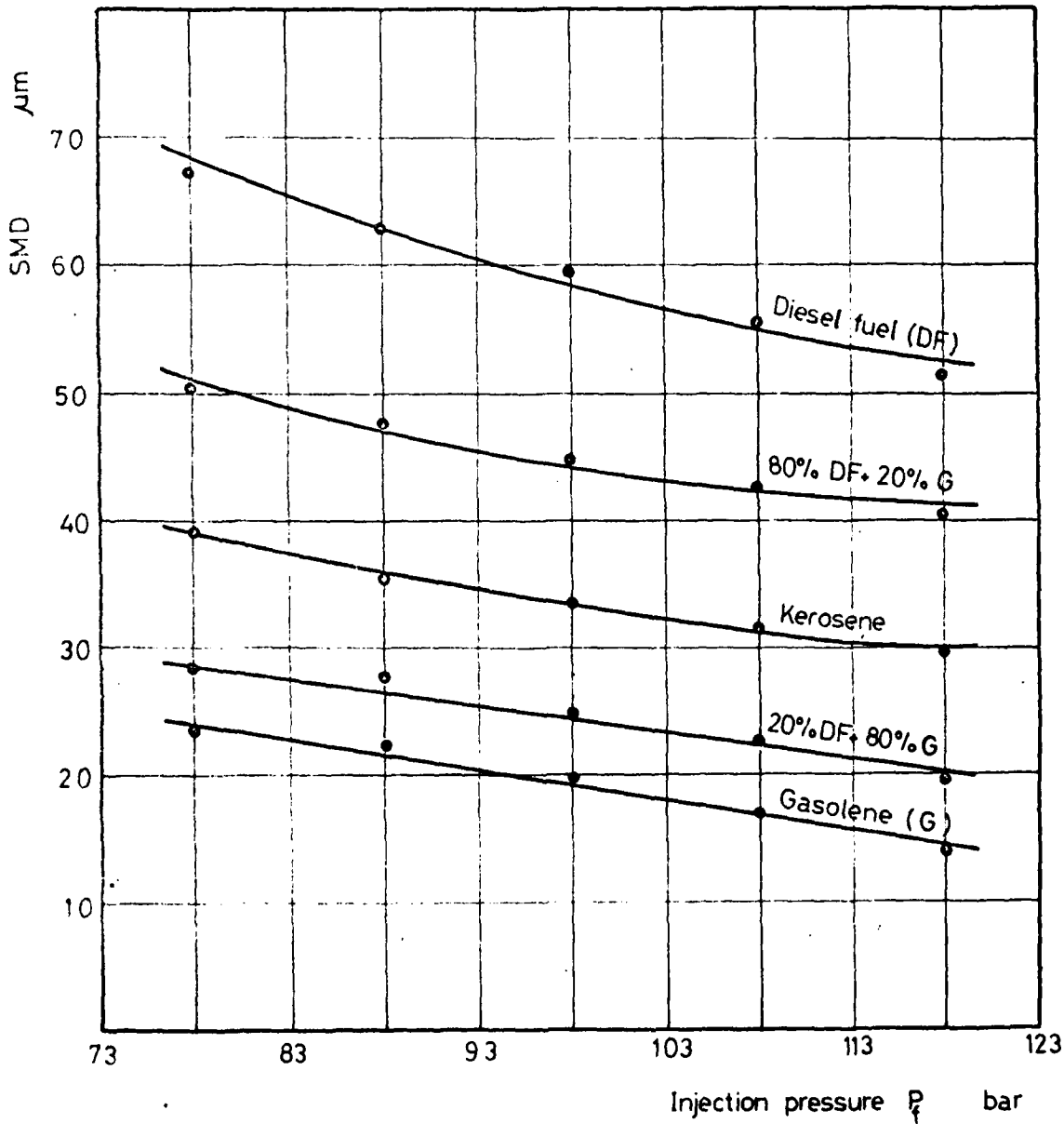

Fig(29) Effect of injection pressure on Sauter mean diameter for clear and multifuel .

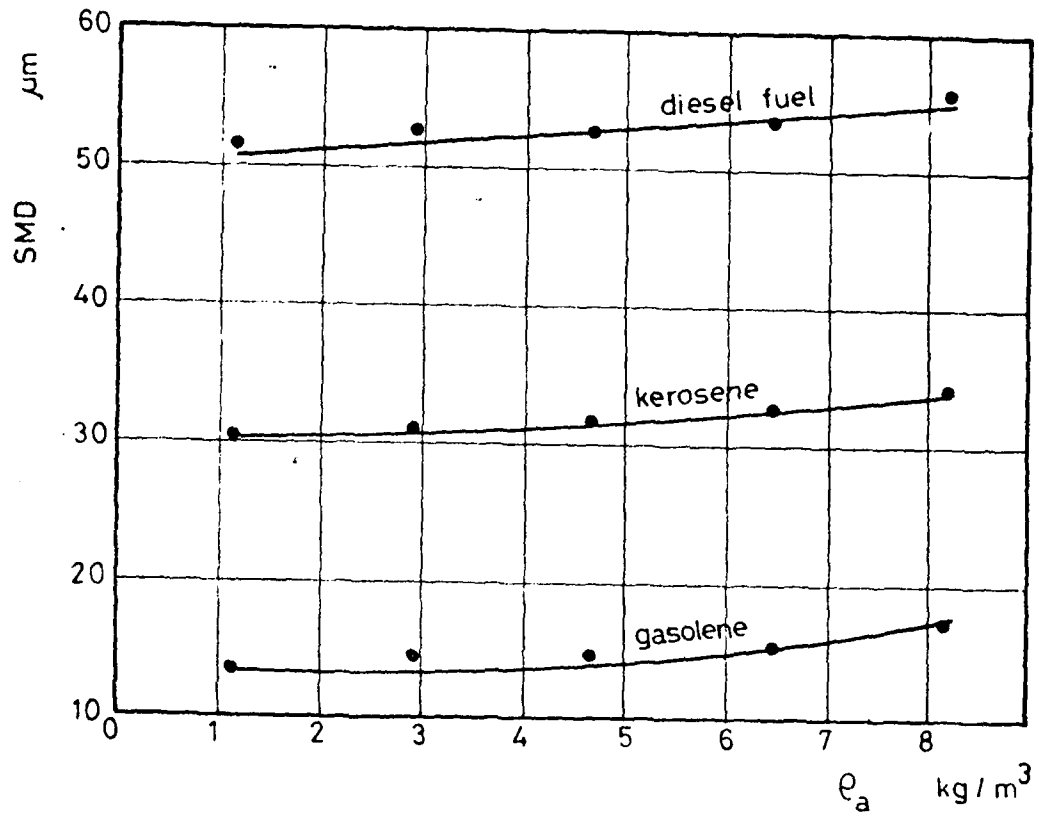

Fig(30) Effect of medium density on Sauter mean diameter for clear fuel at injection pressure bar

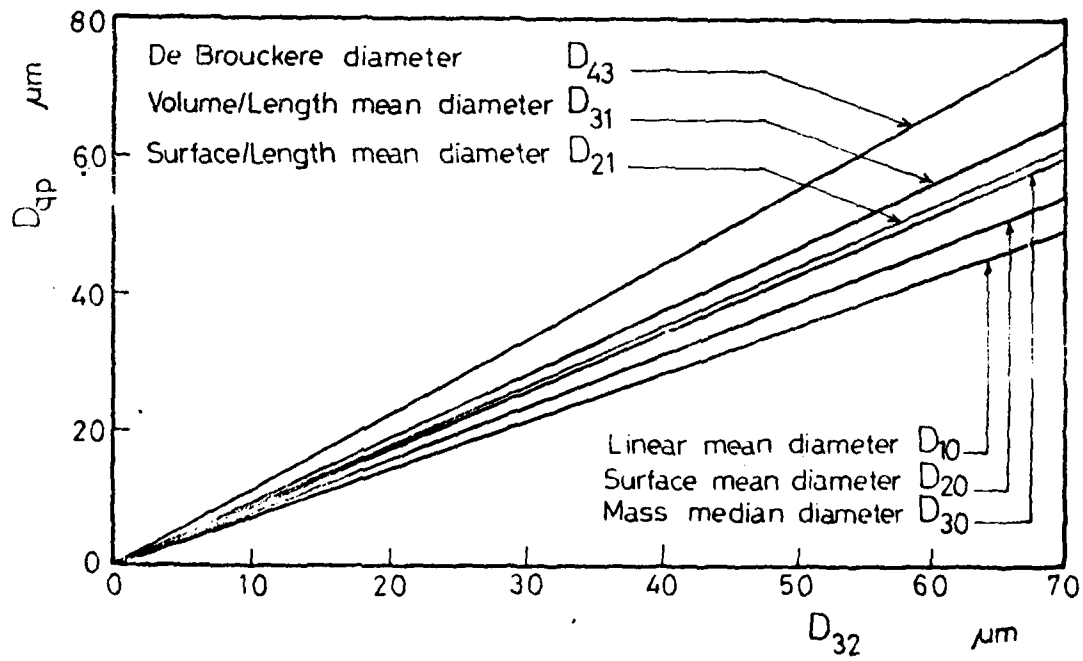

Fig(31) Comparison between Sauter mean diameter D_{32} and other mean diameters.

is higher than in the case of diesel fuel. This may be due to further droplet agglomeration because of the sharp loss of the kinetic energy of droplets leading to faster retardation of droplets.

Studying the variation of Sauter mean diameter across the fuel spray it was found that the local Sauter mean diameter does not change in case of gasolene while in case of diesel fuel it decreases at the periphery of spray. The relation between the Sauter mean diameter and other mean diameters is shown in Fig. (31). As regard to the maximum droplet diameter for multifuel sprays, a general expression is deduced in the following form :

$$D_{max} = 1.75 \; D_{32} \qquad (36)$$

6.6 Generalization of Droplet Size Distribution Data

Since there is no theoretical analysis until now for the calculation of the droplet size distribution of fuel sprays, several probability expressions have been developed by several researchers[72] for this purpose. At the same time the droplet size distribution curve is greatly affected by fuel properties, injection pressure and operating conditions. To generalize such different data it is required to normalize the droplet diameter by dividing it by a suitable mean droplet diameter to transfer these discrete values to a unique curve. In the present work, the mean droplet diameter D_{32} is found to be suitable for this purpose. Figure (33) shows such representation of cumulative frequency distribution of dimensionless droplet diameter.

In order to choose the most suitable distribution function which fits adequetly the experimental data, curve fitting of the experimental data with these previously suggested probability functions are carried out. Curve fitting of the experimental data using the simple Rosin-Rammler distribution function[73] gives the following expression :

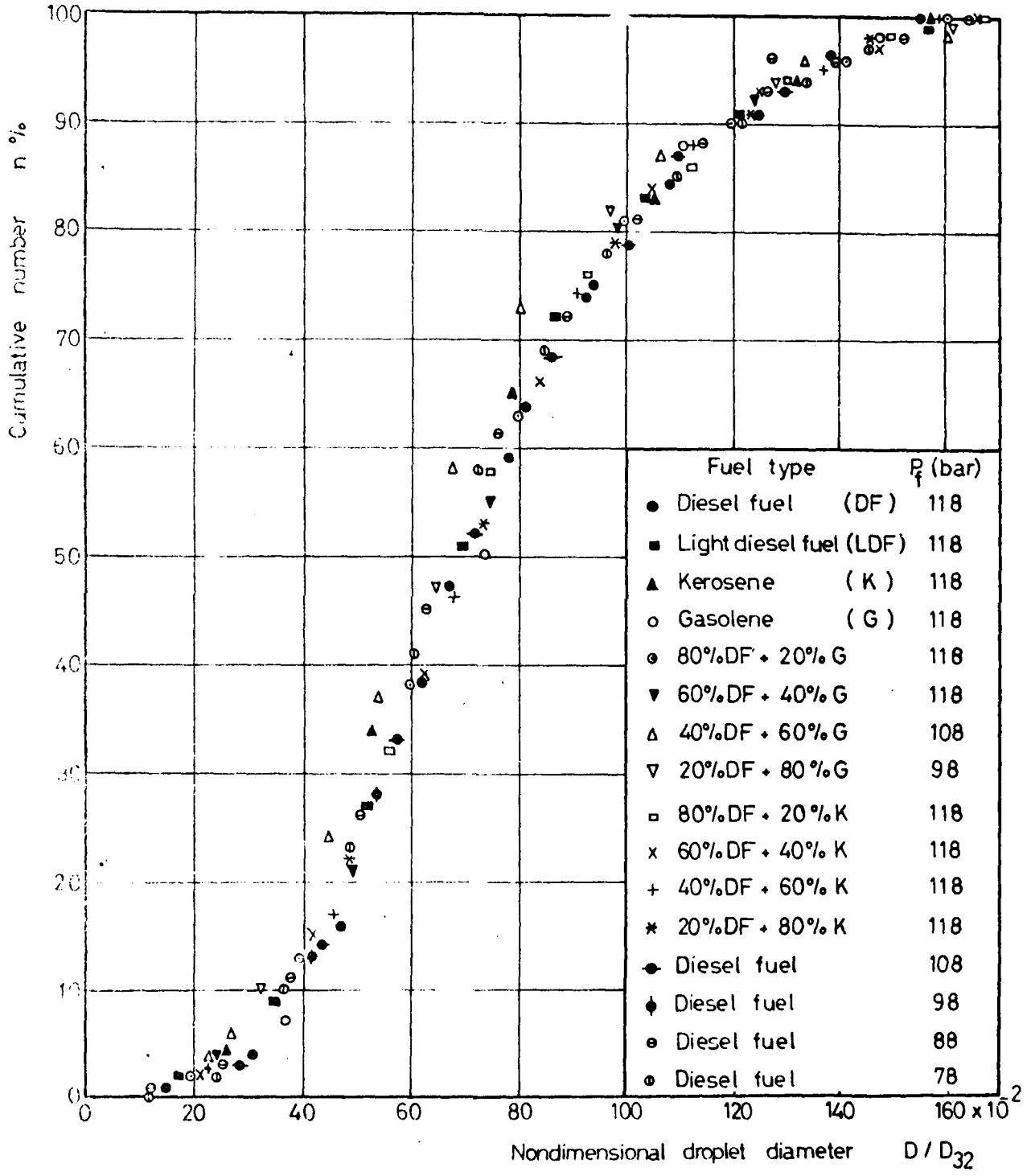

Fig(32) Comulative frquency distribution of droplet size for multifuel sprays with dimensionless droplet diameter .

$$1-v = e^{-0.427/(D/D_{32})^{5.32}} \quad (37)$$

and using log probability distribution function[72] gives the following expression :

$$\frac{dn}{dy} = 0.94 \; e^{-(1.657y + 0.5)^2} \quad (38)$$

where,

$$y = \ln (D/D_{32})$$

and using upper limit log probability distribution function[72] gives the following expression :

$$\frac{dn}{dy} = 0.572 \; e^{-(1.015y+0.913)^2} \quad (39)$$

where,

$$y = \ln \left| \frac{0.76 \; (D/D_{32})}{1.99 - (D/D_{32})} \right|$$

It has been found[69] that the droplet size in diesel fuel sprays was well correlated with the chi-square distribution function when using the cumulative distribution of volumes instead of numbers. An attempt is made to correlate the size of the droplet sampled with the chi-square distribution and to find the degree of freedom as shown in Fig.(33). It is clear from the figure that the degree of freedom f=9 which was given by Hiroyasi cannot fit the data while f = 17 fits adequatly the experimental data. The smaller diameters obtained by Hiroyasi may be attributed to the location of immersion cell at a distance of 160 mm from the nozzle. The chi-distribution function which fits the experimental data can be written in the following form :

$$\frac{dv}{v} = 1953 \; (D/D_{32})^{7.5} \; e^{-7.5(D/D_{32})} \, d(D/D_{32}) \quad (40)$$

An attempt to correlate the droplet sampled with the Tanasawa-Tesima distribution function[74] is also carried out. This droplet size distribution function can be written in the following form for the normalized curve:

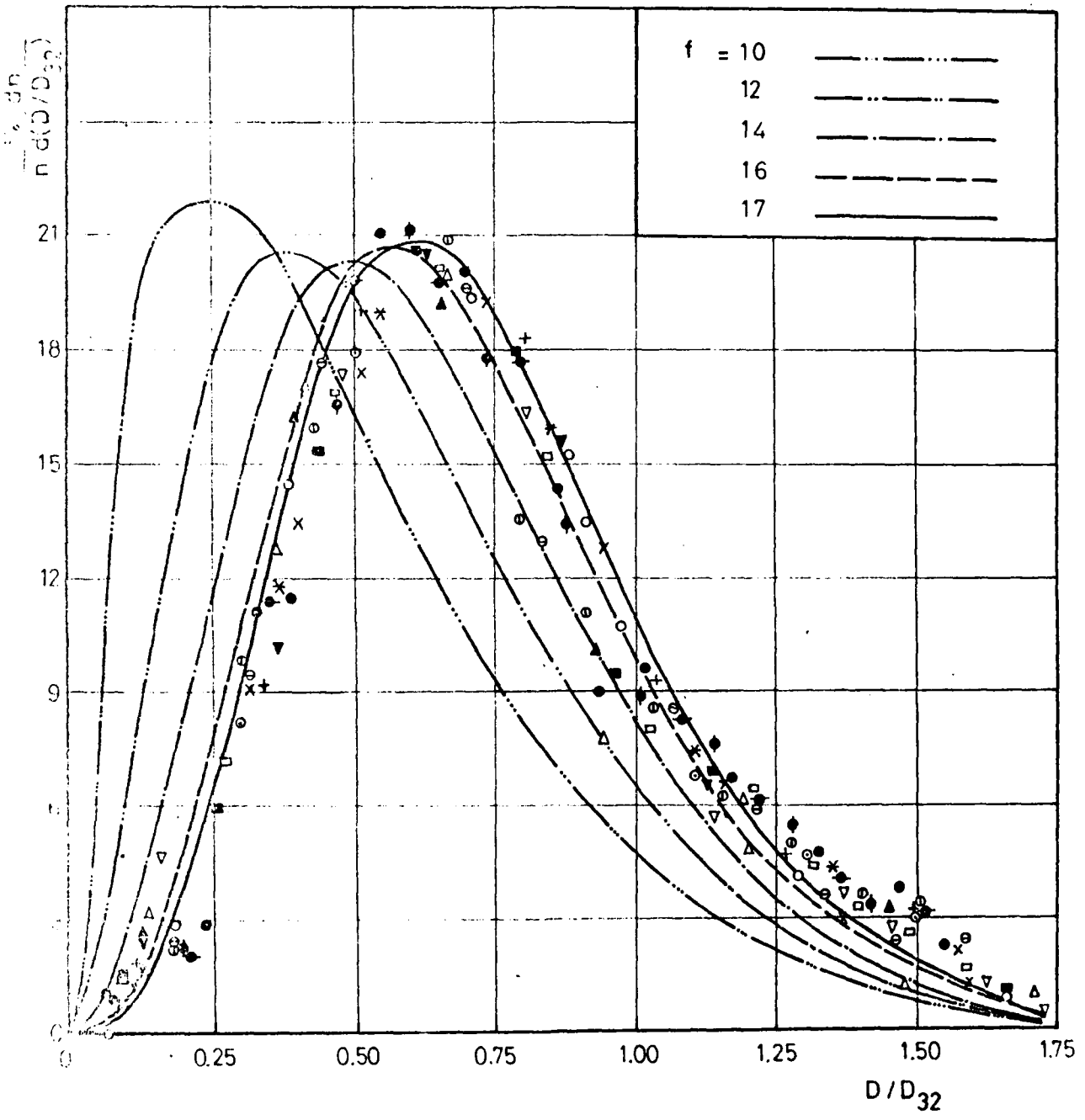

Fig (33) Chi-square distribution curves for different degrees of freedom against experimental values .

$$\frac{dn}{nd(D/D_{32})} = a(D/D_{32})^{\alpha} e^{-b(D/D_{32})^{\beta}} \qquad (41)$$

where

$$b = \left| \Gamma\left(\frac{\alpha+4}{\beta}\right) / \Gamma\left(\frac{\alpha+3}{\beta}\right) D_{32} \right|^{\beta}$$

$$a = \left| \Gamma\left(\frac{\alpha+4}{\beta}\right) / \Gamma\left(\frac{\alpha+3}{\beta}\right) \right|^{\alpha+1} \beta \, n/D_{32} \quad \left(\frac{\alpha+1}{\beta}\right)$$

$$n = a\Gamma\left(\frac{\alpha+1}{\beta}\right) / \beta \, b^{(\alpha+1)/\beta}$$

which can be written in the following straight line form :

$$\ln \left| \frac{dn/n \; d(D/D_{32})}{(D/D_{32})^{\alpha}} \right| = \ln a - b(D/D_{32})^{\beta} \qquad (42)$$

plotting $(1/(D/D_{32})^{\alpha})\ dn/n\ d(D/D_{32})$ against $(D/D_{32})^{\beta}$ for different assumed values of α and β one can get the most suitable values of α and β which satisfy the minimum square deviation. Determining the values of α and β from the experimental values it is possible to write the equation in the following form :

$$\frac{dn}{(nd(D/D_{32})} = 10(D/D_{32})^{2.4} e^{-2.4(D/D_{32})^{2}} \qquad (43)$$

It is required now to find out the most suitable function from these five expressions which fit the experimental data adquatly and allow for easy use and extrapolation. A comparison of these expressions with experimental data is given in Fig. (4). This comparison shows that both the T-T and chi-square equations give a sufficiently accurate fit of the data while the R-R equation shows poor fitting of the data. The upper limit log probability equation shows an acceptable fitting of data but it has a complicated form which does not permit direct evaluation of the droplet size distribution. Regarding the log probability equation it is found that it fits well the largest droplets range while greater deviations are obtained in the small diameter range. Therefore, it is possible to conclude that both the

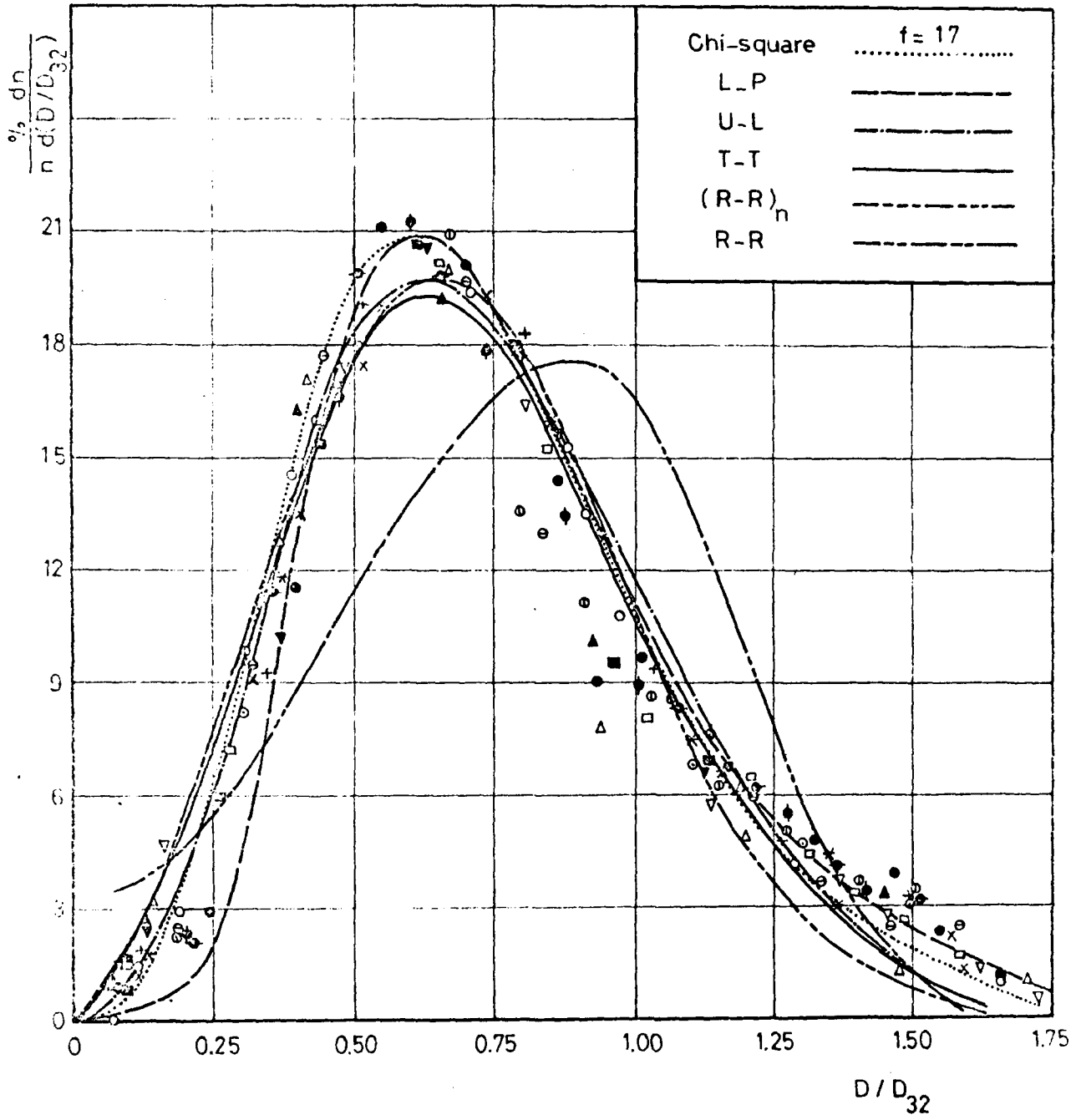

Fig(34) Comparison of various distribution equations with experimental values .

T-T and chi-square distribution functions satisfy adequatly the experimental data of either clear or multifuel sprays injected through pintle nozzle injector within the accuracy of the used experimental technique.

6.7 Generalization of Mean Droplet Diameter

The mean droplet diameter of certain fuel spray depends on a large number of variables such as fuel properties, operating conditions and geometrical dimensions of the fuel nozzle. Dimensionless analysis facilitates experimental determination of mean droplet diameter at various conditions. The dimensionless groups decrease the number of experiments required to obtain an empirical expression. Dimensional analysis gives the following relation for Sauter mean diameter :

$$D_{32}/d = A\ Re^{a}\ We^{b}\ C_d^{e} (\rho_f/\rho_a)^{f} (\ell_n/d)^{g}$$

where, A,a,b,d,e, f and g are constants to be determined from the experimental results. The indices that fit the experimental data by a smooth curve were determined and the general equation of Sauter mean diameter is derived by plotting $Re^{-0.434} We^{-1.05} C_d^{-1.0} (\rho_f/\rho_a)^{-0.12}$ versus D_{32}/d as shown in Fig.(35). The following relation is determined for the Sauter mean diameter

$$D_{32}/d = 107\ Re^{-0.183} We^{-0.442} C_d^{-0.422} (\rho_f/\rho_a)^{-0.05} \qquad (44)$$

An explicit form of this relation with various parameters is found in the following form :

$$D_{32} = 6156\ \nu^{0.385}\ \sigma^{0.737}\ \rho_f^{0.737}\ \rho_a^{0.06}\ \Delta P^{-0.54}\ \mu m \qquad (45)$$

A satisfactory coincidence is obtained when the results determined by this relation is compared with the experimental results as shown in Fig.(36).

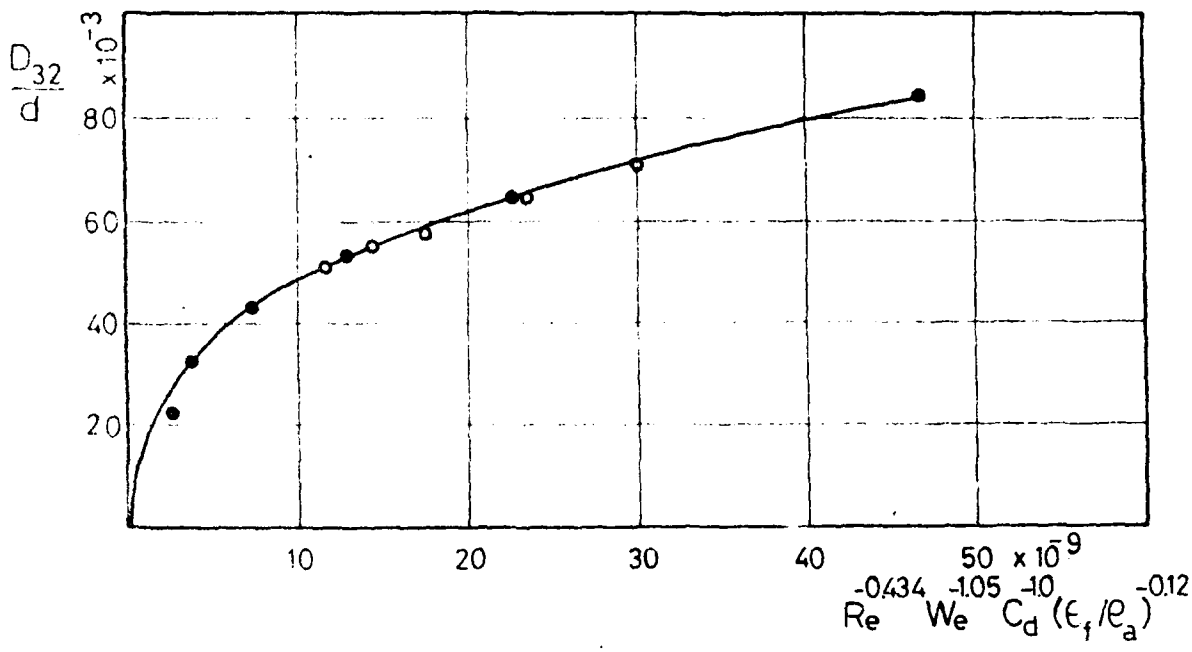

Fig (35) Graphical representation of equation 44 .

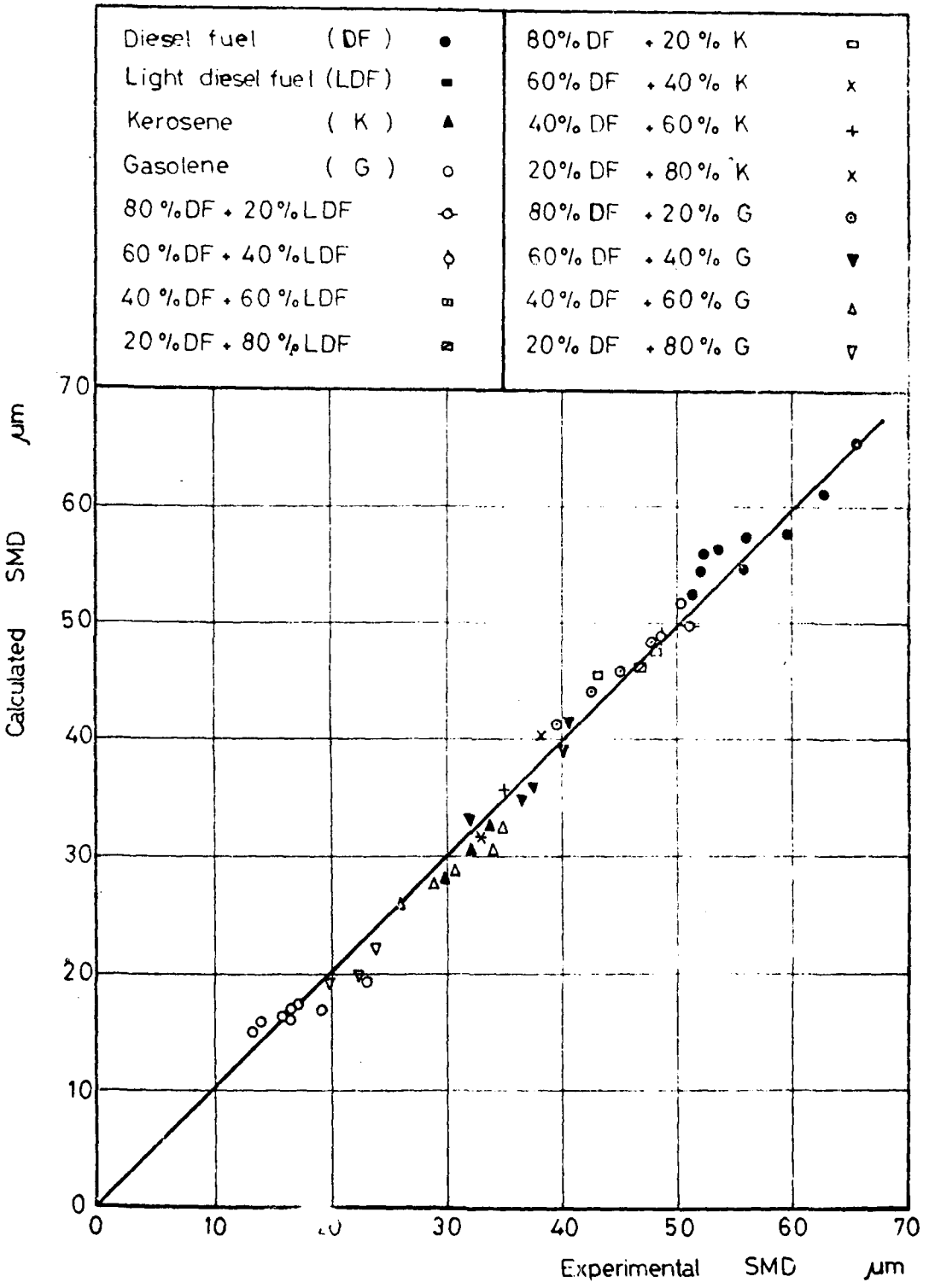

Fig(36) Comparison of calculated and experimental values of Sauter mean diameter .

AD-A116 818 CAIRO CENTER FOR COMBUSTION (EGYPT) F/G 21/5
SPRAY MODELLING FOR MULTIFUEL ENGINES.(U)
JUL 82 M M ELKOTB. DA-ERO-79-G-0017
UNCLASSIFIED NL

CHAPTER 7

CONCLUSIONS

Theoretical calculation of the fuel spray behaviour inside multifuel engine combustion chambers which leads to better evaluation of heat release requires complete knowledge of the air flow field. In the same time theoretical calculation of the flow field is very complicated due to the presence of transient, compressible and turbulent flow. So a mathematical model supported by experimental results capable to investigate clearly the flow field inside diesel engine swirl chamber, and describing the effect of the working conditions and constructional parameters on it is required.

Development of a complete mathematical model for the prediction of turbulent flow field in swirl chambers has been carried out in the present work by considering geometrical and operating conditions. The mathematical model of the turbulence flow has been obtained by solving the finite-difference form of the equations of energy, mass, momentum, the turbulence kinetic energy K and its dissipation rate ε taken the compressiblity effects in consideration.

The source term for the turbulence dissipation rate ε has been modified to suit the geometrical and operating conditions as follows :

$$S_\varepsilon = \frac{\varepsilon}{k} \left(C_1 (1 - C_3 R_f)\, G - C_2\, \rho\varepsilon\right)$$

Where the coefficient F has been determined experimentally from the local shear stress and the turbulence generation as follows :

$$C_\mu = C_\mu \cdot F$$

$$C_D = (\tau/\rho\, K)^2 = C_{D_o} F$$

$$C_2 = 2\, C_D$$

$$C_1 = \frac{C_2}{C_D} - \frac{\lambda^2\, n^2}{\sigma_\varepsilon\, C_D^{\frac{1}{2}}}$$

An experimental set-up has been built up to facilitate the measurements of air velocity components, and turbulence fluctuating velocities and to investigate the effect of various constructional and working conditions on the flow field. A careful comparison of the experimental results over a wide range with the predicted values has been carried out to obtain reliable information about the coefficients turbulence model. Velocity components have been measured by a temperature compensated hot-wire anemometer. In addition a microphone condenser pick up has been developed for the measurement of velocity components inside the swirl chamber.

Based on the experimental and predicted results carried out in this work the major contributions can be summarized as follows :

1- The hot-wire anemometer is sensible to the medium pressure and therefore calibration of anemometer at various pressures has been done. A formula for the relation between velocity, pressure and anemometer responce has been obtained in the following form :

$$PU = 32\ (V - Vo)^{1.8}$$

2- The velocity in swirl chamber of diesel engine can be adequately determined by the microphone-condenser after it has been calibrated at various pressuresand temperatures.

3- A mathematical model has been developed to determine the flow field in swirl chambers taking into consideration the effect of constructional and operating conditions upon the local turbulence value.

4- The coefficient C_D determining the local turbulence value has been determined experimentally and it is affected by the radial distance, engine speed, port area and swirl volume. Relations with these parameters are obtained as follows :

$$C_D = 1.16\ (r/R_s)^{-0.08}$$
$$C_D = 1.2255\ (N/N_c)^{-0.88}$$
$$C_D = 33.359\ (A_j/A)^{0.704}$$
$$C_D = 1.303\ (V_s/V_c)^{0.229}$$

and a general dimensionless correction factor is obtained in the following form :

$$F=33.47(r/R_s)^{-0.08}(N/N_c)^{-0.88}(A_j/A)^{0.704}(V_s/V_c)^{0.229}$$

5- The effect of streamline wall curvature and centripetal accelerations has been introduced to correct the length scale of turbulence determining ε -equation, by multipling the coefficient C_1 with the Richardson number function $(1-C_3R_f)$, the constant C_3 has been obtained equal to 0.04 from the comparison of experimental and predicted results.

6- The suggested theoretical model gives satisfactory results than the previous model and gives also logic values for the length scale of turbulence.

7- The effect of various constructional and operating conditions has been investigated and the following results are obtained :

a) The port area has the most significant effect on the tangential velocity and turbulence intensity than other parameters.

b) Two eddies are noticed at both sides of the inlet port. The intensity of these eddies increases during the compression stroke, and intensifing with the decrease of the port area ratio (A_j/A), increase of engine speed and increase of swirl chamber volume ratio (V_s/V_c).

c) The radial velocity has smaller values than the tangential velocity.

d) The turbulence mixing length ℓ for a wide range of results at various constructional and operating conditions can be' expressed as follows :

$$\ell/R_s = \text{const}$$

This constant takes values varies from 0.1 to 0.2.

8- A spray model inside the combustion chambers of diesel engines is suggested. The model is based on the combination of the discrete droplet model with a multidimensional gas flow prediction method. The variation of droplet diameter and velocity and consequently the variation of heat transfer to droplet and drag force are taken into consideration. However, this model requires the determination of the droplet size distribution and mean droplet diameter.

The droplet size distribution and mean droplet diameter have been determined experimentally for clear fuel as well as for multifuel using the slide sampling technique. Droplet size distribution functions and Sauter mean diameter data are obtained. The use of these relations demonstrated substantially better results of the spray model. The model is capable of determining the spray behaviour for any fuel.

In the past, research efforts have not emphazised the effects caused by changes in the fuel. Many new efforts have been started to determine the evaporation of clear and multifuel under various operating conditions, and the multifuel droplet behaviour. The variation of droplet velocity at different introduction locations is also required. The application of these new efforts in spray model will emphasize the effect of the fuel character on the heat release pattern and facilitates successful prediction of fuel concentration required for the calculation of the concentrations of nitric oxide and soot in diesel engines.

1- Austen, A.E.W. and Lyn,W.T., Relation between fuel injection and heat release in a direct-injection engine and the nature of the combustion processes, Proc.Instn.Mech.Engrs (AD) 1,47 (1960-1).

2- Austen, A.E.W. and Lyn,W.T., The application of heat release analysis to engine combustion study, 1067, CIMAC (1962).

3- Whitehouse , N.D. and Way, R.J.B., Rate of heat release in diesel engines and its correlation with fuel injection data, Proc.Instn. Mech.Engrs. 184 Part 3J, 17 (1969-70).

4- Whitehouse, N.D. and Way, R.J.B., A simple method for the calculation of heat release rate in diesel engines based on the fuel injection rate, SAE paper 710134 (1971).

5- Whitehouse, N.D. and Sareen, B.K., Prediction of heat release in a quiescent chamber diesel allowing for fuel air mixing, SAE paper 740084 (1974).

6- Whitehouse, N.D. and Abughres, S.M., Calculation of fuel/air mixing in a diesel engine with swirl for the purpose of heat release prediction, in combustion in Engines, P.147, Instn of Mech.Engrs, London and New York, 1975.

7- Schweitzer, P.H., Penetration of oil sprays, Pennsylvania state college Bull. No. 46 (1937).

8- Porks, M.V., Polanski,C. and Roye, R., Penetration of diesel fuel sprays in gases, SAE paper 660747, (1966).

9- Taylor, D.H. and Walsham, B.E., Combustion processes in a medium spreed diesel engine, Proc. Instn. Mech. Engrs, 184, Part 3J, 67 (1969-70).

10- Dent, J.C., A basis for the comparison of various experimental methods for studying spray penetration, SAE paper 710571, (1971).

11- Hay,N. and Jones, P.L., Comparison of the various correlations for spray penetration, SAE, paper 720776 (1972).

12- Williams, T.J., Parameters for correlation of penetration re-

results for diesel fuel sprays, proc. Instn.Mech.Engrs,187, 771 (1973).

13- Hycak,P. and Lee, D.T., Evaluation of maximum velocity decay in wall jets, JI. Spacecraft Rockets 7, No.5, (1970).

14- Sridhar, K. and Tu,P.K.C., Experimental investigations of curvature effects on turbulent wall jets,Aeronaut. Soc.73, No. 707 (1969).

15- Elkotb, M.M., A prediction model for the fuel film motion over the surface of swirl chambers, HMT series, Heat and Flow in Power system components, Editor spalding, D.B., pergamon press, 1979.

16- Lyn,W-T, Colculations of the effect of rate of heat release on the shape of Cylinder-pressure diagrams and cycle efficiency, Proc. Auto. Div. Instn mech, Engrs No.1, 34, (1960-61)

17- Spalding, D.B., Some fundamentals of combustion, Academic Press, New York, (1955).

18- Cook, H.A., Appraisal of effects of operating conditions and engine design on combustion in reciprocating engines by engine cycle calculations, SAE, paper No. 633C, (1963).

19- Cook, H.A., Diesel engine cycle analysis of relationships of fuel injection to fuel compression-ignition charateristics and best fuel utilization, SAE, paper No. 656449, (1965).

20- Nagao F., Ikegami M. and Oshima, K.,An analysis of combustion knock in a diesel engine, Bulletin Japan Soc. mech. Engrs, No 39, 10, 532, (1967).

21- Propert, R.P., The influence of Spray particle size and distribution in the combustion of oil droplets, Phil. Mag. Ser7, 37, 94, (1946).

22- Tanasawa,Y., On the combustion rate of a group of fuel particles, Tech. Rept Tohoku Univ., No.1, 18, 61, (1953).

23- Shipinski,J.H., Relationships between rates of injection and rates of heat release in diesel engines, Ph.D. thesis, Univ. of Wisconsin, (1967).

24- Shipinki, J.H, Myers, P.S. and Uyehara, O.A., A spray-droplet model for diesel combustion, Proc. Instn mech. Engrs, Vol 184 Pt 3J, 28-35, (1969-70).

25- Ogasawara, M. and Sami, H., A study on the behaviour of a fuel droplet injected into the combustion chamber of a diesel engine, SAE, paper 670468 (1967).

26- Shahed, S.M., Chiu, W.S. and Lyn, W.T., A mathematical model of diesel combustion, in combustion in Engines, Instn.Mech. Engrs, 1975.

27- Hiroyasu, H., and Kadota, T., Models for combustion and formation of nitric oxide and soot in direct injection diesel engines, SAE, paper 760129, (1976).

28- Elkotb, M.M. and Rafat, N.M., Fuel spray Trajectory in diesel engines, Transactions of ASME J. of Engng for power, 100, 326, April 1978.

29- Elkotb, M.M., Elsabilgi, H.M. and Diab, M.R., Spray behaviour inside a swirl chamber of diesel engine, proc. of 1st Conf. of Mech. Power Engng, vol. 11. Cairo, 1977.

30- Schweitzer, P.H., Mechanism of disintegration of liquid Jets, J. Appl. Phys., 8, 513 (1937).

31- Parks, M. Polonski, C. and Toye, R. Penetration of diesel fuel sprays in gases, SAE, paper 660747, Chicago (1966).

32- Burt, R. and Troth, K., Penetration and vaporization of diesel fuel sprays, Diesel Engine Combustion, Proc. Instn. Mech. Engrs, 184 Part 3J, 147 (1970).

33 - Dent, J.C., A basis for the comparison of various experimental methods for studying spray penetration, SAE, paper 716571, (1971).

34 - Taylor, D.H. and Walsham, B.E., Combustion Processes in a medium speed diesel engine, Diesel Engine combustion, Proc. Instn. Mech. Engrs, 184, Part 3J, P 67, (1970).

35 - Riehm, W., Untersuchungen Uber einspritz vorgang bei diesel maschinen, Z.V.D.I. 68, No. 25 (1924).

36 - Triebnigg, H., Der einblase und einspritzvorgang bei diesel maschinen, J. Springer, Wien (1925).

37 - Sitkei, G., Krafstoffaufbereitung und verbennung bei diesel motoren, J. springer-verlag (1964).

38 - Mehlig, H., Zur physik der brennstoffstrahlen in diesel maschinen, A.T.Z., 37, No.16 (1934).

39 - Hakki OZ, I., Calculation of spray penetration in diesel engines, SAE, paper No. 690254 (1969).

40 - Wakuri, Y. et al, study on penetration of fuel spray in diesel engines, J. Japan soc. Mech. Engrs, 3, (1960).

41 - Catton, I. et al., Study of liquid jet penetration in a hypersonic stream, A.I.A.A. Jl 6, (1968).

42 - Adler, D. and Lyn, L.T., The steady evaporation and mixing of a spray in a gaseous swirl, Int. J. Heat and Mass Transfer, 14, 793, 1971.

43 - Crowe, C.T., A computational model for the gas droplet field in the vicinity of an atomizer, Western states section, The comb. Inst., paper No. 74, 25, (1974).

44 - Gosman, A.D. and Johns, R.J.R., Computer Analysis of Fuel-air mixing in direct-injection engines, paper accepted for presentation at 1980 SAE congress, Detroit. (1980).

45 - Elkotb, M.M., Rafat, N.M. and Abdel Meguid, S.M., Droplet distribution in open combustion chamber of diesel engines

5th Int. Symposium on combustion processes, Poland, 1977.

46 - Elkotb, M.M., Rafat, N.M. and Abou Elleil, M.M., Theoretical behaviour of fuel spray in gas turbine combustion chamber, Bull. of Faculty of Engng, Cairo University, paper 9, 1976.

47 - Ingebo, R.D., Vaporization rates and drag coefficients for isooctane sprays in turbulent air stream, NACA Tech, Note 3265, 1954.

48 - Bird, R.B., Stewart, W.E. and Lightfoot, E.N., Transport Phenomena, John Wiley and Sons, 1960.

49 - Elwakil, M.M., Uyehara, D.A. and Myers, P.S., A theoretical investigation of the heating up period of injected fuel droplets vaporising in air, NACA TN 3179, 1954.

50 - Viropoff, D.N., Evaporation of fuel drops, Bull. of the Central Scientific Aviation Institute, vol.3, 1939.

51 - Ranz, W.E. and Marshall, W.R., Evaporation from drops Part I. and 2, Chemical Eng. Progress, vol 48, 141, (1952).

52 - Iskander, A.M., Prediction of spray Motion on the swirl chamber walls of diesel engines, Msc dissertation supervised by Elkotb, M.M., 1980.

53 - Elkotb, M.M., Spray Modelling for Multifuel engines, First Annual T.R., European Research Office, U.S. Army July 1980.

54 - Elkotb, M.M., Spray Modelling for Multifuel engines, 2nd Annual T.R., European Research Office, U.S. Army, 1981.

55 - Lord Rayleigh, On the stability, of jets, Proc. London Math. Soc. vol 10, 4, Nov. 1878.

56 - Weber,C., Zum Zerfalleines Flussigkeitsstrahls, Angew. Math.U. Mech.II, 136, 1931.

57 - Lishefsku, A.S. About the boundaries of the Jet diintegration regimes, J. of the Institute News,Energy USSR, No.1 1964.

58 - York, J.L. Stubbs, H.F. and Tek, M.R., The mechanism disintegration of liquid sheets, Trans ASME, vol.75, 1279, 1953.

59 - Rabin, E., Schallenmuller, A.R. and Lawhead , R.B., Displacement and shattering of propellant drops, AFOSR TR60-75, Final Report, March (1960).

60 - Burstein, S.Z., Hammer, S. and Agostu, V.D., A spray combustion model with droplet break up including gas dynamic coupling, U.S. Air Force Office of Scientific Research, AFOSR No. 433, June (1961).

61 - Lambiris, S., Combs, L.P. and Levine, R.S.,Stable combustion processes in liquid propellant rocket engines, Combustion and Propulsion , Fifth AGARD Colloquim, 569,(1962).

62 - Azzopardi, B.J., Measurement of drop sizes, Int.J. Heat Mass Transfer, 22, 1245,(1979).

63 - McCreath, C.G. and Beer, J.M., A review of drop size measurement in fuel sprays, Appl. Energy 2,3 (1976).

64 - Swithenbank, J., Beer, J.M., Taylor, D.S. , Abbot, D. and McCreath, G.C., A laser diagnostic for the measurement of droplet and particle size distributions, Exp. Diagnostics Gas Phase Combustion Systems. Prog. Astonaul. Aeronauti 53, 421 (1976).

65 - Farmer, W.M., Measurement of particle size, number density and velocity using a laser interferometer, Appl. Optics 11, 2603 (1972).

66 - Fristrom, R.M., Jones , A.R., Schwar, M.J.R. and Weinberg, F.J.,Particle sizing by interference fringes and signal coherence in Doppler Vilocimetry, Faraday Symp. Chem. Soc.7, 183 (1973).

67 - Elkotb, M.M., Abou-Elleil, M.M. and Rafat, N.M., Droplet size distribution in a hollow conical sprays, The Bull. of the Faculty of Engng, paper 8 (1977).

68 - Elkotb, M.M., Rafat, N.M., and Sayed, M.I. Fuel droplet size distribution in diesel engines, Proc. of Ist conference of

Mechanical Power Engng, Vol.II, (1977).

69 - Hiroyasu, H. and Kadota, T., Fuel droplet size distribution in diesel combustion chamber, SAE paper No.740715 (1974).

70 - Hiroyasu, H., Toyota, Y. and Kodota, T., Transient characteristics of droplet size distribution in diesel sprays, The Ist Int. Conference on Liquid Atomization and Spray systems , paper 5-3, Tokyo (1978).

71 - AbdAllah, M.A., Atomization of multifuel sprays in diesel engines , Msc dissertation supervised by Elkotb, M.M.(1981)

72 - Mugele, R.A. and Evans, H.D., Droplet size distribution in sprays, Ind. Eng. Chem. ,vol.43, No.6, 1317 (1961).

73 - Rosin, P. and Rammler, E., The laws governing the fineness of powdered coal, J. Inst Fuel, 7, 29 (1933).

74 - Tanasawa, Y. and Tesima T. , On the theory of combustion rate of liquid fuel spray, Bull. of JSME, 1,36, (1958).


MED
8